ATOMISTIC SIMULATION STUDIES OF LITHIATED MnO_2 NANOSTRUCTURES

by

KENNETH MOMPATI KGATWANE

RESEARCH THESIS

Submitted in fulfilment of the requirements for the degree of

DOCTOR OF PHILOSOPHY

in

PHYSICS

in the

FACULTY OF SCIENCES AND AGRICULTURE

(School of Physical and Mineral Sciences)

at the

UNIVERSITY OF LIMPOPO

SUPERVISOR: Prof P.E. Ngoepe

2020

DEDICATIONS

TO

My late grandmother Elizabeth Gadifele Ramorola who inspired the bookworm in me

My family, Mereki, Maria, Kedibone, Johannes, Jeffrey, Bakang Kgatwane

Close relatives

My former teacher the late Mrs Dolly Seroke

DECLARATION

I declare that the thesis hereby submitted to the University of Limpopo (Turfloop Campus) for the degree of Doctor of Philosophy (PhD) in Physics has not been previously submitted by me for a degree at this or any other university; that it is my work in design and in execution, and that all material contained herein has been duly acknowledged.

28 May 2020

_____ _____

Kenneth Mompati Kgatwane **Date**

ACKNOWLEDGEMENTS

I offer my sincere gratitude to my supervisor Prof. Phuti E. Ngoepe for his patience, motivation, indispensable ideas, valuable discussions and continuous guidance throughout this PhD thesis.

A special thanks to Dr Dean C. Sayle in the University of Kent who provided valuable discussions and insight especially in the work of mechanical properties, Prof. Richard Catlow in University College London for his comments that contributed towards the improvement of this research work, and Beauty Shibiri and Njabulo P. Sithole for their contributions on microstructure diagrams.

Many thanks to the members of the Materials Modelling Centre research laboratory for engaging discussions in research and sharing ideas.

I acknowledge the National Research Foundation (NRF) for providing financial support and the Centre for High Performance Computing (CHPC) for providing the much needed computational resources.

I would also like to thank my family, especially my mother and father Maria and Mereki Kgatwane, who supported throughout writing this thesis and in my life.

Finally, I give thanks to God for spiritual guidance.

ABSTRACT

We employ molecular dynamics simulations, using DL_POLY code, to study the structural behaviour of β-MnO_2 cathode material during discharging through lithium-ion intercalation into the bulk, nanoparticle, nanorod, nanosheet, and nanoporous β-MnO_2. It is shown that lithium-ions have an average coordination number of about 5.70 and prefer surface sites with high oxygen coordination. The average lattice parameter values at intercalation of 0.85 Li/Mn are found to be under 4% relative to the experimental values obtained at 0.92 Li/Mn. Moreover, all the lithiated β-MnO_2 structures did not collapse at 0.85 Li/Mn as observed in the β-MnO_2 mesoporous in experimental work. As lithium is limited, sodium is a good alternative charge carrier in lithium-ion batteries. As a result, we have also performed studies on sodium intercalation into bulk, nanoparticle, nanorod, nanosheet and nanoporous β-MnO_2. The microstructures and radial distribution functions show that the β-MnO_2 structures could be intercalated up to 0.24 Na/Mn without any obvious structural degradation. Beyond this sodium concentration, the microstructure collapses and become amorphous thus predicting a potentially lower capacity for Na-MnO_2-β batteries. Also, as the voltage is an important factor in the energy density of lithium-ion batteries, we have studied the trends in the average intercalation potentials in relation to the various nano architectures. The trend, in increasing value of average intercalation potentials, were found to be bulk structure, nanorod, nanosheet, nanoporous and nanoparticle. This suggests that nanostructuring can enhance cell voltage.

Mechanical properties studies on the pure and lithiated bulk and nanorod β-MnO_2 were also performed through uniaxial compressive and tensile strain application. The results show that under compressive strain the bulk structure and nanorod mitigate stress through the contraction and collapse of the inherent tunnel structures, known to cause electrochemical inactivity, and also through the shifting of the MnO_6 octahedral planes. The collapsing of tunnels was found to occur more on the bulk structure and less on the nanorod, while the MnO_6 octahedral plane shifts were found to occur more on the nanorod and less on the bulk structure. Unoccupied 1x2 or conjoined 1x2 were found to result in structural collapse irrespective of the host nanoarchitecture. The X-ray diffraction pattern

plots suggest that lithium intercalation and compressive stress application have a similar impact on the underlying structure of the various nanostructures. The microstructure analysis for bulk β-MnO_2 under tensile strain reveals that fracture occurred in the brookite region and along the dislocation/stacking fault. The nanorod β-MnO_2 mitigated stress through a rutile-to-brookite phase transition which occurred in the unstrained $Li_{0.73}MnO_2$-β and under tensile strain in Li_xMnO_2-β for x = 0.00, 0.03, 0.12, and 0.24. In both the bulk and nanorod β-MnO_2 the brookite phase was succeeded by structural breakdown leading to fracture and served as an indicator for imminent structural failure upon more tensile strain application.

TABLE OF CONTENTS

LIST OF FIGURES

LIST OF TABLES

Chapter 1

Introduction & Background

1.1 Introduction on Lithium-ion Batteries

Global warming which is caused by carbon dioxide, methane and other greenhouse gases that are released into the atmosphere through the burning of fossil fuels is predicted to detrimentally impact the planet as a whole through a dangerous climate change. This has prompted world governments, such as those in the Paris climate agreement [1], to formulate and implement a mandatory strategy for reducing greenhouse emissions. The use of batteries in electric vehicles provide a potential solution for curbing greenhouse emissions in the motor industry. Also, the generation of electrical energy from renewable resources such as sunlight, wind and rain and its storage in batteries within electrical power grids can help mitigate greenhouse gas emissions produced from electrical energy generation through the burning of coal. Moreover, modern technological devices such as cameras, mobile phones, and computers have placed an ever-increasing demand for portable power sources. In order to satiate these demands, battery technologies capable of providing high storage capacities and high rate capabilities are required. Lithium-ion batteries can meet these demands because they can provide more energy per unit weight [2] and can deliver high rate capabilities [3]. However, lithium is a limited resource and the potentially high demands from renewable energy storage in grid applications and electric vehicles will require large amounts of lithium [4] which would create a shortage in lithium and high lithium prices. The higher abundance of sodium makes sodium-ion batteries an attractive alternative to lithium-ion batteries and sodium-ion batteries have been shown to provide competitive energy and power densities [5]. However, the relatively larger sodium ion size can cause increased volume

expansion during intercalation and thus more research pertaining to sodium intercalation is required.

A battery is a device that converts the chemical energy contained in its active materials directly into electric energy by means of an electrochemical oxidation-reduction (redox) reaction [6]. The first-generation lithium-ion battery consists of a graphite negative electrode and a $LiCoO_2$ positive electrode separated by a non-aqueous electrolyte (Figure 1-1). On charging, lithium ions are deintercalated from the layered $LiCoO_2$ intercalation host, pass through the electrolyte, and are intercalated into the graphite layers within the anode. The electrons pass around the external circuit (load) and into the anode thus producing electrical power.

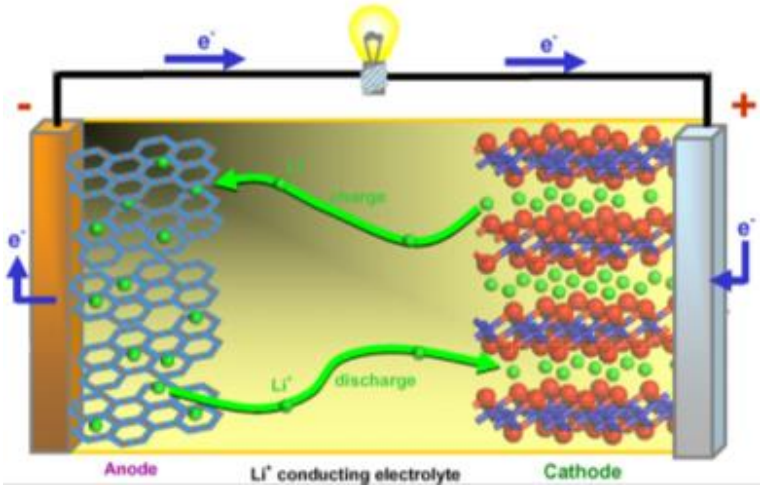

Figure 1-1: Schematic representation of a lithium-ion battery. The negative electrode is graphite and the positive electrode is $LiCoO_2$ [7].

Lithium is attractive as a battery anode because the lithium-ion has the most negative reduction potential [2] and thus the lowest tendency to be reduced to a metallic state. Moreover, the lithium metal has a higher electrochemical capacity (3860 $mAhg^{-1}$) versus graphite (360 $mAhg^{-1}$) and the greatest quantity of charge per unit weight. As lithium is a limited resource, sodium is an attractive alternative charge carrier to lithium because it is abundant. Electrolytes used in batteries may be aqueous or solid [2]. To maximize cell performance the electrolyte should have metal

ion conductivity but should be an electronic insulator in order to avoid internal short-circuiting. High ionic conductivity is essential to minimize the ohmic resistance and achieve good rate capability [8].

Current first-generation lithium-ion batteries available in the market have capacities that range from 550 mAh to 2.5 Ah for portable applications and up to 45 Ah for motive power and stationary applications [9]. However, cobalt is expensive and environmentally toxic when compared to manganese. This has led to the exploitation of transition metal oxides as a replacement for $LiCoO_2$, particularly the MnO_2 systems.

Nanomaterials have the potential to improve the performance and capacity of rechargeable lithium-ion batteries and thus address the portable power demands of applications such as hybrid electric vehicles and clean energy storage from renewable energy sources [3, 10, 11]. Reducing the dimensions of electrode particles from micrometre to the nanometre scale significantly increases the rate of lithium insertion/removal because of the short distances for lithium-ion transport. The nanoparticulate materials have a high contact area with the electrolyte and hence a high lithium-ion flux across the interface which is due to their high surface area [12]. However, the porosity between the particles is random in shape and size. Therefore some pores will be too small for effective lithium-ion transport, while others will be too large thus resulting in reduced volumetric energy density [13].

Mesoporous materials may be used instead of nanoparticles. Such materials are composed of micrometre-sized particles and contain pores of nanometre dimensions. The pores are identical in size and are separated by walls of similar thickness. Because the particles are of micrometre dimensions, fabrication into cathodes is similar to dense micrometre-sized particles with a similar packing density. The internal pores can be flooded with the electrolyte leading to a high contact area with the electrode. The ordered pores ensure even distribution of the

electrolyte within the electrode surface. The wall thickness and pore size can be adjusted in order to increase rate performance and maximize volumetric energy density [13]. However, mesoporous materials may be more difficult to synthesize than the nanoparticles.

1.2 Literature Review

Manganese is the 10th most abundant element in the Earth's crust and it's oxidised at the earth's surface to form more than 30 manganese oxide/hydroxide minerals [14] which are found in a wide variety of soils and sediments. Manganese oxides participate in a wide variety of redox and acid-base reactions in the environment because they form interfacial barriers on soils and sediments in marine and freshwater environments and on rock and other mineral surfaces [14, 15]. The high adsorption capacities of manganese oxides allow them to be used in the purification of contaminated water where they can adsorb phosphates [15] and trap heavy metals [16] or as catalysts [17].

Although it was first used as a depolarizing agent in Zinc/Ammonium Chloride/Carbon battery by Leclanché in 1866, MnO_2 has also found application as a cathode material in dry cell batteries [18]. These batteries provided much better performance than the Leclanché cells. γ-MnO_2 which is categorised natural manganese dioxides, chemical manganese dioxides and electrolytic manganese dioxides has been used predominantly as a cathode in alkaline cells. Some of the earliest MnO_2 secondary batteries include the Zn/MnO_2 cells with electrolytes salts such as $NHCl_4$ (Leclanché cells), $ZnCl_2$ and KOH. During discharge, the protons are inserted into the interstitial sites of the cathode which is accompanied by a simultaneous reduction of manganese ions by the electrons introduced in the external circuit in order to maintain electrical neutrality [19]. MnO_2 phases such as the layered-type (δ-MnO_2 or birnessite-related MnO_2) have also been tested as possible cathode materials for Zn/MnO_2 rechargeable cells with $ZnSO_4$ as the

electrolyte. The cathodic charge/discharge involves the dissolution of MnO_2 to Mn^{2+} during discharge and the re-deposition of Mn^{2+} ions to MnO_2 during charging. These cathodes lose their initial capacity within a few cycles due to improper discharging and the formation of basic zinc sulphate on the cathode surface [20].

1.2.1 Structural Properties of MnO_2

Among all the metal oxides (MO_2), MnO_2 has a series of most complex structures such as α-, β-, R-, γ-, δ-MnO_2 polymorphs with distinct properties [21]. The most active forms known as γ- and ε-MnO_2 were difficult to characterize due to the defects they incorporate [21]. Both these compounds are known to be non-stoichiometric and contain some protonic species. Moreover, the manganese dioxides comprise internal tunnel structures with sizes comparable to those of cations spanning from hydrogen to caesium and can, therefore, act as host lattices for insertion and extraction of cations, and hence charge which is central to electrochemical performance. In addition, MnO_2 comprises a complex microstructure such as that found in the γ-MnO_2 polymorph which is widely used as a cathode material in primary alkaline batteries. This microstructure, which includes the De Wolff disorder, microtwinning [21] and point defects, governs the electrochemical [22] as well as the mechanical properties [23] of the material. The De Wolff disorder is likely to influence the electrical conductivity, ion-exchange, ion-absorption and gas reactivity within the material [22].

The manganese atoms in MnO_2 polymorphs are often octahedrally coordinated [21] where the MnO_6 octahedrons form the basal crystallographic building blocks found in all manganese oxide type compounds. These octahedrons share edges and corners in order to form tunnel structures of different sizes crucial for intercalation. The relative stability of these MnO_2 compounds is greatly affected by their magnetic properties as reported by D. Balachandran et al [24]. The computational generation of the MnO_2 nanostructures results in the introduction of defects such as the De

Wolff disorder thereby forming pyrolusite and ramsdellite-like domains which are the building blocks of γ-MnO_2 [22].

Pyrolusite

Pyrolusite, also known as β-MnO_2, is the most stable, densest and abundant polymorph of manganese dioxide [14, 21]. It consists of a hexagonal close-packed lattice of oxygen ions with manganese cations occupying half the octahedral sites. Pyrolusite is tetragonal with a space group of $P4_2/mnm$ and lattice parameters of a = 4.40 Å and c = 2.88 Å [3, 25]. It is formed by a three-dimensional network of edge and corner-sharing MnO_6 octahedra arranged in simple chains. This kind of arrangement leads to the formation of 1x1 tunnel structures (Figure 1-2). Thus pyrolusite is isostructural with titanium dioxide (TiO_2). However, the tunnels in pyrolusite are considered to be too small to accommodate other chemical species. β-MnO_2 has a band gap of 1 eV [26].

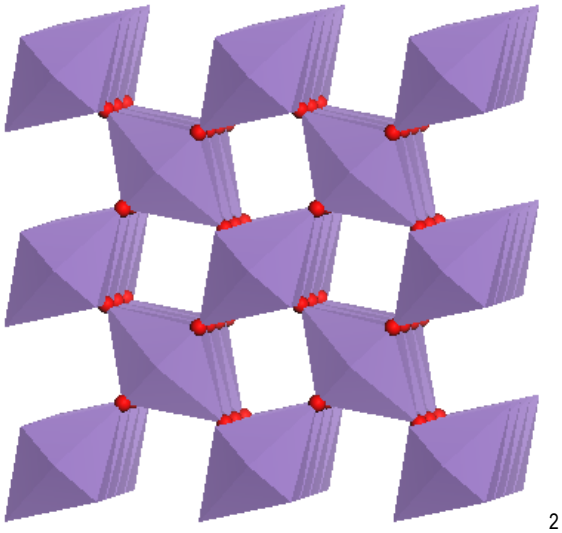

Figure 1-2: Crystal structure of pyrolusite viewed down the 1x1 tunnels [25]. Manganese is coloured purple and oxygen is red.

Ramsdellite

Ramsdellite (R-MnO_2) is a rare mineral found in low temperature hydrothermal deposits and it is often mixed with pyrolusite. It is orthorhombic with a space group of *Pbnm* and its structure consists of a hcp anionic lattice but the ordering of the cations is different from the rutile arrangement. In the ramsdellite structure, two adjacent single MnO_6 octahedral chains form a double chain that shares octahedral edges. The double chains are then connected to others by sharing corners, forming a framework consisting of rectangular tunnels that are 2x1 octahedra (Figure 1-3) in size [14]. These tunnels usually contain small amounts of water and cations that stabilize the structure [27, 28]. Ramsdellite is isostructural with goethite (FeOOH) and gibbsite (AlOOH).

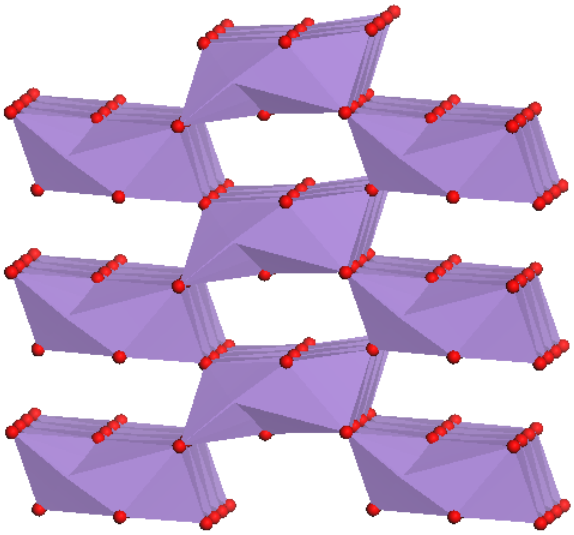

Figure 1-3: The crystal structure of ramsdellite [29] viewed down the 2x1 tunnels. Manganese is coloured purple and oxygen is red.

γ-MnO_2

The electrochemically active polymorph of MnO_2 used in batteries today is referred to as γ-MnO_2 [24]. Based on the method of production, γ-MnO_2 can be categorised into natural manganese dioxides (NMDs), chemical manganese dioxides (CMDs) and electrolytic manganese dioxides (EMDs). Pyrolusite, ramsdellite, ε-MnO_2 and

other polymorphs are said to comprise γ-MnO_2 where ramsdellite is thought to be the dominant structure in γ-MnO_2 [30].

The γ-MnO_2 polymorph is a highly disordered material. This disorder which broadens and leads to selective extinction of X-ray diffraction reflections [21] is thought to be due to a variety of structural features. Based on x-ray diffraction patterns, De Wolff proposed that γ-MnO_2 is a random intergrowth of pyrolusite and ramsdellite where the boundary between the two units is referred to as the De Wolff defect. However, the model cannot account for most features of X-ray scattering data of γ-MnO_2 such as the lack of resolution on most γ-MnO_2 X-ray diffraction patterns. In particular, it cannot explain the characteristically broad and diffuse X-ray diffraction peaks.

The most popular defect model of MnO_2 was proposed by Ruetschi [24]. This model states that the crystal structure of MnO_2 is based on a closely packed array of oxygen and that vacancies occur only on the cationic lattice. Cation vacancies and Mn^{3+}/Mn^{4+} are compensated for by four protons. The protons are present in the form of OH^- ions which replace the O^{2-} ions in the anionic lattice without significant changes in the lattice parameters. Because Ruetschi's model is based on an ideal ramsdellite structure it cannot account for the XRD patterns of all manganese dioxides.

Chabre and Pannetier introduced the concept of microtwinning [21] in γ-MnO_2 in order to explain the nature of the diffusion peaks. Microtwinning generates new local environments for manganese ions located in the twinning plane. In the ideal ramsdellite structure, each Mn^{4+} ion has 4 in-plane nearest neighbour Mn^{4+} ions. In the twinned structure some of the Mn ions have 5 in-plane nearest neighbour Mn^{4+} ions. According to Chabre and Pannetier, the formation of a twin is favourable in the presence of either Mn^{3+} ions or Mn vacancies. The XRD patterns obtained by incorporating both the De Wolff disorder and microtwinning closely matched those obtained from experiments. Heuer et al studied the microstructure and

crystallography of electrolytic manganese dioxide (EMD) using transmission electron microscopy and discovered that not only did EMD comprise approximately 15% pyrolusite and 50% ramsdellite but also 30% of ε-MnO_2.

Bowden studied lithiation of bulk heat-treated electrolytic MnO_2 (HEMD) which is a defect pyrolusite structure formed from the rearrangement of ramsdellite MnO_2 [31]. During discharge, pyrolusite is lithiated in an irreversible process where the lattice rearranges to recreate ramsdellite. This is followed by the additional lithiation of the ramsdellite. The material cycled well achieving 80% of MnO_2 theoretical capacity.

1.2.2 MnO_2 Nanostructures

The one-dimensional β-MnO_2 nanorods were synthesised by Kim et al from solid-state precursors MnO, Mn_2O_3, β-MnO_2 and $Li_2Mn_2O_4$. It was found here that the formation of β-MnO_2 was dependent on the oxidation of manganese (≤3). The nanorod prepared from the MnO precursor had the highest capacity ranging 240-290 $mAhg^{-1}$ at the fifth cycle when used as a lithium intercalation cathode. It was concluded that this capacity had resulted mainly from adsorption of lithium-ions at the nanorod surfaces [10]. Thus the authors attributed the performance of the nanorod relative to the bulk sample to larger surface areas they possess.

Jiao and Bruce synthesized the mesoporous β-MnO_2 with a highly ordered pore structure by impregnating the mesoporous silica template (KIT-6) precursor possessing a highly ordered 3D pore structure with an aqueous solution of $Mn(NO_3)_2$, heating under air to 400 °C, then dissolving the SiO_2 template to leave a replica of a mesoporous structure [3]. Zhou et al also synthesised this type of mesoporous β-MnO_2 using the same technique for applications in supercapacitors [32]. Adding to the success of Bowden and his colleagues, Jiao and Bruce [3] lithiated this crystalline mesoporous β-MnO_2 and showed that the material could accommodate large amounts of lithium ions (Li/Mn = 0.92:1) with a capacity retention of 81%. The removal of lithium resulted in the restoration of lattice dimensions and

minimal distortion of the β-MnO_2. These studies suggest that the mesoporous structures have a higher specific capacity and can cycle longer than other nanostructures while retaining their structural integrity. Studies concerning adsorption of lithium ions on β-MnO_2 surfaces were performed by Mellan et al. where it was found that lithium preferred sites that were highly oxygen-coordinated [33].

1.2.3 Simulated MnO_2 Nanostructures

In order to study properties of MnO_2 nanoarchitectures through atomistic simulations, realistic models of MnO_2 comprising the microstructure and defects observed in experiments are needed. These defects include dislocations, substitutions, vacancies, stacking faults, grain boundaries and twinning. However, manually adding these structural features into crystalline pyrolusite does not yield the x-ray diffraction patterns observed in experimental work [21]. Generating models of MnO_2 nanostructures using the simulated amorphisation and recrystallisation technique allows for a natural evolution of most structural features that exist in a real system. The evolution of the structure depends solely on the interatomic potentials and the lattice misfit rather the intuition of the simulator [34]. In summary, the process of generating the various MnO_2 nano-forms involved cutting a cube of about 24696 atoms from the crystalline bulk MnO_2 material, placing it at a basis position within the cell, amorphising it by increasing the lattice parameter by 36.3 % to induce strain, and running a molecular dynamics simulation at 2000 K. The nanorod was then generated by reducing one cell dimension so that the neighbouring amorphous nanoparticles could agglomerate along one dimension through periodic boundary conditions. The nanosheet was generated by reducing two cell dimensions, while the nanoporous was generated by reducing three cell dimensions. Finally, a constant volume molecular dynamics calculation was performed for each MnO_2 nanoarchitecture until crystallisation was achieved [35]. The external view of the A&R prepared MnO_2 structures to be used in this study and their corresponding experimental counterparts, if available, are presented in Figure 1-4 to Figure 1-7.

The simulated nanoparticle and nanorod have diameters of 7.6 nm and 6.4 nm, respectively, while the nanosheet has a thickness in the range of 2.3 to 8.8 nm with a channel diameter of about 5.4 nm.

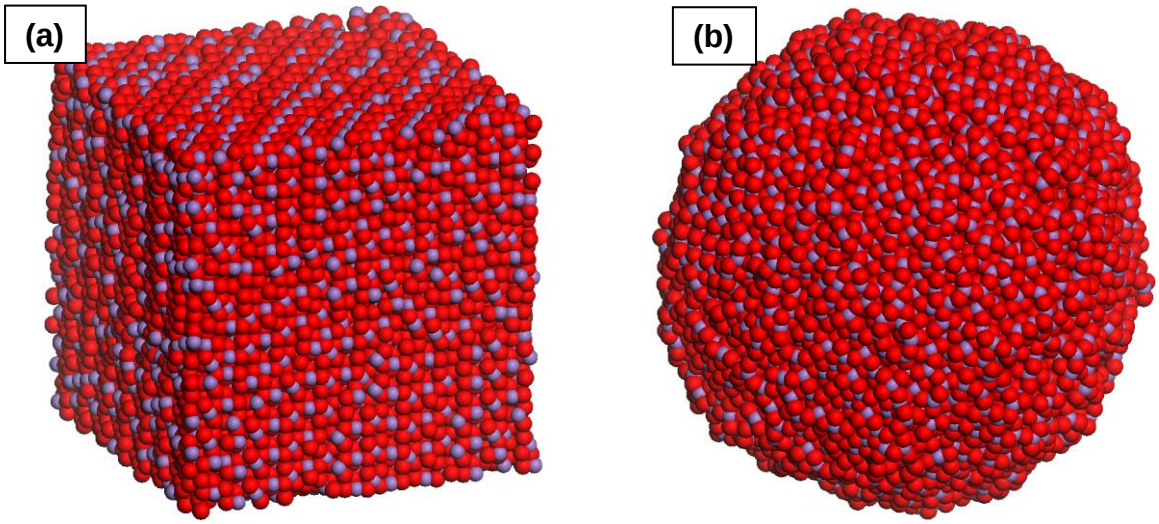

Figure 1-4: External view of the simulated β-MnO_2 (a) bulk structure and (b) nanoparticle.

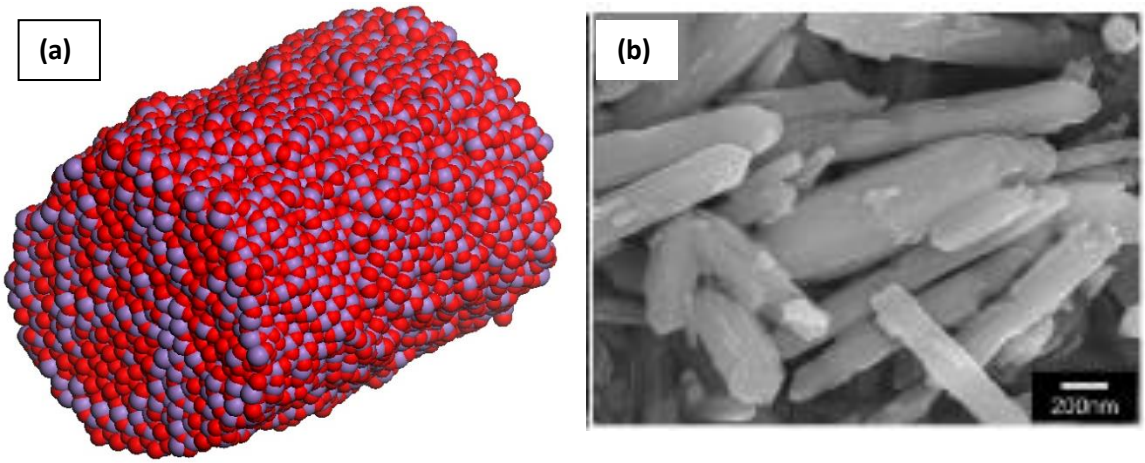

Figure 1-5: External view of (a) a simulated β-MnO_2 nanorod and (b) SE-TEM image of β-MnO_2 nanorods of Kim et al [10].

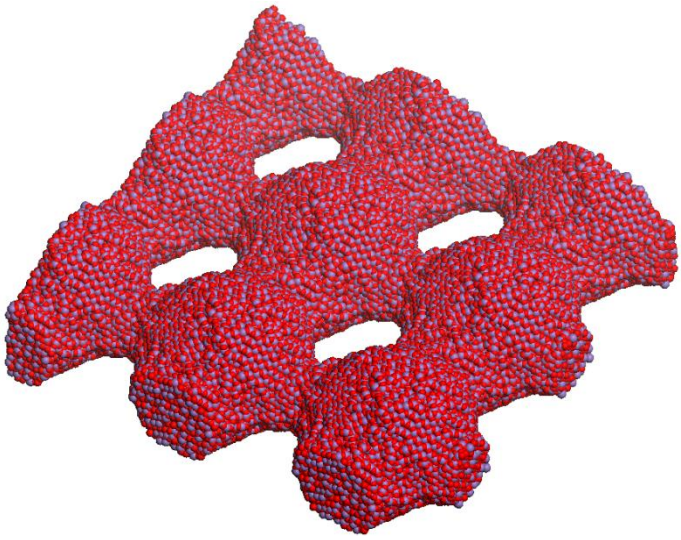

Figure 1-6: External view of the simulated β-MnO_2 nanosheet.

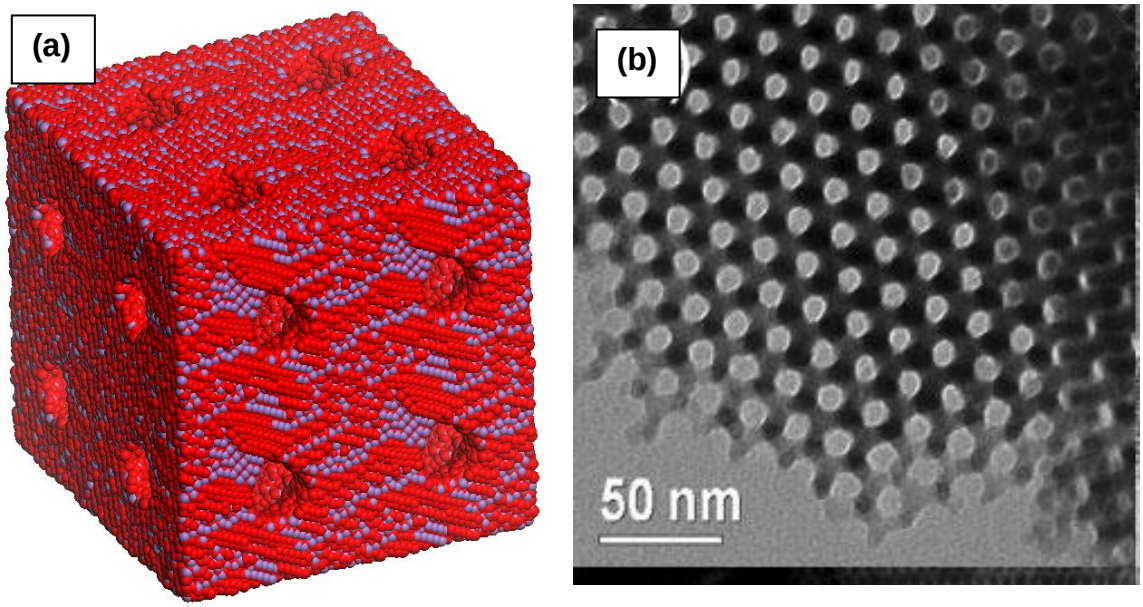

Figure 1-7: (a) External view of the simulated β-MnO_2 nanoporous. (b) A TEM image of the mesoporous β-MnO_2 [3].

These models resemble the real system in terms of defects and the complex microstructure as can be seen in Figure 1-8 below.

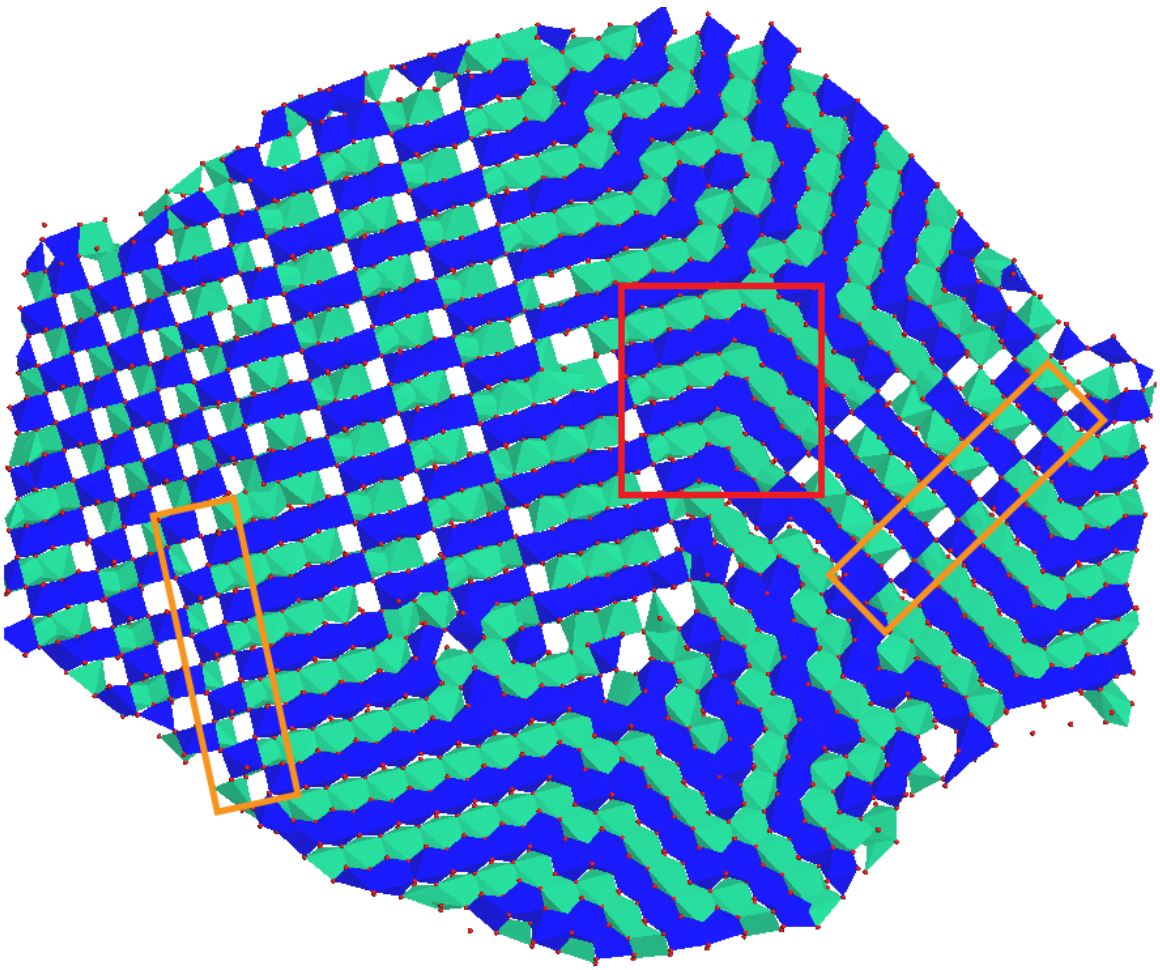

Figure 1-8: Microstructural slice of the nanosheet β-MnO_2 generated via the amorphisation and recrystallization technique showing. Rectangles depict microstructural features that exist in real materials.

1.2.4 Simulated Mechanical Properties

Studies on mechanical properties of the lithiated/discharged bulk and nanoporous β-MnO_2 was conducted by Sayle et al [23, 36]. In the first study, intercalation was performed by incorporating lithium-ions into the amorphous MnO_2 followed by the crystallisation of the whole system [23] into a nanoporous morphology. It was shown that the $Li_{0.16}MnO_2$ nanoporous deformed via grain boundary sliding resulting in the amorphization of grain boundary regions. On the second study, lithium-ion intercalation on the crystallised bulk and nanoporous MnO_2 structures was

performed by a program described in section 2.7 of this thesis. It was found here that plastic deformation and fracture took place through the sliding of grain boundaries along the thinnest nanoporous walls. It was reported that under compressive stress the 1x1 tunnels contracted within the bulk structure and remained unchanged within the nanoporous. The pores or channels within the nanoporous assisted in the mitigation of stress.

1.3 Research Problem

1.3.1 Problem statement

Manganese dioxide (MnO_2) is a promising cathode material for use in lithium-ion batteries because it offers a higher energy density, higher rate capability, is non-toxic and is relatively inexpensive. These attractive properties have prompted intensive research on MnO_2 compounds which has been focused mostly on understanding the structural evolution of MnO_2 during charging and discharging [2] in relation to crucial cathode material properties such as high rate capability, high capacity, capacity retention [3, 31] and high volumetric energy density. The characteristic behaviour of MnO_2 cathodes is still not fully understood and consequently hinders its applications in electric vehicles and intermittent energy storage from renewable sources that are vital in curbing carbon dioxide emissions and reducing the dependence on fossil energy sources. Numerous experimental methods such as X-ray diffraction (XRD), Scanning Electron Microscopy (SEM), Transmission Electron Microscopy (TEM) [3, 4], Magic Angle Spinning (MAS), and Nuclear Magnetic Resonance (NMR) have been used to study the properties of MnO_2 but are limited in their ability to characterise the structural properties of MnO_2 at the nanoscale [5]. Computational modelling techniques and analysis tools including molecular graphics can aid in studying properties that are difficult or currently impossible to obtain using experimental methods.

1.3.2 Significance of the study

South Africa is the largest producer of manganese in the world and accounts for about 33% of global manganese production. Moreover, South Africa is believed to have the highest reserves of manganese globally totalling about 70% [37]. Of the mined manganese about 80% [38] is exported mainly as ore for beneficiation and the products derived from the ore are then imported back at a higher cost. Despite having the highest manganese production and the highest manganese reserves in the world, South Africa is still lagging in terms of mineral beneficiation i.e. the process of transforming the manganese mineral into higher-value products. This study contributes to the knowledge base required to produce high-value products, stage 4 of mineral beneficiation [39], that derive from beneficiation of the manganese mineral in South Africa such as the manganese dioxide (MnO_2) compounds used as cathode materials in lithium-ion batteries. Moreover, good battery technologies are required in order to meet energy storage demands in power grid applications and electric vehicles [4, 5] or replace the lithium-ion batteries which are dependant on the environmentally limited lithium.

This research aims to take advantage of the nanoarchitecture which can enhance the properties of cathode materials such as specific capacity, voltage and rate capability [3, 13] or produce materials with new properties such as the structurally resilient nanoporous [36]. In addition, nanostructuring can improve charge carrier ion transport and intercalation kinetics in previously electrochemically inactive materials such as the bulk β-MnO_2 resulting in high specific capacities [40]. Mechanical properties are important in characterising the dynamical behaviour of MnO_2 nanomaterials. The key to fully understanding the mechanical properties of MnO_2 lies on its complex, feature-rich microstructure which transforms during charging and discharging [19, 21]. The simulated amorphisation and recrystallization technique allows for generating bulk and nano-architectured MnO_2 structures comprising microstructural features and defects observed in experimental samples [21, 22, 23,

35, 36, 41, 42]. These structures can be studied in a simulated cathode environment through atomistic simulation techniques where the dynamical behaviour of MnO_2 in response to localised stress caused by intercalation or external stress applied to the material. This will aid experimental work in further understanding MnO_2 structural properties at the atomic and nano-scale levels. The resulting knowledge is essential in the development of cathodes that are vital in the storage of renewable energy through lithium-ion or sodium batteries which if used could help mitigate the country's current electrical power demand problems.

1.3.3 Aim of the study

The aim of this research is to study the structural, mechanical properties and intercalation potentials of the bulk structure, nanoparticle, nanorod, nanosheet and nanoporous manganese dioxide during discharging for application as cathode materials in lithium-ion batteries. A deduction on the mechanisms of structural transformation and structural degradation will be provided.

1.3.4 Objectives of the study

(i) Develop a computer algorithm for intercalating lithium and sodium into the nanoparticle, nanosheet, nanorod, nanoporous and bulk structures comprising about 25 000 atoms.
(ii) Develop a program code that reads the DL_POLY STATIS file and calculates the strain values relative to each applied stress value needed for the calculation of mechanical properties.
(iii) Investigate the evolution of microstructural features of the various nanostructures with respect to lithiation and uniaxial compressive stress loading. Such information will shed insights on how the changes in elasticity of the nanostructures are related to atomistic details.
(iv) Validate the calculated results with experimental information and make predictions on lithium concentrations that lead to structural breakdown of the

MnO_2 cathodes, which should guide experiments on the extent of charging and discharging of lithium-ion batteries.

(v) Estimate and investigate the trends in the intercalation voltages of the nanoparticle, nanosheet, nanorod, nanoporous and bulk structures

1.3.5 Outline of this Thesis

Chapter 1: An overview concerning the motivation for the use of lithium-ion batteries, lithium-ion battery model, the technical aspects that impacts the performance and lifespan of lithium-ion batteries, current problems, and intentions of this research study. A literature review on the manganese mineral, applications of manganese dioxides, and desirable properties of manganese dioxide cathode in lithium-ion battery applications.

Chapter 2: Molecular simulation methods and all of the theoretical methodologies necessary to understand this research are presented in detail. A description of the program code that intercalates our nanostructures is described.

Chapter 3: Analysis and discussions on the results of the lithium and sodium intercalated bulk, nanoparticle, nanosheet, nanorod and nanoporous β-MnO_2 using various techniques. Discussions on the approximated average intercalation potentials.

Chapter 4: Analysis and discussions on the results of the mechanical properties of lithiated bulk and nanorod β-MnO_2.

Chapter 5: Conclusions of this research are summarised.

Chapter 2

Methodology

2.1 Introduction

Atomistic simulations can bridge the gap between theory and experiment [43] by giving insight into the nature of real systems [44]. This is accomplished by characterising accurately the behaviour of molecular systems such protein folding [44] in structural biology and predicting the properties of materials such as structural, mechanical, thermal, electrical, etc. that are not readily accessible to laboratory experiments [45]. The combination of simulation, experiment and theory has proven much more effective in obtaining physically useful results than any single approach or pair of approaches [46]. Quantum mechanics provides a true description of matter by solving the Schrödinger equation [47]. However, the system size which quantum mechanics-based simulation codes can handle is limited to a few hundred atoms which is not adequate to sample the whole phase space. Simulation codes based on classical methods can perform large-scale simulations. Recent advances in high-performance computing systems resulting in over 100 petaflops of computation [48] have fostered large-scale simulations comprising up to approximately three million atoms [49].

All dynamical simulations in this study are performed using the DL_POLY simulation package [50] which is essentially a molecular dynamics code based on classical methods. These simulations are based on the Born model of ionic solids. A brief overview of molecular dynamics theory follows.

2.2 Molecular Dynamics (MD)

In MD the system to be studied is simulated by an ensemble of particles or atoms contained within a simulation box called a supercell. Periodic boundary conditions are used to infinitely replicate the supercell in three dimensions. The motion of particles is normally assumed to be classical and governed by Newton's laws, and the forces are treated as acting centrally along lines drawn between pairs of particles. The simulation progresses by iteratively solving classical Newton's equations of motion for all particles within the simulation box after a small time-lapse Δt [45]:

$$x_i(t + \Delta t) = x_i(t) + v_i(t)\Delta t \tag{2.1}$$

$$v_i(t + \Delta t) = v_i(t) + \frac{f_i(t)}{m_i}.\Delta t \tag{2.2}$$

where m_i, x_i, and v_i are the mass, position and velocity of the *i*th particle while f_i is the total force acting upon the *i*th particle. The forces are calculated from the derivatives of the interatomic potentials. The verlet algorithm can also be used [50]. The choice of Δt is very important and must be smaller than the time scale of any important dynamical processes at the atomic or molecular level. MD simulations are considered as a rich simulation technique because it yields dynamic data as well as structural information [51].

2.3 Potential Models

Atomistic simulation techniques use analytic functions to describe interactions between ions in a crystal. The basis for these functions is to calculate the total interaction energy often called the lattice energy and requires an appropriate potential model to describe interactions in the system.

2.3.1 Born Model of Ionic Solids

The crystals are assumed to comprise spherically charged ions with formal or partial charges. The Born model of ionic solids is used to evaluate the lattice energy E_{tot} of ionic crystals as a sum of energy terms arising from the short-range and long-range interactions between ions with charges Q_i and Q_j separated by a distance r_{ij}:

$$E_{tot} = \sum_{ij} \left(E_{long-range} + E_{short-range} \right) \tag{2.3}$$

2.3.2 Rigid Ion Model

The simplest form of potential is one in which the electronic polarizability is neglected; the rigid ion model. This model is good in reproducing structural parameters for static systems. However, lattice vibrations are poorly modelled as they are strongly coupled to polarizability. Also, once a defect is introduced, polarization will be expected to occur around a defect to stabilize it. The problem of defect energies in static conditions can be handled by refitting short-range potential parameters to model the static dielectric constants overestimating the polarization due to lattice relaxation to compensate for the shortfall to the neglect of electronic polarizability and thus obtain correct defect energies.

2.3.3 Long-Range Interactions

By simplifying the interactions to include only the pairwise interaction, the long-range interaction can be easily defined. It is essentially the Coulomibc electrostatic interaction between an ion pair and can be either attractive, as in the case of oppositely charged ions, or repulsive if the charges are alike. The long-range interaction energy $E_{long-range}$ of two ions i and j with charges q_i and q_j at a separation distance of r_{ij} is described by the expression:

$$E_{long-range} = \frac{1}{4\pi\varepsilon_0}\frac{q_i q_j}{r_{ij}} \tag{2.4}$$

where ε_0 is the permittivity of free space. While the definition of the long-range interaction is simple, calculating it explicitly would be computationally expensive due to the slow rate at which contributions to the interaction energy fall off with distance (r_{ij}^{-1}). This means that for each ion, a huge number of interactions must be considered in order to compute this interaction with accuracy. Ewald developed an approximate method of calculating this summation which involves splitting the calculation into a short-range real-space component and a long-range reciprocal space component. This method is highly accurate and results in a rapid convergence of the energy when compared with that of a direct summation.

2.3.4 Short-Range Interactions

The short-range interaction can be either repulsive or have a combination of attractive and repulsive components depending on the ions that are interacting. The repulsive interaction originates from the overlap of two electron clouds of both atoms at small ionic separations. This is partly due to the Pauli Exclusion Principle with the rest of the contribution due to the nuclear-nuclear interactions. The generalized version of the Pauli Exclusion Principle states that no two fermions can occupy the same quantum state. When the electron clouds overlap the Pauli Exclusion Principle forces the ground state charge distribution of the electrons to have higher energy. This increase in energy is manifested as a repulsive force that increases in strength as the ions move closer to each other.

At slightly larger separations, an overall small attractive force exists which is generally known as the van der Waals-London interaction [52]. This attraction is due to the spontaneous formation of instantaneous dipoles on each of the interacting ions [53]. London was able to determine a general expression for this interaction by

describing it as a correlated motion of the electrons in both atoms. London found that for the case of a pair of identical ions i and j this force varies as a function of r_{ij}^{-6} where r_{ij} is the separation of the ions. Clearly, this force will be stronger for polarizable ions. The short-range interaction is clearly complex and consequently, it is possible to approximate it using a number of functional forms.

Buckingham Potential

While the electrostatic energy often accounts for the majority of the binding, the non-Coulombic contributions are equally critical since they determine the position and shape of the energy minimum. There must always be a short-ranged repulsive force between ions to counter the Coulombic attraction and prevent the collapse of the solid. The analytical function used to model the short-range potential energy in this study is the Buckingham potential. It is essentially a Lenard-Jones potential function which combines the repulsive term and an attractive van der Waals potential using the r_{ij}^{-6} dependence. The r_{ij}^{12} term is replaced by the dual parameter exponential term:

$$E_{short-range} = A_{ij} exp\left(-\frac{r_{ij}}{\rho_{ij}}\right) - \frac{C_{ij}}{r_{ij}^{6}} \tag{2.5}$$

The A_{ij} and ρ_{ij} parameters are related to the hardness and size of the ion while the C_{ij} parameter represents the attractive van der Waals interaction. The first term is the repulsive force which dominates at short distances while the second term represents the long-range attractive forces. These parameters are fitted in order to reproduce experimental data.

Potential Parameter Derivation

The parameters of the short-range analytical function $E_{short-range} = Buckingham$ were varied in order to accurately approximate the experimental properties of the

system such as the lattice parameter, elastic constants, bulk modulus, and the dielectric constants [54].

2.4 Average Intercalation Potentials

The voltage of the cell, the potential difference between the cathode and the anode, and the specific capacity of the electrodes are crucial properties that determine the energy density of a lithium-ion battery. Energy density is the product of the voltage and specific capacity. In order to design batteries with high energy densities, the voltage and specific capacity need to be increased. It is important for us to get a rough measure of the intercalation potentials and thus assess the possible energy densities that the various MnO_2 nano-architectures may be capable of. In general, the cell voltage or open-circuit voltage (OCV) is the chemical potential (μ) difference between the anode and the cathode:

$$V(x) = \frac{\mu_{anode} - \mu_{cathode}}{e} \tag{2.6}$$

where e is the magnitude of the charge on the electron. Within the anode that is comprised purely of lithium metal, the chemical potential is constant and equals to the Gibbs free energy of the lithium metal. The electrical energy, E, obtained by discharging between $Li_{x_1}MnO_2$ and $Li_{x_2}MnO_2$ is calculated by integrating the voltage multiplied by the displaced charge [55]:

$$E = \int_0^{Q_{tot}} V(x)dQ \tag{2.7}$$

$$E = -\left[G\left(Li_{x_2}MnO_2\right) - G\left(Li_{x_1}MnO_2\right) - (x_2 - x_1)G(Li)\right] \tag{2.8}$$

$$E = -\Delta G_r \tag{2.9}$$

The average intercalation potential as a function of lithium intercalated between two intercalation limits x_1 and x_2 $(x_2 > x_1)$ is calculated as follows:

$$\bar{V} = -\frac{\Delta G_r}{(x_2 - x_1)F} \tag{2.10}$$

$$\bar{V} = -\frac{G\left(Li_{x_2}MnO_2\right) - G\left(Li_{x_1}MnO_2\right) - (x_2 - x_1)G(Li)}{(x_2 - x_1)F} \tag{2.11}$$

where G is the Gibbs free energy of the compound and F is the Faraday constant. The Gibbs free energy between the charged and discharged states is given by [56]:

$$\Delta G_r = \Delta H_r - T\Delta S_r \tag{2.12}$$

where $H_r = \Delta E_r + P\Delta V_r$ is the enthalpy of the system, ΔE_r is its internal energy, P is the pressure, ΔV_r is the change in volume, T is the simulation temperature and S_r relates to the change in the vibrational and configurational entropies of ion lithium-ion insertion. For a quantum mechanical approach such as the density functional theory, the free energies can be approximated to the internal energies at 0 K because $P\Delta V_r$ and $T\Delta S_r$ is much smaller than ΔE_r [55]. Thus equation *2.11* can be approximated to:

$$\bar{V} = -\frac{E\left(Li_{x_2}MnO_2\right) - E\left(Li_{x_1}MnO_2\right) - (x_2 - x_1)E(Li)}{(x_2 - x_1)F} \tag{2.13}$$

In this study, the simulation model of lithium intercalation into MnO_2 using the DL_POLY molecular dynamics package is based on Newton's laws where the Li, Mn and O are treated as particulate ions with a fixed charge. In this model the term $P\Delta V_r$ is also much smaller than the internal energy and can be omitted with little error. DL_POLY simulations at 0 K are not permitted and we thus opted to run our simulations at 1 K instead. Moreover, DL_POLY does not calculate entropy making it difficult for us to determine if $T\Delta S_r$ at 1 K is substantial or negligible.

2.5 Mechanical Properties

After molecular dynamics (MD) simulations of the mechanical properties of the nanorod and bulk structure were concluded, the strain ε along the axis of the applied stress was calculated using the relation [57]:

$$\varepsilon = \frac{l - l_0}{l_0} = \frac{\Delta l}{l_0} \tag{2.14}$$

where l_0 is the cell length of the unstrained nanorod or bulk structure and l is the cell length. This relation produces positive tensile strain values and negative compressive strain values. We have multiplied the compressive strain values by -1 in order to get positive values for the purpose of stress versus strain plots. The Young's modulus Y is defined as the ratio of the applied stress and the resulting strain within the region of the stress versus strain plot where the stress is proportional to strain. This is quantified using the following relation [57]:

$$Y = \frac{\sigma}{\varepsilon} = \frac{\sigma}{(\Delta l / l_0)} \tag{2.15}$$

where σ is the stress due to the applied force along the axis of the force. Alternatively, as in our case, we compute the young's modulus by taking the slope of the stress versus strain plot within the region where stress is proportional to strain.

2.6 Radial Distribution Functions

The radial distribution function $g(r)$ is a useful way to describe the structure of a system. They give the probability of finding an atom or molecule in a shell δr at a distance r from another atom or molecule [58]. Consider a spherical shell of thickness δr at a distance r from the reference atom, the volume of the shell is:

$$V_{shell} = \frac{4}{3}\pi(r + \delta r)^3 - \frac{4}{3}\pi r^2 \tag{2.16}$$

$$V_{shell} = \frac{4}{3}\pi(r^2\delta r + r\delta r^2 + \delta r^3) \quad (2.17)$$

$$V_{shell} \approx 4\pi r^2 \delta r \quad (2.18)$$

For a sufficiently small δr, $\delta r^2 \approx 0$. If $\rho = N/V$ is the number of atoms per volume and dn_r is the number of atoms within the shell then $g(r)$ is expressed as:

$$g(r) = \frac{dn_r}{V_{shell} * \rho} \quad (2.19)$$

$$g(r) = \frac{dn_r}{4\pi r^2 \delta r * \rho} \quad (2.20)$$

g(r) is a dimensionless quantity. Radial distribution functions can be measured experimentally using x-ray diffraction. The regular arrangement of atoms in a crystal gives the characteristic x-ray diffraction pattern with bright, sharp spots.

2.7 Intercalation Program

2.7.1 Overview

The armophisation and recrystallisation (A&R) technique [22, 34] generates MnO_2 structures that are defect-rich and non-crystalline with wide atom-atom bond distributions [35, 22, 23, 41, 36]. Consequently, this causes an irregular arrangement of manganese atoms in the material leading to an irregular distribution of manganese cationic sites essential for lithium-ion intercalation. Because it is difficult to come up with a mathematical formula that simply identifies all the manganese cationic sites, an alternative and easier method is presented below. We have developed a lithium insertion program that generally scans A&R generated MnO_2 structures, identifies the coordinates of the octahedral sites and cations at varying concentrations. The intercalation program, Figure 2-1, was developed as part of this research project using Microsoft Visual C# 2008/2010 programming language. It can intercalate

lithium, sodium and magnesium ions into rutile-type and ramsdellite-type bulk structures directly into their respective tunnel sites. The tunnel site detection algorithm is also capable of correctly detecting tunnel sites around the surface of the nanostructures and consequently allowing for intercalation of nano-architectures with virtually any surface morphology. Intercalating a section of the bulk structure, nanoparticle, nanorod, nanosheet and nanoporous is also possible. Intercalation of amorphous structures is possible where the random coordinates are calculated from two nearest manganese neighbours.

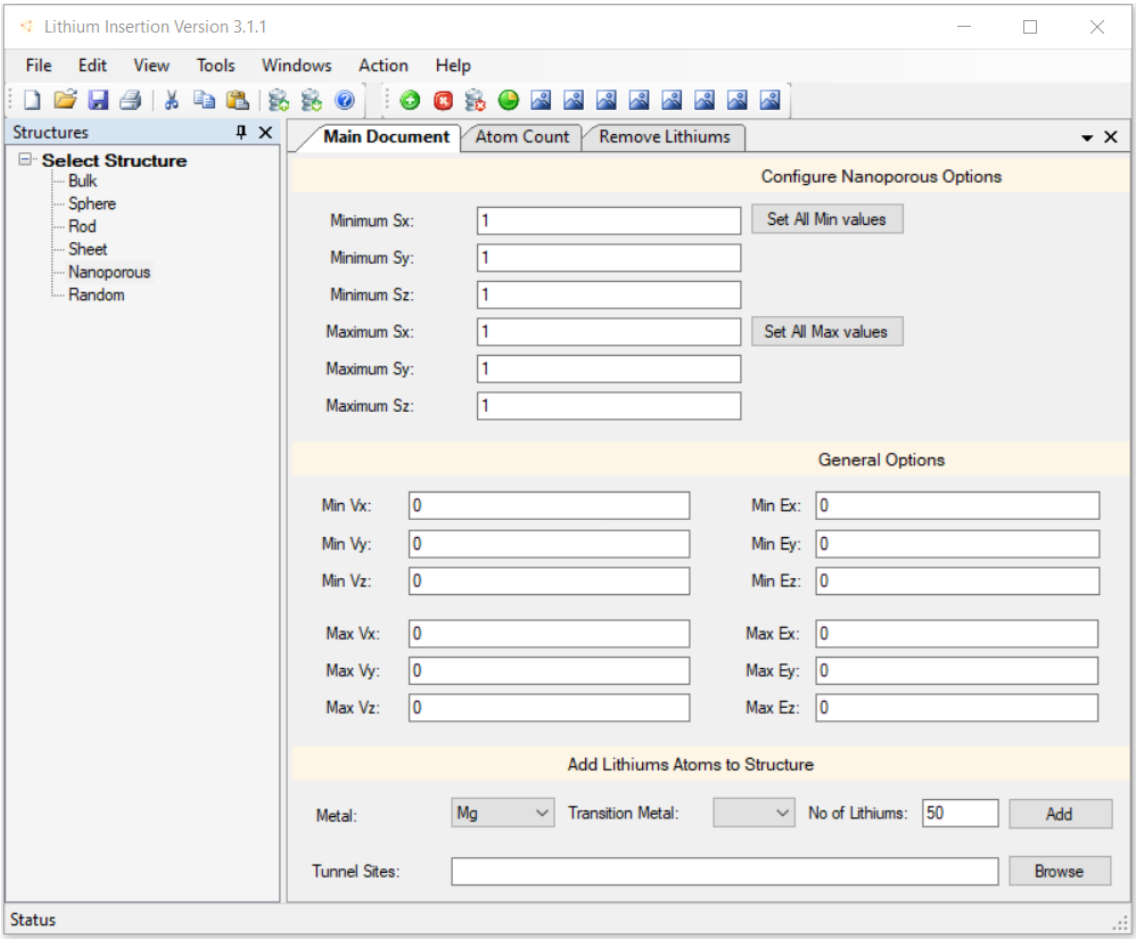

Figure 2-1: The main window of the intercalation program.

2.7.2 Finding Intercalation Sites

The pristine MnO_2 nanostructures are large and comprise 24696 atoms; 8232 manganese atoms and 16464 oxygen atoms. Additionally, they are heavily twinned with low crystallinity making it difficult to compute the coordinates of the 1x1 tunnel sites by using the knowledge of crystal symmetry and lattice constants. However, each tunnel is enclosed by four walls of linked edge-sharing MnO_6 octahedral chains with slightly varying inter-chain distances. We developed a program that uses manganese atoms in these twinning octahedral chains to calculate the octahedral tunnel sites where cations will be intercalated.

Slicing the MnO_6 octahedral chain planes and rendering in polyhedral view reveals different tunnel configurations shown in Figure 2-2 below. During intercalation, cations are placed at specific locations in the tunnels which we denote as insertion sites. The estimation of the coordinates of these cation insertion sites is calculated using the midpoint formula for different tunnel configurations. The coordinates (x, y, z) of the insertion sites depicted in Figure 2-2 (a) and (b) is calculated by using the coordinates of the two manganese atoms that are separated by an arrow in a midpoint formula:

$$(x, y, z) = \left(\frac{x_1 + x_2}{2} + \frac{y_1 + y_2}{2} + \frac{z_1 + z_2}{2}\right) \tag{2.21}$$

For a tunnel configuration in Figure 2-2 (c), the insertion site is calculated by applying the midpoint formula twice. Applying the midpoint formula once result in a coordinate in the middle of the two tunnel sites. Using the newly computed coordinate with the coordinate of one of the manganese atoms at the ends of the arrow in the formula gives the coordinate of the insertion site (yellow circle):

$$(x, y, z) = \left(x_1 + \frac{x_1 + x_2}{2}, x_2 + \frac{y_1 + y_2}{2}, z_1 + \frac{z_1 + z_2}{2}\right)$$

$$(x, y, z) = \left(\frac{3x_1 + x_2}{2}, \frac{3y_1 + y_2}{2}, \frac{3z_1 + z_2}{2}\right) \quad (2.22)$$

Finally, for a tunnel configuration in Figure 2-2 (d) the calculation of the insertion sites is performed by using the coordinates of three manganese atoms in the triangle midpoint formula:

$$(x, y, z) = \left(\frac{x_1 + x_2 + x_3}{3}, \frac{y_1 + y_2 + y_3}{3}, \frac{z_1 + z_2 + z_3}{3}\right) \quad (2.23)$$

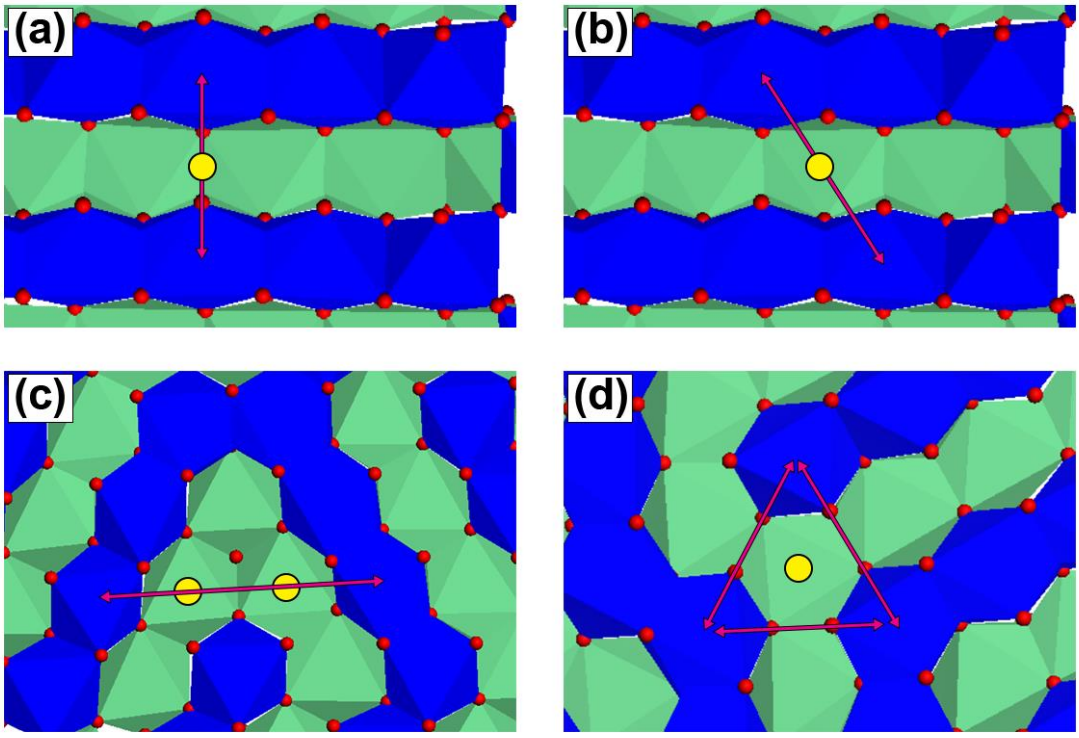

Figure 2-2: Slices cut from the nanoparticles and nanoporous showing various tunnel configurations. The yellow circles depict cation insertion sites and the arrows indicate the distance separating two manganese cations that are straddling an insertion site.

The decision of whether two or three manganese atoms can be used to compute an insertion site depends on the separation distance between them. Mn-Mn radial distribution functions of the nanostructure provide us with a good estimate of these

separation distances. The program computes the lithium insertion sites by using the separation distance between each pair of manganese atoms in the range specified by the third, fifth and ninth peaks (Figure 2-3) in the radial distribution function plot of a rutile-type structure in conjunction with the appropriate form of the midpoint formula. The insertion site is validated by first constructing a small cube with dimensions slightly larger than the Mn-O separation distance and computing the separation distance the insertion coordinate. If there is an atom (Mn, O, Li^+, etc) which is closer to the insertion site by more than 1.6 Å (provided as program input) then the insertion site is not valid and it is discarded. All valid insertion sites are then saved in a file that is later used during cation insertion into the various nanostructures. The insertion sites determined in this manner are mostly octahedral interstitials in the pyrolusite or ramsdellite type crystal lattice with a few being manganese vacancies.

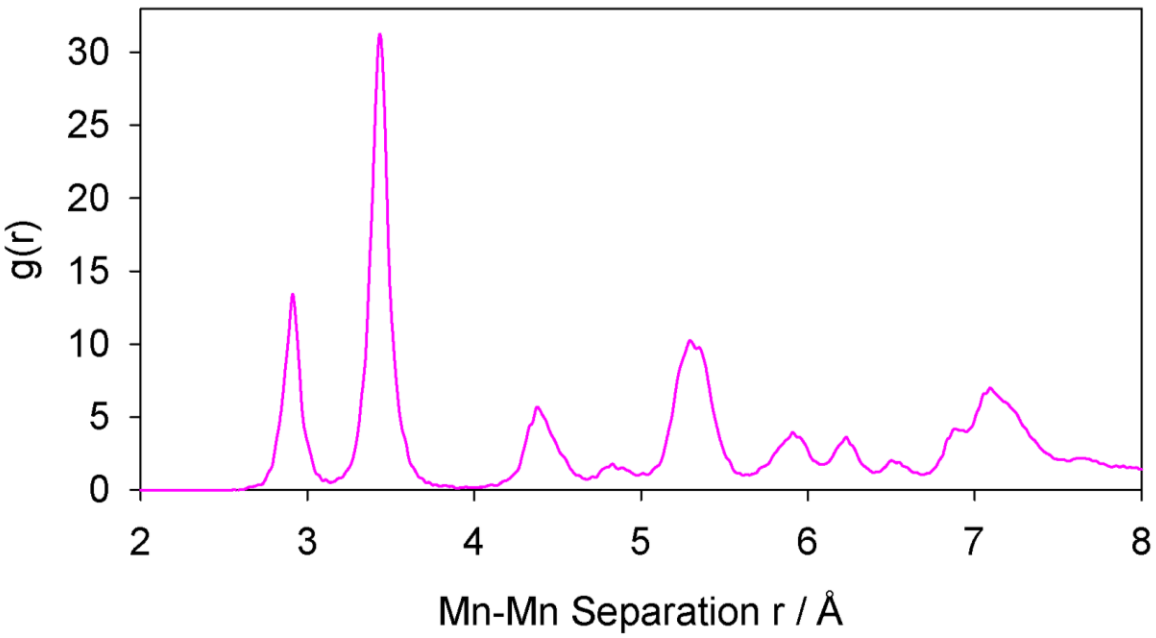

Figure 2-3: The Mn-Mn radial distribution function of the nanorod. The third peak corresponds to two Mn atoms straddling a pyrolusite tunnel in Figure 2-2 (a), while the fifth and the ninth peaks correspond to the tunnel configurations in Figure 2-2 (b) and Figure 2-2 (c) respectively.

2.7.3 Intercalation Workflows

The program uploads the coordinates of the intercalation sites from the file produced in the previous step, randomly selects a tunnel site, and inserts a cation at the chosen coordinates thus ignoring or bypassing surface intercalation dynamics like surface area, surface terminations and surface energy barriers. Charge compensation in the structure is achieved by changing the manganese atom with 4+ oxidation state (Mn^{4+}) closest to the lithium cation into the Jahn-Teller active manganese with 3+ oxidation state (Mn^{3+}). If the cation being intercalated is Mg^{2+} then two manganese atoms closest to Mg^{2+} ion are reduced to Mn^{3+}. This process is repeated for all the cations inserted into the structure. The flowcharts that describe the calculation of the insertion sites are depicted in Figure 2-4 and Figure 2-5.

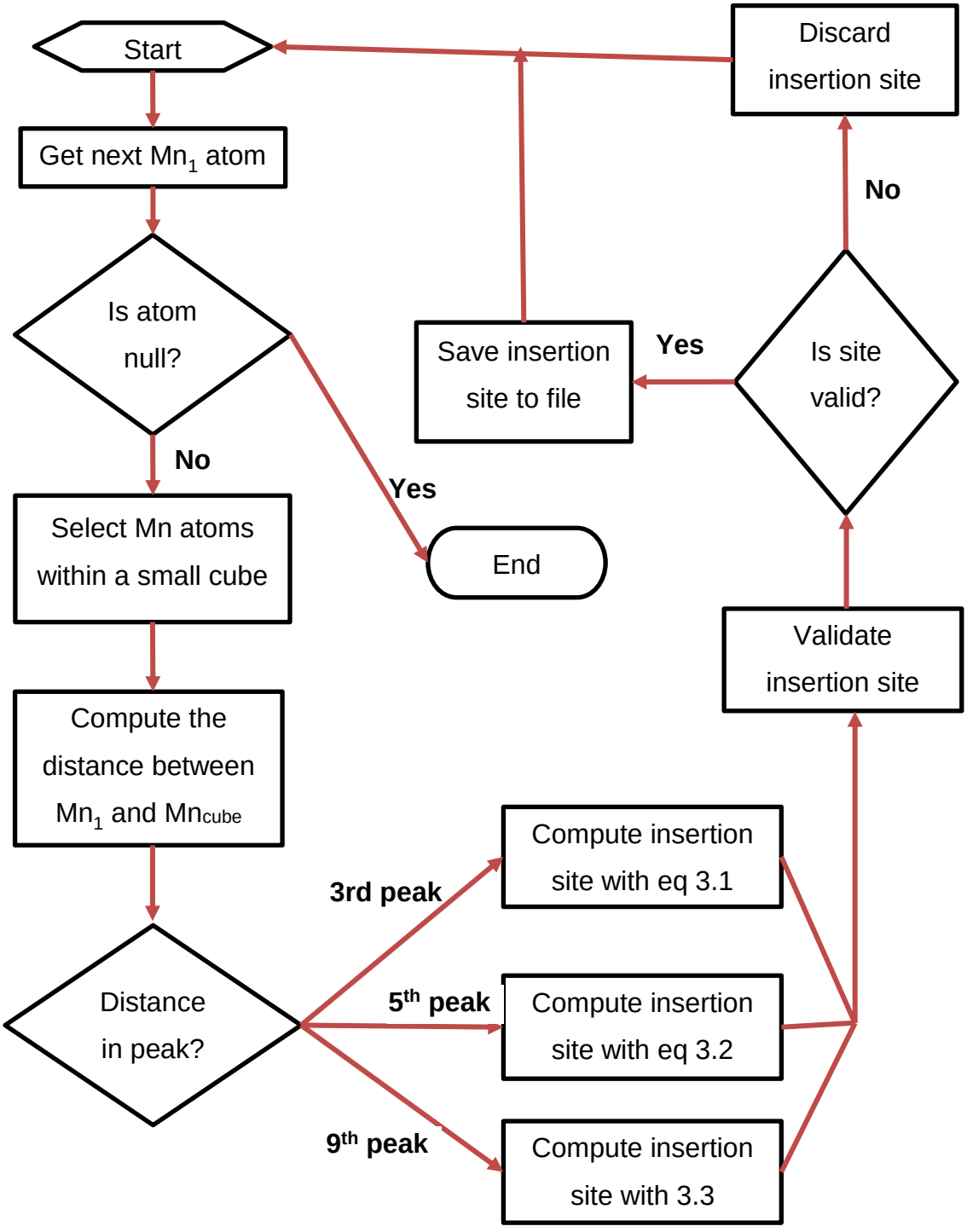

Figure 2-4: Flowchart showing how the program searches for insertion sites in the uploaded structure.

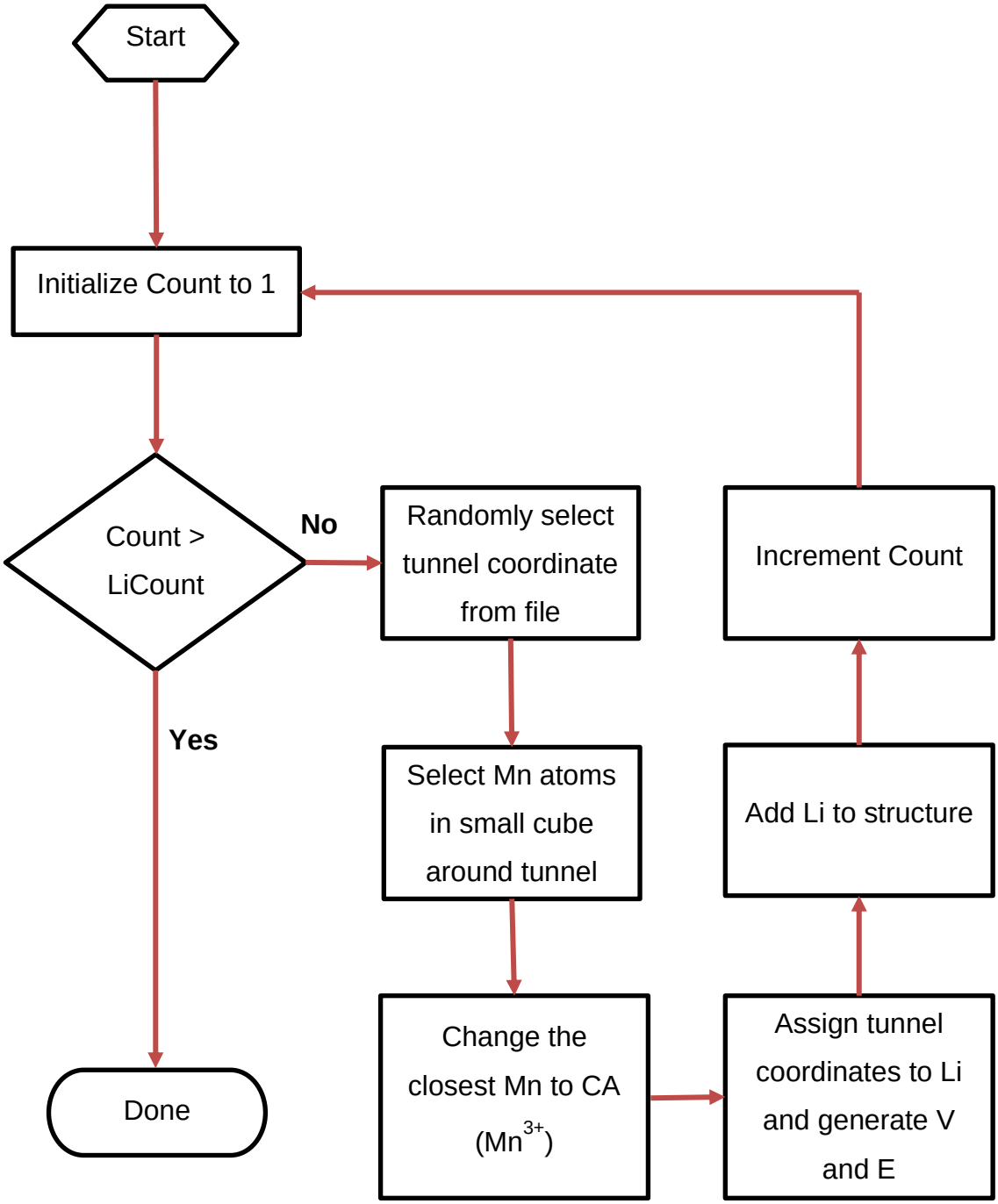

Figure 2-5: A flow chart that indicates the steps taken by the program in the lithium-ion intercalation process including charge compensation.

2.7.4 Validation of Intercalation

In order to validate the lithiation program and assess the distribution of intercalated cations, we intercalated 0.85 Li/Mn into each structure. Typical 1x1 tunnels found in these structures are shown in Figure 2-6 where the positions of the octahedral and tetrahedral sites to be intercalated are identified relative to the microstructure's orientation.

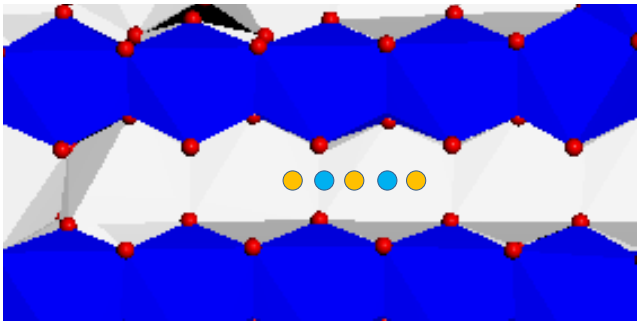

Figure 2-6: The positions of the octahedral and distorted tetrahedral interstitial sites within the 1x1 tunnel of a rutile type structure. Yellow circles represent octahedral sites while the cyan circles represent distorted tetrahedral sites.

Microstructure slices cut from the bulk structure, nanoparticle, nanorod, nanosheet and nanoporous at 0.85 Li/Mn intercalation are shown in Figure 2-7 below. The diagrams show a good placement of lithium ions inside the octahedral sites before molecular dynamics simulations. Note that the lithium ions can be inserted in two other ways; Li can also be inserted in tetrahedral sites only or in a mixture of tetrahedral and octahedral sites. The latter is applicable to experimental rutile TiO_2 where the energy difference between the tetrahedral and octahedral sites is small and the tetrahedral sites are more preferable due to their lower energy [59]. In this study, lithiation at lower concentrations is accomplished by randomly selecting a fraction of the intercalation sites from the total available sites discovered by the lithiation program. Doing this results in an even distribution of lithium cations within the structures.

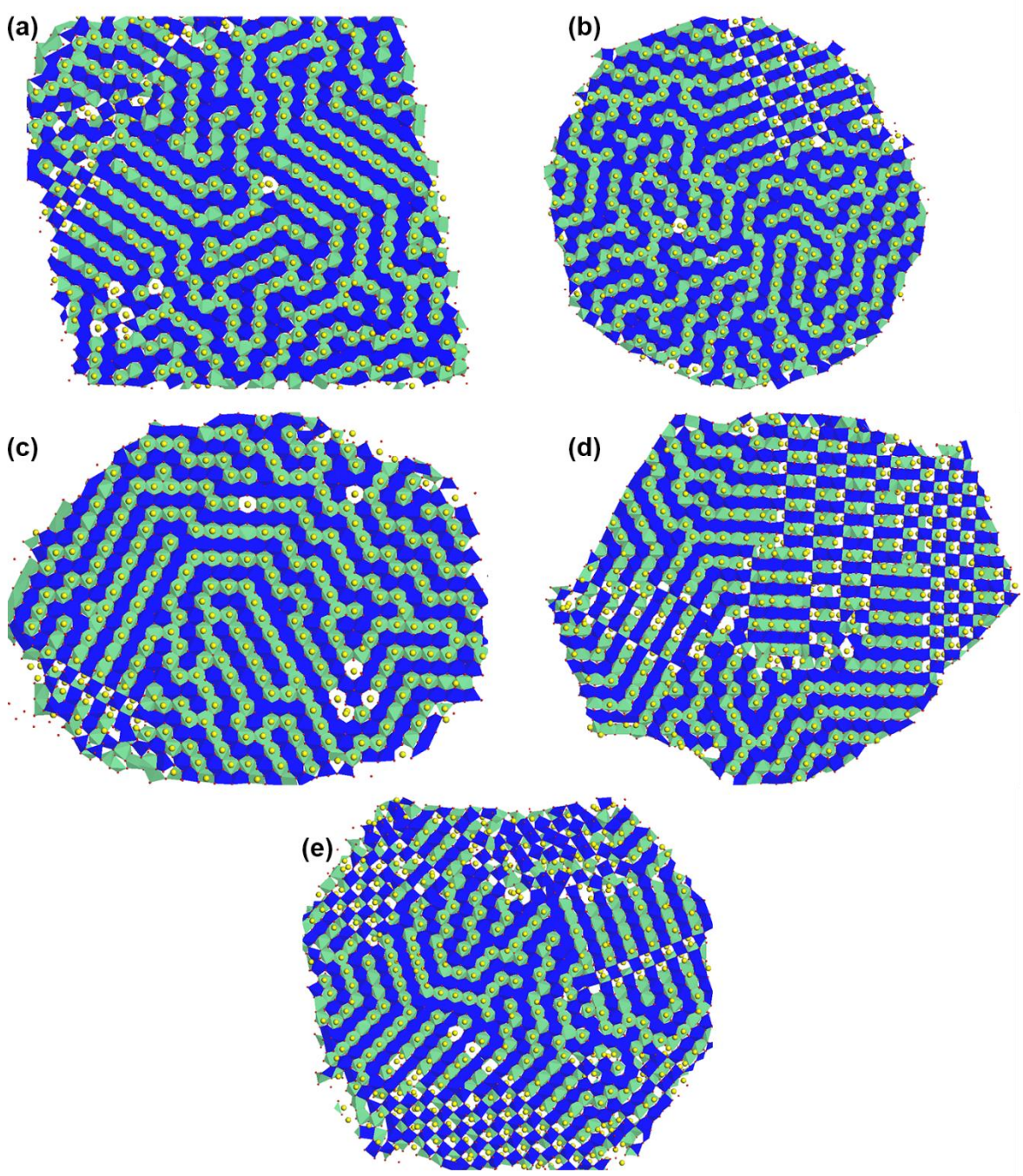

Figure 2-7: A slice cut through (a) the bulk structure, (b) nanoparticle, (c) nanorod, (d) nanosheet and (e) nanoporous MnO_2 showing the placement of the lithium ions in the octahedral sites before molecular dynamics simulations. Yellow balls represent lithium ions, while the blue and green octahedral represent the top and bottom octahedral planes respectively.

Validation of charge balancing in the bulk structure with 0.03 Li/Mn before molecular dynamics simulation is shown in Figure 2-8 below. It is readily visible that the program performed charge compensation, transfer of an electron from lithium-ion to neighbouring manganese atom, properly for lithium ions within the red rectangles. Here, each lithium-ion is located close to a manganese 3+ cation lying either on the top octahedral plane represented by a light blue colour or bottom octahedral plane represented by dark green colour. Note that 1x1 tunnels are enclosed by four MnO_6 octahedral chains and that the octahedral chains containing manganese 3+ cations located closer to the lithium-ions in pink rectangles have been removed to aid clarity.

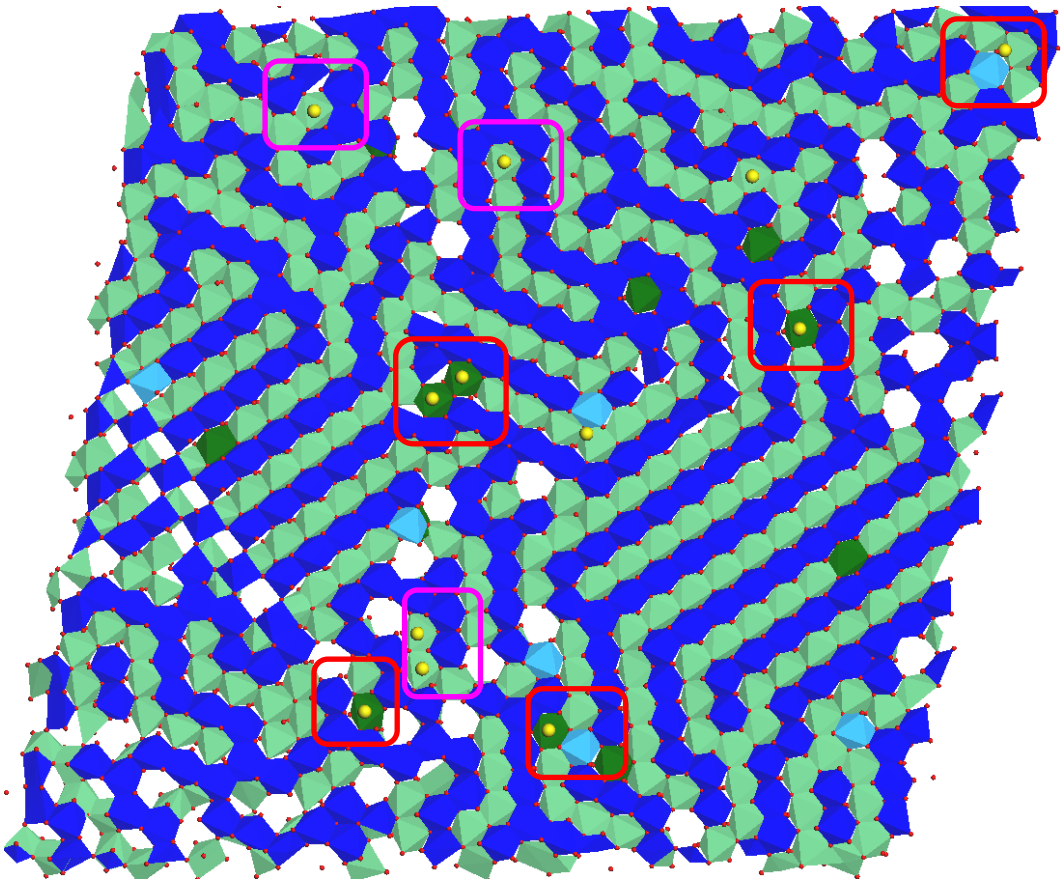

Figure 2-8: A slice cut through the bulk structure intercalated with 0.03 Li/Mn showing Mn^{4+} cations (dark blue – top layer, light green – bottom layer) and Mn^{3+} cations (light blue - top layer, dark green - bottom layer) adjacent to the respective lithium ions after charge compensation.

2.8 Simulation Details

2.8.1 Potential Method

All atomistic simulations calculations performed in this study are based on the Born model of ionic solids. The total energy E_{tot} of the system is described by equation (2.3) where the short-range and long-range analytical expressions used are represented by the Buckingham and the Coulombic forms, respectively. The potential parameters, Table 2-1, of the Buckingham interactions for MnO_2 were previously fitted [22] to reproduce the lattice parameters of pyrolusite and ramsdellite MnO_2 to within 3% and 4%, respectively. The parameters for Li-O and Li-Li were fitted by Sayle [60] for studies on Li_2O nanoparticles. These potential parameters were previously used to successfully model the generation of the chemically or electrochemically lithiated MnO_2 bulk structure, nanoparticle, nanorod, nanosheet, nanoporous as well as the Li_2O nanoparticle through the amorphisation and recrystallization technique [36, 41, 22, 60, 23, 35]. The parameters for Na-O were fitted to reproduce the lattice parameters and elastic constants of Na_2O [61].

Table 2-1: Interatomic potential parameters describing the short-range potential terms between the component ion species of Li-MnO_2

Interaction	*A*(Å)	*ρ*(Å)	*C*(eVÅ^{-6})	Charge
Mn^{4+} – Mn^{4+}	23530.5000	0.1560	16.0000	2.2
Mn^{3+} –Mn^{3+}	33883.9200	0.1560	16.0000	1.65
O^{2-} – O^{2-}	11782.7600	0.2340	30.2200	-1.10
Li^{+} – Li^{+}	270000.0000	0.1430	0.0000	0.55
Mn^{4+} – Mn^{3+}	28707.2100	0.1560	16.0000	
Mn^{4+} – O^{2-}	15538.2000	0.1950	22.0000	
Mn^{3+} – O^{2-}	18645.8400	0.1950	22.0000	
Li^{+}-O^{2-}	30000.0000	0.1540	0.00000	
Na^{+}-O^{2-}	29000.0000	0.1900	0.0000	
Na^{+}-Na^{+}	64500.000	0.1900	0.0000	0.55

2.8.2 Lithium/Sodium Intercalation

Using our intercalation program described in a prior section, the bulk, nanoparticle, nanorod, nanosheet and nanoporous β-MnO_2 were each programmatically lithiated with 250, 500, 750, 1000, 2000, 2700, 3000, 4000, 5000, 6000 and 7000 lithium/sodium ions corresponding to 0.03, 0.06, 0.09, 0.12, 0.24, 0.33, 0.36, 0.49, 0.61, 0.73 and 0.85 Li,Na/Mn fractions respectively.

All dynamical simulations in this study were performed with the DL_POLY code [50]. We performed molecular dynamics simulation (MD) of the bulk structure, nanoparticle, nanorod, nanosheet, and nanoporous within the NST, NVT, NPT, NPT and NST ensembles, respectively. The NPT ensemble was selected in order to prevent the nanorod from aggregating and forming a three-dimensional nanoporous-like structure. The NVT ensemble was needed to prevent the nanoparticles from agglomerating and forming a three-dimensional nanoporous-like structure, while the NST ensemble was suitable for allowing the bulk structure, nanosheet and nanoporous to expand independently in three dimensions. A short-range cutoff of 10 Å was used and all simulations ran for 450 ps at a temperature of 1 K. The potential parameters used to describe Li-MnO_2 are given in Table 5.1 and have been used previously to model the structure of nanoparticles, nanorods, nanosheets and nanoporous architectures [35, 22]. The bulk structure, nanorod, nanosheet and nanoporous requires that the simulation cell self-interact via periodic boundary conditions and thus a small time step was used for these structures in order to prevent the formation of unphysical stress. If the timestep is too large atoms move at high velocities resulting in large forces which in turn induces stress in the β-MnO_2 material.

2.8.3 Mechanical Properties on Bulk Structure

Uniaxial compressive stress was applied in increments of 0.01 GPa along the Y-axis of the bulk Li_xMnO_2 with lithium fractions of 0.00, 0.03, 0.12, 0.24 and 0.73. After

each stress increment, a DL_POLY molecular dynamics was performed at 300 K using an NST ensemble with a timestep of 0.005 picoseconds and 1000 steps which is equivalent to 5 picoseconds of real-time simulation. This was followed by a 5 picoseconds equilibration period, 0.005 timestep and 1000 steps, needed to mitigate the effects of high strain rate. This process was repeated until the bulk structure collapsed. An NST ensemble was selected because it allowed the bulk structure to relax by expanding in the directions perpendicular to the applied stress. Uniaxial tensile stress is simulated in the same manner as above but with successive stress increment of -0.01 GPa.

2.8.4 Mechanical Properties on Nanorod

The uniaxial compressive strain was performed on the β-MnO_2 nanorods intercalated with lithium concentrations of 0.00, 0.03, 0.12, 0.24 and 0.73. Each nanorod was first relaxed in the target NVT ensemble by running a DL_POLY MD simulation for 2000 steps and 0.005 picoseconds timestep at 300 K followed by 5000 steps of equilibration. The simulation of uniaxial compressive strain on each nanorod was implemented through a series of successive DL_POLY MD simulations. Each MD simulation was performed in the NVT ensemble for 1000 steps, 0.005 picoseconds, and equilibration of 1000 steps at a temperature of 300 K during which the cell vector along the length of the nanorod was decremented by a factor of 0.001. The rationale behind the use of the NVT ensemble is that the nanorod is provided with a fixed space along the X and Z and axes that it can expand into during compression. The NST ensemble is unsuitable in this case because during MD simulation the neighbouring nanorods move closer to each other and agglomerate forming a nanoporous-like structure. Uniaxial tensile stress is simulated in the same manner as above but with successive increment in the cell vector by a factor of 0.001.

Chapter 3

Results and Discussions: Intercalated Nanostructures

3.1 Lithium Intercalated MnO_2 Nanostructures

Figure 3-1 gives the external view of the bulk structure and the nanostructures after they were lithiated up to 0.33 Li/Mn) and undergone molecular dynamics simulations. Some of the lithium ions are visible at the surface, however since the program generally places the lithium ions in between two manganese atoms, no lithium-ion is placed on the surface but in an interstitial located near the nanostructure surface. Note, however, that some of the lithium ions may be diffused to the surfaces during MD simulation.

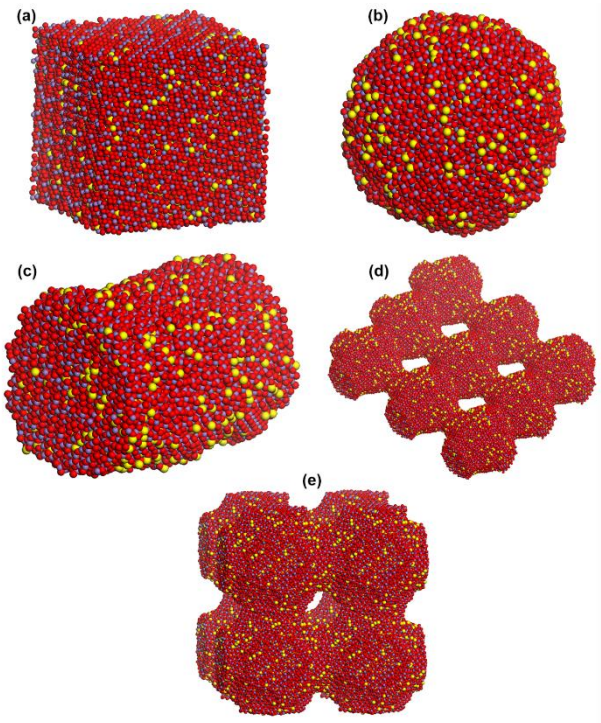

Figure 3-1: The sphere model representation of the atoms comprising the β-MnO_2 (a) bulk, (b) nanoparticle, (c) nanorod, (d) nanosheet and (e) nanoporous. Oxygen atoms are coloured red, manganese atoms (Mn^{4+} and Mn^{3+}) are coloured purple and lithium ions are coloured is yellow.

3.1.1 Lithium ions on Nanostructure Surfaces

The slice of the concave nanoporous surface depicts a defective β-MnO_2 (110) surface configuration (Figure 3-2) where Mn(5f) and Mn(6f) are the five-fold and six-fold coordinated manganese atoms respectively, and O(b) and O(i) are the bridging oxygen coordinated to two manganese atoms (all 6-fold Mn) and in-plane oxygen coordinated to three manganese atoms(two 5-fold and one 6-fold Mn) respectively (diagrams b,d).

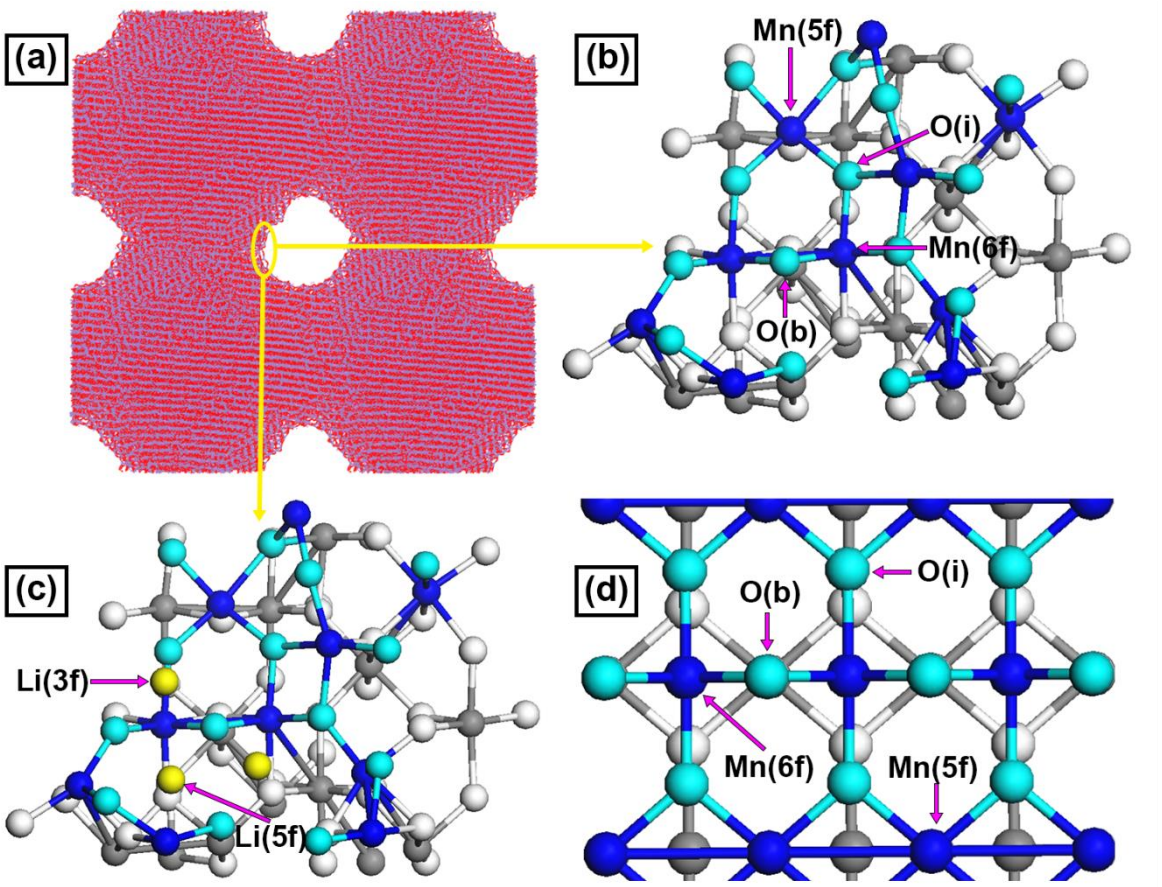

Figure 3-2: (a) Graphical representation of a concave nanoporous $Li_{0.85}MnO_2$-β surface. Microstructure slice cut from the nanoporous surface on a channel showing (b) a highly defective β-MnO_2 (110) surface configuration with lithium ions hidden, (c) β-MnO_2 (110) surface configuration with lithium ions visible, and (d) top view of β-MnO_2 (110) surface [33].

We see after molecular dynamics simulation that lithium is located on sites of high oxygen coordination as was reported in the work of Mellan et al [33]. Here the lithium can be on a Li(3f) triply coordinated site or other highly coordinated sites like the Li(5f) five-fold coordinated site. However charge transfer isn't modelled correctly by interatomic potentials; some of the manganese cations including six-fold coordinated ones on the nanocrystallite surface, have been manually reduced to 3+ oxidation state contrary to the work of Mellan and colleagues where the charge was transferred to next nearest five-fold coordinated manganese.

A slice of a channel cut from the nonporous is presented in Figure 3-3. Shown here are the entry points, arrows, to the 1x1 tunnels that are crucial for intercalating lithium ions from the electrolyte at the surface.

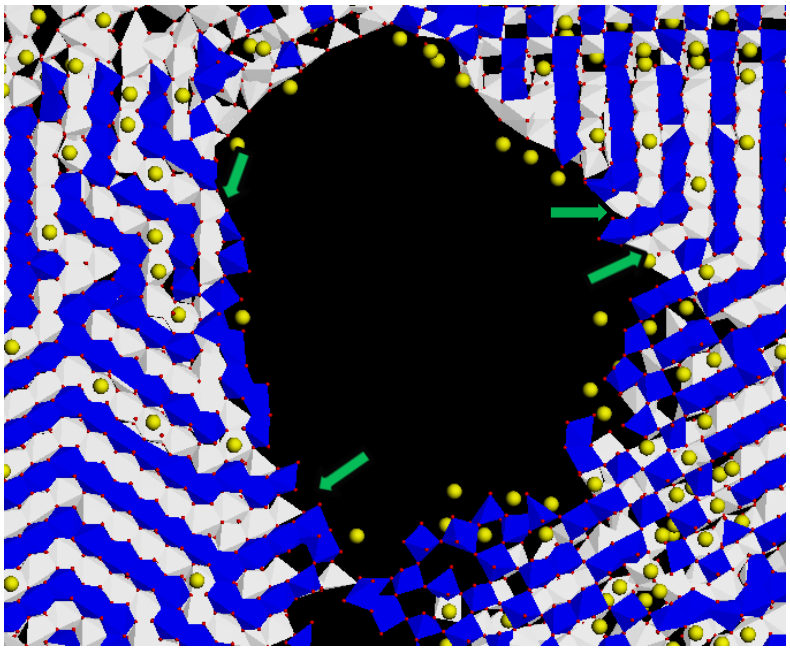

Figure 3-3: (a) The polyhedral rendering of a β-MnO_2 nanoporous channel. Blue and grey depict the top and bottom MnO_6 octahedral layers while the yellow balls depict lithium ions. Green arrows show the directions in which the lithium ions can insert.

3.1.2 Lithium-ion Distribution

We used concentration profiles in Figure 3-4 to show the relative concentration of lithium-ions within the bulk structure, nanoparticle, nanorod, nanosheet and nanoporous along (1 0 0), (0 1 0) and (0 0 1) directions. The concentration of lithium-ions within the bulk structure, diagram (a), fluctuates about a value of 1.0 for all three spatial directions indicating an even distribution. A drop in concentration at the beginning and the end indicates a low lithium-ion concentration at the surfaces. Within the nanoparticle, lithium-ion concentration is low at the edges, increases and reaches its maximum at the centre, then declines and reaches its minimum at the opposite edge along all perpendicular spatial directions (1 0 0), (0 1 0) and (0 0 1). This indicates a good lithium-ion distribution within the nanoparticle. Lithium-ion concentration within the nanorod also conforms to its three-dimensional morphology; Lithium-ion concentration across the circular part of the nanorod, diagram (b), is similar to that of the nanoparticle. The concentration is more or less evenly distributed along the long axis of the nanorod and fluctuates about an average value. Overall, the concentration profiles confirm that lithium-ions are more or less evenly distributed within the nanorod.

The nanosheet and nanoporous have concentration profiles similar to the nanoparticle but with a less concave shape. This is a result of calculating concentration profiles from a section of a nanosheet or nanoporous that is replicated during molecular dynamics simulations into a three-dimensional framework through periodic boundary conditions. The spherical-like nature indicated by the concentration profiles for these nanostructures is a consequence of a spherical shape each section has. In reality, these concentration profiles plots repeat in two dimensions for nanosheet and three dimensions for nanoporous forming sinusoidal-like shapes. We thus conclude that the nanosheet and nanoporous also have an even lithium-ion concentration.

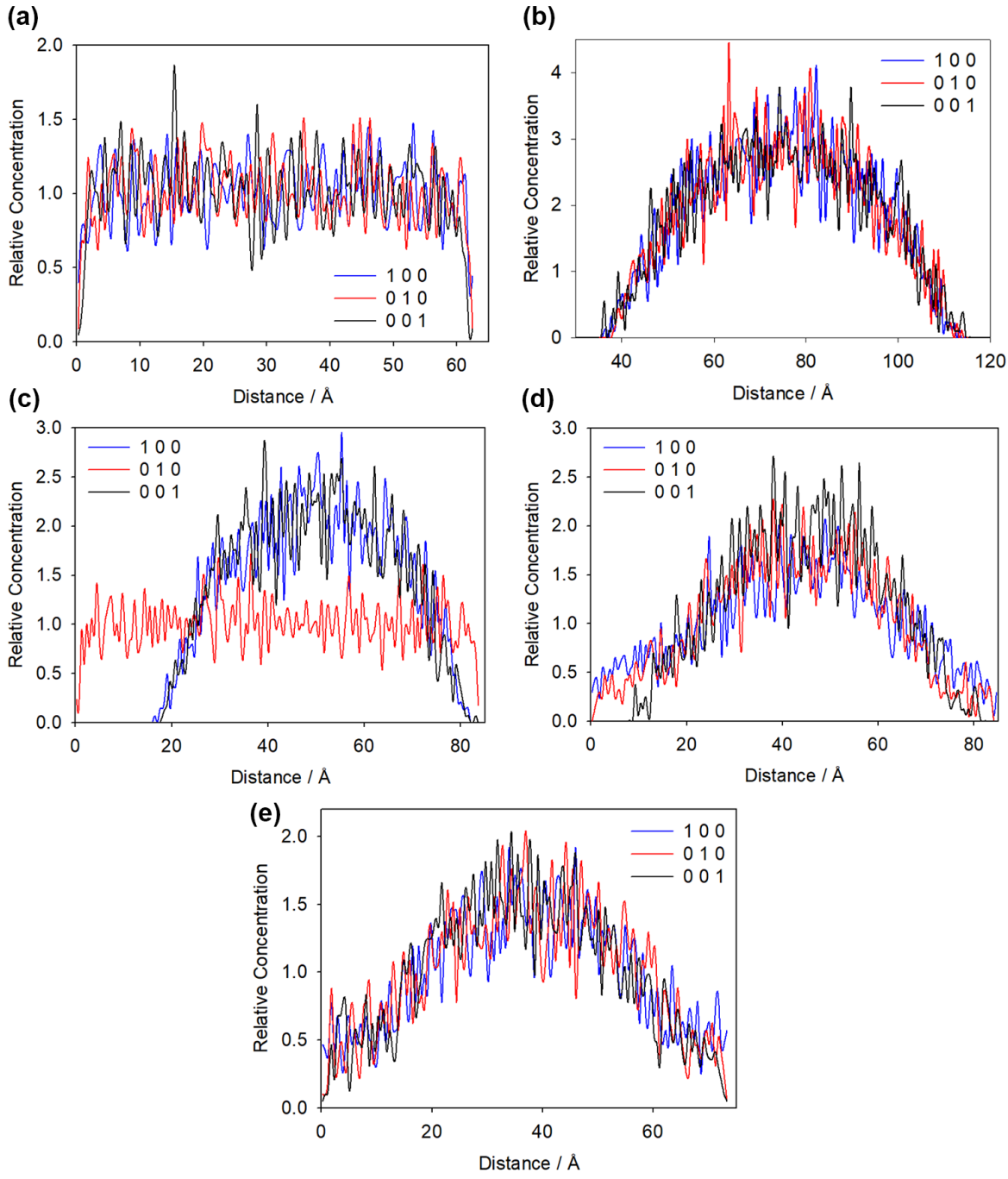

Figure 3-4: Concentration profiles for the $Li_{0.33}MnO_2$-β (a) bulk, (b) nanoparticle, (c) nanorod, (d) nanosheet and (e) nanoporous after molecular dynamics simulation.

3.1.3 Li-MnO_2 Volume Expansion

In Figure 3-5, we have plotted the change in volume versus lithium concentration for all structures. The volumes of the bulk, nanosheet and nanoporous β-MnO_2 increased monotonically with increasing lithium content, however, there was a deviation in the volume expansion from 10% lithium-ion concentration where the nanosheet and nanoporous expanded by about 1% more than the bulk structure. Between 36% and 73% lithium-ion concentration, the nanoparticle experienced the highest volume expansion which then increased non-monotonically to about 17%. This volume expansion value of 17% at 85% lithium-ion concentration is 1% higher than the one extrapolated by Sayle et al. for nanoporous β-MnO_2 at 92% lithium-ion concentration [23] in comparison to the experimental work of Jiao and Bruce [3]. We have also observed similar behaviour in the bulk and nanorod β-MnO_2. The abrupt decrease in the bulk β-MnO_2 volume expansion rate could be ascribed to the limited space the bulk β-MnO_2 could expand into, while the nanorod could have been limited by the neighbouring nanorods. The nano-architectures having the two highest surface area, nanosheet and nanoporous, achieved almost 18% volume expansion at 85% lithium-ion concentration.

On average, all nanostructures expanded slightly more than the bulk β-MnO_2 during lithiation. The sudden decrease in the expansion rate of the nanoparticle and nanorod could suggest structural modification [62]. By ignoring or bypassing effects of surface area size, exposed surface morphology and surface energy barriers [63] during lithium insertion, we were able to intercalate all nanostructures, including the bulk, up to 0.85 Li/Mn without incurring any structural collapse or transformation. This could suggest that part of the problem of low capacity observed on bulk structures [19] could be ascribed to the low accessibility of intercalation sites at the surface as opposed to the inability of the bulk structure to accommodate more lithium ions.

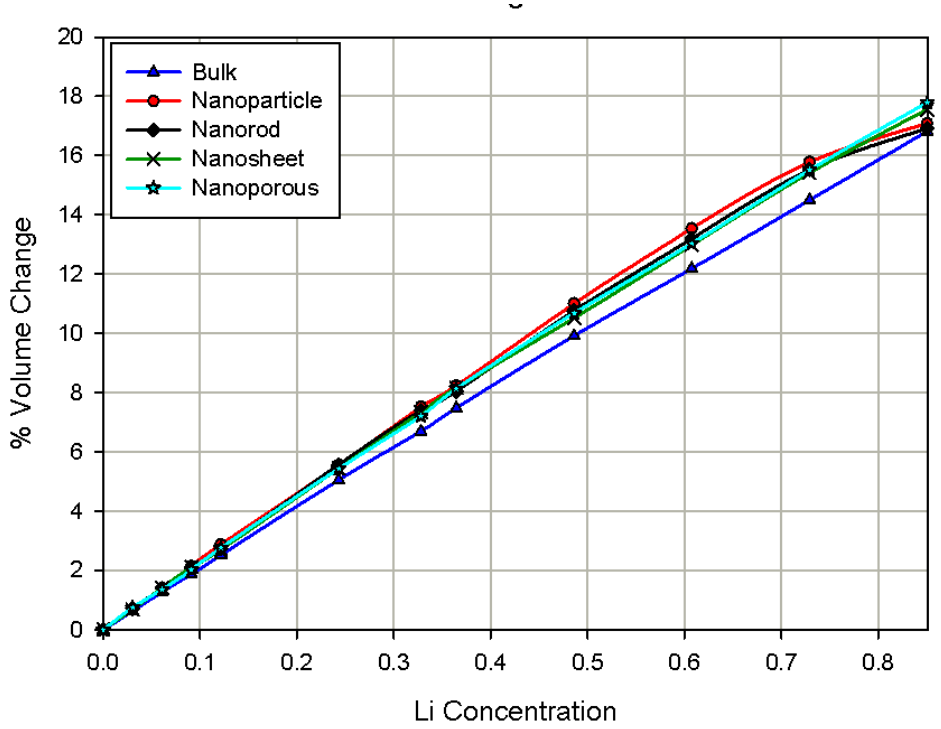

Figure 3-5: Volume expansion of the β-MnO_2 nanostructures as a function of lithium concentration.

3.1.4 Li-MnO_2-β Microstructural Response

Conventional experimental methods such as X-ray diffraction and TEM [3, 12] employed in the studies of lithiation of manganese dioxides are often limited in characterizing the structural transformation. However computational methods with the aid of visualization tools, such as those provided by molecular graphics [64], allow us to further analyse the structures by probing the materials at some instance in time in three dimensions. Diagrams (b) to (e) in Figure 3-6 to Figure 3-10 below show the evolution of the microstructure in the bulk structure, nanoparticle, nanorod, nanosheet and nanoporous during lithiation. The microstructure diagrams of the bulk structure and all nanostructures as lithium-ion concentration is increased show little or no structural deformation, even at high lithium-ion concentrations.

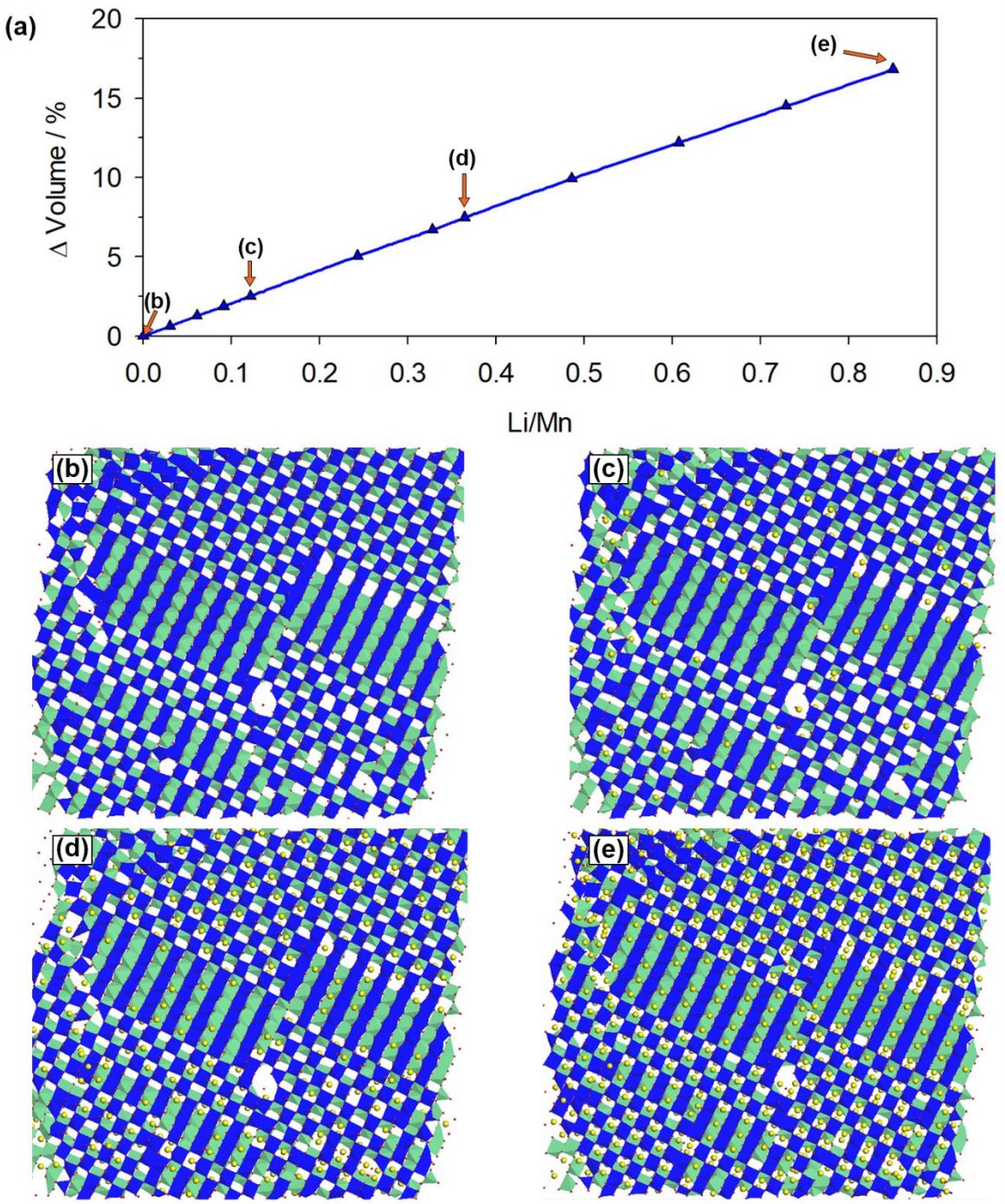

Figure 3-6: (a) A plot of change in volume versus lithium-ion concentration for bulk Li_xMnO_2-β (x = 0.0, 0.03, 0.06, 0.09, 0.12, 0.24, 0.33, 0.36, 0.49, 0.61, 0.73 and 0.85). Microstructure slices were taken at Li/Mn fractions of (b) 0.00, (c) 0.12, (d) 0.36 and (e) 0.85. Blue and cyan represent the top and bottom MnO_6 octahedral planes. Lithium ions are depicted by yellow spheres.

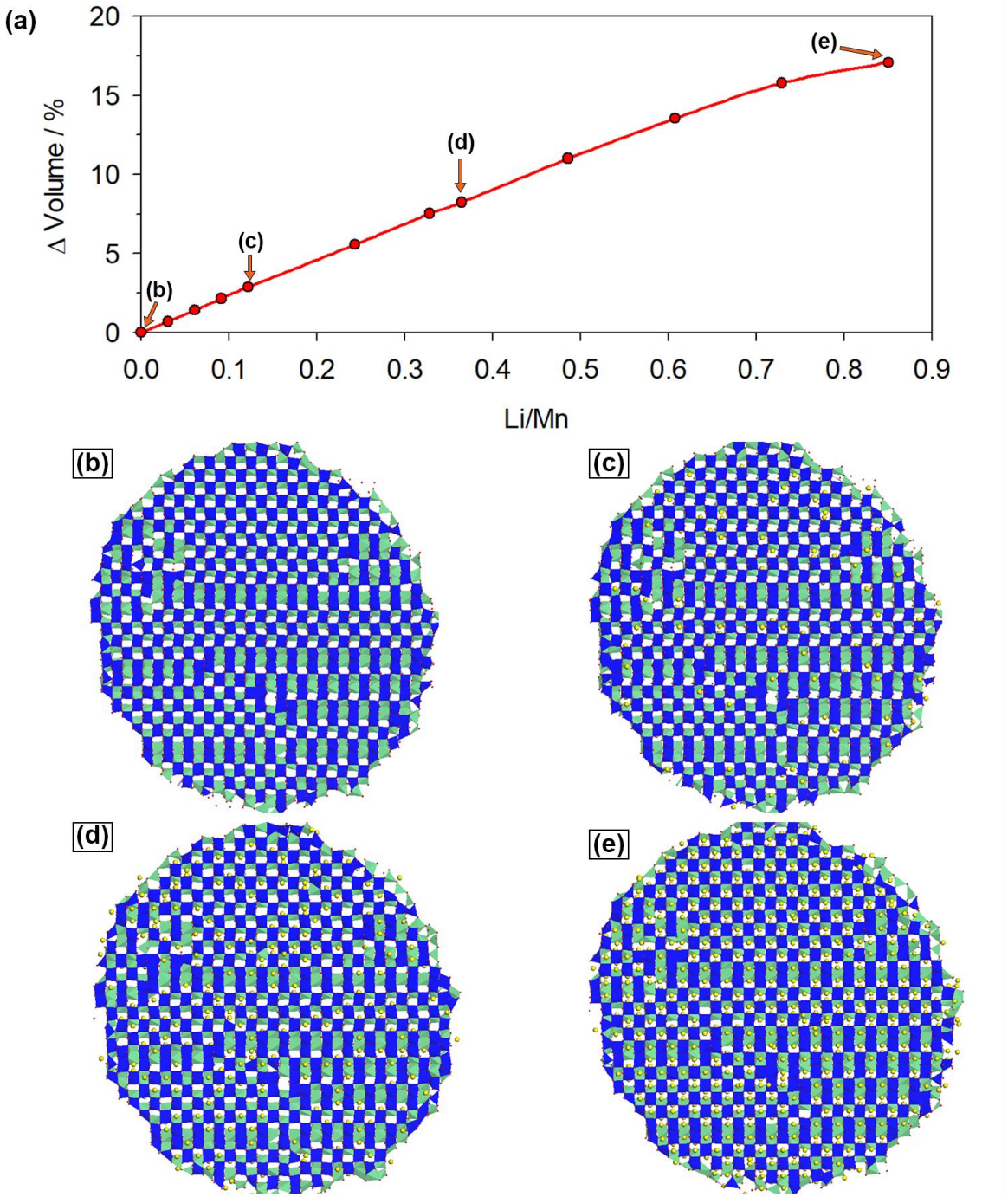

Figure 3-7: A plot of change in volume versus lithium-ion concentration for nanoparticle Li_xMnO_2-β (x = 0.0, 0.03, 0.06, 0.09, 0.12, 0.24, 0.33, 0.36, 0.49, 0.61, 0.73 and 0.85). Microstructure slices were taken at Li/Mn fractions of (b) 0.00, (c) 0.12, (d) 0.36 and (e) 0.85. Blue and cyan colours represent the top and bottom MnO_6 octahedral planes. Lithium ions are depicted by yellow spheres.

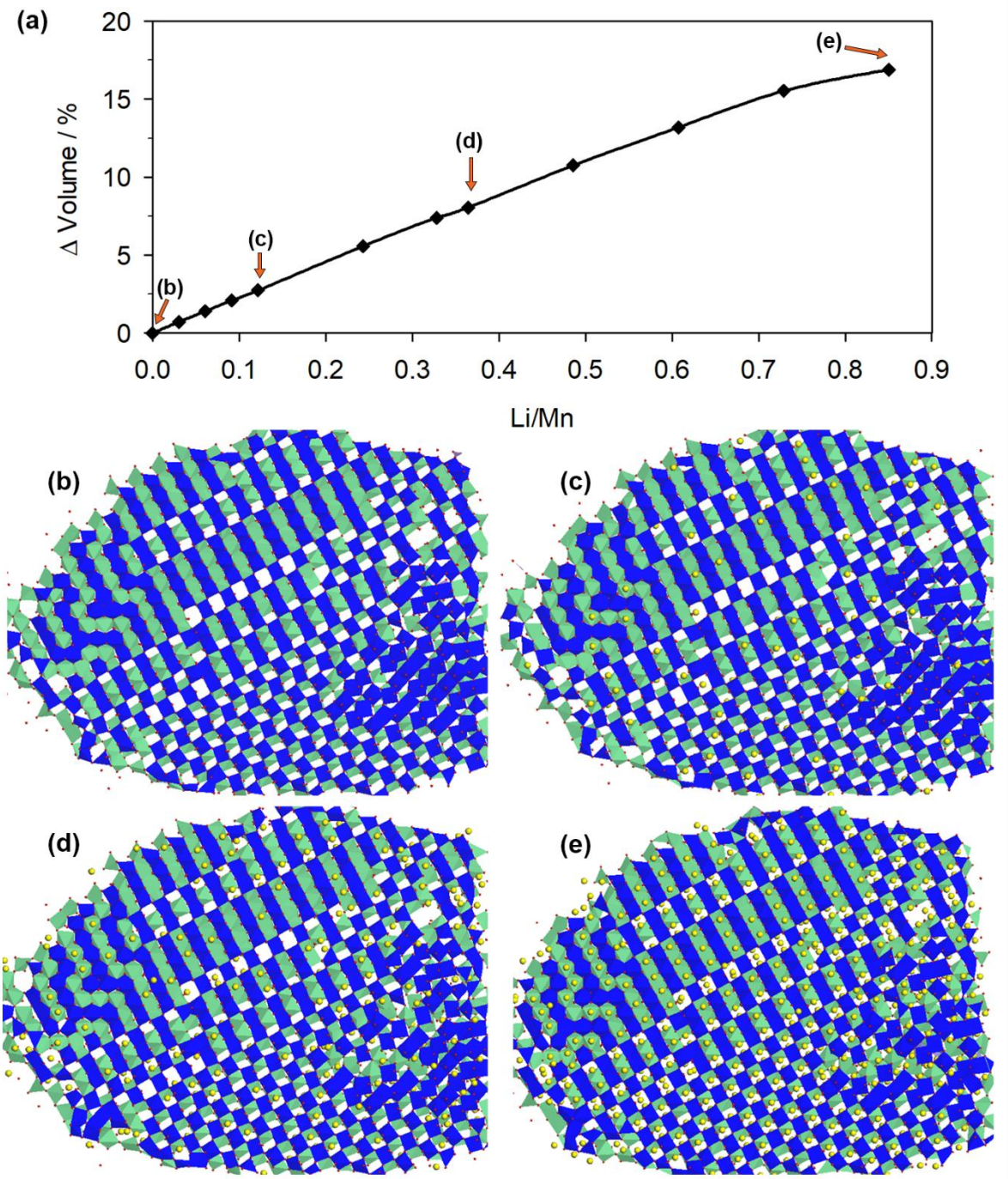

Figure 3-8: A plot of change in volume versus lithium-ion concentration for nanorod Li_xMnO_2-β (x = 0.0, 0.03, 0.06, 0.09, 0.12, 0.24, 0.33, 0.36, 0.49, 0.61, 0.73 and 0.85). Microstructure slices were taken at Li/Mn fractions of (b) 0.00, (c) 0.12, (d) 0.36 and 0.85. Blue and cyan colours represent the top and bottom MnO_6 octahedral planes. Lithium ions are depicted by yellow spheres.

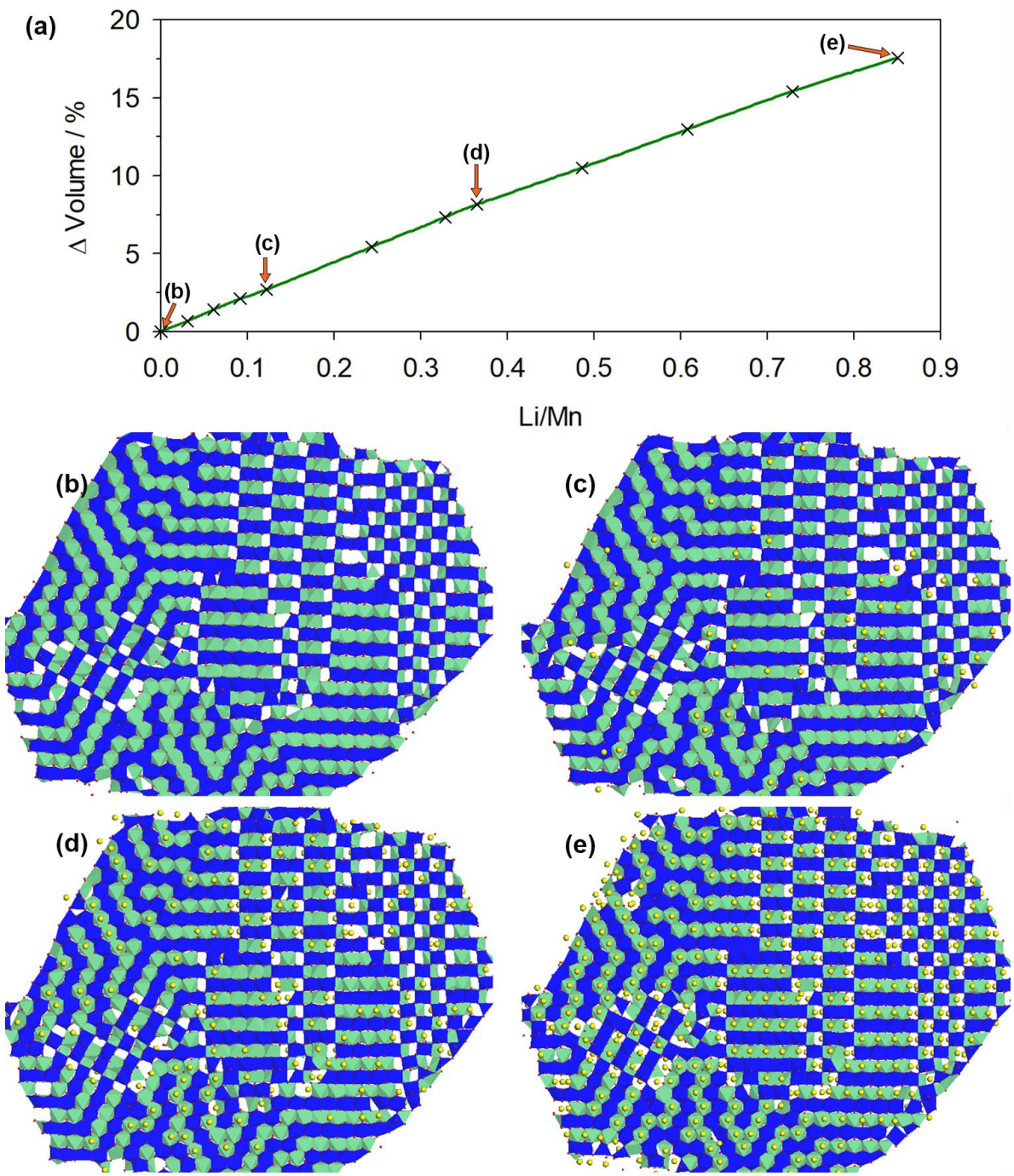

Figure 3-9: A plot of change in volume versus lithium-ion concentration for nanosheet Li_xMnO_2-β (x = 0.0, 0.03, 0.06, 0.09, 0.12, 0.24, 0.33, 0.36, 0.49, 0.61, 0.73 and 0.85). Microstructure slices were taken at Li/Mn fractions of (b) 0.00, (c) 0.12, (d) 0.36 and 0.85. Blue and cyan colours represent the top and bottom MnO_6 octahedral planes. Lithium ions are depicted by yellow spheres.

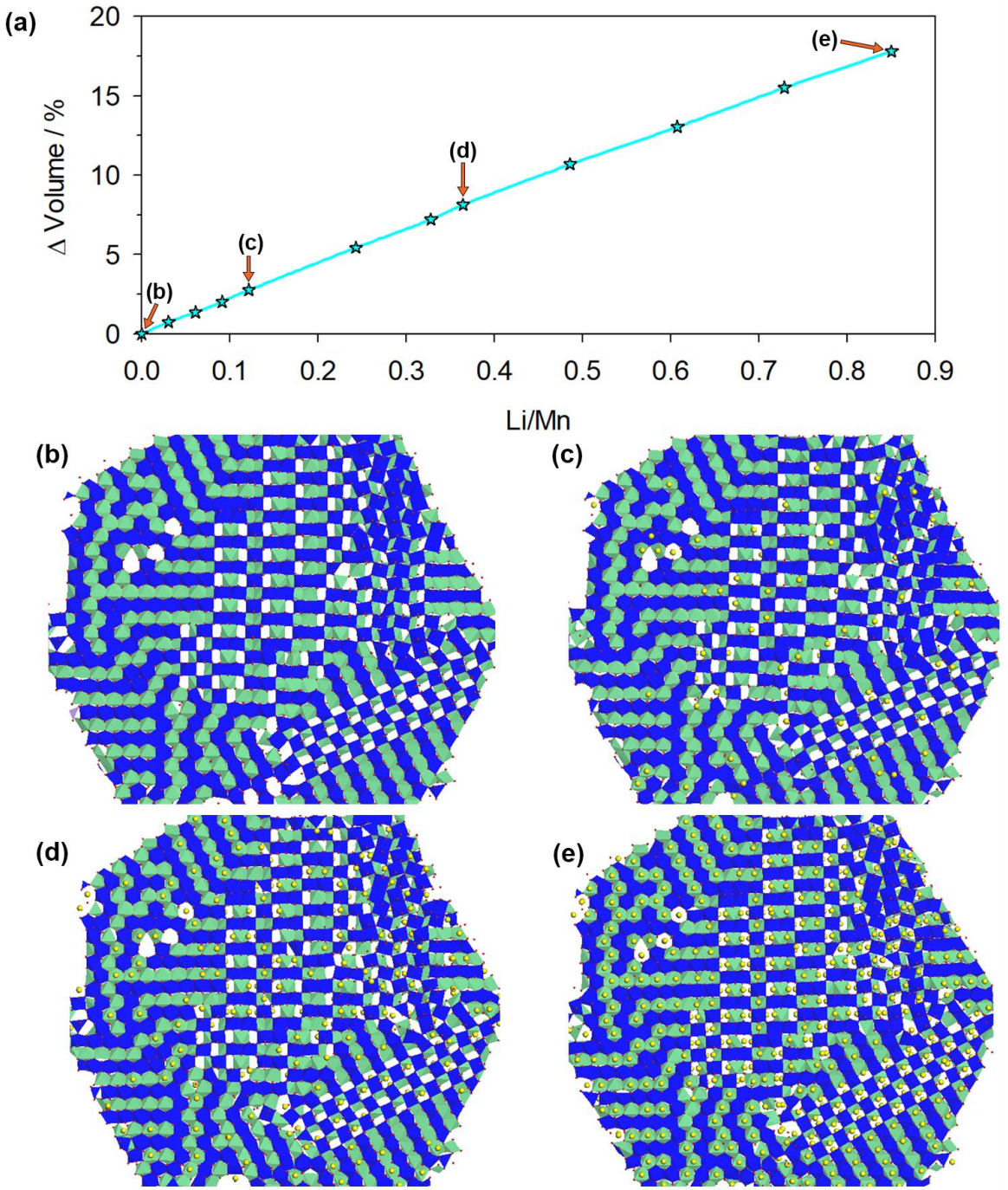

Figure 3-10: A plot of change in volume versus lithium-ion concentration for nanoporous Li_xMnO_2-β (x = 0.0, 0.03, 0.06, 0.09, 0.12, 0.24, 0.33, 0.36, 0.49, 0.61, 0.73 and 0.85). Microstructure slices were taken at Li/Mn fractions of (b) 0.00, (c) 0.12, (d) 0.36 and 0.85. Blue and cyan colours represent the top and bottom MnO_6 octahedral planes. Lithium ions are depicted by yellow spheres.

3.1.5 Radial Distribution Function Analysis

The relationship between the tunnel configuration formed by the manganese framework and the RDF peaks allows us to extract useful insight into the dynamic behaviour of the Mn atoms in response to intercalation. The first, second, third and fourth peaks represent the first, second, third and fourth nearest-neighbour Mn distances respectively. The first RDF peak is the distance between two nearest neighbour manganese atoms and represents the *c* lattice parameter in the tetragonal crystal lattice of β-MnO_2. The second RDF peak is the shortest distance between two manganese atoms in two adjacent MnO_6 octahedral chains that form a 1x1 tunnel, while the third peak is the shortest distance between two manganese atoms located in two MnO_6 octahedral planes oriented at opposite sites of a 1x1 tunnel. Peak three is the *a* or *b* lattice parameter in a tetragonal crystal lattice of β-MnO_2. The graphical representation of the configuration of manganese atoms in relation to the RDF peaks is shown in Figure 3-11. We use radial distribution functions to track changes in the manganese-manganese distances and consequently monitor the size of the tunnel structures constructed by the manganese atomic framework.

Mn-Mn radial distribution functions (RDFs) of the lithiated bulk structure, nanoparticle, nanorod, nanosheet and nanoporous are presented in Figure 3-12. These RDF peaks are similar to those obtained from crystalline bulk β-MnO_2 [25] with the exception of having a broader peak width indicative of a wide bond length distribution. The peaks also show long-range order however the small values of *g(r)* for the bulk structure indicates that the bulk structure is more disordered. In general for all nano-architectures, most of the peaks except the first have shifted to the right as more lithium ions were intercalated. There was minimal change in the first peak as it relates to nearest-neighbour Mn atoms having no tunnel in between. This suggests that the MnO_6 octahedral chains did not stretch in response to lithiation. Of great importance are the second and third peaks which represent two manganese atoms in adjacent octahedral chains that form a 1x1 tunnel and two manganese

atoms at the opposite sides of a 1x1 tunnel, respectively. The peak shift to the right in response to subsequent additional lithiation is indicative of an expansion in the Mn-Mn distance and consequently the two-dimensional expansion of the 1x1 tunnel.

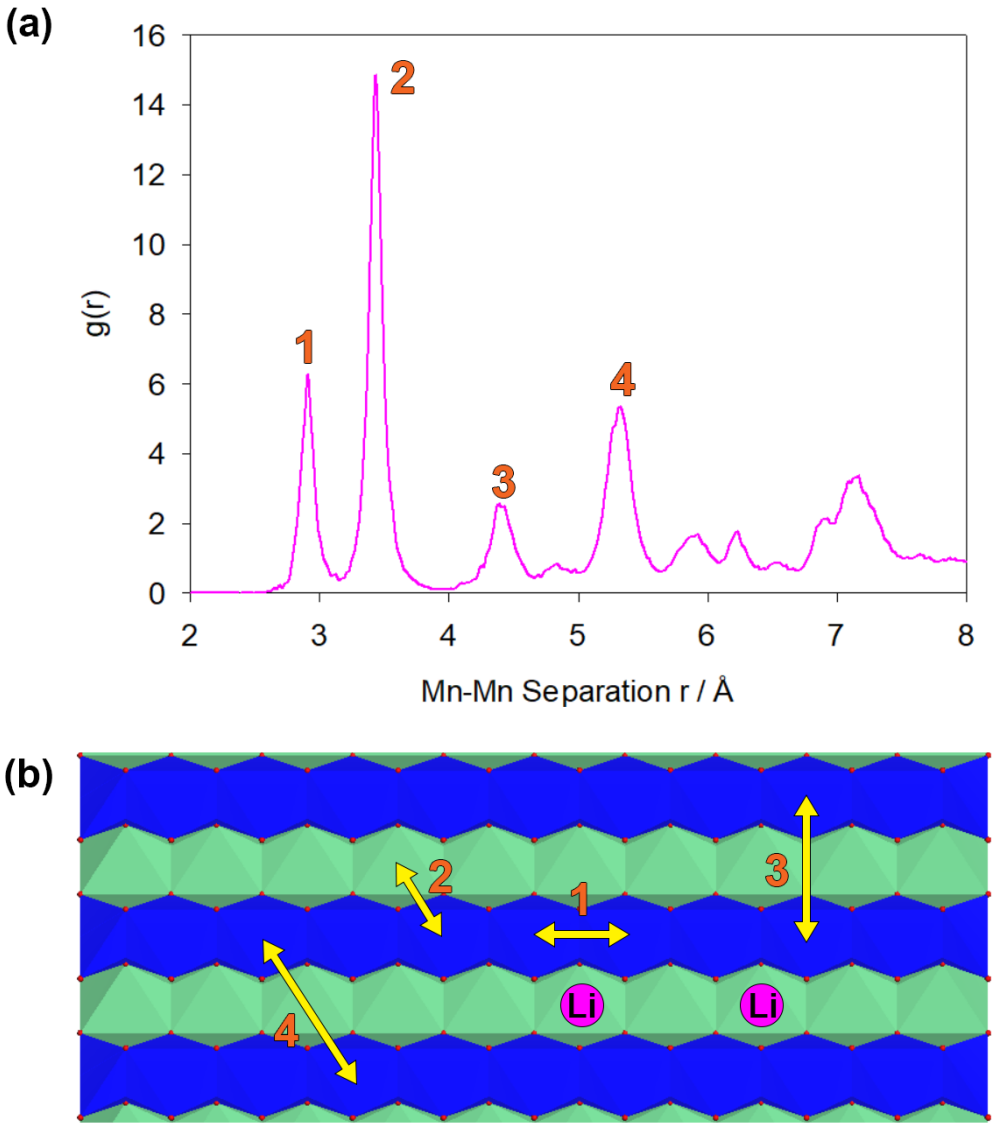

Figure 3-11: (a) Mn-Mn radial distribution function plot of β-MnO_2. (b) A microstructure slice of β-MnO_2 showing various Mn distances that correspond to the first four peaks in the plot.

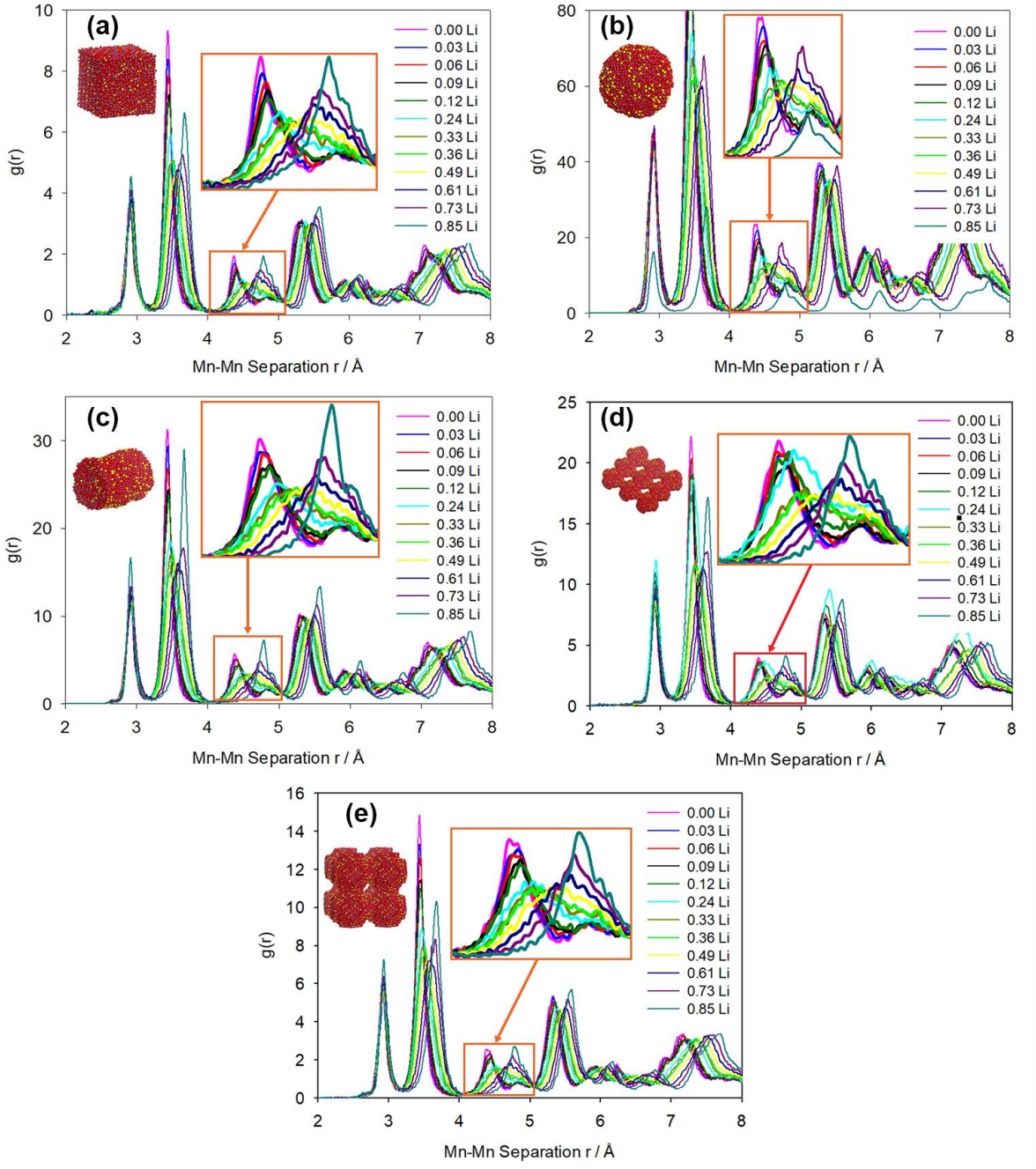

Figure 3-12: Radial distribution functions of the Mn-Mn pair in the lithiated (a) bulk structure, (b) nanoparticle, (c) nanorod,(d) nanosheet and (e) nanoporous β-MnO_2.

Structural analyses based on the RDFs of the pristine and lithiated nanostructures tare summarised in Table 3-1. In order to calculate the average coordination numbers, a cutoff radius must be selected as the value of the first minimum in the RDF plot. We have chosen a cutoff radius of 3.18, 2.15 and 3.2 Å for the Mn-Mn, Mn-O and O-O pairs, respectively, in the pristine nanostructures and for the lithiated nanostructures we have selected 3.2, 2.3, 3.4 and 2.6 Å for Mn-Mn, Mn-O, O-O and Li-O pairs, respectively. The average coordination number for Mn-O varied from 5.68 to 5.77 Å while that of O-Mn ranged from 2.84 to 2.89 Å suggesting that on average each manganese atom is surrounded by about 6 oxygen atoms and each oxygen atom has three manganese neighbouring atoms. These values are similar to those of the crystalline bulk pyrolusite [65]. The coordination numbers for Li-O in the various structures is also provided and range from 5.51 to 5.69 Å consistent with those of Mn-O pairs. This indicates that most of the lithium ions have occupied the octahedral cation positions and Mn vacancies in the lattice. Upon lithiation from 0 to 85%, the average coordination numbers remain similar suggesting that there is no structural loss as in the previous sections; the bulk structure and nanostructures retain their rutile form but merely distorts as observed by Ren et al [13].

Table 3-1: Structural characteristics of lithiated β-MnO_2 nanostructures as a function of lithium concentration. r_{ij} is the first neighbour distance while Z_{ij} is the average coordination number.

		r_{ij} (Å)				Z_{ij}				
Structure	**Li/Mn**	**Mn-Mn**	**Mn-O**	**O-O**	**Li-O**	**Mn-Mn**	**Mn-O**	**O-Mn**	**O-O**	**Li-O**
Bulk	0.00	2.90	1.90	2.67		1.99	5.68	2.84	11.08	
	0.85	2.91	2.00	2.80	1.95	1.98	5.68	2.84	11.10	5.63
Nanoparticle	0.00	2.90	1.90	2.68		2.06	5.77	2.88	11.14	
	0.85	2.91	2.00	2.81	1.99	2.05	5.76	2.89	11.18	5.69
Nanorod	0.00	2.91	1.90	2.70		2.02	5.73	2.87	11.35	
	0.85	2.93	2.01	2.81	1.99	2.01	5.74	2.87	11.11	5.70
Nanosheet	0.00	2.91	1.90	2.69		2.06	5.74	2.87	11.09	
	0.85	2.92	2.01	2.80	1.98	2.05	5.75	2.88	11.13	5.61
Nanoporous	0.00	2.92	1.91	2.69		2.03	5.71	2.86	11.05	
	0.85	2.92	2.00	2.81	1.96	2.02	5.72	2.86	11.07	5.51

Table 3-2 shows the lattice parameters as a function of lithium concentration. The interatomic potentials we have chosen [42] reproduces the lattice parameters of pyrolusite MnO_2 reasonably well to within 2% of the experimentally determined values in both static lattice (GULP) and DL_POLY MD calculations. Lattice parameters can be determined by indexing the XRD patterns of the nanostructures (Figure 3-13 to Figure 3-18) however it is tedious to do so due to the broad nature of the peaks. Alternatively, we have estimated the lattice parameters *a* and *c* from the first and third peak maximums on the Mn-Mn radial distribution functions respectively. These values show that at our highest lithium concentration (85%) the lattice parameter *a* expanded from a range of 4.38-4.40 Å to a range of 4.77-4.78 Å while the lattice parameter *c* expanded slightly from a range of 2.90-2.92 Å to 2.91 to 2.92 Å for the various nanostructures. This corresponds to a maximum of 9.36 % expansion by lattice parameter *a* and 0.34% expansion by lattice parameters *c*. These values are smaller in comparison to those of the 92% lithiated mesoporous β-MnO_2 of Jiao et al [3] and Ren [13] et al. who observed 13.9% expansion of *a* and 2% contraction of *c*.

Table 3-2: Lattice parameters of lithiated β-MnO_2 nanostructures as a function of lithium concentration.

Structure	MnO_2		$Li_{0.85}MnO_2$			
	a (Å)	c(Å)	a (Å)	% diff a	c (Å)	% diff c
β-MnO_2 ^{exp} [65]	4.4008	2.8745				
β-MnO_2 ^{GULP} [42]	4.4040	2.9312				
Bulk	4.38	2.90	4.78	9.13	2.91	0.34
Nanoparticle	4.39	2.90	4.78	8.88	2.91	0.34
Nanorod	4.38	2.91	4.79	9.36	2.91	0.34
Nanosheet	4.39	2.91	4.77	8.66	2.92	0.34
Nanoporous	4.40	2.92	4.78	8.64	2.92	0.00
Mesoporous^{exp} [3]	4.40	2.88	4.96	12.73	2.82	-2.08

3.1.6 Simulated X-Ray Diffraction Patterns

The simulated x-ray diffraction patterns (XRD) were calculated using the Reflex module within Biovia Materials Studio software over the 2θ range of 10° to 70° with a step size of 0.05 and the Cu Kα radiation (λ = 1.54 Å). The calculated XRD patterns of the computationally generated bulk and nanostructures (Figure 3-13) have broadened peaks which suggest lattice strains [66] and structural defects in the lattice such as stacking faults and twin faults. The crystalline bulk β-MnO_2 has less lattice strain as indicated by its sharp XRD peaks [67]. We see from the characteristic peaks at 2θ values of 28°, 37°, 41°, 43°, 57°, 59° corresponding to the reflections by the (1 1 0), (1 0 1), (2 0 0), (1 1 1), (2 1 1) and (2 2 0) planes that the bulk structure and nanostructures have a pyrolusite-type crystal structure. However, the small peaks due to the reflections by the (2 1 0), (2 2 0) and (0 0 2) planes are not present. These XRD patterns, though lower in crystallinity relative to the experimental samples, compare accurately with those of the heat-treated electrolytic manganese dioxide (HEMD) of Dose et. al [68]. As in the XRD patterns of our modelled MnO_2 structures. The (2 1 0) and (2 2 0) peaks are also absent in the XRD pattern of the HEMD.

This is remarkable since the two materials were prepared using completely different methods. The nanostructures were prepared by amorphising a cube of crystalline MnO_2 by increasing the lattice parameter by 36.3 % to induce strain and running a molecular dynamics simulation at 2000 K. This was followed by a molecular dynamics simulation within the NVT ensemble at 2000 K causing the material to recrystallize. Finally, the materials were annealed to 0 K [35]. The crystallization into the defect β-MnO_2 polymorph was driven by the potential model describing the ionic interactions and the lattice misfit. In contrast, the HEMD synthesis started with the preparation of electrolytic manganese dioxide (EMD) by anodic electrodeposition. The EMD was then heated at 350 °C (about 650 K) to remove water resulting in the

conversion of EMD to the HEMD phase [68]. The time for the MD simulation is in the order of a few nanoseconds while that of HEMD preparation of Dose is in days.

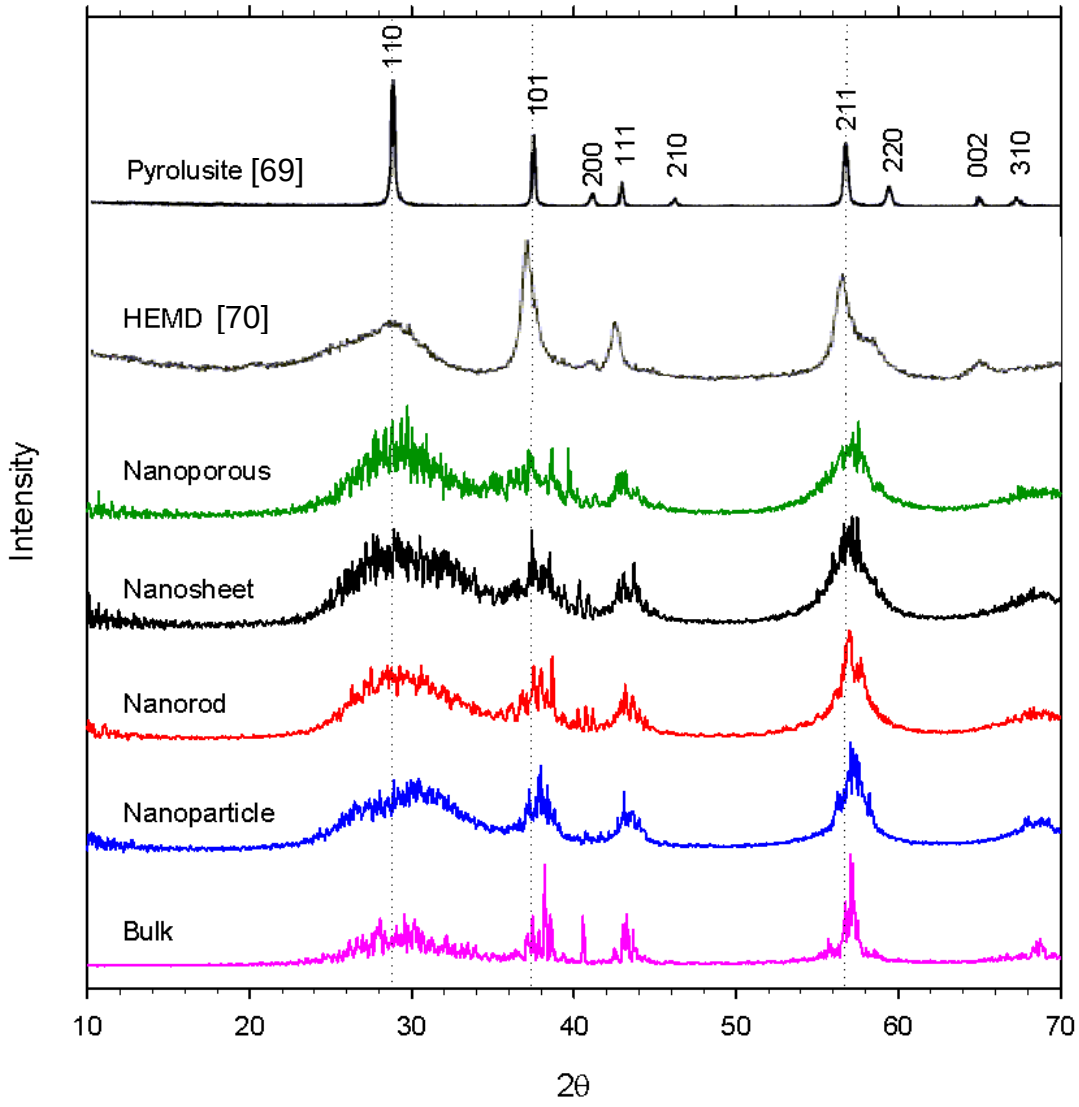

Figure 3-13: Simulated X-ray diffraction (Cu K_α) patterns of the pristine β-MnO_2 bulk and nanostructures.

The X-ray diffraction plots of the bulk structure and nanostructures at various lithium-ion concentrations are presented in Figure 3-14 to Figure 3-18. As more lithium is added all the characteristic β-MnO_2 peaks shift to lower diffraction angles. Also, the (1 0 1) and (2 0 0) peaks gradually moved closer and merged at higher lithium concentrations for the bulk structure, nanorod and nanosheet. The (2 0 0) peak is not easily distinguishable in the x-ray diffraction plots for the nanoparticle and nanoporous. Note that the (2 0 0) peak is closely related to the lattice parameter *a*. We can calculate the lattice parameter *a* by using Bragg's law:

$$\lambda = 2d_{hkl} \sin\theta \tag{3.1}$$

$$\frac{1}{d_{hkl}} = \frac{h^2}{a^2} + \frac{k^2}{b^2} + \frac{l^2}{c^2} \tag{3.2}$$

Since $k = l = 0$,

$$\frac{1}{d_{hkl}} = \frac{h^2}{a^2} \tag{3.3}$$

$$a = h\sqrt{d_{hkl}} \tag{3.4}$$

From equation (3.1), the interplanar spacing d_{hkl} increases as θ decreases. Also, we see from equations (3.4) that the *a* lattice increases as d_{hkl} increases. Thus we discern from the x-ray diffraction plots of the bulk structure, nanorod and nanosheet that the lattice parameter *a* decreased with increasing lithium-ion concentration. The (1 1 0) gradually decreased in intensity for all structures while the (1 1 1) peak also decreased in intensity except for all the nano-architectures except the nanorod. Also, the (2 1 1) peak located at $2\theta = 57°$ at 0.00 Li/Mn split as it shifted but only in the x-ray diffraction plot for the bulk structure. Overall, all the nanostructures exhibited the same trend that is slightly different from the bulk β-MnO_2.

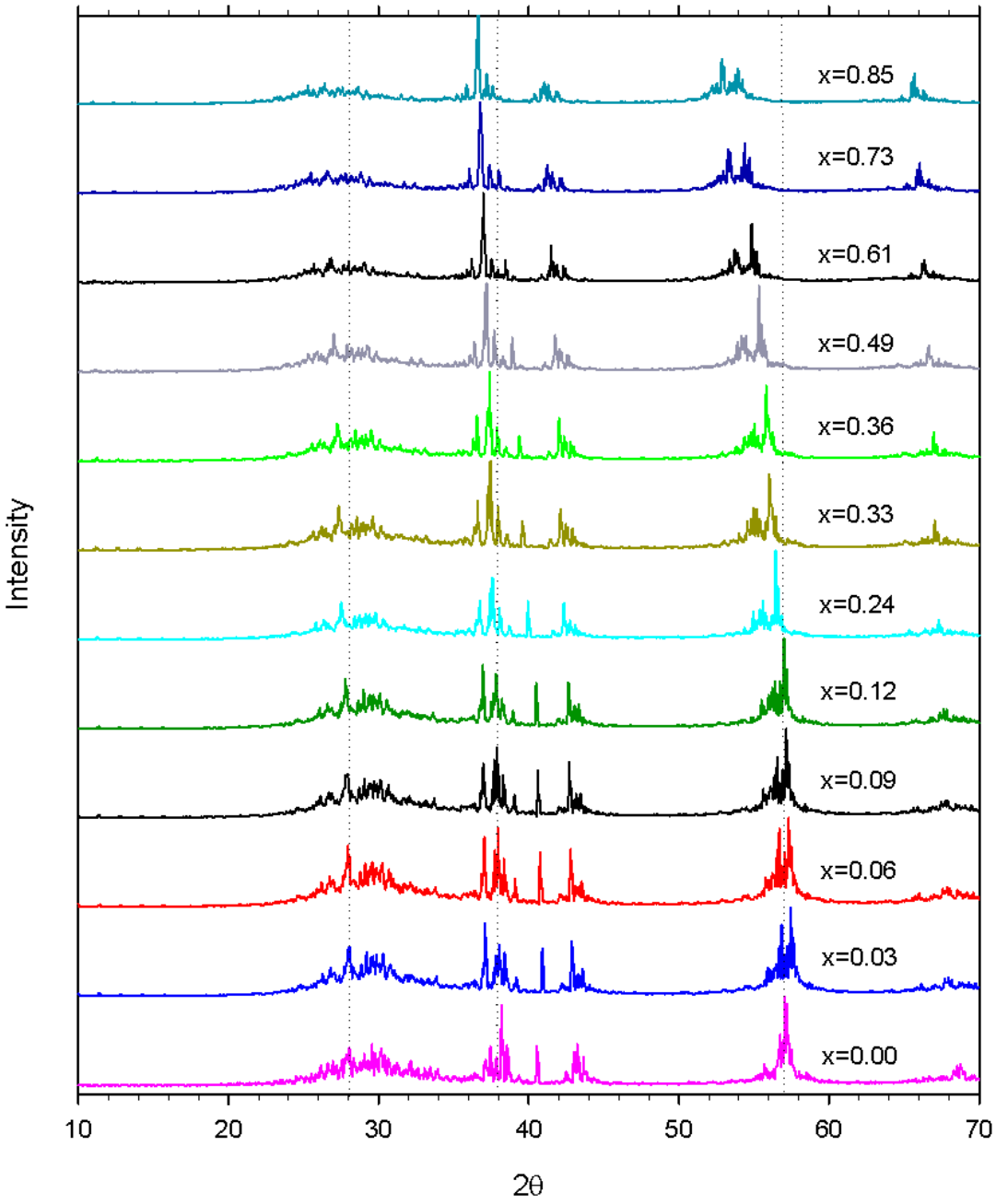

Figure 3-14: Simulated X-ray diffraction patterns of Li_xMnO_2-β bulk structure.

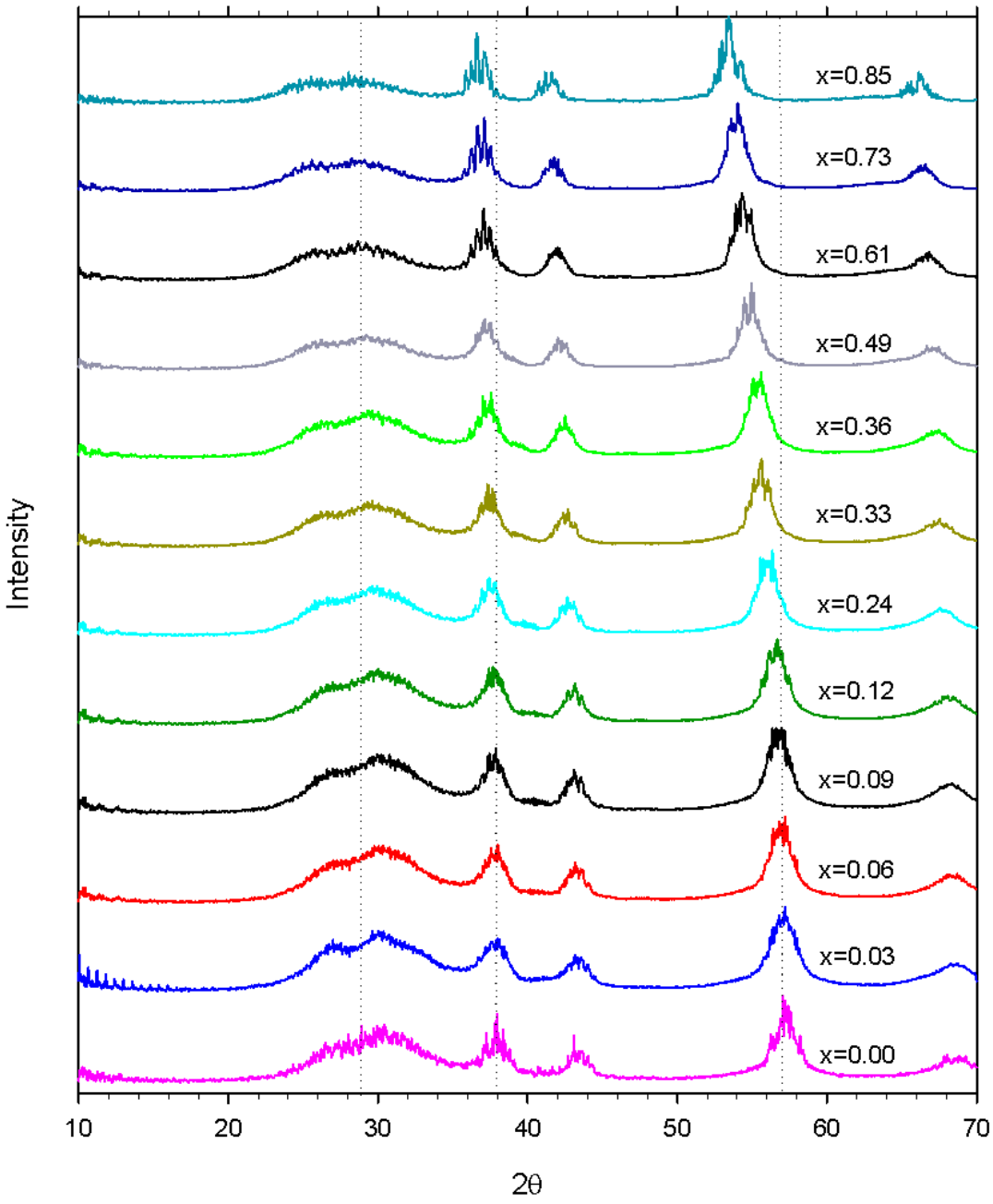

Figure 3-15: Simulated X-ray diffraction patterns of Li_xMnO_2-β nanoparticle.

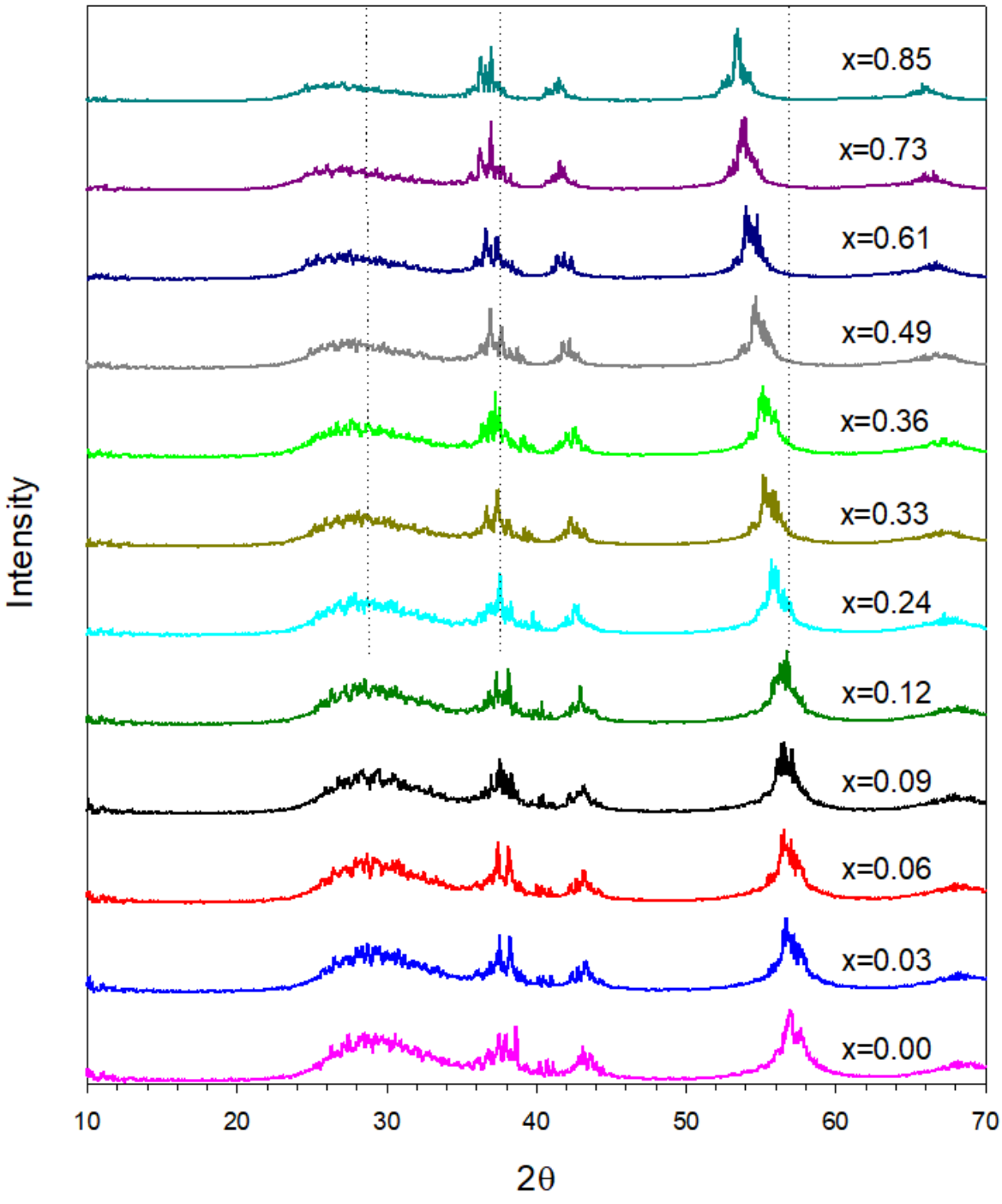

Figure 3-16: Simulated X-ray diffraction patterns of Li_xMnO_2-β nanorod.

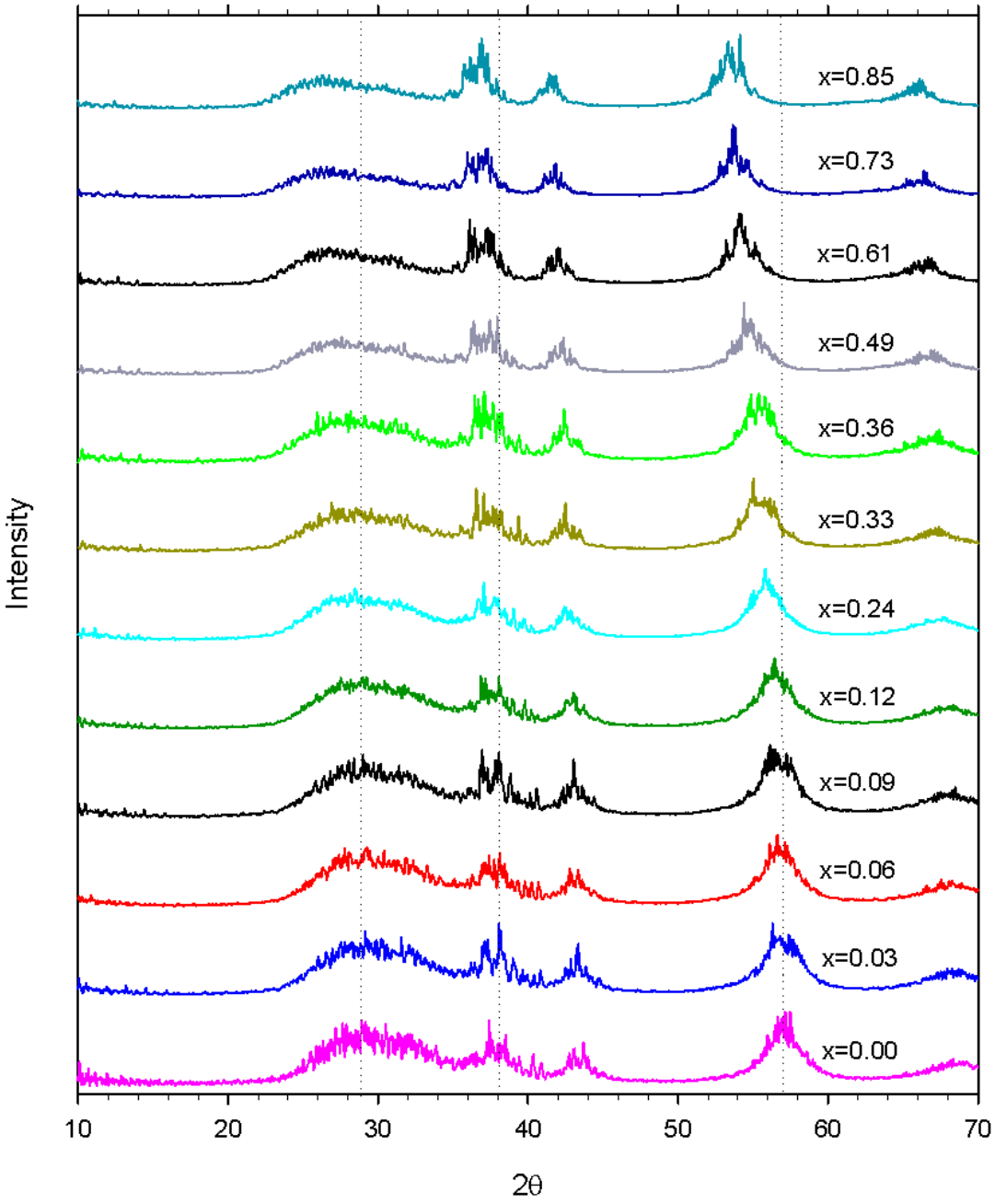

Figure 3-17: Simulated X-ray diffraction patterns of Li_xMnO_2-β nanosheet.

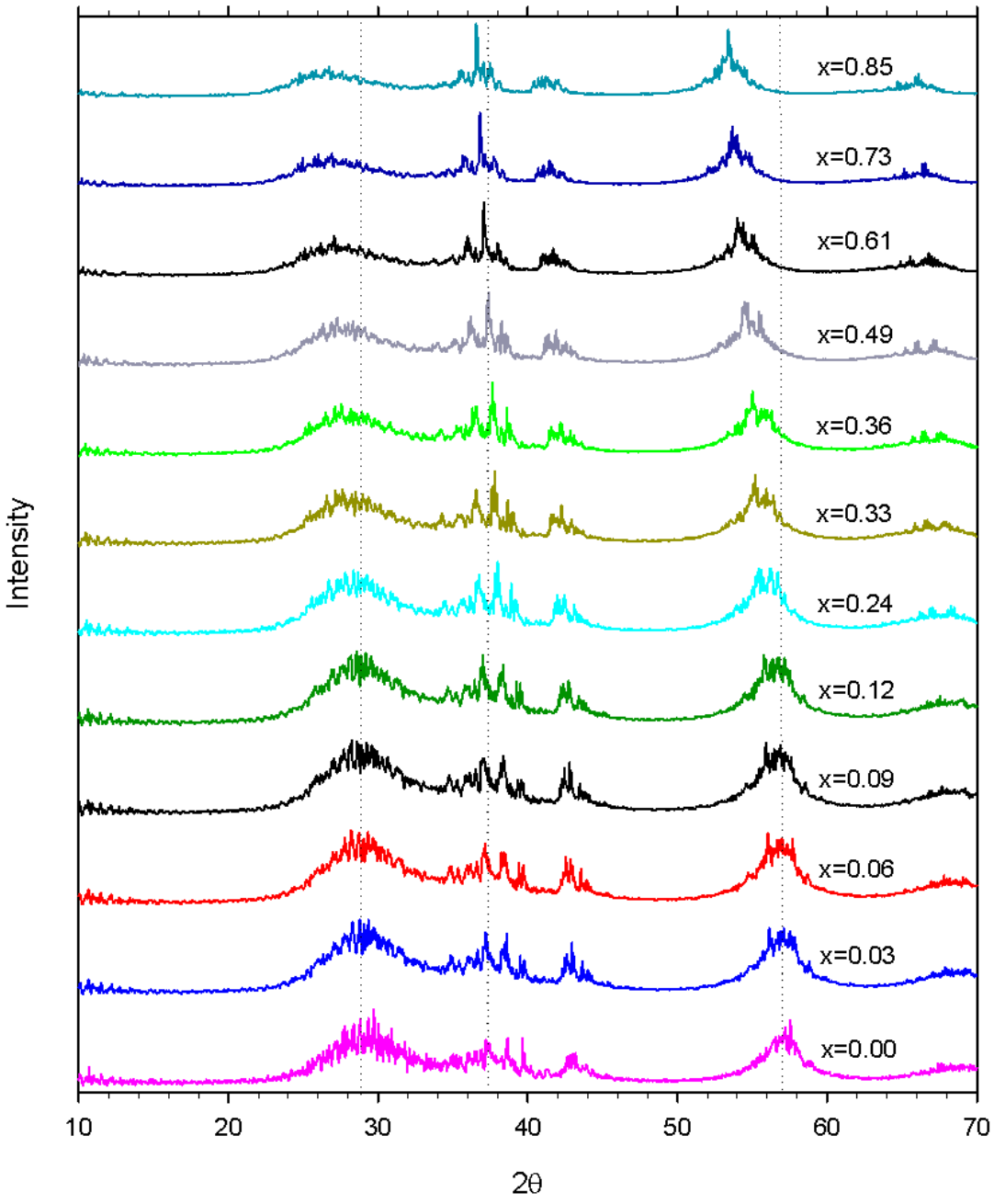

Figure 3-18: Simulated X-ray diffraction patterns of Li_xMnO_2-β nanoporous.

The x-ray diffraction plots for the bulk and nanoporous β-MnO_2 under compressive strain ranging from 1 to 5% are presented below in Figure 3-19, whereas the x-ray diffraction plots for the bulk and nanoporous Li_xMnO_2-β are given in Figure 3-20. We investigate the internal process involved in stress mitigation.

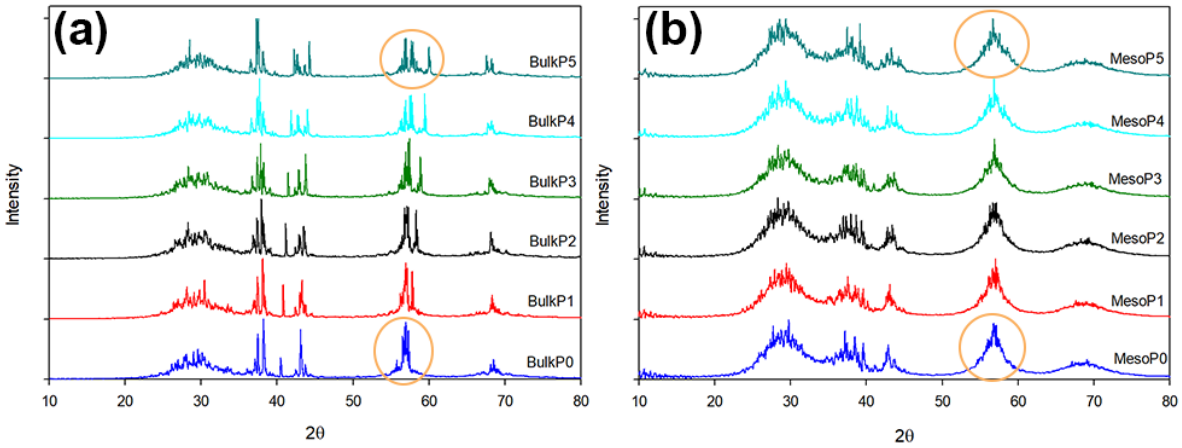

Figure 3-19: X-ray diffraction patterns calculated as a function of strain for (a) bulk and (b) nanoporous β-MnO_2. Labels P0-P5 indicate strains of 0-5%, respectively [36].

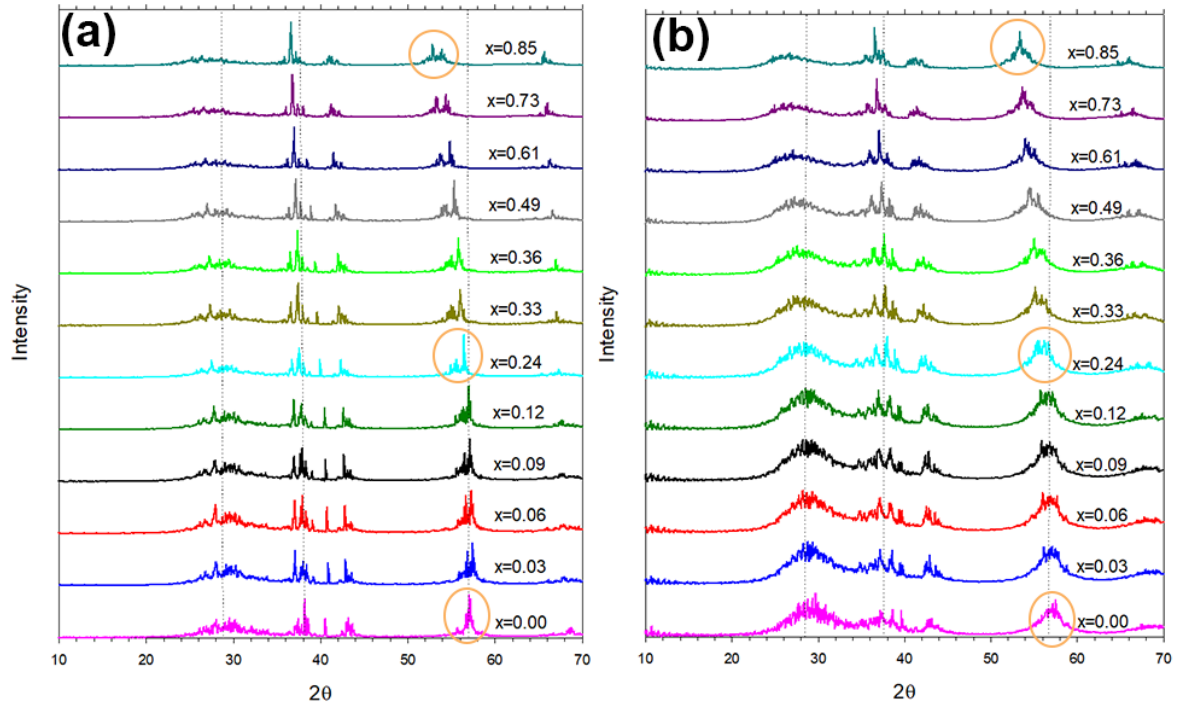

Figure 3-20: X-ray diffraction patterns for (a) bulk and (b) nanoporous Li_xMnO_2-β.

The peaks were reported to shift to the right indicating a reduction in the lattice parameters. Of importance within the unlithiated bulk β-MnO_2 under compressive strain is the (2 1 1) peak located at 2θ values of about 57° which split and produced the (2 2 0) peak at 59° for 4 and 5% strains. The same peak also splits as more lithium-ions are intercalated into the bulk β-MnO_2. Uniaxial strain application on the unlithiated bulk β-MnO_2 induces stress on the tunnels along one dimension causing them to contract, whereas lithiation into some of the tunnels causes them to expand and induce localised stress in nearby unlithiated tunnels. In the latter case, the unlithiated tunnels within the lithiated bulk β-MnO_2 experience compressive strain akin to the manually applied compressive strain in the former case. In both cases, the bulk structure gives a similar dynamical response. This result is important and suggests that lithiation and strain application have a similar impact on the underlying β-MnO_2 framework.

The (2 1 1) peak in the x-ray diffraction patterns for the unlithiated nanoporous under compressive strain and the lithiated nanoporous show no splitting in both cases. The nanoporous under compressive strain was previously studied and found to be structurally resilient where the 1x1 tunnel size remained unchanged [36]. Since the size of the 1x1 tunnels within the bulk structure has been shown contract with a simultaneous occurrence of the splitting (2 1 1) peak, the peak splitting could be related to atomic rearrangements leading to structural modification. The (2 1 1) peak in the x-ray diffractions plots for the nanoparticle, nanorod and nanosheet discussed above did not show any splitting. More descriptive details on the stress mitigation mechanisms employed by the bulk structure and nanorod at a microstructural level are discussed in chapter 4.

3.1.7 Average Intercalation Potentials

Battery technologies for applications in the electrical power grid and electric vehicles have a requirement of high energy densities i.e. high capacity and high voltage.

Nanostructuring has the potential to improve high rate capability and enhance cell voltage [69]. As some aspects of nanostructuring can affect the cell voltage, we study the trends in the voltage profiles for the various β-MnO_2 nanostructures in relation to the bulk structure which is known to be electrochemically inactive. It is important to first mention in detail the limitations of the model and how it may affect the calculation of the intercalation potentials.

We used the Li-Mn-O interatomic potentials described in Table 2-1 in GULP and performed geometry optimisation calculations on a pure and lithium-ion intercalated β-MnO_2 unit cell to study the intercalated structures at a small scale. The β-MnO_2 crystal structure has several lattice sites which can be exploited for cation insertion. We have studied lithium-ion intercalation into the *4c* and *8h* octahedral sites described by $\left(\frac{1}{2}\ 0\ \frac{1}{2}\right)$ and $\left(\frac{1}{2}\ 0\ \left\{\frac{1}{4} \pm \frac{1}{20}\right\}\right)$ respectively. We have also studied lithium-ion intercalation into the *4d* and *8i* tetrahedral sites described by $\left(\frac{1}{2}\ 0\ \frac{1}{4}\right)$ and $\left(0.4023\ 0.1523\ \frac{1}{2}\right)$ respectively. These lattice intercalation sites are depicted in Figure 3-21 below.

We prepared β-MnO_2 structures for GULP classical simulations by intercalating one lithium-ion (0.5 Li/Mn) at the above-mentioned sites and reduced one manganese atom from 4+ to 3+ oxidation state to balance the charge. However, the β-MnO_2 unit cell has two manganese atoms and multiple lithium-ion sites. We thus created $Li_{0.5}MnO_2$ structures with all possible combinations of Li^+ and Mn^{3+}.

Table 3-3 below shows the total energies of $Li_{0.5}MnO_2$ with lithium-ion intercalated at the *4c*, *4d*, *8h*, and *8i* interstitial sites after GULP geometry optimisation calculations. The results of the GULP classical simulations suggest the *4c* octahedral sites as the only preferred site for lithium-ion intercalation. Within the classical simulations, the lithium-ions that were initially intercalated in the *8h* octahedral site and the *4d* and *8i* tetrahedral sites migrated to the neighbouring *4c* octahedral site.

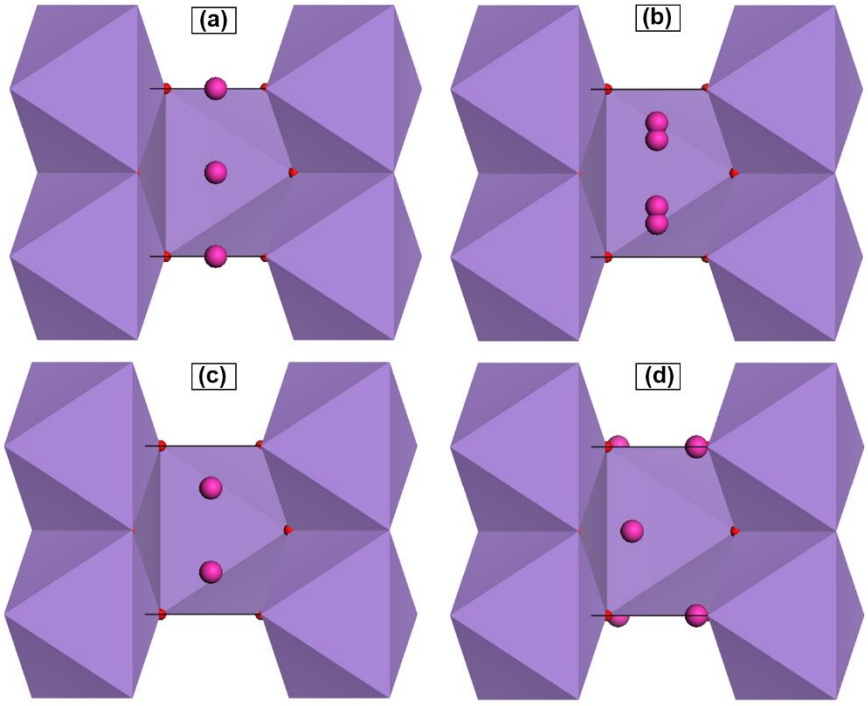

Figure 3-21: Polyhedral rendering of a β-MnO_2 unit cell showing lattice sites that can be used for cation intercalation. Octahedral sites are shown by lithium in (a) and (b) while (c) and (d) show lithium in tetrahedral sites.

Table 3-3: Total energies of β-MnO_2 intercalated with 50% lithium-ion or lithium at the *4c*, *4d*, *8h*, and *8i* interstitial sites after geometry optimisation.

		GULP Interatomic Potentials	
Initial Li Site	**O Coordination**	**Etot (eV)**	**Final Li Site**
4c	8	-72.0728	4c
8h	8	-72.0728	4c
4d	4	-72.0728	4c
8i	4	-72.0728	4c

The electrochemical topotactic redox reactions can be written as:

$$xLi^+ + xe^- + xMn^{(IV)}O_2 \Leftrightarrow (Li^+)_x\left[Mn^{(III)}O_2\right]_x \quad (3.5)$$

We assume that the uptake of a lithium-ion is accompanied by a simultaneous transfer of an electron to the Mn^{4+} ion. Average intercalation voltages for the bulk, nanoparticle, nanorod, nanosheet and nanoporous β-MnO_2 calculated using the internal energies from DL_POLY molecular dynamics simulations are given in Figure 3-22. We couldn't simulate a system consisting of pure lithium on DL_POLY using Buckingham potentials used in this study. To study the trends in the intercalation voltages of nanostructures, we arbitrarily chose a value for the total energy of the lithium metal in equation *2.13* that would give a reasonable intercalation voltage. We see that the voltage increases with increasing lithium content contrary to experimental observations [13, 11]. As more lithium ions are intercalated, the chemical potential is expected to decrease leading to a decrease in the voltage. The nanoparticle was found to have the highest values of intercalation potentials followed by the nanoporous, nanosheet, nanorod and finally the bulk structure. Except for nanoparticle, the trend seems reasonable and is comparable to the trend of the surface to volume ratios.

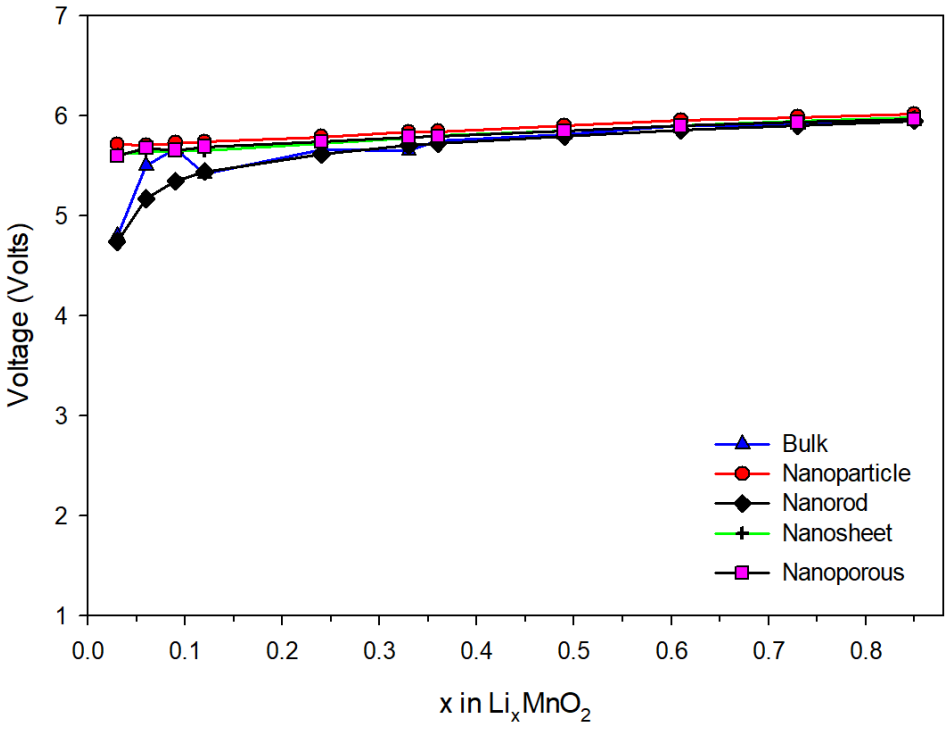

Figure 3-22: Average intercalation voltages of β-MnO_2 nanostructures calculated from DL_POLY internal energies.

To study the discrepancy in the trends of the average intercalation voltages obtained from DFT and classical GULP simulations, we compare the trends in the lowest total energies of Li_xMnO_2-β obtained from calculations of each method. Table 3-4 below shows the total energies of lithium/lithium-ion intercalated β-MnO_2 cell. The GULP total energies increase with increasing lithium content. This trend is opposite to that observed in the intercalation of Mg^{2+} into Mo_6S_8 where the $MgMo_6S_8$ and $Mg_2Mo_6S_8$ structures have total energies that the initial Mo_6S_8 structure [70].

Table 3-4: Trends in the classical and DFT total energies for the lithium/lithium-ion intercalated β-MnO_2 unit cell.

Li/Mn	Etot Interatomic Potentials (eV)
0.0	-82.8028
0.5	-72.0724
1.0	-71.5465

The total energies obtained from the DL_POLY MD simulations of lithium-ion intercalated nanostructures exhibit the same trend as those of GULP classical simulations. Since both approaches implemented the same interatomic potentials, we ascribe this to a discrepancy in the interatomic potentials. The O-O, Mn^{4+}-O and Li-O interatomic potentials have been previously shown to model both the $Mn^{(IV)}O_2$ [22] and Li_2O [60] well, thus we suggest that the interatomic potentials for the Mn^{3+}-O interaction, need to be optimised.

3.2 Sodium Intercalated MnO_2 Nanostructures

3.2.1 Na-MnO_2-β Volume Expansion

Figure 3-23 presents the plot of volume expansion of various nanostructures in response to sodium intercalation. The volume expansions of the lithiated

nanostructures were added for comparison. All sodium intercalated nanostructures expanded slightly more than the bulk structure. Overall, all structures expanded up to 60% at 85% sodium intercalation. This has far exceeded the volume expansion of 16% for β-MnO_2 nanoporous at full lithium intercalation predicted by Sayle et al [23].

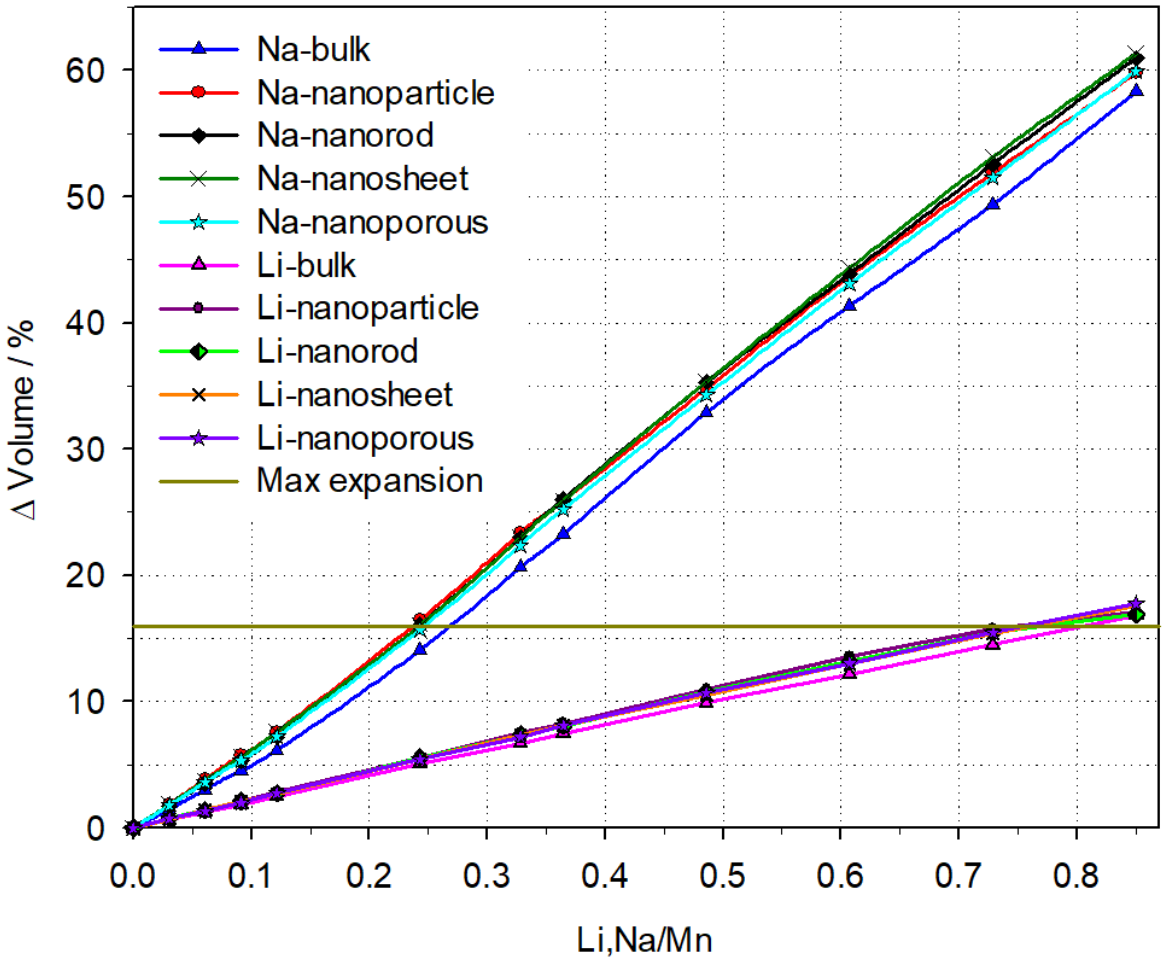

Figure 3-23: Volume expansion of the nanostructures as a function of lithium and sodium concentration. Maximum expansion value was predicted by Sayle [23].

All sodium intercalated structures expanded more than the lithiated one due to the inherently larger ion size of sodium relative to the lithium-ion.

3.2.2 Na-MnO_2-β Microstructural Response

Diagrams (b) to (e) in Figure 3-24 to Figure 3-28 below show the evolution of the microstructure in the bulk structure, nanoparticle, nanorod, nanosheet and nanoporous in response to sodium ion concentration. The microstructure diagrams of the bulk structure and all nanostructures as sodium ion concentration is increased was preserved up to about 0.24 Na/Mn. The volume expansion at this sodium concentration is around the 16% value predicted by Sayle et al [23] as the maximum volume expansion the nanoporous β-MnO_2 could achieve at full lithium intercalation. Beyond this value, the bulk structure and all the nanostructures experienced gradual structural deformation. The degree of deformation increased with increasing sodium concentration until an amorphous state was reached. Microstructure diagram (e) shows that the β-MnO_2 intercalation host is severely at 49%. The high volume expansion caused by the larger sodium ions has exceeded the volume expansion threshold at a relatively lower sodium concentration when compared to the lithium concentration. Sodium is favoured to replace lithium as a charge carrier within lithium-ion batteries because it is abundant, safe and costs less. However, the volume expansion limitation corresponding to around 0.24 Na/Mn found in this study could severely limit the capacity of Na-MnO_2.

The Mn-Mn radial distribution functions of the sodium intercalated bulk structure, nanoparticle, nanorod, nanosheet and nanoporous are presented in Figure 3-29. The second and third peaks corresponding to manganese ions on the MnO_6 octahedral chains that surround the 1x1 pyrolusite tunnel shifted to the right indicating tunnel expansion and decreased in intensity as more sodium ions were intercalated. This loss in peak RDF peak intensity resulted from a wide variation in bond distances for the second and third nearest neighbour manganese ions. From 0.24 Na/Mn, the third peak and other subsequent peaks flattened showing loss of long-range order within the radial distribution functions indicating that the β-MnO_2 had transformed into an amorphous consistent with the microstructure results.

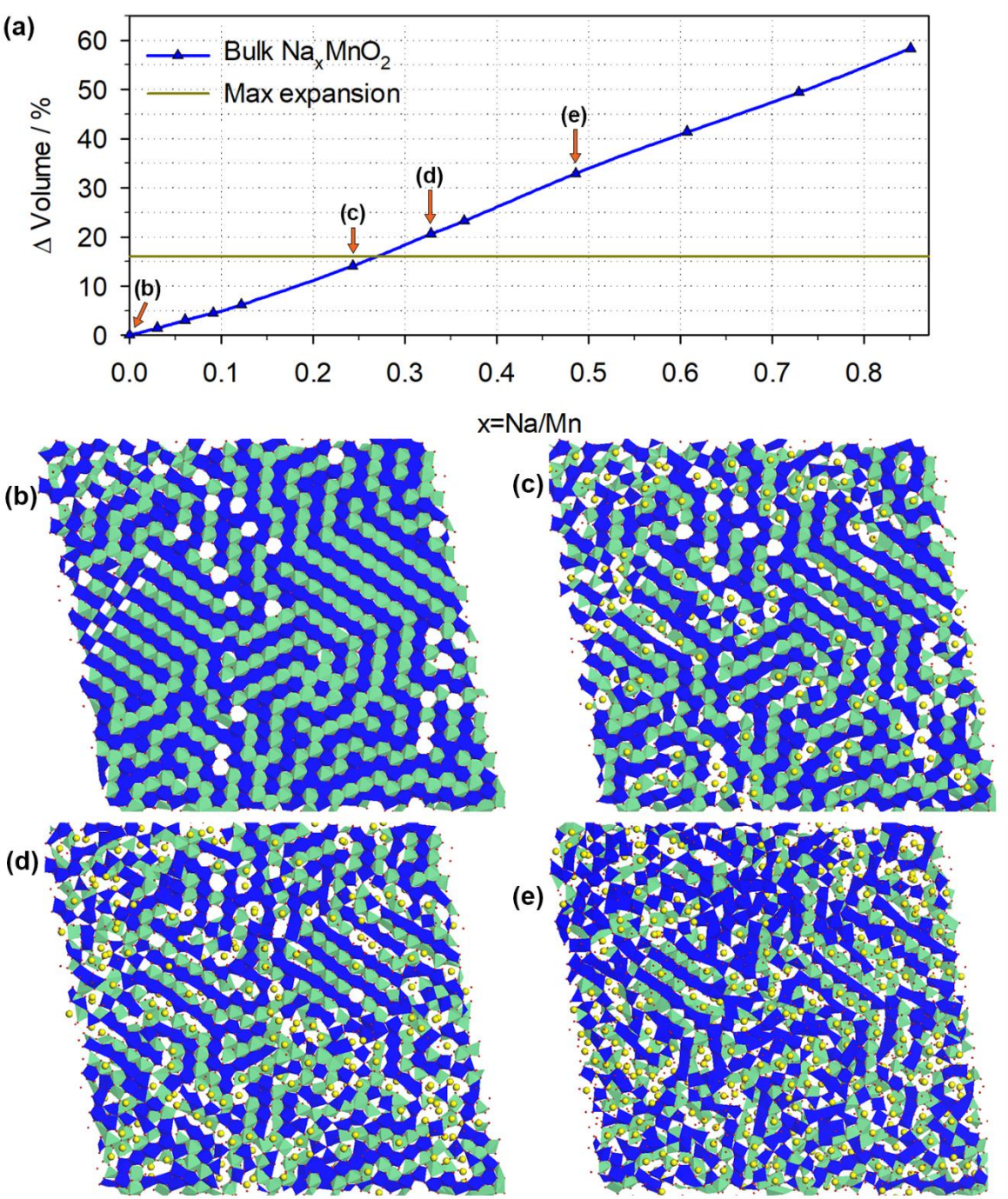

Figure 3-24: (a) A plot of change in volume versus sodium-ion concentration for bulk Na_xMnO_2-β (x = 0.0, 0.03, 0.06, 0.09, 0.12, 0.24, 0.33, 0.36, 0.49, 0.61, 0.73 and 0.85). Microstructure slices were taken at Na/Mn fractions of (b) 0.00, (c) 0.24, (d) 0.33 and (e) 0.49. Blue and cyan represent the top and bottom MnO_6 octahedral planes. Sodium ions are depicted by yellow spheres.

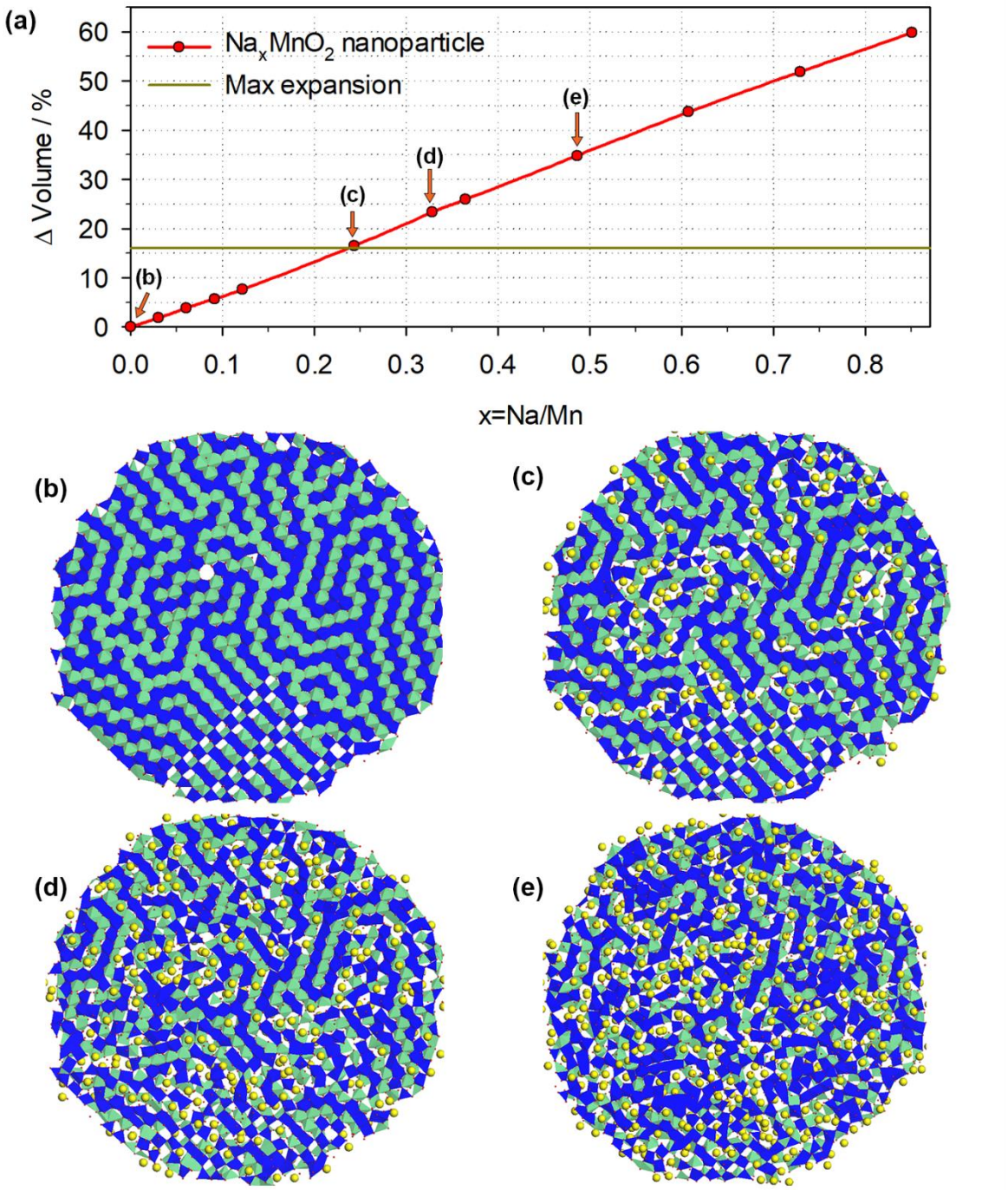

Figure 3-25: (a) A plot of change in volume versus sodium-ion concentration for nanoparticle Na_xMnO_2-β (x = 0.0, 0.03, 0.06, 0.09, 0.12, 0.24, 0.33, 0.36, 0.49, 0.61, 0.73 and 0.85). Microstructure slices were taken at Na/Mn fractions of (b) 0.00, (c) 0.24, (d) 0.33 and (e) 0.49. Blue and cyan represent the top and bottom MnO_6 octahedral planes. Sodium ions are depicted by yellow spheres.

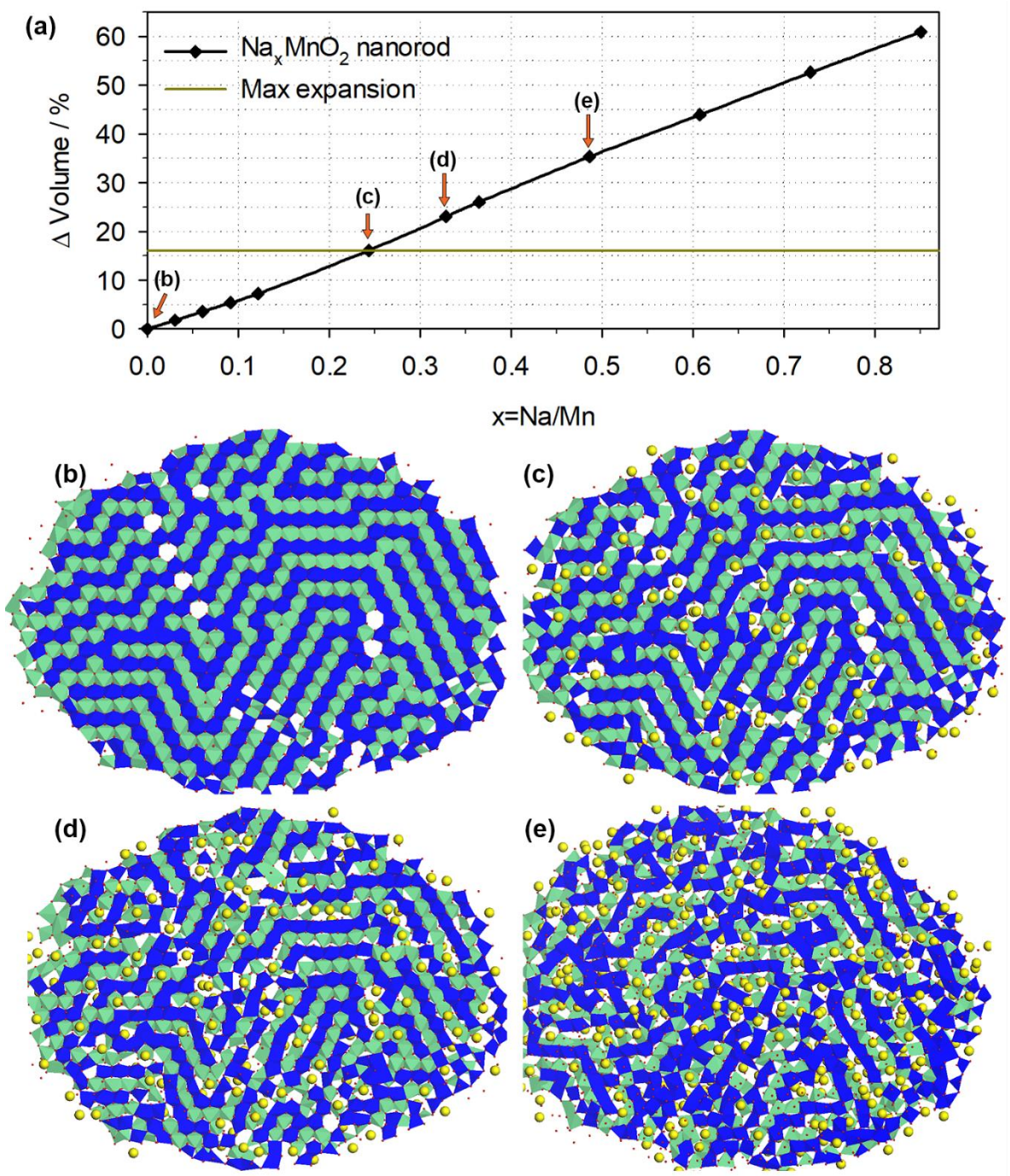

Figure 3-26: A plot of change in volume versus sodium-ion concentration for nanorod Na_xMnO_2-β (x = 0.0, 0.03, 0.06, 0.09, 0.12, 0.24, 0.33, 0.36, 0.49, 0.61, 0.73 and 0.85). Microstructure slices were taken at Na/Mn fractions of (b) 0.00, (c) 0.24, (d) 0.33 and (e) 0.49. Blue and cyan represent the top and bottom MnO_6 octahedral planes. Sodium ions are depicted by yellow spheres.

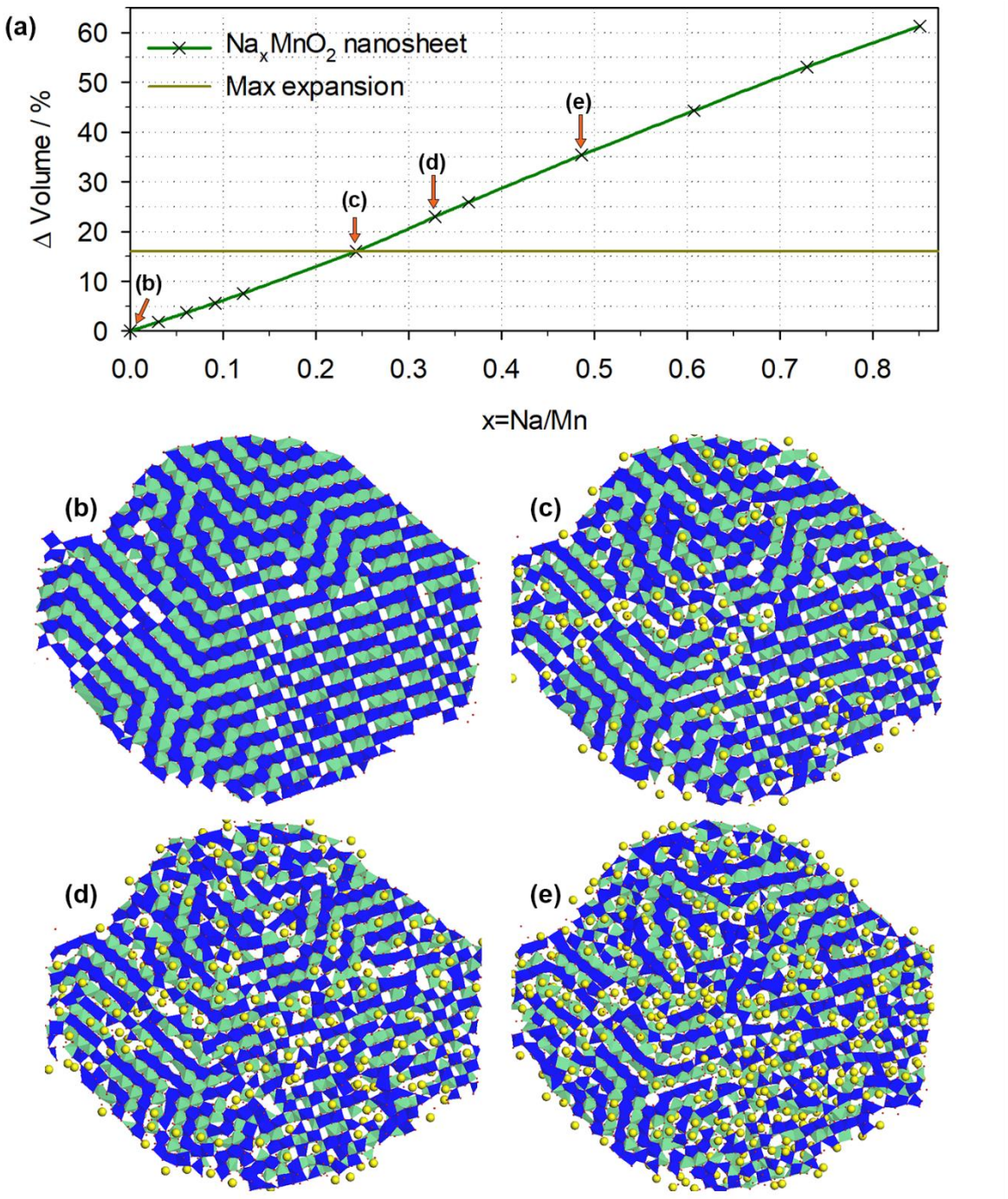

Figure 3-27: A plot of change in volume versus sodium-ion concentration for nanosheet Na_xMnO_2-β (x = 0.0, 0.03, 0.06, 0.09, 0.12, 0.24, 0.33, 0.36, 0.49, 0.61, 0.73 and 0.85). Microstructure slices were taken at Na/Mn fractions of (b) 0.00, (c) 0.24, (d) 0.33 and (e) 0.49. Blue and cyan represent the top and bottom MnO_6 octahedral planes. Sodium ions are depicted by yellow spheres.

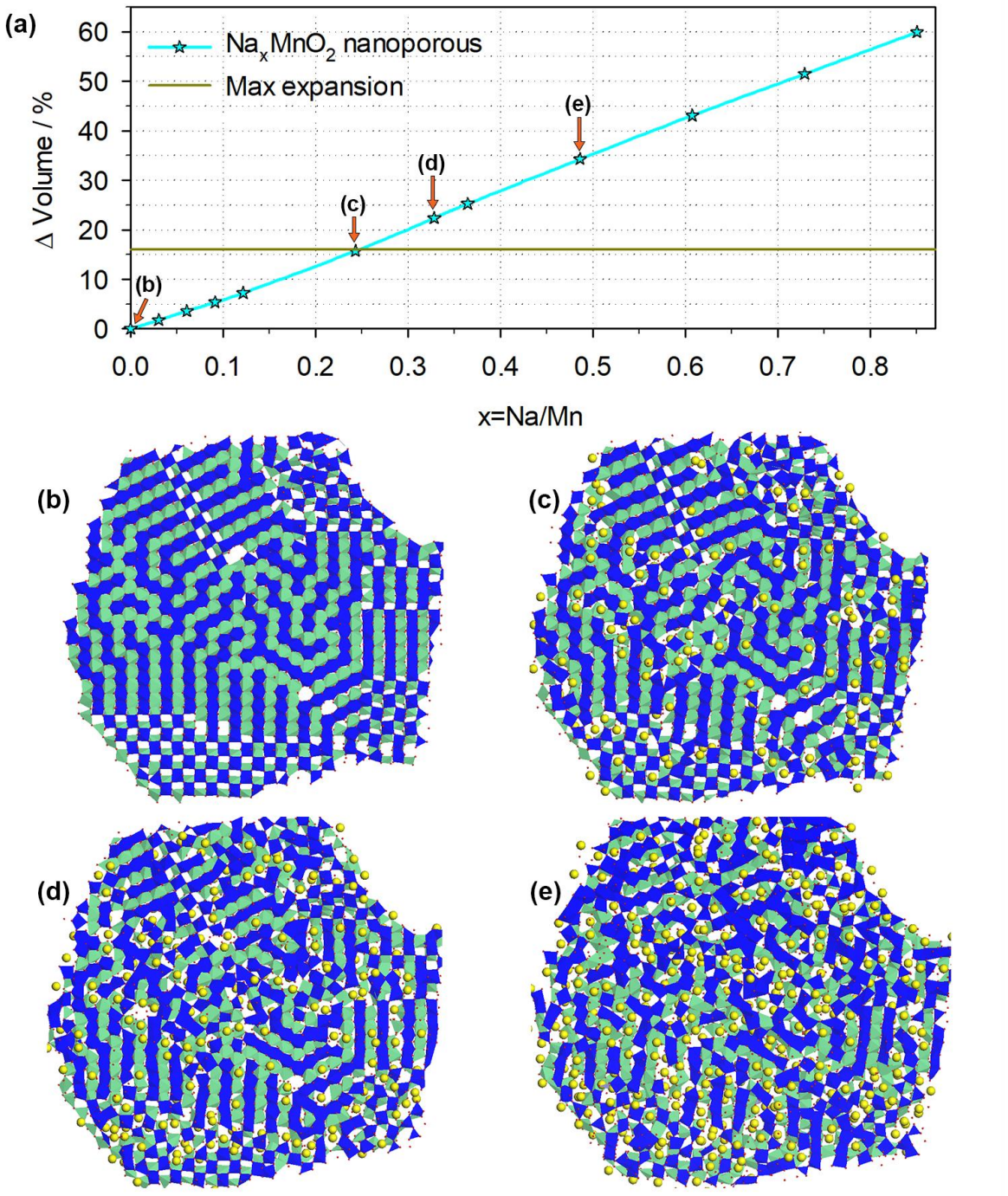

Figure 3-28: A plot of change in volume versus sodium-ion concentration for nanoporous Na_xMnO_2-β (x = 0.0, 0.03, 0.06, 0.09, 0.12, 0.24, 0.33, 0.36, 0.49, 0.61, 0.73 and 0.85). Microstructure slices were taken at Na/Mn fractions of (b) 0.00, (c) 0.24, (d) 0.33 and (e) 0.49. Blue and cyan represent the top and bottom MnO_6 octahedral planes. Sodium ions are depicted by yellow spheres.

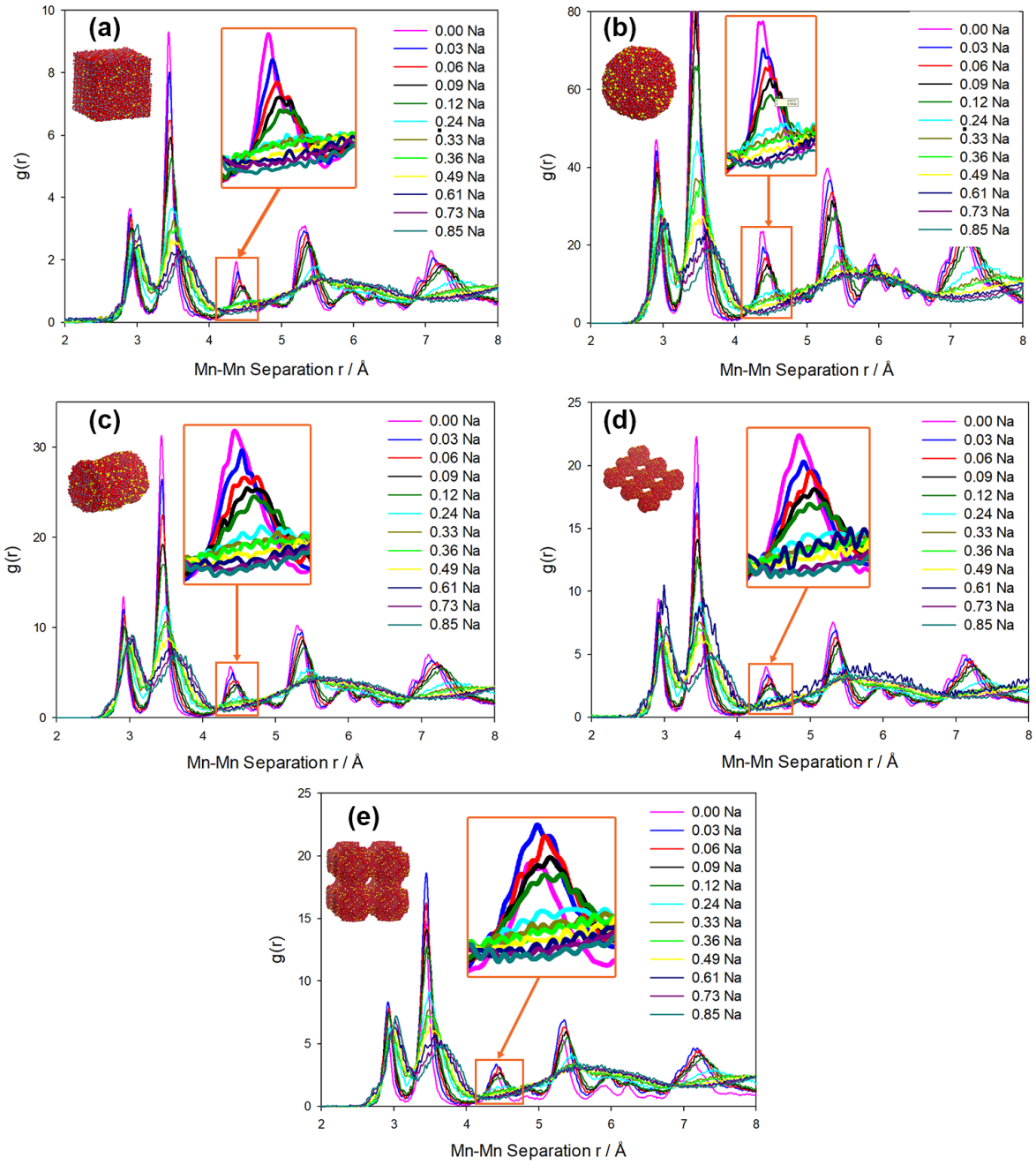

Figure 3-29: Mn-Mn Radial distribution functions of the sodium intercalated (a) bulk structure, (b) nanoparticle,(c) nanorod,(d) nanosheet and (e) nanoporous β-MnO_2.

3.2.3 Simulated X-Ray Diffraction Patterns

The X-ray diffraction patterns for the pure and sodium intercalated bulk, nanoparticle, nanorod, nanosheet and nanoporous β-MnO_2 are presented in Figure 3-30 to Figure 3-34. As more sodium was intercalated all the characteristic β-MnO_2 peaks shifted to lower diffraction angles indicating expansion in the lattice parameters. The x-ray diffraction patterns of the new phase arising from the large anisotropic cell expansion could be indexed on the orthorhombic unit cell for the lithiated mesoporous β-MnO_2 [13]. All x-ray diffraction peaks have significant intensity up to 0.24 Na/Mn. Beyond this sodium concentration, the (1 1 0), (2 0 0), (1 1 1) and (2 1 1) peaks severely decreased in intensity at 0.33 Na/Mn and vanished at higher concentrations.

All x-ray diffraction peaks in bulk β-MnO_2 except the (1 0 1) peak vanish from 0.36 Na/Mn. The large x-ray diffraction peak reduction indicates a transition to an amorphous state which is in agreement to the radial distribution function results where the loss in structural integrity began at Na/Mn fractions above 0.24.

In contrast to the bulk β-MnO_2, the x-ray diffraction peaks for all the nanostructures vanish from 0.49 Na/Mn. This indicates that the transformation to an amorphous state in bulk β-MnO_2 begins earlier than in the nanostructures. Overall, all the nanostructures exhibited the same trend.

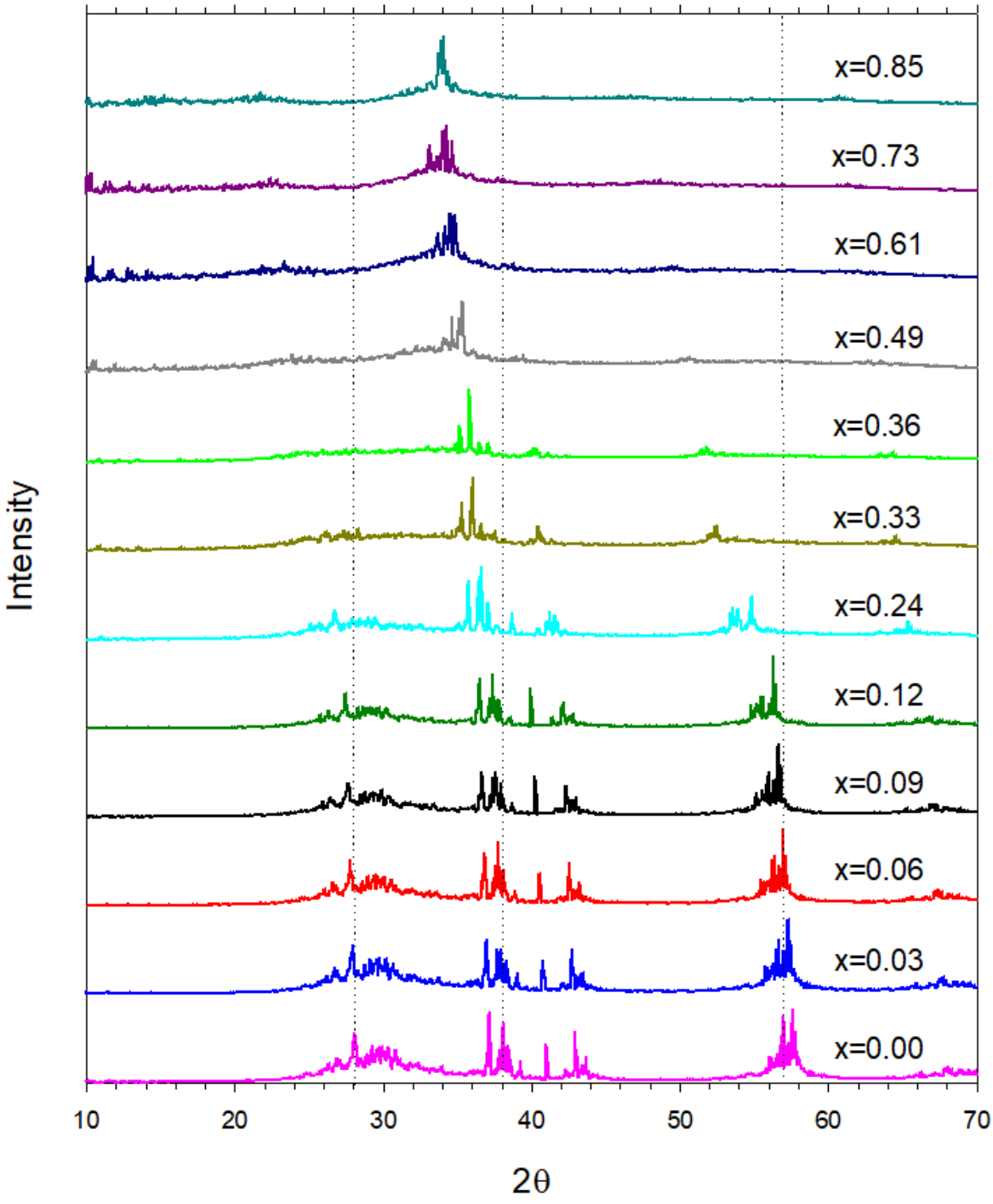

Figure 3-30: Simulated X-ray diffraction patterns of bulk Na_xMnO_2-β.

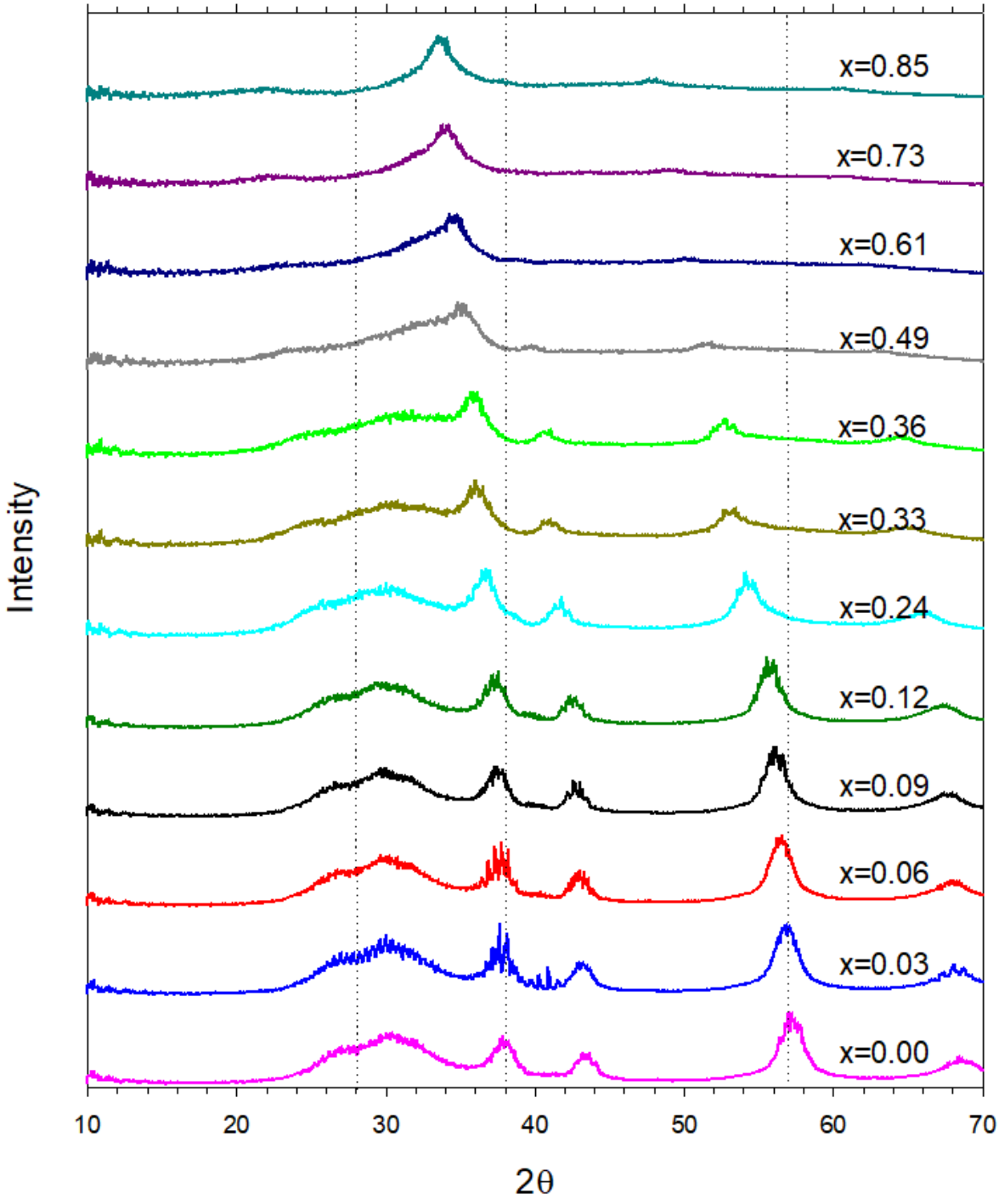

Figure 3-31: Simulated X-ray diffraction patterns of nanoparticle Na_xMnO_2-β.

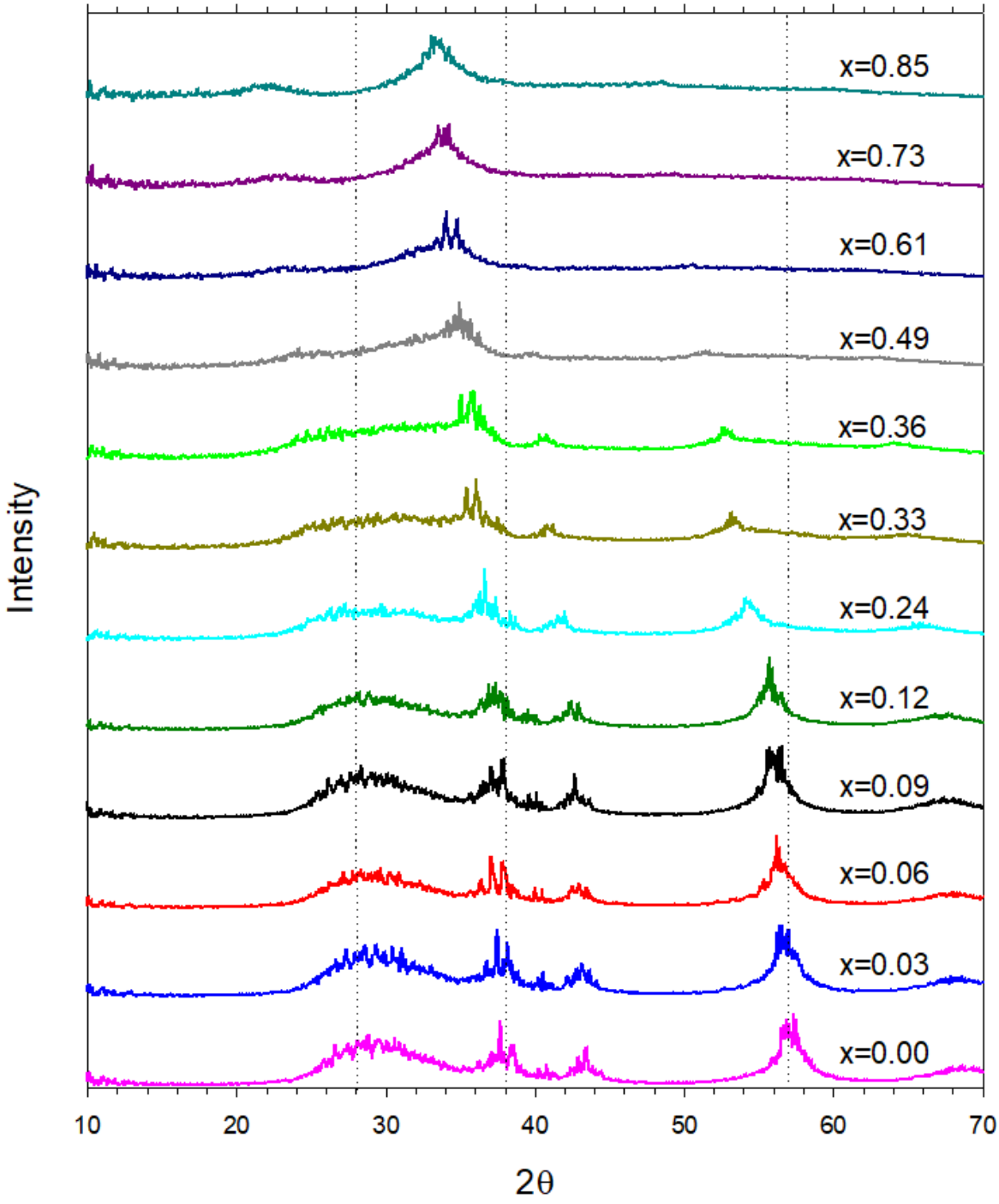

Figure 3-32: Simulated X-ray diffraction patterns of nanorod Na_xMnO_2-β.

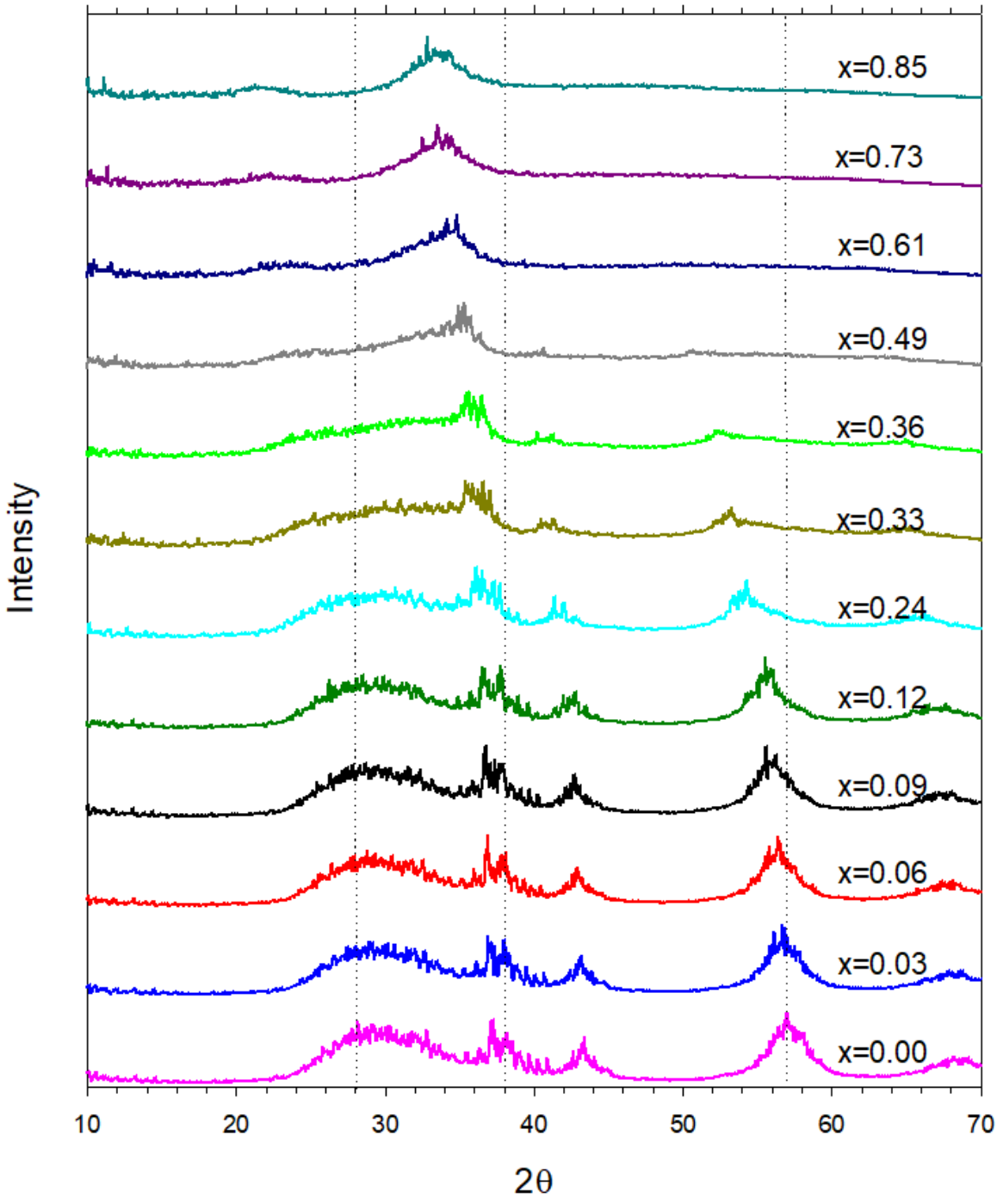

Figure 3-33: Simulated X-ray diffraction patterns of nanosheet Na_xMnO_2-β.

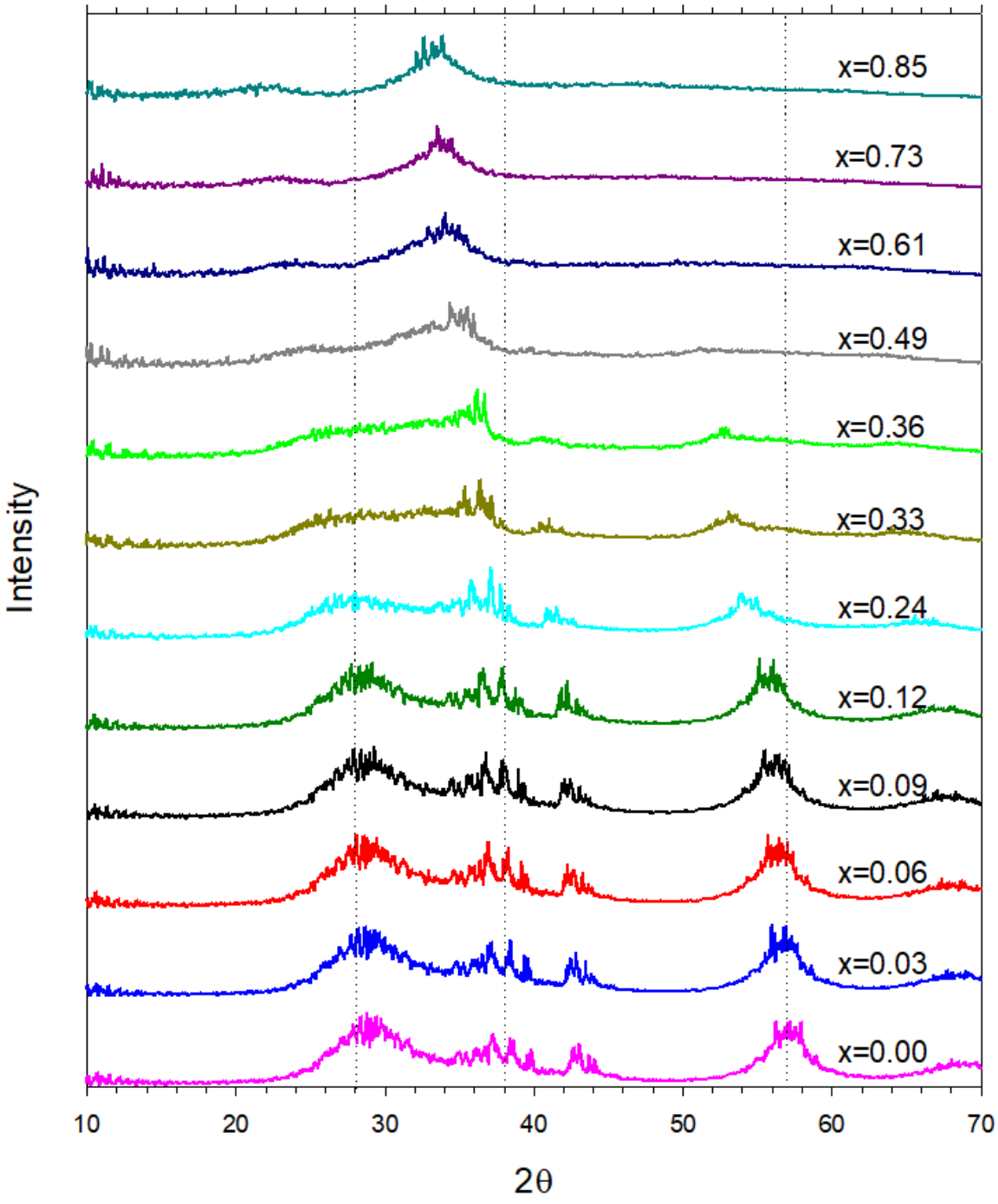

Figure 3-34: Simulated X-ray diffraction patterns of nanoporous Na_xMnO_2-β.

Chapter 4

Results and Discussions: Mechanical Properties

Mechanical properties are important because they give insight into the mechanical and dynamical behaviour of crystals in relation to forces operating on them and also allow us to discern the nature of forces operating on solids. They help in studying the stability and stiffness of solids under various forces and ultimately aid in material characterisation. As such, the results of the mechanical properties of the bulk and nanorod β-MnO_2 are discussed below. The bulk β-MnO_2 is known to be electrochemically inactive and is used merely for comparison against the nanorod.

4.1 Microstructure Selection

Atomistic simulation programs generally save the intermediate states and properties of the system under study at regular intervals as a trajectory and output files. Molecular graphics allow us to visualise and study these intermediate states of the system akin to in situ experiments where the system, molecule or crystal, is studied in its natural environment. Microstructure diagrams are a useful molecular graphics [64] tool we used in the analysis of the bulk structure and nanorod's response to uniaxial compressive load. There are two ways in which one can cut or select microstructure slices from the bulk structure and nanorod to be used for analysis; the first slice can be made on the *ab* plane of the pyrolusite lattice where neighbouring MnO_6 octahedral units bond via sharing of a single oxygen atom at the corner (diagram (a) in Figure 4-1) while the second slice can be cut on the *ac* and *bc* planes oriented perpendicular to the *ab* plane where MnO_6 octahedral units connect via sharing of two oxygen atoms at the edge of the octahedra (diagram (b) in Figure 4-1).

In the slice depicted in diagram (c) of Figure 4-1, the *ab* plane type microstructure shown in diagram (a) is more prevalent and coexist in combination with the *ac* and

bc plane type microstructure shown in diagram (b) and some defects. Here the *ac* and *bc* plane type microstructure exists solely in the form of straight 1x1 pyrolusite tunnels without any twinning. In the slice depicted in diagram (d), the *ac* and *bc* plane type microstructure of diagram (b) is more prevalent than the *ab* plane type microstructure of diagram (a). In contrast to the slice in diagram (c), the 1x1 pyrolusite tunnels twin heavily in the *ac* and *bc* plane type microstructure with very small amounts of the *ab* type microstructure.

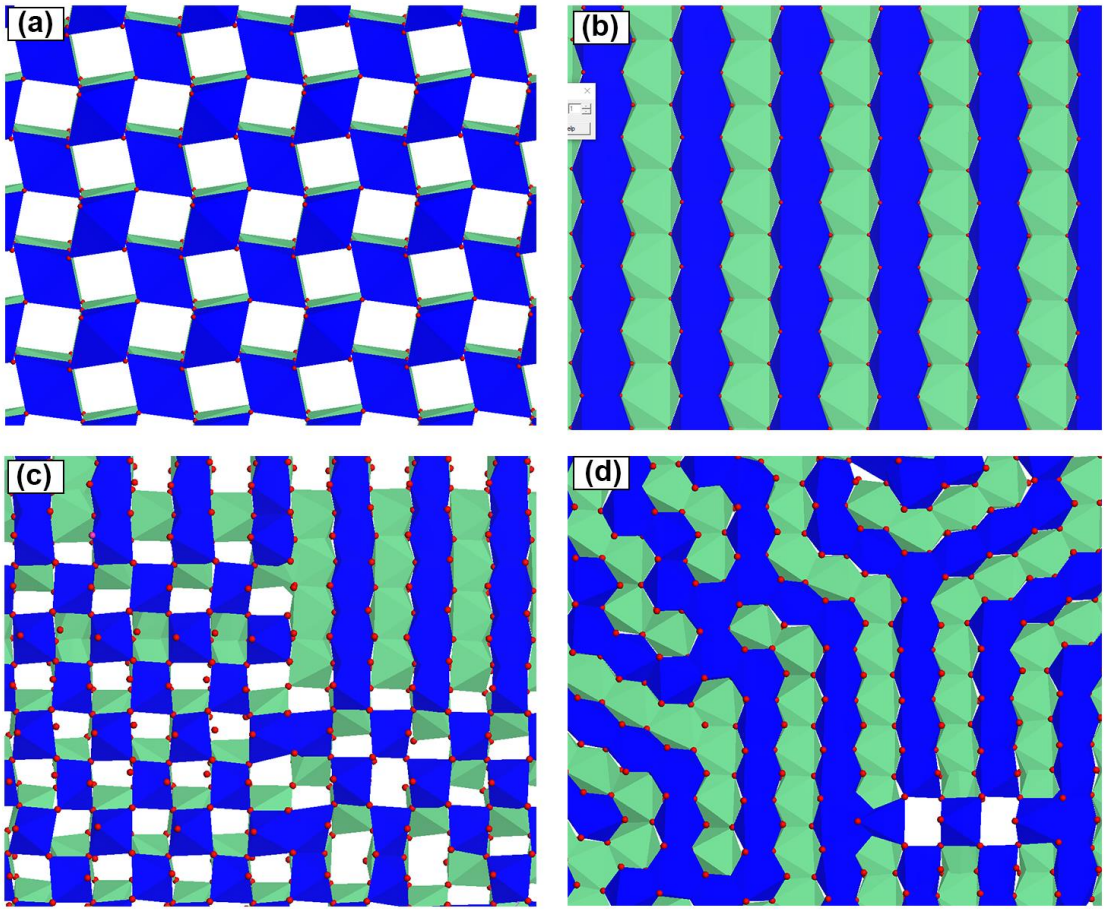

Figure 4-1: Microstructure slices of crystalline pyrolusite MnO_2 showing (a) 1x1 tunnels located on the *ab* plane, (b) 1x1 tunnels located on the *ac* or *bc* planes of the pyrolusite lattice. Slices of microstructure cut from the bulk pyrolusite MnO_2 after amorphisation and recrystallisation. Slices (c) and (d) exist in a perpendicular orientation to each other within the bulk MnO_2 supercell.

We have selected the type of microstructure slice depicted in Figure 4-1 diagram (c) below for use in the analysis of the pristine and lithiated bulk and nanorod MnO_2 under compressive stress because it captures the degradation mechanisms better.

4.2 Uniaxial Compressive Strain on Bulk Li_xMnO_2-β

4.2.1 Mechanical Properties

Stress vs strain curves for uniaxial compressive strain calculations on the pristine and lithiated bulk β-MnO_2 are provided below in diagram (a) of Figure 4-2, Figure 4-3, Figure 4-4, Figure 4-5, and Figure 4-6. Diagram (f) depicts the model used for applying uniaxial stress on the bulk models. Here, the direction of the applied stress is indicated by arrows and the spatial orientation of the microstructures used in the analysis is shown relative to the parent bulk material using three directional cell parameter arrows.

A summary of the mechanical properties of the pure and lithiated bulk β-MnO_2 that were obtained from the stress-strain curves is presented in Table 4-1. Under compressive loading, the bulk structure contracts elastically up to 6.0, 6.0, 6.0, 7.0 and 7.0 % strain for 0.00, 0.03, 0.12, 0.24 and 0.73 lithium fractions, respectively. The proportionality limits, the stress value beyond which stress and strain are no longer proportional, were found to be 14.9, 15.5, 16.9, 19.2 and 17.0 GPa for 0.00, 0.03, 0.12, 0.24 and 0.73 lithium fractions respectively. The proportionality limit generally increases as more lithium ions are inserted except for the specimen with 0.73 Li/Mn.

The calculated elastic moduli were found to be 299, 295, 282, 275 and 252 GPa for 0.00, 0.03, 0.12, 0.24 and 0.73 and 0.73 lithium fractions, respectively. The simulated elastic modulus of 299.73 GPa calculated for our unlithiated bulk structure is comparable to the value of 276.34 GPa obtained through density functional theory methods [71]. These elastic moduli values indicate that under compressive loading

the bulk structure becomes more brittle at subsequently higher lithium content. Structural deformation began at 12.1, 11.7, 11.6, 10.1 and 8.5% strain for 0.00, 0.03, 0.12, 0.24 and 0.73 lithium fractions, respectively, suggesting that as more lithium ions are intercalated the parent bulk material fractures at subsequently lower strains.

Table 4-1: Summarised mechanical properties of lithiated bulk β-MnO_2 under compressive strain.

Li/Mn	Yield Stress		Simulated Elastic Modulus (Y)		DFT (Y)
	katm	GPa	katm	GPa	GPa
0.00	171.60	17.38	2958.11	299.73	276.34 [71]
0.03	168.80	17.10	2911.31	294.99	
0.12	166.70	16.89	2787.57	282.45	
0.24	160.20	16.23	2714.67	275.06	
0.73	168.00	17.02	2494.11	252.72	

4.2.2 Microstructure of Bulk Li_xMnO_2-β (x=0.00, 0.03, 0.12, 0.24, 0.73)

The microstructural response in the bulk Li_xMnO_2-β, x = 0.00, 0.03, 0.12 and 0.24, as the stress is subsequently increased along the Y-axis is presented in diagrams (b), (c), (d) and (e) of Figure 4-2 to Figure 4-5. The following regions enclosed within rectangles are key to the onset of structural degradation mechanisms that occur in the bulk structure during discharge and compressive loading:

(i) A microstructure slice of bulk Li_xMnO_2-β, x = 0.00 and 0.03, under zero stress is shown in diagram (b) where the orange rectangles enclose the 1x1 pyrolusite tunnel structures commonly found within the *ab* plane of the pyrolusite lattice, see diagram (a) of Figure 4-1 for reference. Some of the tunnels are intercalated with lithium ions.

(ii) Most notable are the microstructure domains enclosed in the black rectangles in bulk β-MnO_2 at 0.00, 0.03, 0.12 and 0.24 Li/Mn which comprise

microstructural defects akin to collapsed 1x1 pyrolusite tunnels found before stress application.

(iii) Present in the unlithiated bulk β-MnO_2 is the region enclosed by a purple rectangle that comprises a combination of 1x1 tunnels, 1x2 tunnels, and the conjoined 1x2 tunnels forming an L-shape.

(iv) There is also a highly crystalline region of 1x1 tunnel structures found in *ab* pyrolusite planes denoted by the red rectangle at 0.03, 0.12 and 0.24 Li/Mn.

(v) The pink rectangles comprise long untwinned 1x1 pyrolusite tunnels found in the ac/bc plane of the pyrolusite lattice, diagram (b) of Figure 4-1, shown for 0.00, 0.03, 0.12 and 0.24 Li/Mn.

(vi) A region where 1x1 and 1x2 tunnels join denoted by a yellow rectangle shown for $Li_{0.03}MnO_2$-β in Figure 4-3.

(vii) A region where 1x1 and 1x2 tunnels join denoted by yellow rectangles shown for 0.03 Li/Mn.

Elastic limit

At the elastic limit, point (c) in diagram (a), the bulk structure has contracted through the compression of the tunnels in order to accommodate the applied stress. As expected of the material within the elastic region, the microstructure depicts no obvious structural alterations, see all regions enclosed by rectangles.

Plastic deformation region

For lithium-ion fractions of 0.00, 0.03, 0.12 and 0.24 Li/Mn, we observed a minute structural modification of the microstructure at the plastic limit, point (d) in diagram (a), within and around the defect region enclosed by a black rectangle where structural deformation spread to the nearby regions. There's an exception of a broken/over-extended Mn-O bond located top right in the red rectangle for $Li_{0.03}MnO_2$-β. Note that the octahedral unit that pulled away the previously shared oxygen atom did not form additional bonds with other octahedra so this deformation is not permanent and the bonds may reform if the strain is removed.

Collapse

Point (e) in diagram (a) represents the state of the bulk structure during the collapse phase with the corresponding microstructure provided in diagram (e). We observed that the microstructure in the defective region, black rectangle, spread out to the neighbouring regions and induced structural modifications in the form of collapsed 1x1 tunnels. This took place at 0.00, 0.03, 0.12 and 0.24 Li/Mn. Additionally for the unlithiated bulk, the 1x2 and 2x2 tunnels depicted in the regions enclosed by purple rectangles collapsed and deformation spread to neighbouring 1x1 tunnels regions. The long untwinned 1x1 tunnels of the *ac*/*bc* plane in the pyrolusite lattice, pink rectangles, also collapsed to a high degree along the axis of the applied force for bulk β-MnO_2. In $Li_{0.03}MnO_2$-β several Mn-O bonds along the direction perpendicular to the applied force were broken and new Mn-O bonds formed along the axis of the applied force. At 0.12 and 0.24 Li/Mn, the MnO_6 octahedral planes on the right shifted upwards by one plane forming a grain boundary and were accompanied by the breaking and collapse of the long 1x1 tunnels. The result of this structural deformation mechanism can be seen in the left side of the purple octahedral planes, which initially consisted of defect-free 1x1 tunnels intercalated with lithium ions, and long untwinned 1x1 tunnels denoted by the pink rectangles. Additional defects have been introduced into the material on the grain boundary where the plane shift took place. The pyrolusite region enclosed by red rectangles collapsed for bulk β-MnO_2 at 0.03, 0.12 and 0.24 Li/Mn but not for the unlithiated phase. Another source of structural deformation at 0.03 Li/Mn was a region in the yellow rectangles where the Mn-O bonds in the corner-shared oxygen atoms broke due expansion in the direction perpendicular to the applied force.

Lastly, the 1x1 tunnels extended in the Z-axis which is perpendicular to the direction of the applied stress resulting in the disjoining of the MnO_6 octahedral units at the corner-shared oxygen. This is depicted in the region enclosed by the orange rectangles at low concentrations of lithium ions i.e. 0.00 and 0.03 Li/Mn.

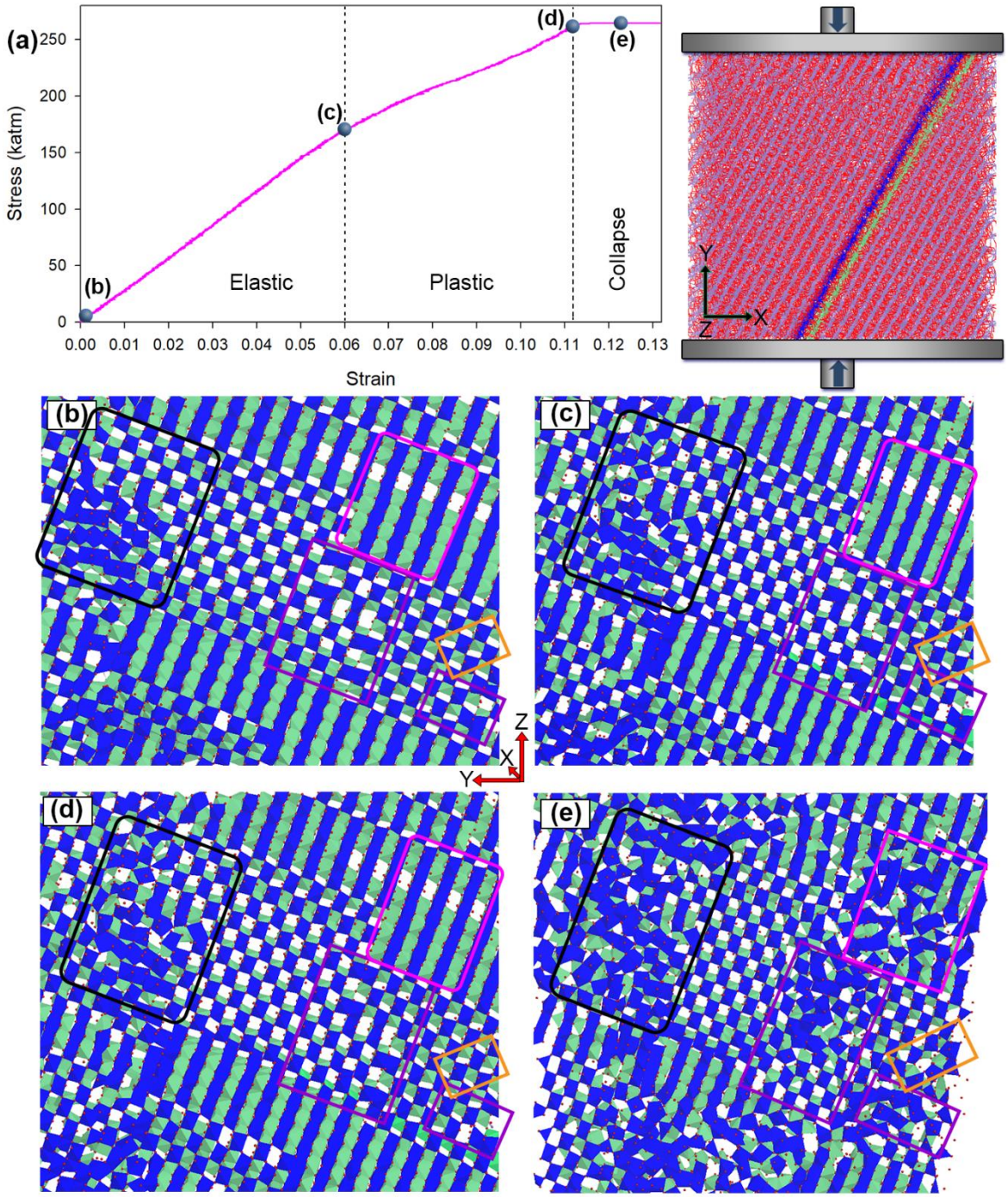

Figure 4-2: (a) Compressive stress-strain plot of bulk β-MnO_2 and microstructure at the (b) zero stress point, (c) elastic limit, (d) plastic limit and (e) collapse region. The model of the stress application and the region where the microstructure slices were taken within the bulk structure are provided in diagram (f). Rectangles highlight the regions of the microstructure where structural degradation under stress originates.

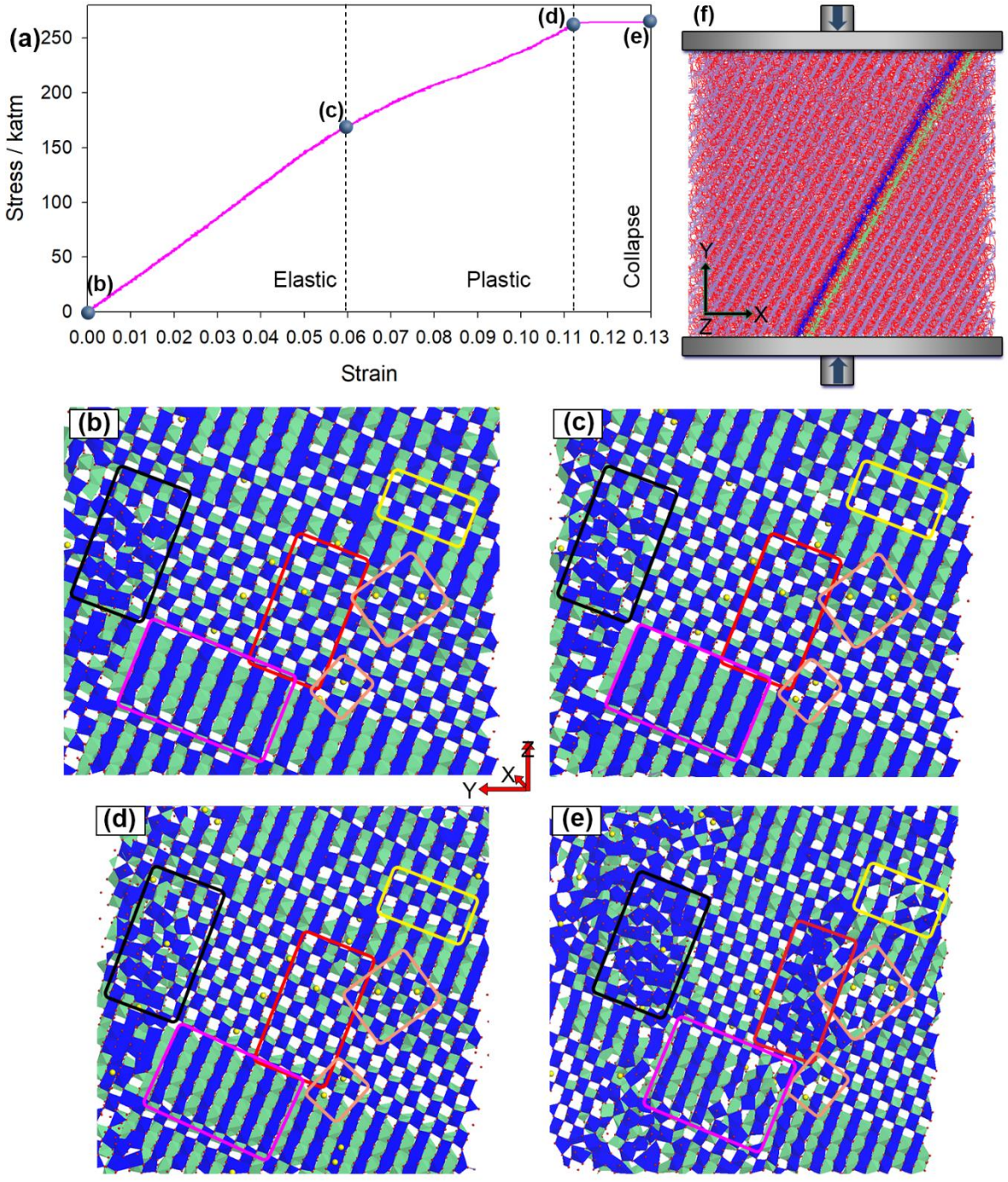

Figure 4-3: Compressive stress-strain plot of bulk $Li_{0.03}MnO_2$-β and microstructure at the (b) zero stress point, (c) elastic limit, (d) plastic limit and (e) collapse region. The model of the stress application and the region where the microstructure slices were taken within the bulk structure are provided in diagram (f). Rectangles highlight the regions of the microstructure where structural degradation under stress originates.

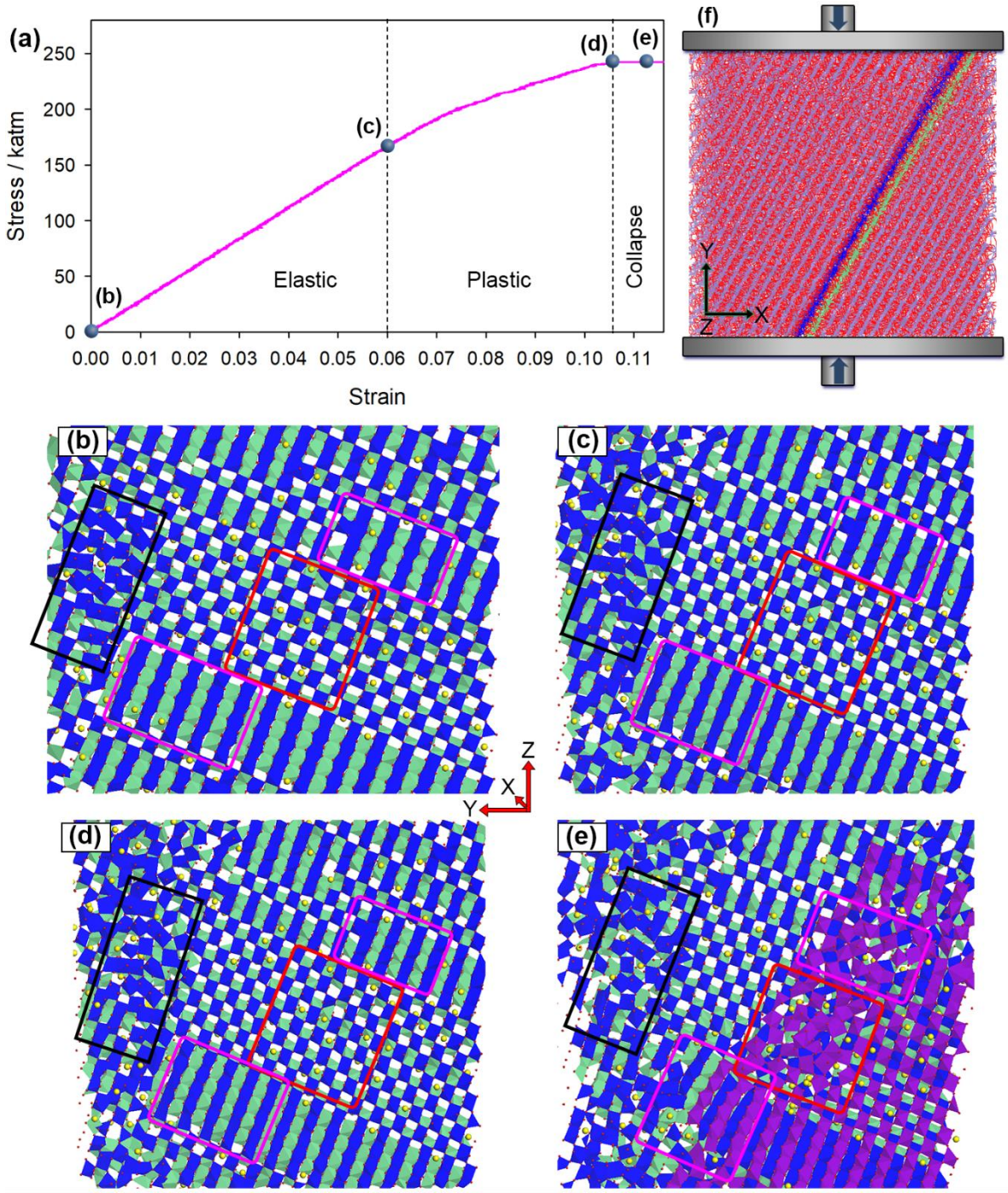

Figure 4-4: Compressive stress-strain plot of bulk $Li_{0.12}MnO_2$-β and microstructure at the (b) zero stress point, (c) elastic limit, (d) plastic limit and (e) collapse region. The model of the stress application and the region where the microstructure slices were taken within the bulk structure are provided in diagram (f). Rectangles highlight the regions of the microstructure where structural degradation under stress originates.

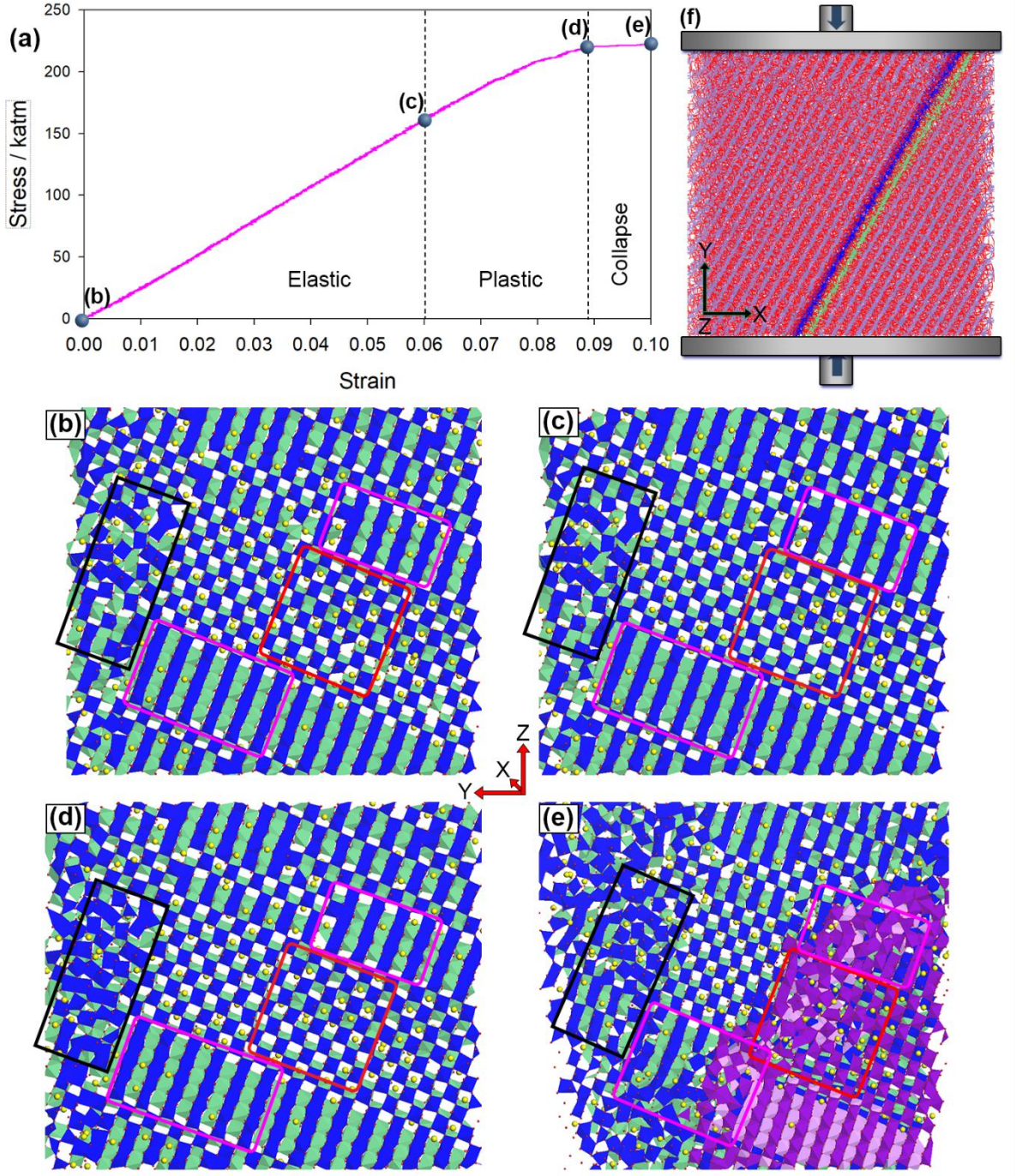

Figure 4-5: Compressive stress-strain plot of bulk $Li_{0.24}MnO_2$-β and microstructure at the (b) zero stress point, (c) elastic limit, (d) plastic limit and (e) collapse region. The model of the stress application and the region where the microstructure slices were taken within the bulk structure are provided in diagram (f). Rectangles highlight the regions of the microstructure where structural degradation under stress originates.

The microstructural response in bulk $Li_{0.73}MnO_2$-β with respect to uniaxial compression is presented in diagrams (b), (c), (d) and (e) of Figure 4-6 with the corresponding lateral views shown in diagrams (g), (h), (i) and (k), respectively. Dashed lines indicate the movement of grain boundaries under compressive loading as the microstructure evolves.

We start off within the elastic region with the microstructure at zero stress shown in diagram (b). Of interest here is the area enclosed by a red rectangle that plays a key role in the initial stage of structural modification and later its progression. This region comprises 1x1 pyrolusite tunnel structures natively found within the *ab* plane of the pyrolusite lattice (see diagram (a) of Figure 4-1). Under compressive loading, the 1x1 tunnels elastically compressed along the axis Y of stress by 6.7 % and expanded in the perpendicular X and Z axes without any permanent structural deformations.

Irreversible structural modification began in the plastic region. Under compressive loading, the lithium ions limited the extent of compression along the Y-axis and stabilised the 1x1 tunnels thus preventing them from collapsing. Additionally, the tunnels expanded more along the X and Z axes. Beyond the tunnels' elastic expansion threshold the bulk structure deformed plastically through the breaking of the Mn-O bonds within the *ab* pyrolusite sublattice planes. In particular:

(i) The central MnO_6 octahedral unit that shares oxygen atoms at the corners with four neighbouring octahedra was pulled away by two of the octahedra in the Z direction perpendicular to the direction of compression and broke off from the other two octahedra.
(ii) This MnO_6 octahedral unit then formed a new additional bond with each of the two adjacent octahedra by sharing two oxygen atoms at the edge instead of the initial sharing of one corner oxygen.
(iii) The formation of two edge-sharing oxygen atoms was accompanied by the shifting downwards of the blue and green MnO_6 octahedral planes as well as other octahedral planes above and below them. Diagram (h) shows that the

blue octahedral plane has shifted almost halfway downwards at the plastic limit and a discontinuity in the octahedral planes has formed in a boundary line where the blue octahedral plane ends.

The two grain boundaries, denoted by dashed lines, maintained their respective alignment. Within the collapse region denoted by microstructures in diagrams (d) and (e), the deformation progressed whereby the blue octahedral plane group shifted further downwards by one plane. Each octahedral plane on the left side then temporarily joined with a corresponding octahedral plane on the right side forming defects that are visible within the rectangle. This movement allowed the blue and purple octahedral plane groups to move closer along the direction of the applied force. Additionally, the blue octahedral plane group slid slightly underneath the purple octahedral plane, see the rectangle in diagram (e). Also during this process, the grain boundaries on the purple octahedral plane group were displaced slightly along the Z-axis in the earlier stages and more in the later stages, see dashed lines.

All these processes allowed the bulk $Li_{0.73}MnO_2$-β structure to mechanically compress along Y-axis. This complex process introduced irreversible structural modifications through breaking of Mn-O bonds on previous octahedral planes, the formation of new Mn-O bonds on the next octahedral planes and the displacement of the MnO_6 octahedral planes on one side. These structural modifications can be seen generally along the boundary between the blue and purple octahedral planes, especially within the red rectangle. Additional structural deformation occurred within the orange rectangle where a subdomain consisting of 1x1 tunnels located in the shifted octahedral plane collapsed. The octahedral plane movement occurred in more than one sub-section of the main octahedral plane. This can be seen in the region within the pink rectangle where the octahedral plane also shifted downwards.

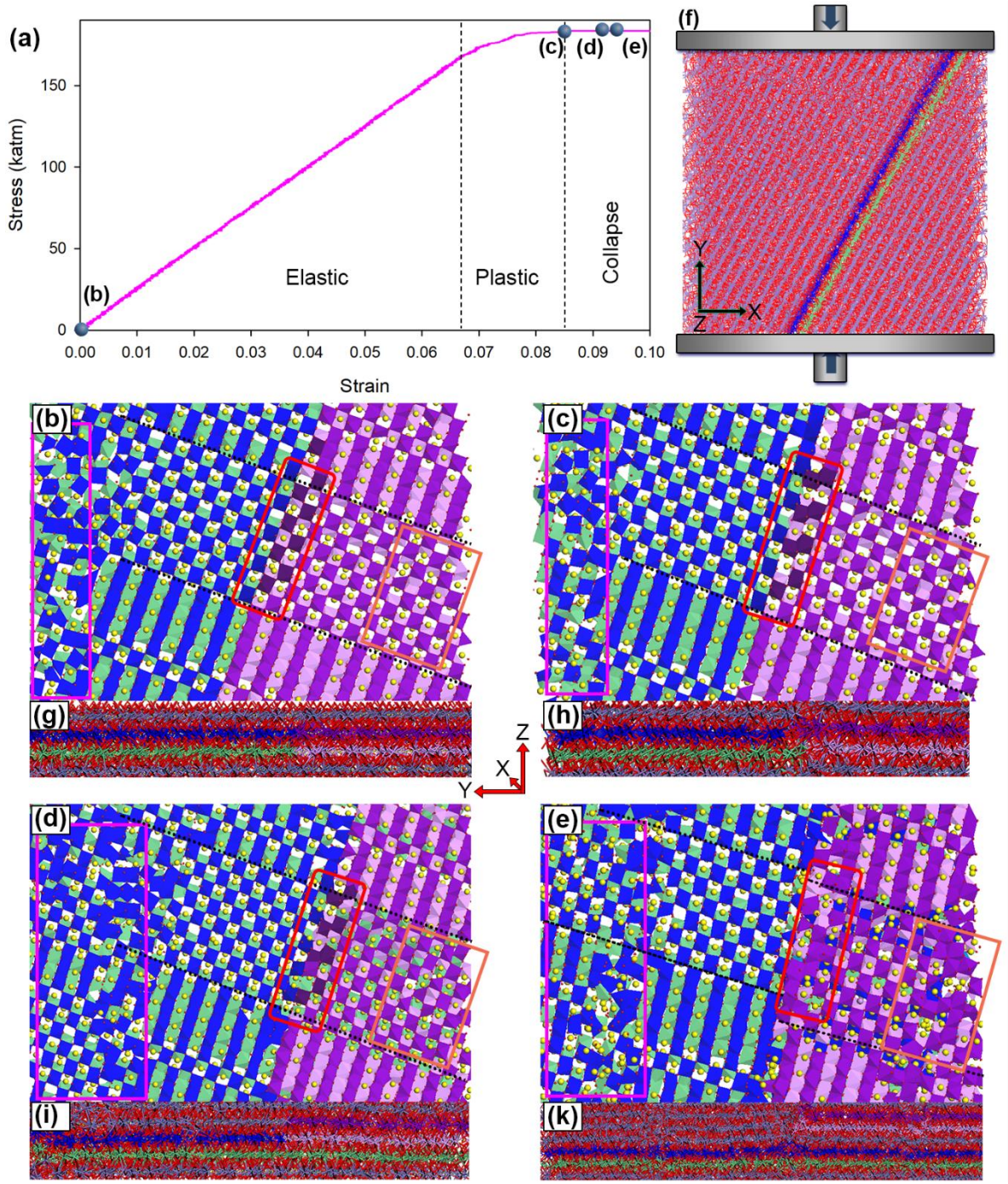

Figure 4-6: (a) Compressive stress-strain plot of bulk $Li_{0.73}MnO_2$-β and microstructure in the (b) elastic, (c) plastic and (d, e) collapse regions. Diagrams (g), (h), (i) and (k) show MnO_6 octahedral plane view of microstructures in (b), (c), (d) and (e) respectively. Rectangles highlight the region where mechanical deformation begins. The top MnO_6 octahedral plane is depicted by blue and purple while the bottom plane is depicted by green and pink.

4.2.3 Mn-Mn Radial Distribution Functions of Bulk Li_xMnO_2-β (x = 0.00, 0.03, 0.12, 0.24 and 0.73)

The M-Mn radial distribution functions (RDFs) at the zero stress, elastic limit, and plastic regions for the β-MnO_2 nanorod at 0.00, 0.03, 0.12, 0.24 and 0.73 Li/Mn are presented in Figure 4-7 to Figure 4-11. In terms of RDF peaks, the second and third peaks represent the distance between two manganese atoms on adjacent and opposite sides of the 1x1 tunnel, respectively. See Figure 3-11 for visual representation.

For all Li/Mn, the second RDF peak shows a slight contraction and a substantial reduction in peak intensity indicating that the two manganese atoms on adjacent sides of the 1x1 tunnels have moved closer thus reducing the tunnel size. The third RDF peak shifted substantially to the left proportional to Li/Mn and reveals that the 1x1 tunnels contracted by 5.8, 5.0, 5.3, 6.1, and 0.4 % at the elastic limit for 0.00, 0.03, 0.12, 0.24 and 0.73 Li/Mn, respectively. Compression of 1x1 tunnels was the lowest at 0.73 Li/Mn minimal because the lithium ions occupying these tunnels prevented tunnel size reduction. Further 1x1 tunnel compression of up to 10.8, 10.4, 10.2, 7.0 and 0.8% at the elastic limit for 0.00, 0.03, 0.12, 0.24 and 0.73 Li/Mn, respectively. Compression of 1x1 continued at the collapse stage until the tunnel size was below 3.7, 3.9, 4.0 and 4.2 Å or tunnels collapsed for 0.00, 0.03, 0.12 and 0.24 Li/Mn, respectively. The collapsed tunnels are indicated by the merger of the 2^{nd} and 3^{rd} peaks and the loss of the long-range order in the RDF peaks. Note that the loss of long order indicates that the bulk β-MnO_2 amorphised and is severe at 0.00, 0.03 and 0.012 Li/Mn. This is evidenced in the RDFs at 0.24 and 0.73 Li/Mn where there was a minimal loss in intensity in the long-range peaks. The MnO_6 octahedral plane shifts that occurred at high lithium-ion concentrations. Overall, there's a large change in the 1x1 tunnel size especially for 0.00, 0.03 and 0.12 Li/Mn where the 1x1 tunnels continued shrinking and eventually collapsed rendering the bulk β-MnO_2 electrochemically inactive. The extensive 1x1 tunnel collapse can be seen in the relevant microstructure diagrams in the previous section.

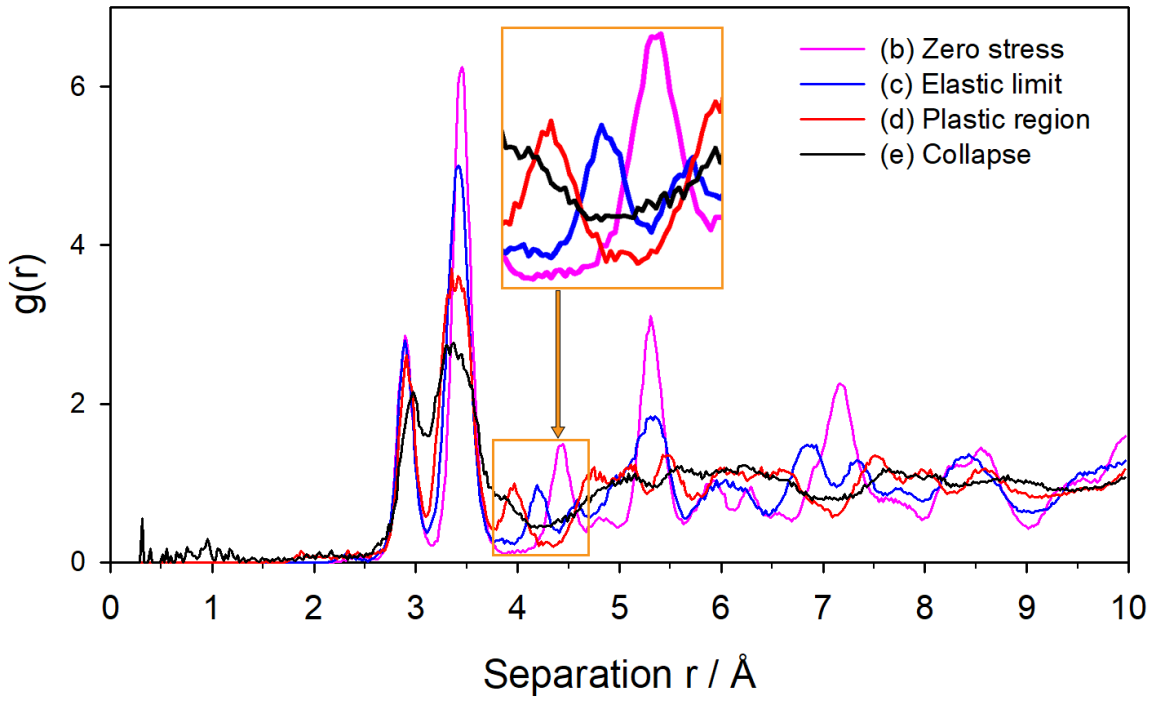

Figure 4-7: Mn-Mn radial distribution functions of the bulk β-MnO_2 at zero stress loading, plastic deformation and collapse regions.

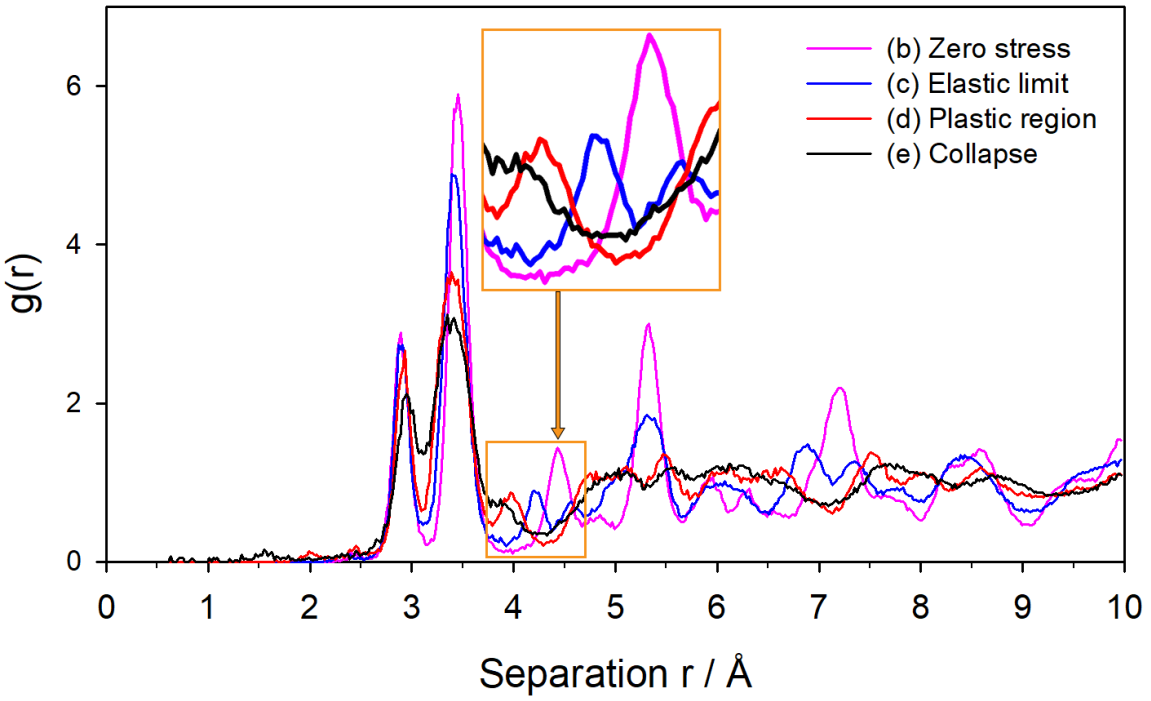

Figure 4-8: Mn-Mn radial distribution functions of the bulk $Li_{0.03}MnO_2$-β at zero stress loading, plastic deformation and collapse regions.

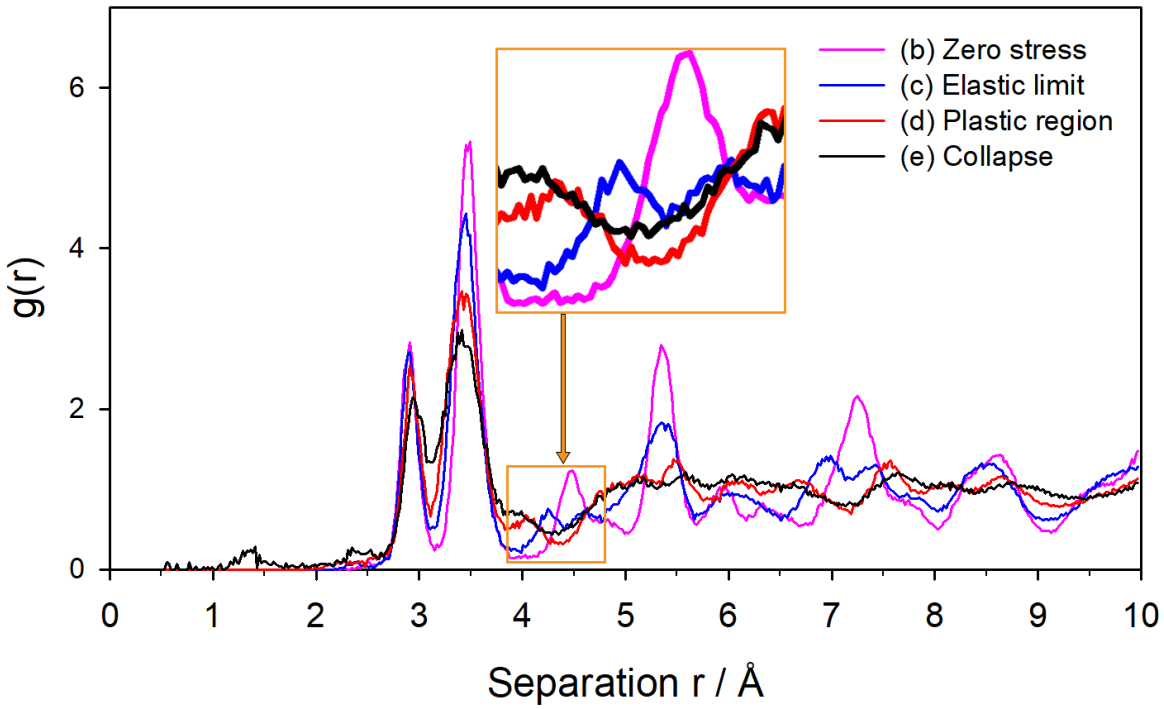

Figure 4-9: Mn-Mn radial distribution functions of the bulk $Li_{0.12}MnO_2$-β at zero stress loading, plastic deformation and collapse regions.

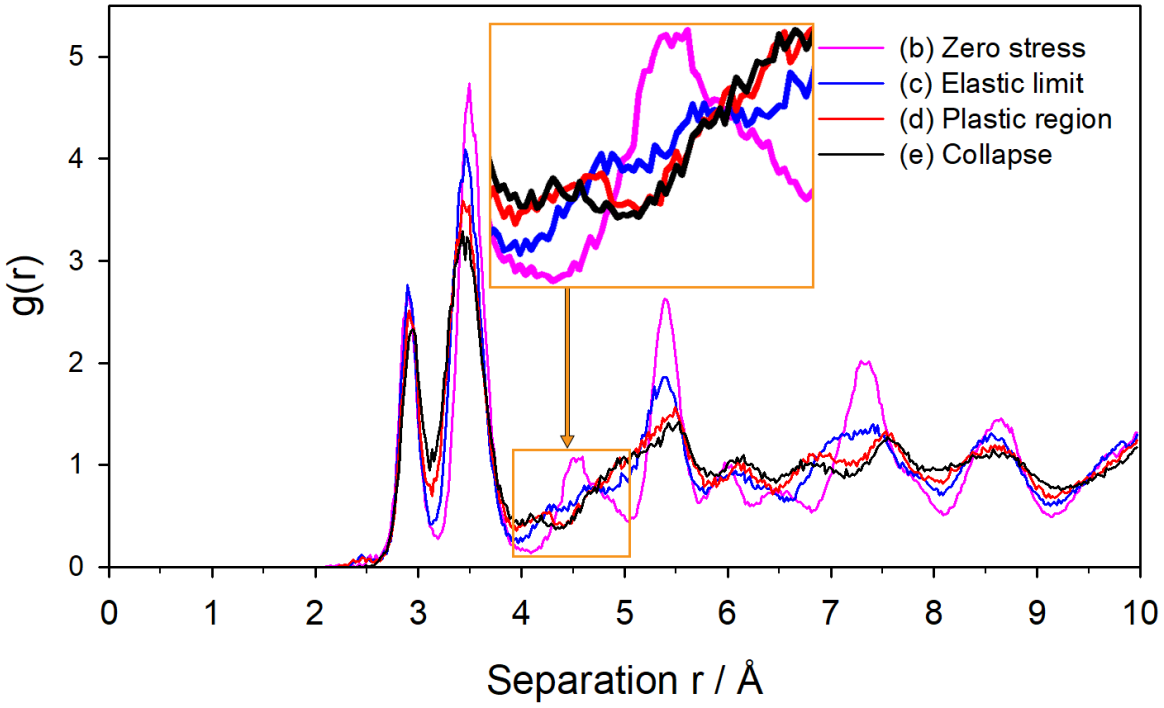

Figure 4-10: Mn-Mn radial distribution functions of the bulk $Li_{0.24}MnO_2$-β at zero stress loading, plastic deformation and collapse regions

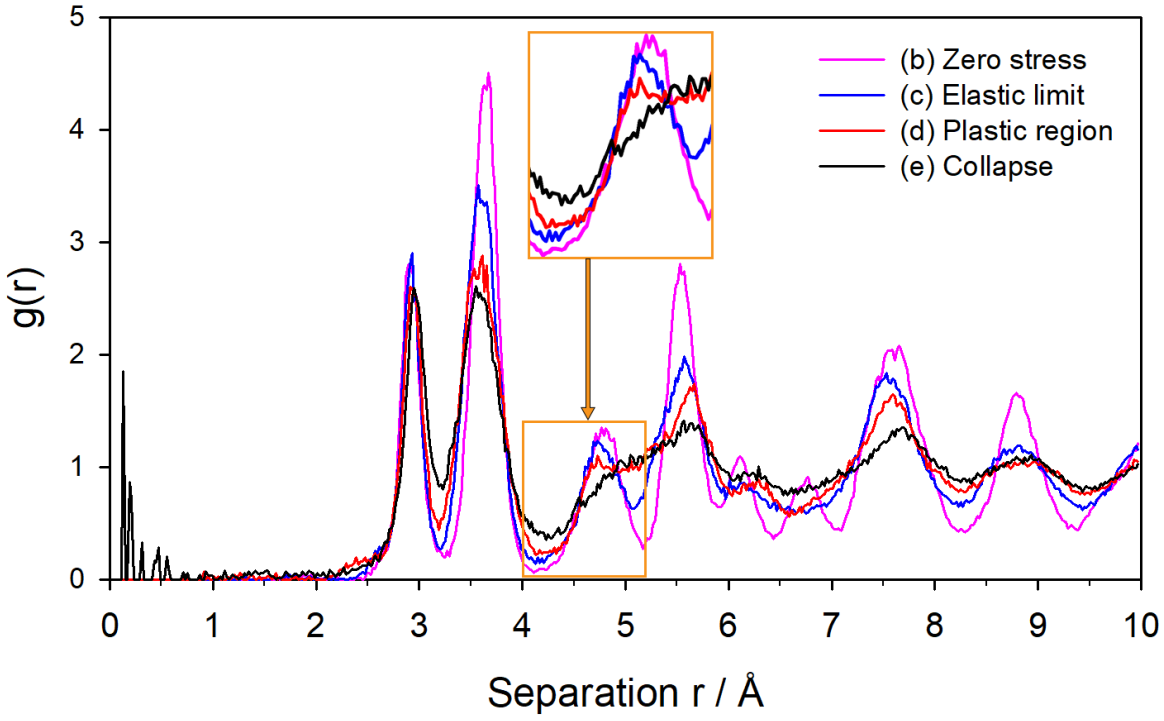

Figure 4-11: Mn-Mn radial distribution functions of the bulk $Li_{0.73}MnO_2$-β at zero stress loading, plastic deformation and collapse regions.

4.2.4 Bulk versus Mesoporous β-MnO_2

Peak number 3 in the Mn-Mn radial distributions for the bulk Li_xMnO_2-β at the elastic limit (~6% strain) was previously shown to shift left in response to uniaxial compressive stress resulting in collapsed tunnels. The degree of the shift lessened for higher lithium-ion concentrations as lithium-ions reduced tunnel contraction.

The collapsed tunnels in the bulk β-MnO_2 lead to reduced lithium-ion intercalation while the smaller 1x1 tunnel size leads to slower lithium-ion diffusion rates thus contributing to the previously reported low capacity and electrochemically inactive nature of bulk samples [19, 40]. In contrast, the RDFs in Figure 4-12 indicate that the 1x1 tunnel size in the mesoporous β-MnO_2 remained constant under compressive stress where stress mitigation occurred through expansion or contraction into the mesoporous channel space.

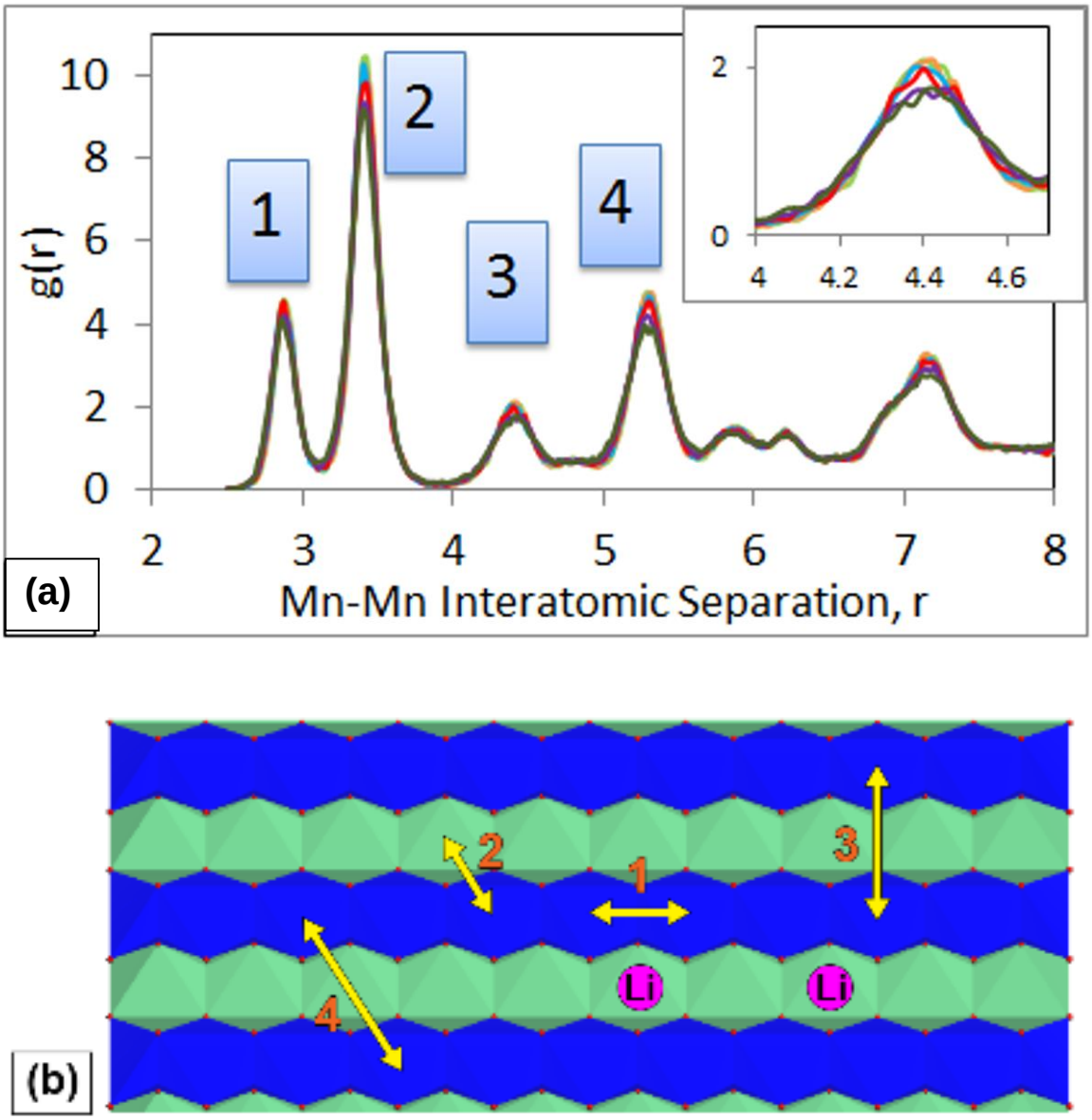

Figure 4-12: (a) Mn-Mn radial distribution functions, calculated as a function of strain, for mesoporous β-MnO_2 [36] at strains of 1, 2, 3, 4, and 5%. (b) Numbers denote Mn-Mn distances labelled in (a).

The resilience of the 1x1 tunnels of the mesoporous β-MnO_2 under compression enables it to retain its functionality as a cathode material through the preservation of lithium-ion diffusion pathways and intercalation sites thus partly explaining the source of electrochemical activity in mesoporous β-MnO_2 materials observed in experiments [3, 40].

4.3 Uniaxial Compressive Strain on Nanorod Li_xMnO_2-β

4.3.1 Mechanical Properties

The stress vs strain curves for the uniaxial compressive strain on the lithiated nanorods are presented below in diagram (a) of Figure 4-13, Figure 4-14, Figure 4-15, Figure 4-16 and Figure 4-17. Diagram (f) in these figures depicts the model used for applying uniaxial stress on the nanorods as well as the spatial orientation of the microstructures that were cut for analysis. The direction of stress is shown by arrows. A summary of the mechanical properties of the lithiated nanorods is presented in Table 4-2. The proportionality limits were found to be 2.5, 2.4, 1.6, 1.5 and 1.1 GPa for 0.00, 0.03, 0.12, 0.24 and 0.73 lithium fractions respectively. The proportionality limit generally decreases with increasing lithium ions. The calculated Young's moduli were found to be 89.2, 88.7, 83.4, 76.1 and 69.2 GPa for 0.00, 0.03, 0.12, 0.24 and 0.73 and 0.73 lithium fractions, respectively. The diameter of these nanorods is about 6.0 nm and increases to 6.5 nm at 0.73 Li/Mn with elastic moduli ranging from 89.17 to 69.16 GPa. Jiang et al. performed a similar experimental study on β-MnO_2 nanowires with diameters ranging from 240 to 185 nm and found Young's modulus values of 33.36 to 77.84 GPa as the diameter decreased from 240 to 185 nm. The Young's modulus of our unlithiated nanorod with a diameter of 6.0 nm was calculated to be 89.17 GPa which is comparable to the elastic modulus of 77.84 GPa for the nanowires with a diameter of 240 nm. However, there is a large discrepancy in the diameters of our nanorod and the nanowires. Nanocrystals with diameters ranging from 1-100 nm are known to have physical and chemical properties that differ from those of their bulk counterparts [72]. In particular, the bulk modulus of

bulk γ-Fe_2O_3 has been shown to increase in its nanocrystals [73]. Similarly, the Young's modulus of the unlithiated nanorod has decreased from the parent bulk material's value of 299.73 GPa to 89.17 GPa. As with the bulk structure, the elastic moduli indicate that the nanorod also becomes more brittle as lithium content increases. Plastic deformation begins at subsequently lower stress as lithium-ion content is increased i.e. the elastic limit decreases with increasing lithium-ion content.

Table 4-2: Mechanical properties of lithiated β-MnO_2 nanorod under compressive strain.

Li/Mn	Yield Stress		Simulated Elastic modulus (Y)		Exp. (Y)
	katm	GPa	katm	GPa	GPa
0.00	61.77	6.26	880.00	89.17	77.84 [74]
0.03	63.72	6.46	875.40	88.70	
0.12	58.89	5.97	822.80	83.37	
0.24	50.63	5.13	750.79	76.07	
0.73	43.66	4.42	682.52	69.16	

4.3.2 Microstructure of Nanorod Li_xMnO_2-β (x = 0.00, 0.03, 0.12, 0.24 and 0.73)

The response of the pure and lithiated β-MnO_2 nanorod under compressive loading is presented in terms of microstructure evolution in diagrams (b), (c), (d) and (e) of Figure 4-13 to Figure 4-17 below. Diagrams (g) to (l) show the side view of the MnO_6 octahedral planes. Within the elastic region, the β-MnO_2 nanorod contracted along the long axis of the nanorod without permanent deformation in the range of 7.0 to 8.0% strain. Since there is little or no change in the microstructure within the elastic region we decided to use one microstructure slice from the elastic region as a benchmark and the take other slices from the plastic region. Plastic deformation began at 7.7, 8.1, 7.6, 7.3 and 7.7% strain and was accompanied by 0.2, 1.5, 1.2, 0.3 and 0.1 GPa drop in stress for Li/Mn values of 0.00, 0.03, 0.12, 0.24 and 0.73,

respectively. See stress vs strain plot in diagram (a) for more details. Similarly, a drop in compressive force resulting from a collapsed zone has been previously observed for thin-wall TiO_2 nanotubes under compressive load in the work of Shokuhfar et al. [75]. In our work, the decrease in stress was caused by the MnO_6 octahedral planes denoted by purple and pink breaking off and shifting upwards by exactly one plane. This process involved the breaking of atomic bonds at the in the region enclosed by an orange rectangle followed by the upward movement of the octahedral planes on the left and then succeeded by the formation of new bonds with atoms on the upper plane resulting in the evolution of a grain boundary. Several 1x2 tunnels located within the orange rectangle may have caused a weakening in the microstructure leading to plastic deformation. In contrast, Han et al. observed that plastic deformation in ceramic SiC nanowires was associated with the formation of dislocations [76].

The black rectangle in diagram (c) shows the deformed microstructure around the grain boundary which accompanied the octahedral plane shifts. Diagram (g) presents a lateral view of the MnO_6 octahedral planes and clearly highlights this plane movement. Note that the initially defective region enclosed by a red rectangle did not spread to the neighbouring regions as we have observed in the case of the unlithiated bulk structure. Furthermore, the 1x1 tunnels did not collapse during plastic deformation except at the grain boundary where plane shifts occurred. Plastic deformation progressed through the second octahedral plane movement, shown in diagrams (d) and (k), and resulted in 3.2, 2.0, 2.3, 2.1 and 1.6 GPa reduction in stress for Li/Mn values of 0.00, 0.03, 0.12, 0.24 and 0.73, respectively.. Further progression of plastic deformation is shown in diagrams (e) and (l) where the planes moved upwards four times in total. The defect region enclosed by red rectangle did not grow or spread and additional deformation occurred only along the grain boundary. In summary, we have observed that when subjected to compressive loading the unlithiated nanorod mitigated stress through expansion along X and Z

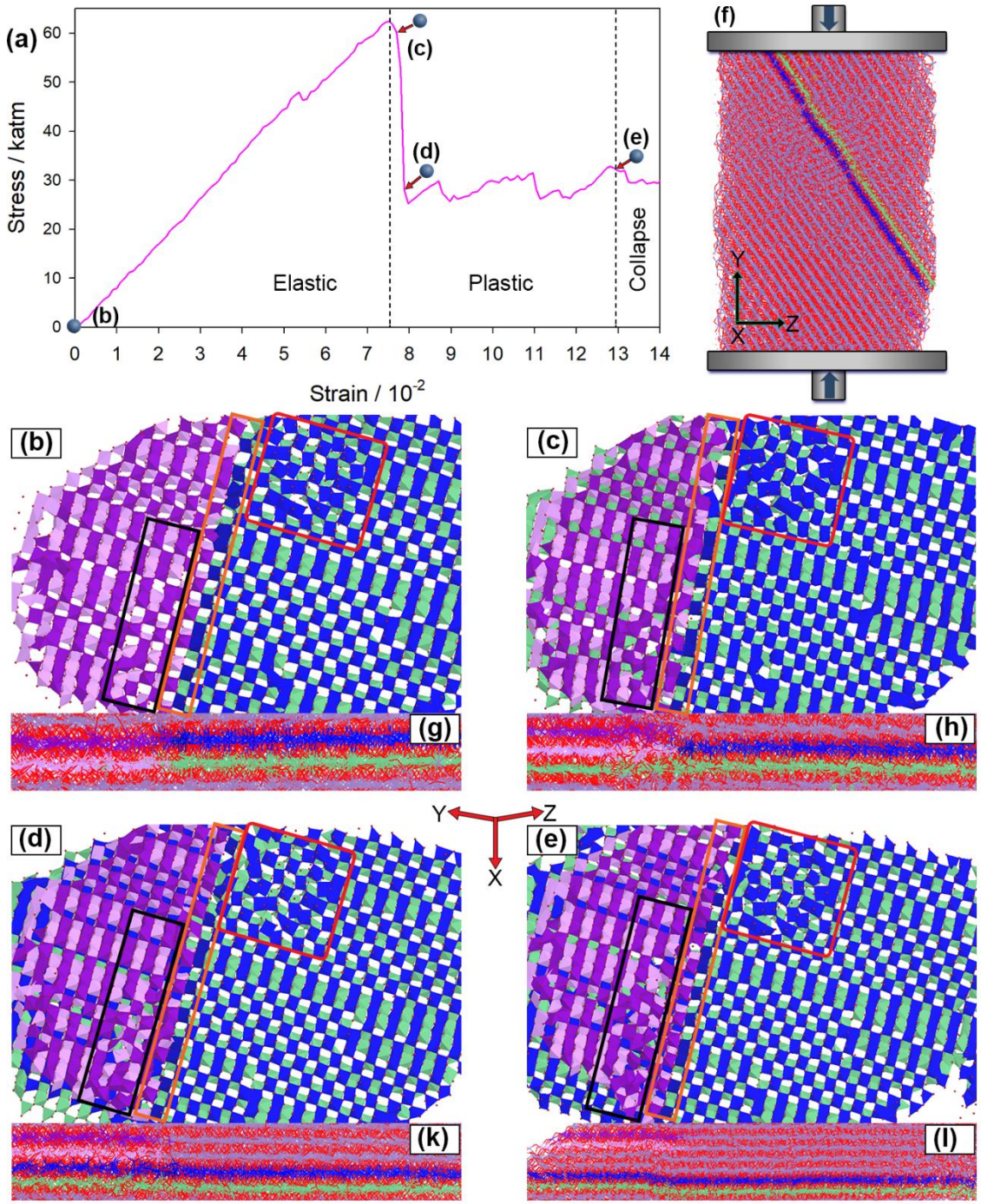

Figure 4-13: Compressive stress-strain plot of β-MnO_2 nanorod and microstructure in the (b) elastic, (c, d) plastic and (e) collapse regions. Diagrams (g), (h), (i) and (k) show respective MnO_6 octahedral plane view of microstructures in (b), (c), (d) and (e). The top MnO_6 octahedral plane is depicted by blue and purple while the bottom plane is depicted by green and pink.

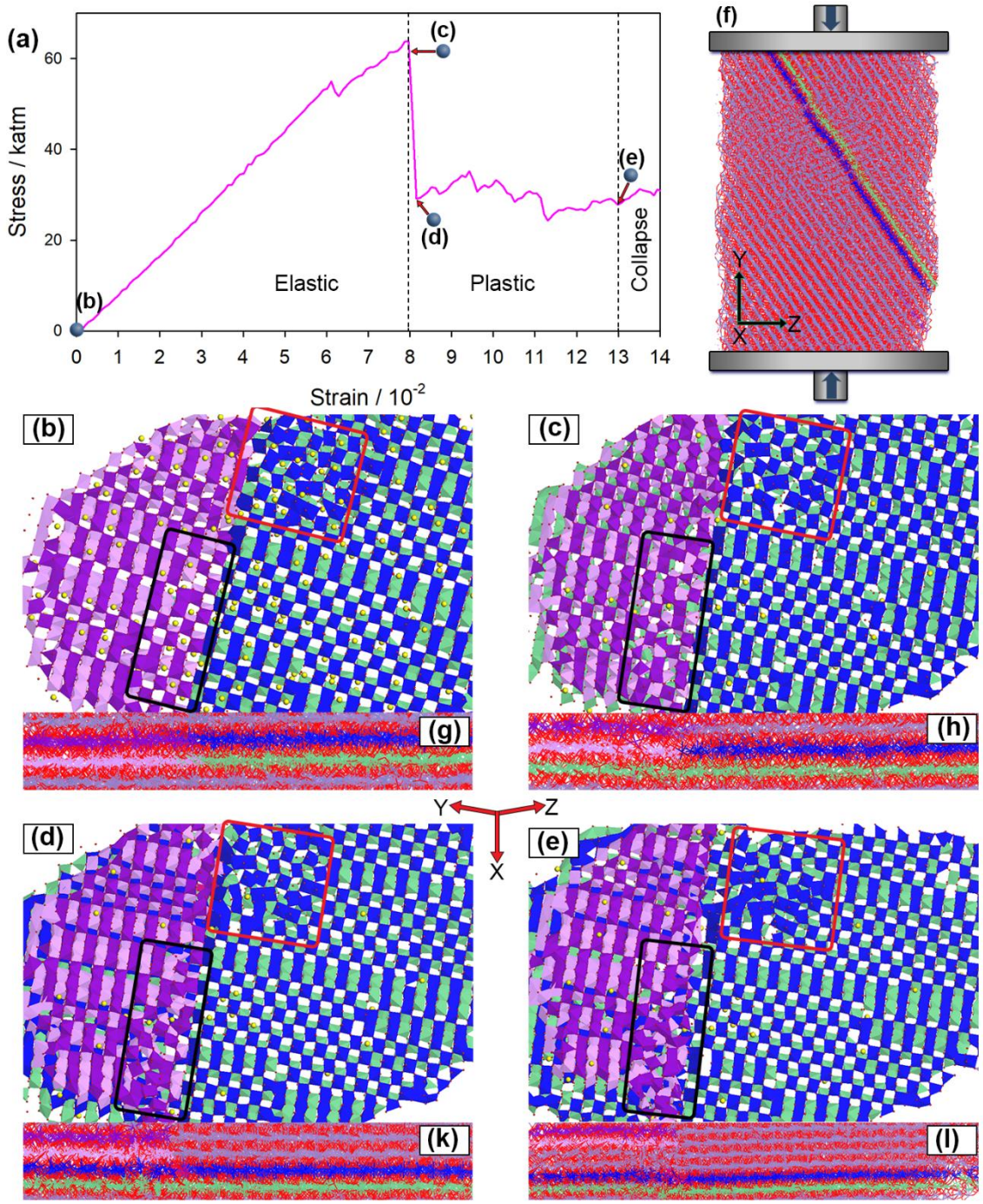

Figure 4-14: Compressive stress-strain plot of nanorod $Li_{0.03}MnO_2$-β and microstructure in the (b) elastic, (c, d) plastic and (e) collapse regions. Diagrams (g), (h), (i) and (k) show MnO_6 octahedral plane view of microstructures in (b), (c), (d) and (e) respectively. The top MnO_6 octahedral plane is depicted by blue and purple while the bottom plane is depicted by green and pink.

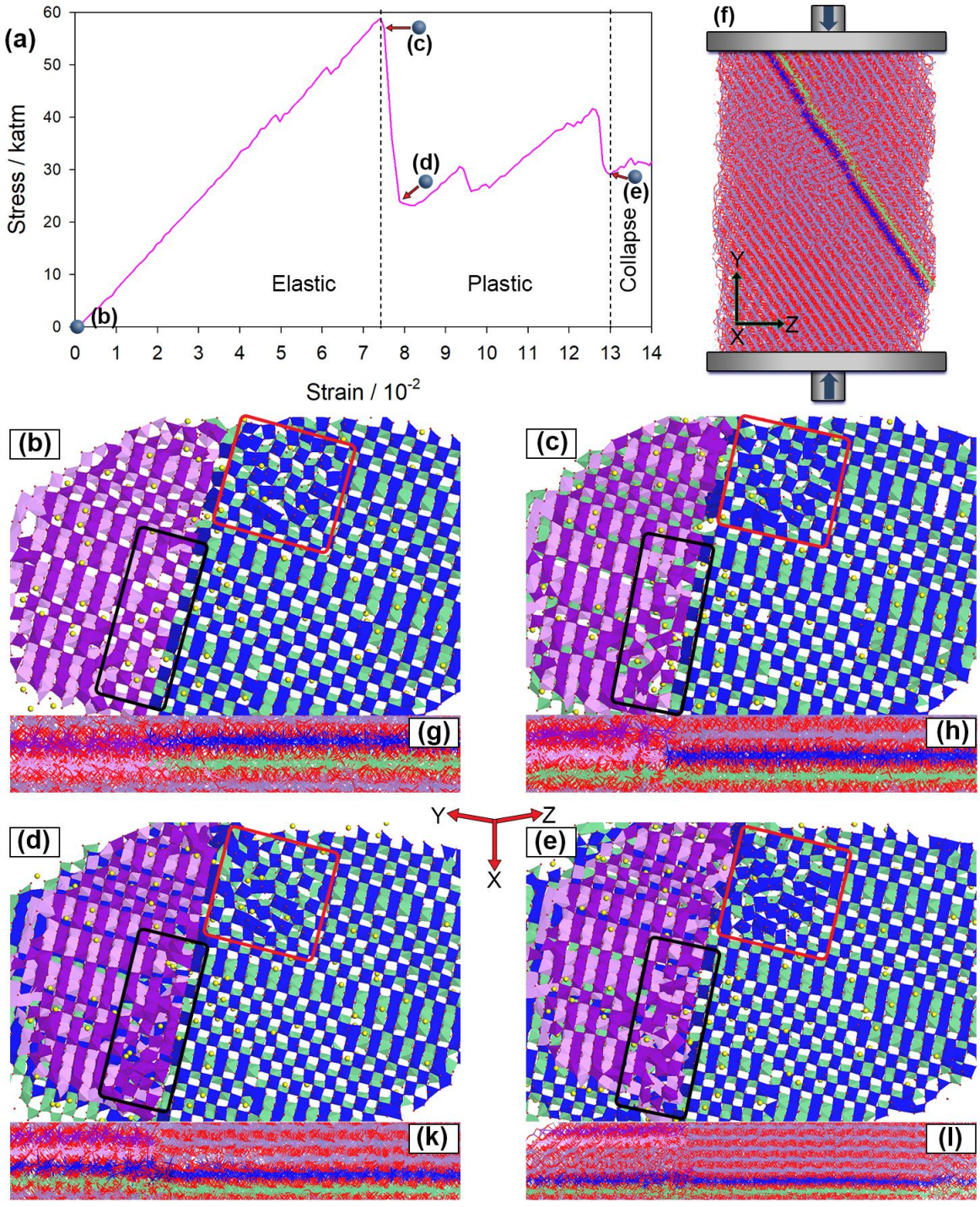

Figure 4-15: Compressive stress-strain plot of nanorod $Li_{0.12}MnO_2$-β and microstructure in the (b) elastic, (c, d) plastic and (e) collapse regions. Diagrams (g), (h), (i) and (k) show MnO_6 octahedral plane view of microstructures in (b), (c), (d) and (e) respectively. The top MnO_6 octahedral plane is depicted by blue and purple while the bottom plane is depicted by green and pink.

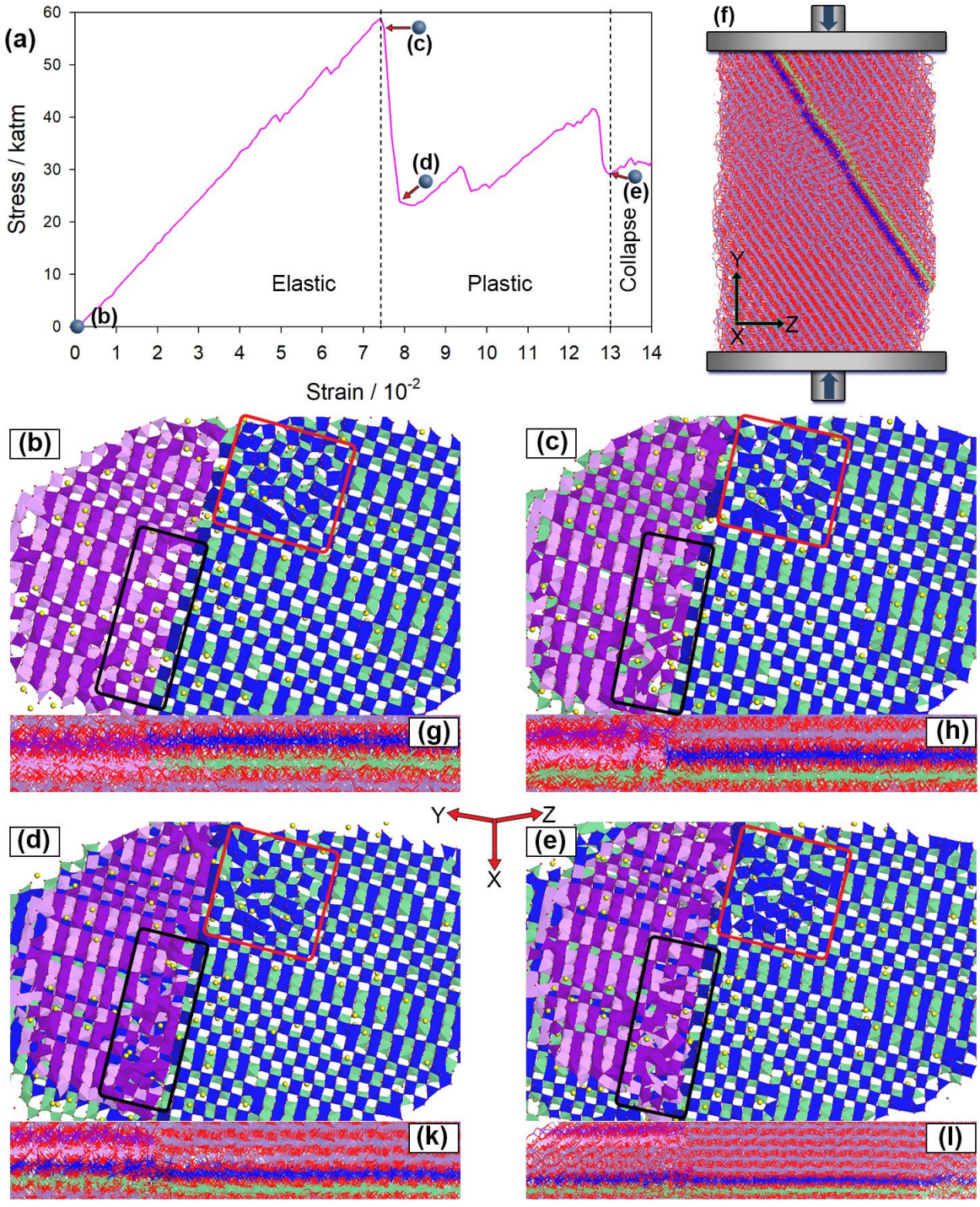

Figure 4-16: Compressive stress-strain plot of nanorod $Li_{0.24}MnO_2$-β and microstructure in the (b) elastic, (c, d) plastic and (e) collapse regions. Diagrams (g), (h), (i) and (k) show MnO_6 octahedral plane view of microstructures in (b), (c), (d) and (e) respectively. The top MnO_6 octahedral plane is depicted by blue and purple while the bottom plane is depicted by green and pink.

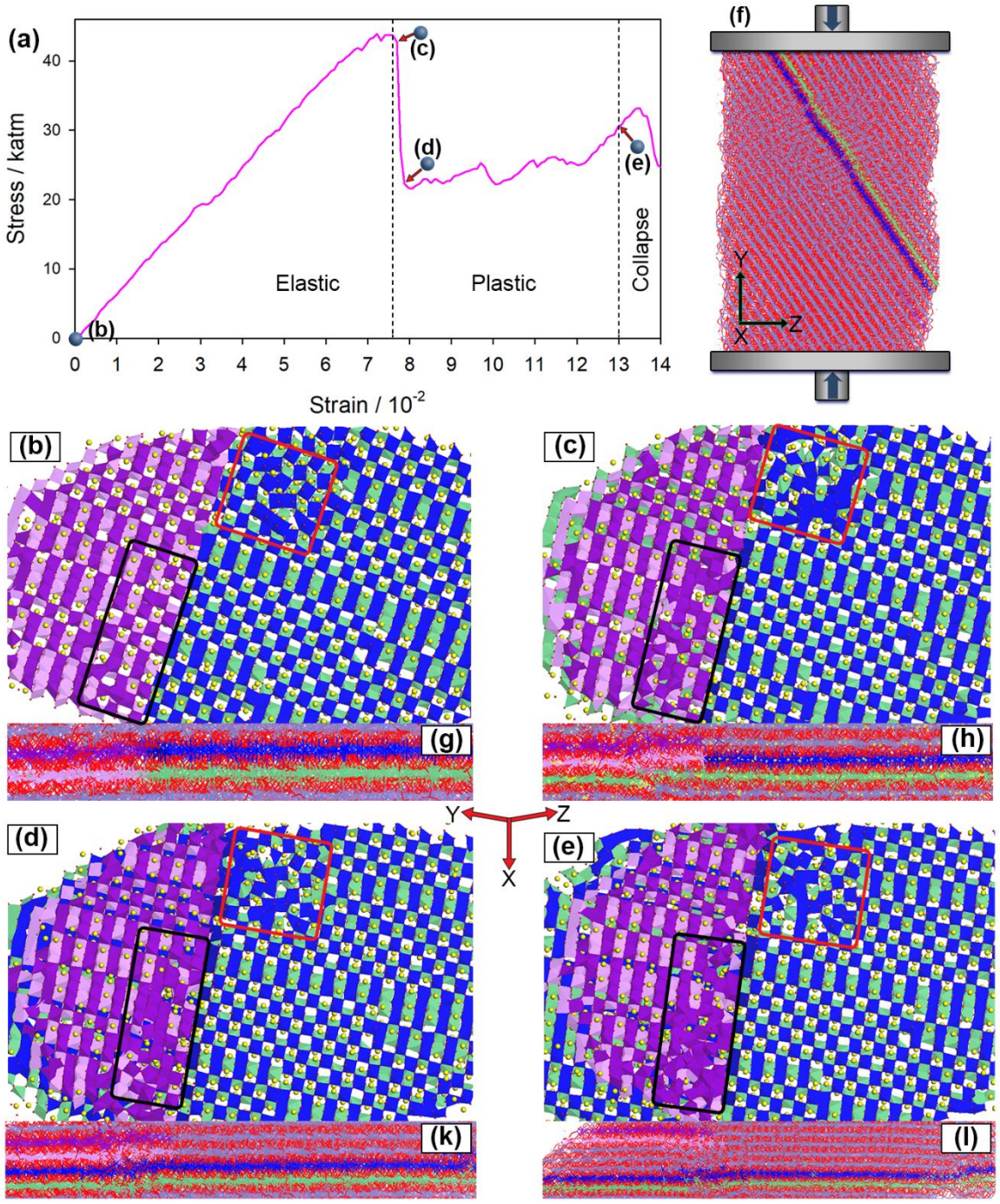

Figure 4-17: Compressive stress-strain plot of nanorod $Li_{0.73}MnO_2$-β and microstructure in the (b) elastic, (c, d) plastic and (e) collapse regions. Diagrams (g), (h), (i) and (k) show MnO_6 octahedral plane view of microstructures in (b), (c), (d) and (e) respectively. The top MnO_6 octahedral plane is depicted by blue and purple while the bottom plane is depicted by green and pink.

axes followed by shifting of the MnO_6 octahedral planes without collapsing the tunnels except at the grain boundary where the octahedral plane shifting occurred. The octahedral plane shifts at 0.00, 0.03 and 0.12 Li/Mn resulted in a slight restoration of the size of the 1x1 tunnels. We find this behaviour to be in contrast to our unlithiated bulk structure where stress mitigation occurred solely through deformation of faceted microstructural regions which then spread to neighbouring regions. Octahedral plane shifting enabled the nanorod to preserve more 1x1 tunnel structures when compared to the bulk counterpart.

4.3.3 Mn-Mn Radial Distribution Functions of Nanorod Li_xMnO_2-β (x = 0.00, 0.03, 0.12, 0.24 and 0.73)

The M-Mn radial distribution functions (RDFs) at the zero stress, elastic limit, and plastic regions for the β-MnO_2 nanorod at 0.00, 0.03, 0.12, 0.24 and 0.73 Li/Mn are presented in Figure 4-18 to Figure 4-22. In terms of RDF peaks, the second and third peaks represent the distance between two manganese atoms on adjacent and opposite sides of the 1x1 tunnel, respectively. Consequently, we can observe how the 1x1 tunnel size is affected by monitoring these two peaks. For all Li/Mn, the second RDF peak shows a slight contraction and a reduction in peak intensity indicating that the two manganese atoms on adjacent sides of the 1x1 tunnels have moved closer thus reducing the tunnel size. The third RDF peak reveals that the 1x1 tunnels contracted by 4.3, 2.0, 2.9, 0.4, and 0.4 % at the elastic limit for 0.00, 0.03, 0.12, 0.24 and 0.73 Li/Mn, respectively. Compression of 1x1 tunnels at 0.24 and 0.73 Li/Mn was minimal because the lithium ions occupying these tunnels prevented tunnel size reduction. The third RDF peak remained constant after the second octahedral plane shift for 0.24 and 0.73 Li/Mn and expanded for 0.00, 0.03 and 0.12 Li/Mn. Contrary to the bulk material, the 1x1 tunnels in the nanorod stopped contracting before collapsing and expanded during octahedral plane shifts. This could indicate why the β-MnO_2 nanorod is electrochemically active and the parent bulk is not.

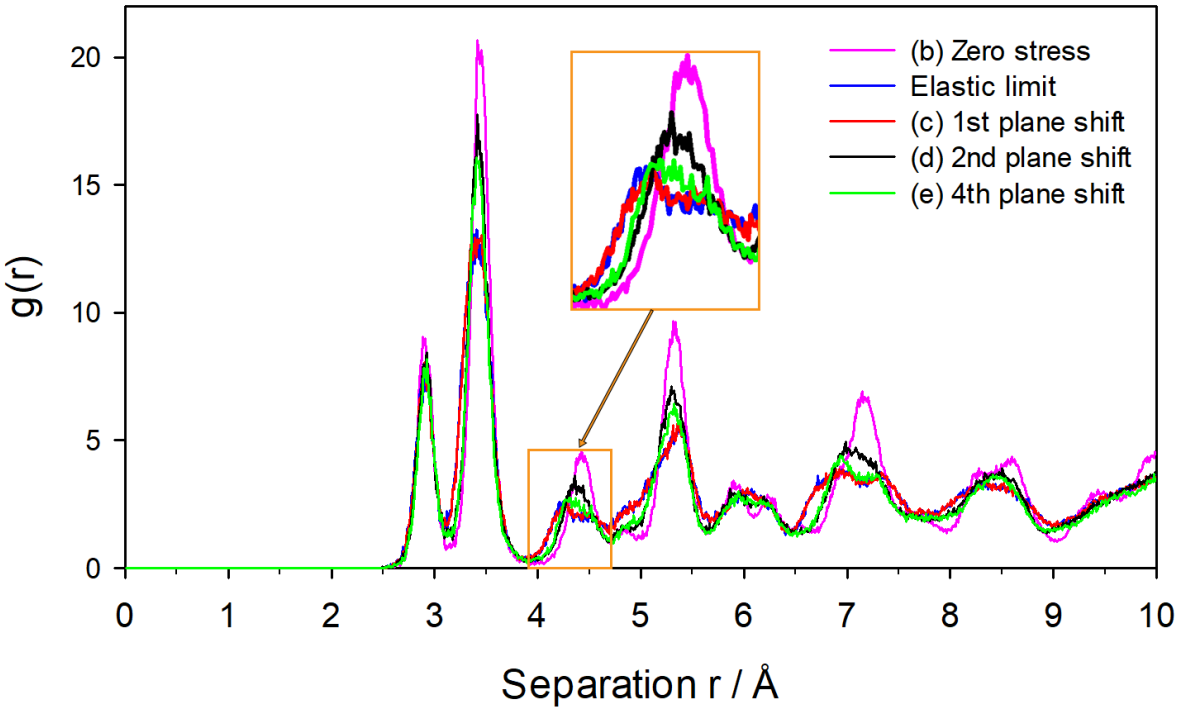

Figure 4-18: Mn-Mn radial distribution functions of the β-MnO_2 nanorod at zero stress loading and at the plastic deformation region.

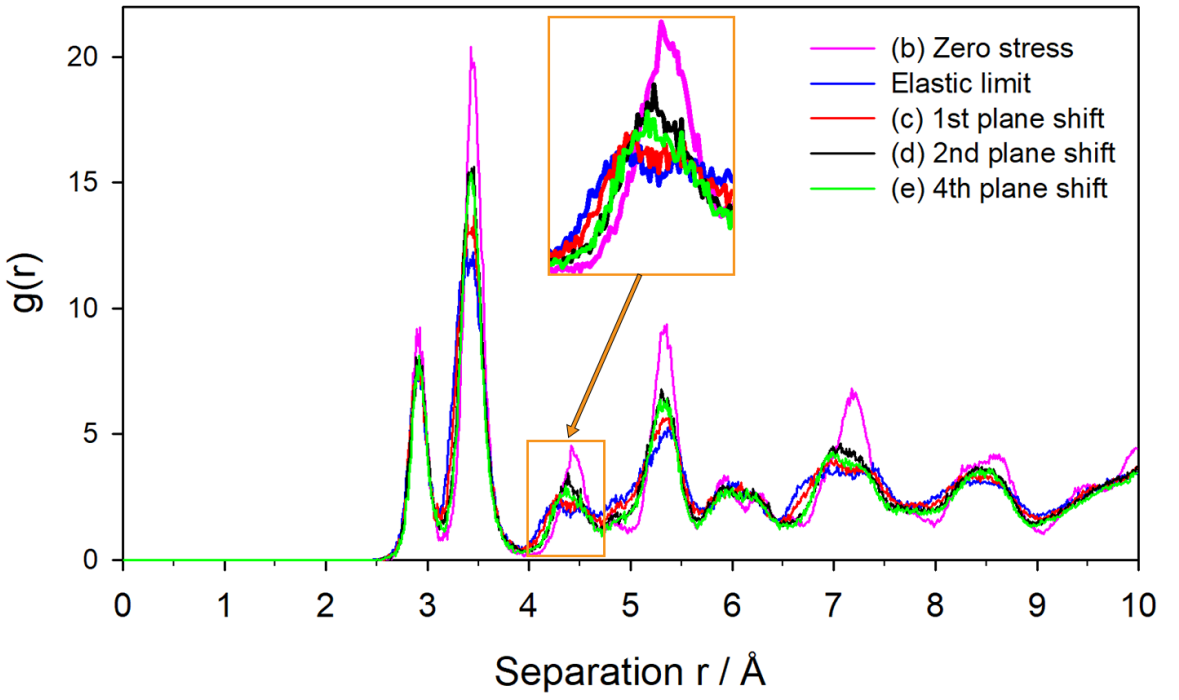

Figure 4-19: Radial distribution functions of the $Li_{0.03}MnO_2$-β nanorod at zero stress loading and at the plastic deformation region.

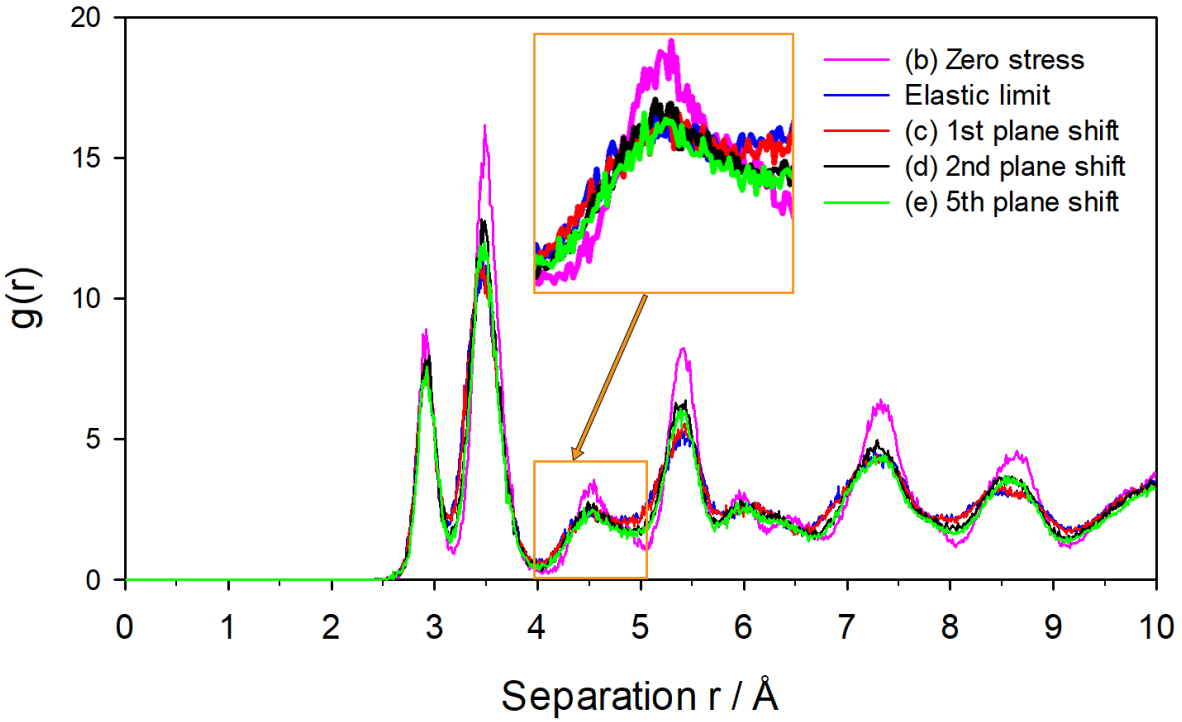

Figure 4-20: Mn-Mn radial distribution functions of the $Li_{0.12}MnO_2$-β nanorod at zero stress loading and at the plastic deformation region.

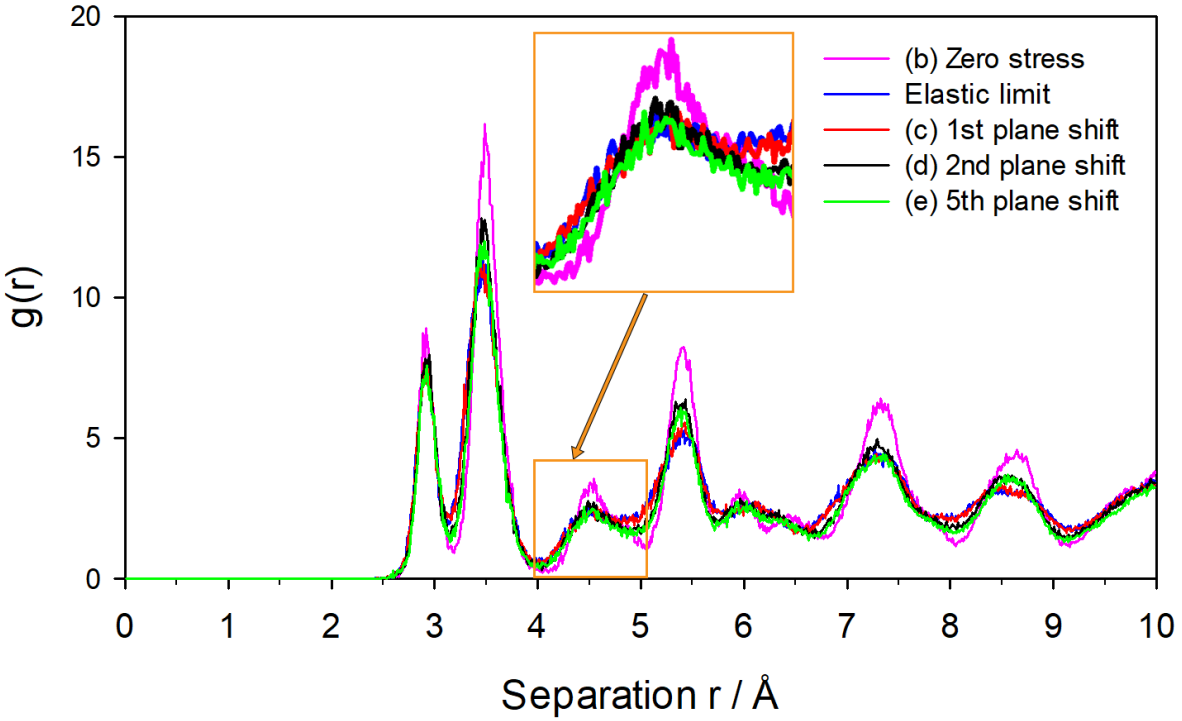

Figure 4-21: Mn-Mn radial distribution functions of the $Li_{0.24}MnO_2$-β nanorod at zero stress loading and at the plastic deformation region.

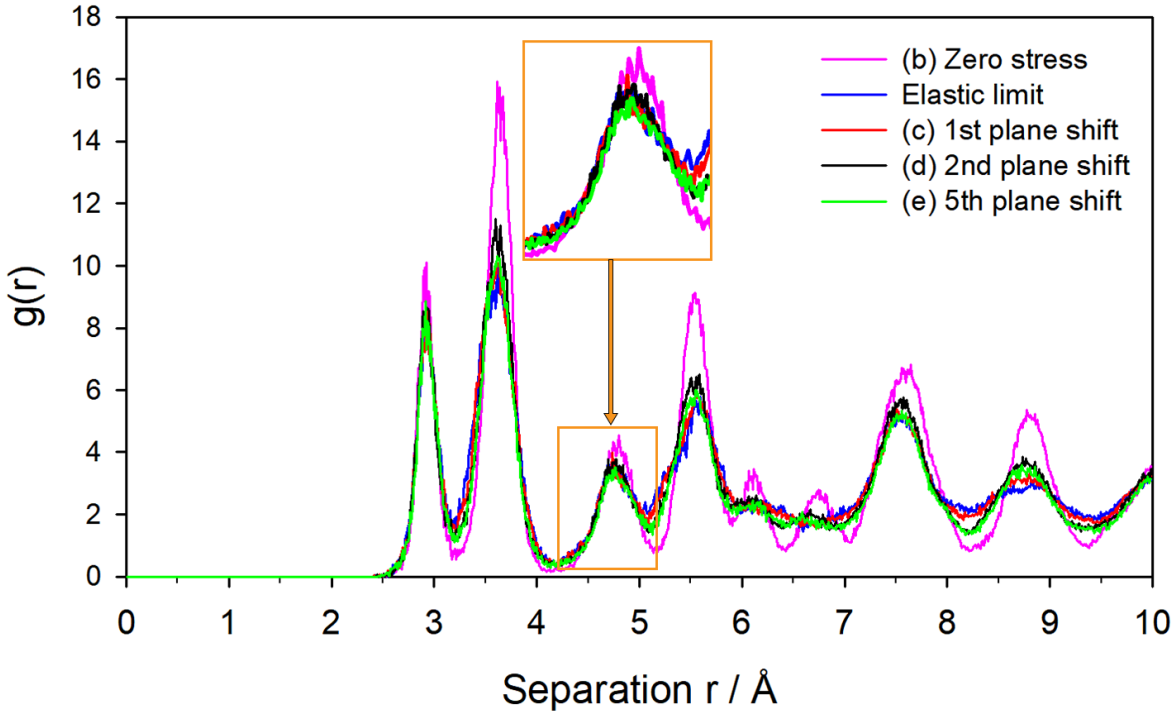

Figure 4-22: Mn-Mn radial distribution functions of the $Li_{0.73}MnO_2$-β nanorod at zero stress loading and at the plastic deformation region.

4.3.4 β-MnO_2 Nanorod versus Mesoporous

Peak number 3 in the Mn-Mn radial distributions for the nanorod Li_xMnO_2-β at the elastic limit (~7.4-8.0% strain) was previously shown to shift left in response to uniaxial compressive stress resulting in a partial contraction of 1x1 tunnels without collapsing. Similar to mesoporous β-MnO_2, more 1x1 tunnels are retained relative to the bulk material thus contributing to the electrochemical activity of the nanorods observed in experiments [10]. However, the smaller tunnel size could limit lithium-ion mobility within the nanorods.

4.4 Pressure Comparisons

Presented in Figure 4-23 and Figure 4-24 are the plots of stress versus strain in the bulk structure, nanorod and the mesoporous β-MnO_2 from previous work [36]. The

plot indicates that the bulk structure experiences significantly higher stress than the nanorod and nanoporous at the same strain.

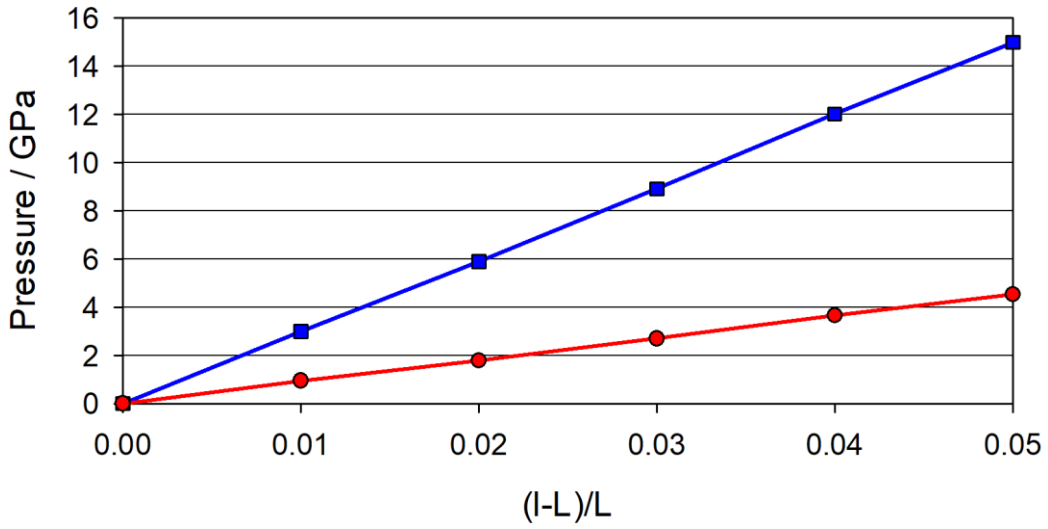

Figure 4-23: Stress-strain plot of the bulk and nanorod β-MnO_2 under uniaxial compressive strain.

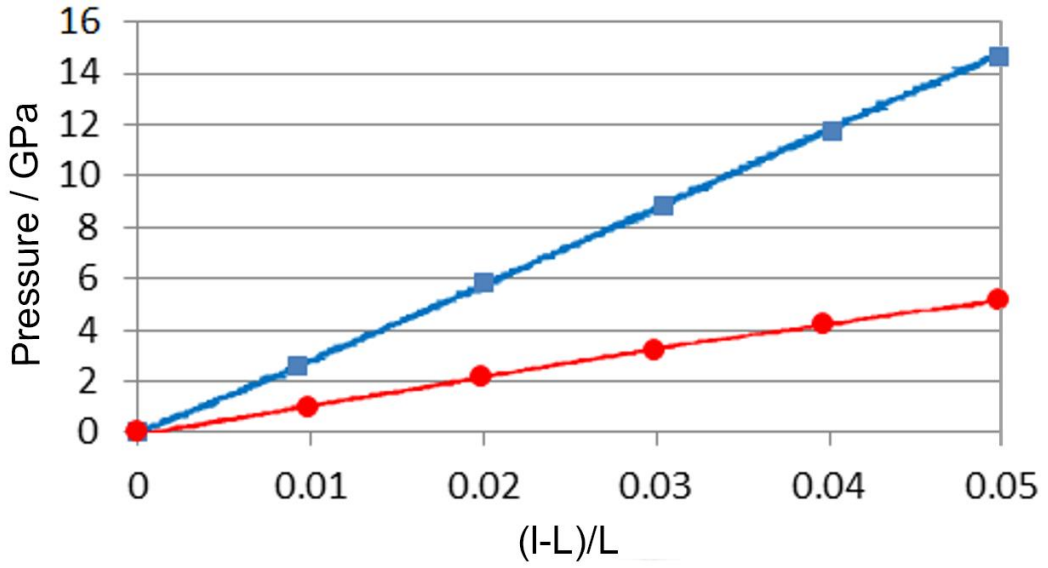

Figure 4-24: Stress-strain plot of the bulk and nanoporous β-MnO_2 under uniaxial compressive strain.

4.5 Uniaxial Tensile Strain on Lithiated Bulk β-MnO_2

4.5.1 Mechanical Properties

Stress vs strain curves for the uniaxial tensile strain on the pristine and lithiated bulk β-MnO_2 are provided diagram (a) of Figure 4-25 to Figure 4-29 with the corresponding mechanical properties presented in Table 4-3. Under tensile strain, the bulk structure expands elastically up to 7.9, 7.2, 7.1, 7.5 and 6.8 % strain for 0.00, 0.03, 0.12, 0.24 and 0.73 lithium fractions, respectively. The proportionality limits occurred around small strains ranging from 0.020 to 0.024 and were found to be 5.28, 5.67, 5.59, 4.56 and 4.89 GPa for 0.00, 0.03, 0.12, 0.24 and 0.73 lithium fractions respectively. We observe no trend in the proportional limits versus lithium-ion concentration. The calculated elastic moduli were found to be 265.28, 259.50, 239.13, 228.54 and 243.12 GPa for 0.00, 0.03, 0.12, 0.24 and 0.73 and 0.73 lithium fractions, respectively. The simulated elastic modulus of 265.28 GPa calculated for our unlithiated bulk structure is comparable to the value of 276.34 GPa obtained through density functional theory methods.

Table 4-3: Mechanical properties of lithiated bulk β-MnO_2 under tensile stress.

Li/Mn	Yield Stress		Simulated Elastic modulus (Y)		Exp. (Y)
	katm	GPa	katm	GPa	GPa
0.00	160.20	16.23	2618.12	265.28	276.34 [71]
0.03	152.40	15.44	2561.11	259.50	
0.12	142.00	14.39	2359.98	239.13	
0.24	139.50	14.13	2255.50	228.54	
0.73	109.10	11.05	2399.42	243.12	

These elastic moduli values indicate that under tensile loading the bulk structure becomes more brittle at subsequently higher lithium content. Structural deformation

began at yield stress values of 16.23, 15.44, 14.39, 14.13 and 11.05 GPa for 0.00, 0.03, 0.12, 0.24 and 0.73 lithium fractions, respectively, suggesting that as more lithium ions are intercalated the parent bulk material yielded at subsequently lower stress.

4.5.2 Microstructure of Bulk Li_xMnO_2-β (x = 0.00, 0.03, 0.12, 0.24 and 0.73)

The microstructural behaviour of the pure and lithiated bulk β-MnO_2 in response to tensile strain in the elastic region, plastic region and collapse point is presented in diagrams (b), (c), (d) and (e) of Figure 4-25 to Figure 4-29. There is no obvious change in the microstructure at the elastic limit for all lithium-ion concentrations. Structural deformation in pure and unlithiated bulk structures began at the dislocation/stacking fault located in the region enclosed by the red rectangle. This region also comprises a large hole on the bottom left of the microstructure and is oriented perpendicular to the direction of the tensile stress. Microstructure slices taken at the plastic deformation phase show minor deformation along the dislocation/stacking fault as the structure broke apart at the top of the red rectangle. Additional structural deformation occurred in the region enclosed by a pink rectangle where the microstructure domain isostructural to brookite TiO_2, zigzag tunnels, became amorphous. The microstructure slices at the point of collapse show that the bulk MnO_2 has broken into two along the dislocation/stacking fault line for all lithium-ion concentrations. SiC nanowires were also shown to evolve dislocations during bending deformation and amorphised at the strained region [76]. The hole on the bottom left also contributed to the splitting of the structure along the grain boundary. In addition to experiencing to above-mentioned microstructural transformations, the bulk $Li_{0.24}MnO_2$-β also became amorphous as it broke apart, see diagram (e) where the MnO_6 octahedral chains on the top and bottom octahedral planes are severely destroyed. This behaviour has not been observed for the bulk structures with other lithium-ion concentrations.

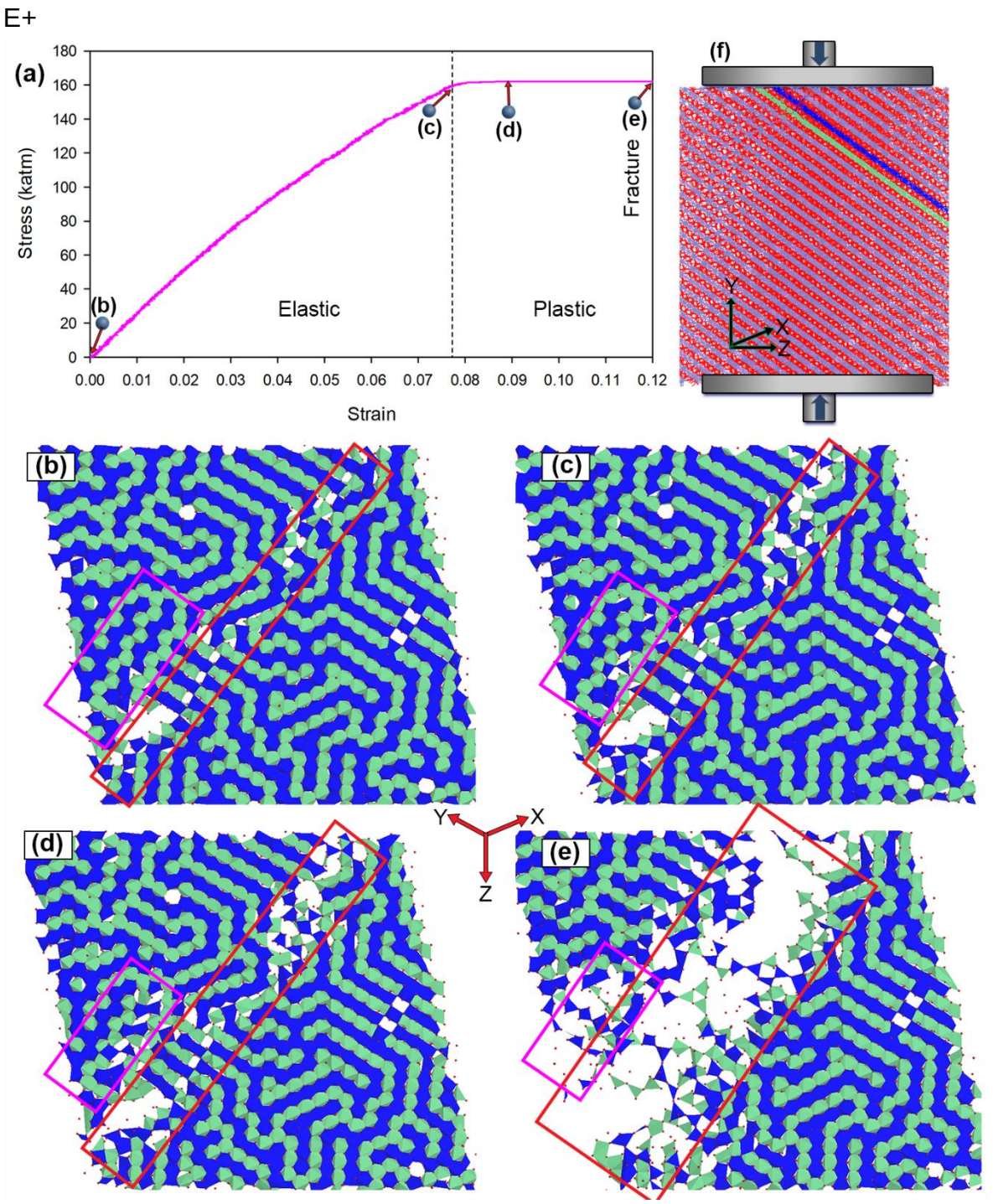

Figure 4-25: Tensile stress-strain plot of bulk β-MnO_2 and microstructure slices in the (b) elastic, (c, d) plastic and (e) collapse regions. The top MnO_6 octahedral plane is depicted by blue while the bottom plane is depicted by green.

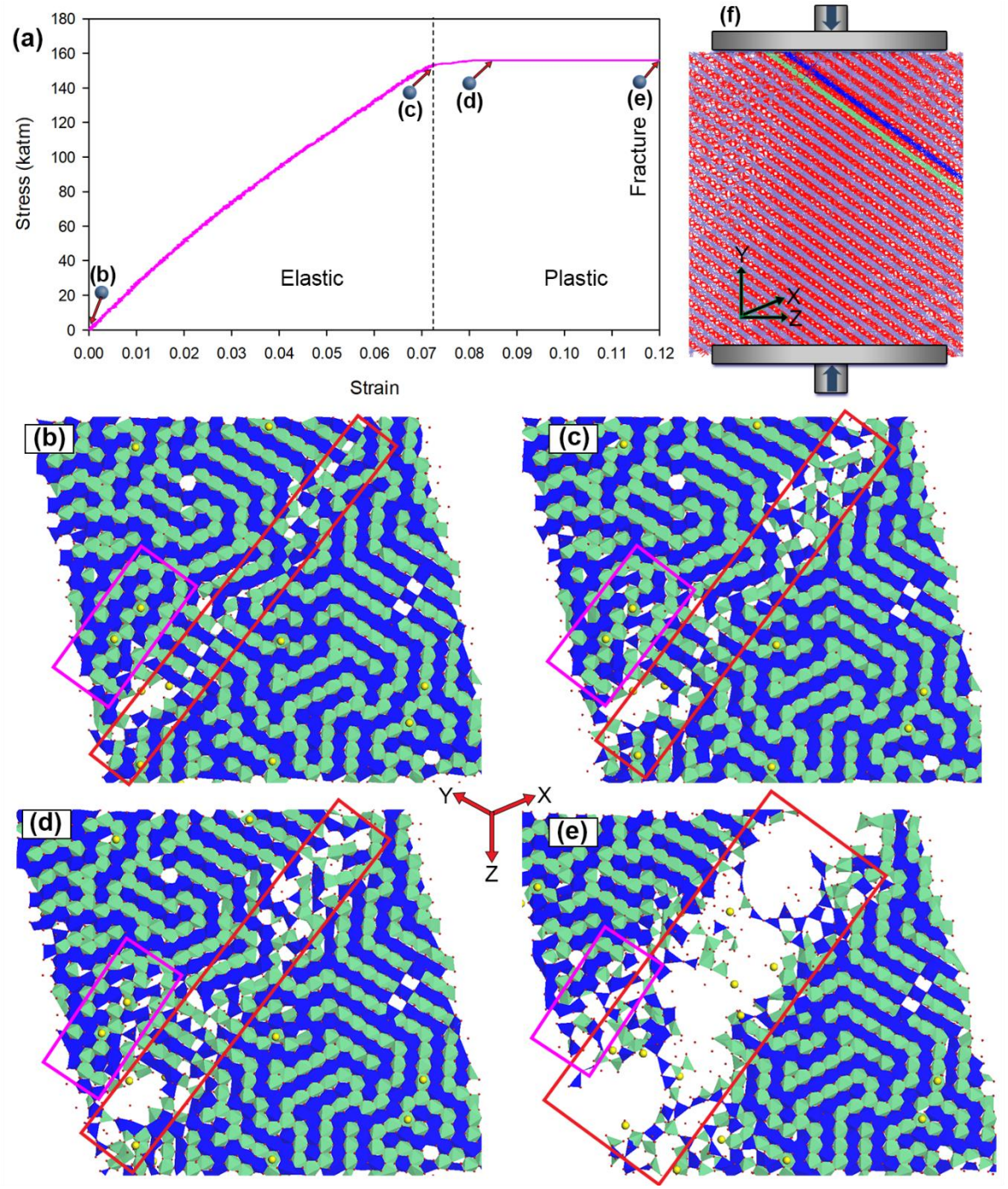

Figure 4-26: Tensile stress-strain plot of bulk $Li_{0.03}MnO_2$-β and microstructure slices in the (b) elastic, (c, d) plastic and (e) collapse regions. The top MnO_6 octahedral plane is depicted by blue while the bottom plane is depicted by green.

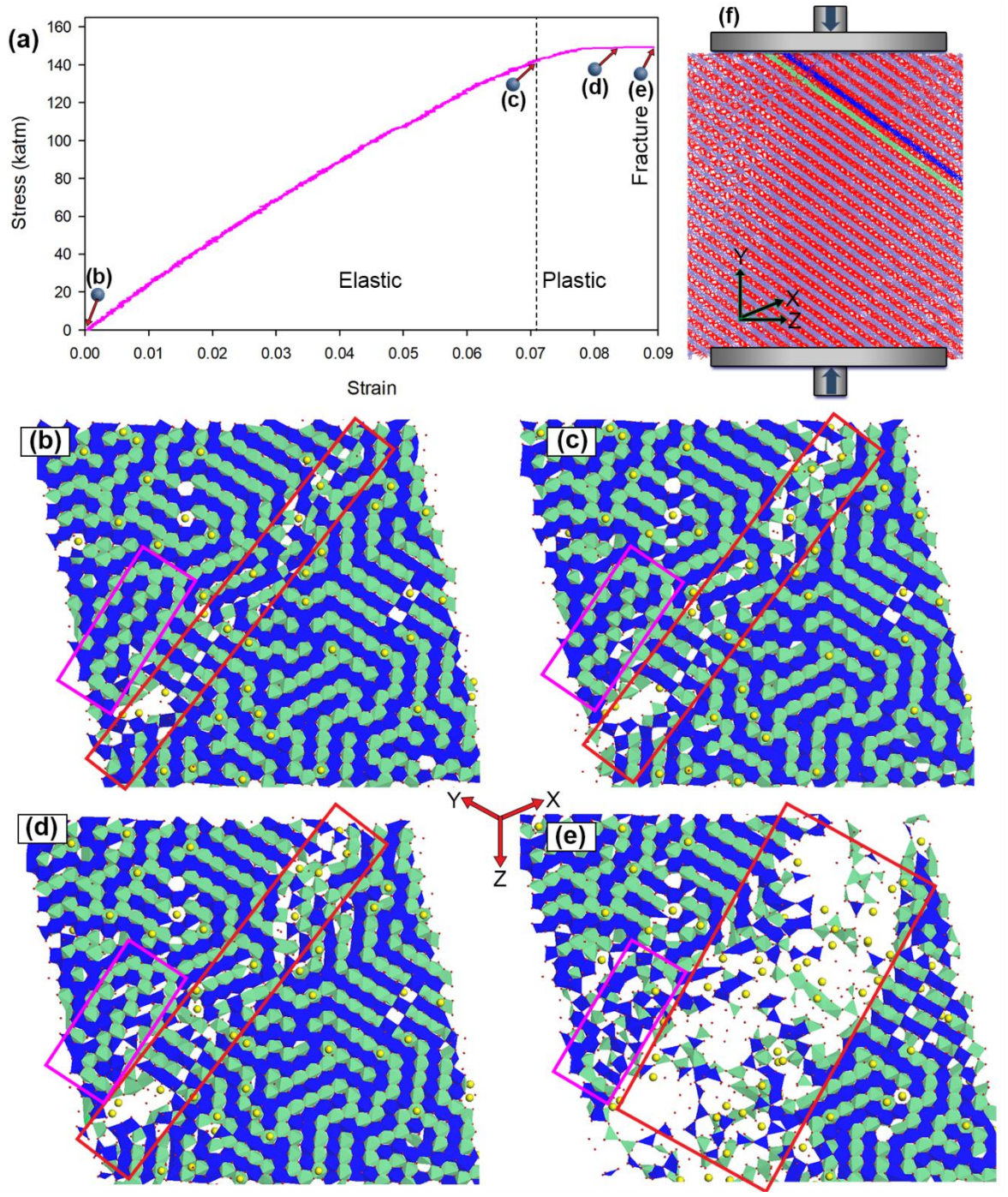

Figure 4-27: Tensile stress-strain plot of bulk $Li_{0.12}MnO_2$-β and microstructure slices in the (b) elastic, (c, d) plastic and (e) collapse regions. The top MnO_6 octahedral plane is depicted by blue while the bottom plane is depicted by green.

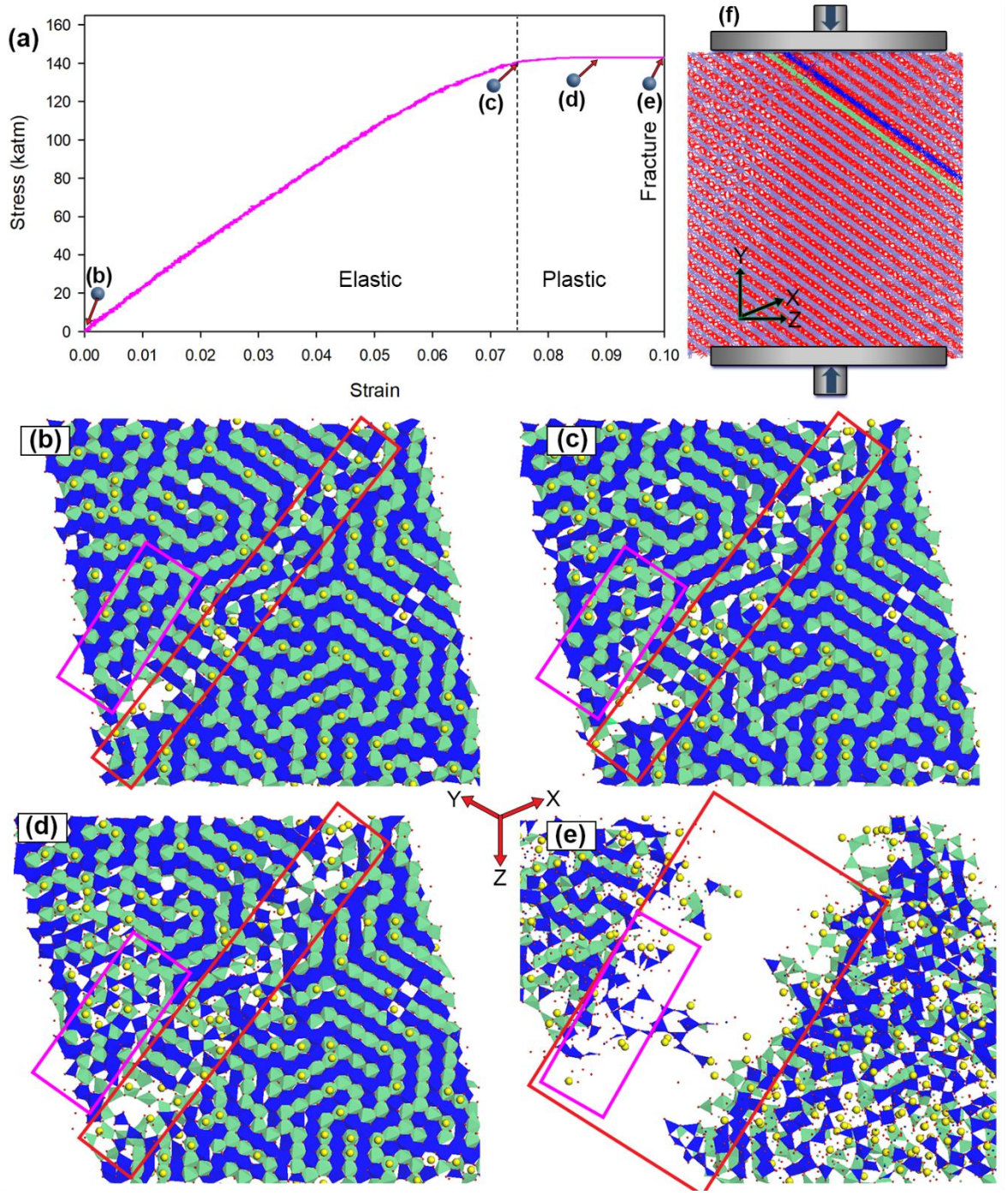

Figure 4-28: Tensile stress-strain plot of bulk $Li_{0.24}MnO_2$-β and microstructure slices in the (b) elastic, (c, d) plastic and (e) collapse regions. The top MnO_6 octahedral plane is depicted by blue while the bottom plane is depicted by green.

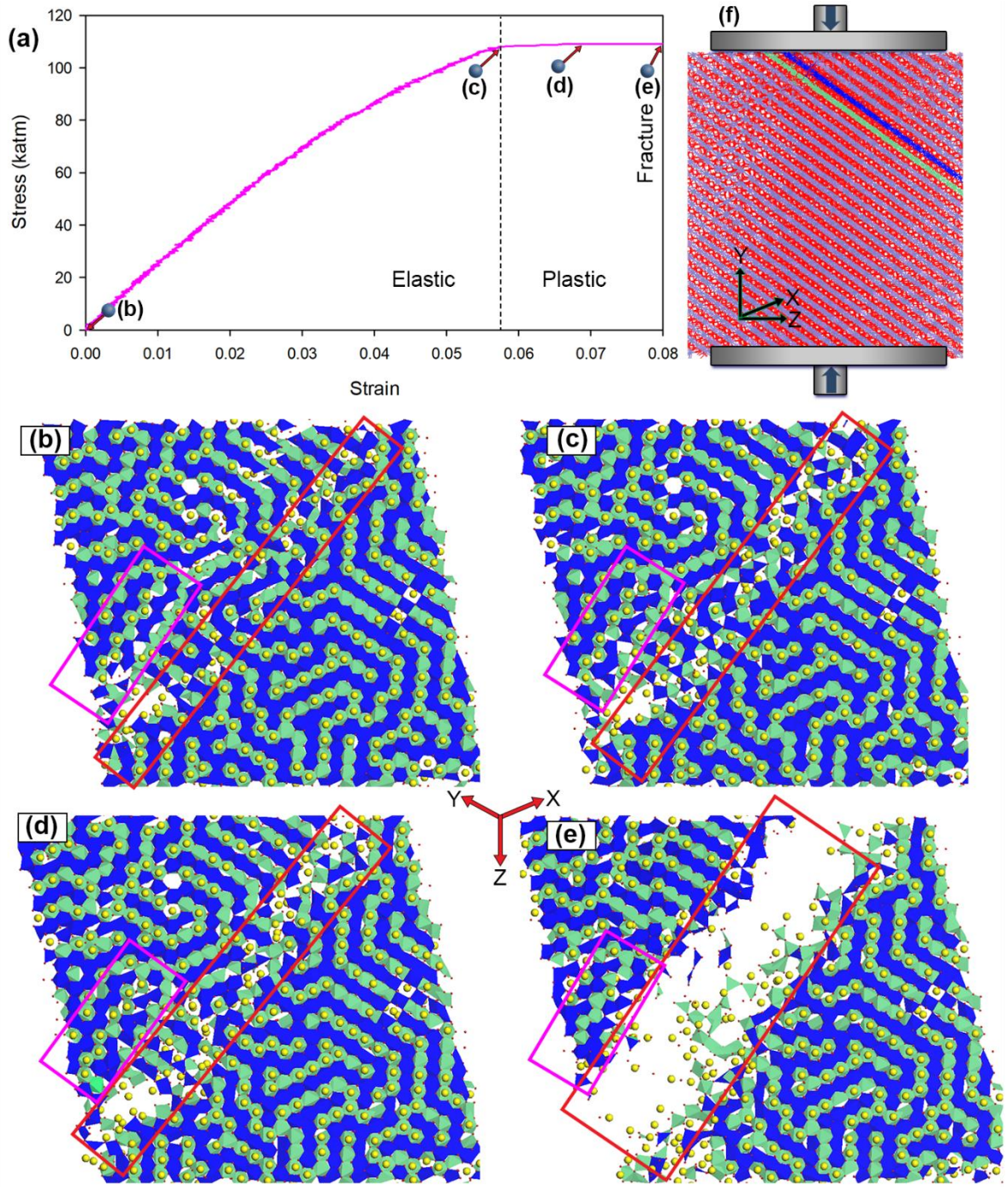

Figure 4-29: Tensile stress-strain plot of bulk $Li_{0.73}MnO_2$-β and microstructure slices in the (b) elastic, (c, d) plastic and (e) collapse regions. The top MnO_6 octahedral plane is depicted by blue while the bottom plane is depicted by green.

4.5.3 Mn-Mn Radial Distribution Functions of Bulk Li_xMnO_2-β (x = 0.00, 0.03, 0.12, 0.24 and 0.73)

The radial distribution functions (RDFs) at the zero strain, elastic limit, and plastic region and fracture point are presented in Figure 4-30 to Figure 4-34. The maximums for the second and third peaks shifted to the right as these peaks expanded to the right indicating an increase in the 1x1 tunnel size. The larger peak widths indicate a wide 1x1 tunnel width distribution, especially for the bulk sample with 0.03 Li/Mn. This peak shift is less for samples with higher lithium-ion concentrations because the unstrained bulk structure had already expanded significantly due to lithium-ion intercalation. The 1x1 tunnels remained extended during plastic deformation. The peaks at 2.9 and 3.5 Å in the RDFs for the bulk $Li_{0.24}MnO_2$-β have merged while the others flattened resulting in a radial distribution function pattern of a liquid. This indicates a transition to an amorphous state as previously seen in the microstructure diagram in Figure 4-28.

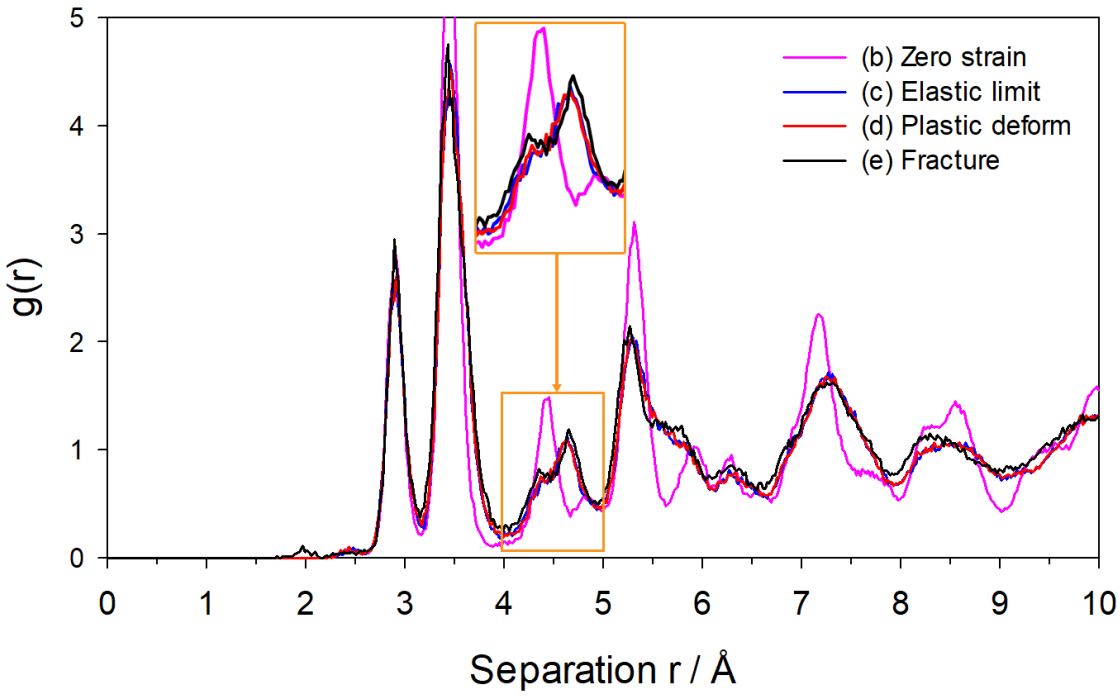

Figure 4-30: Mn-Mn radial distribution functions of the bulk β-MnO2 at zero strain, plastic deformation and fracture point.

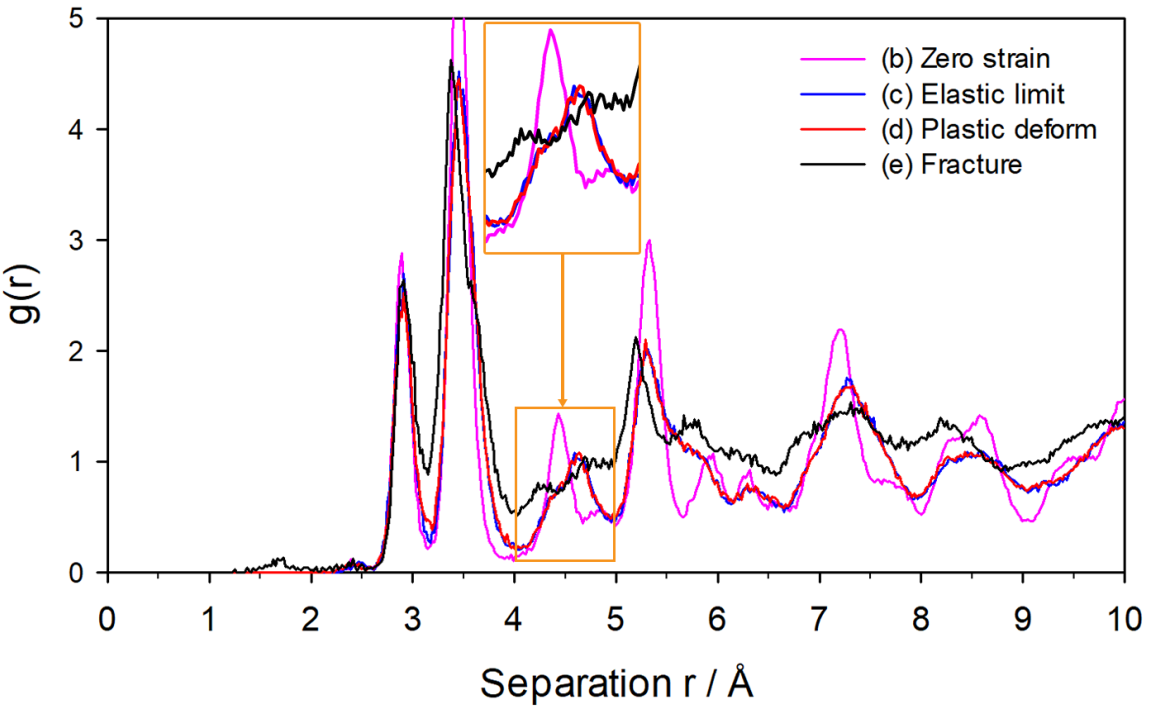

Figure 4-31: Mn-Mn radial distribution functions of the bulk $Li_{0.03}MnO_2$-β at zero strain, plastic deformation and fracture point.

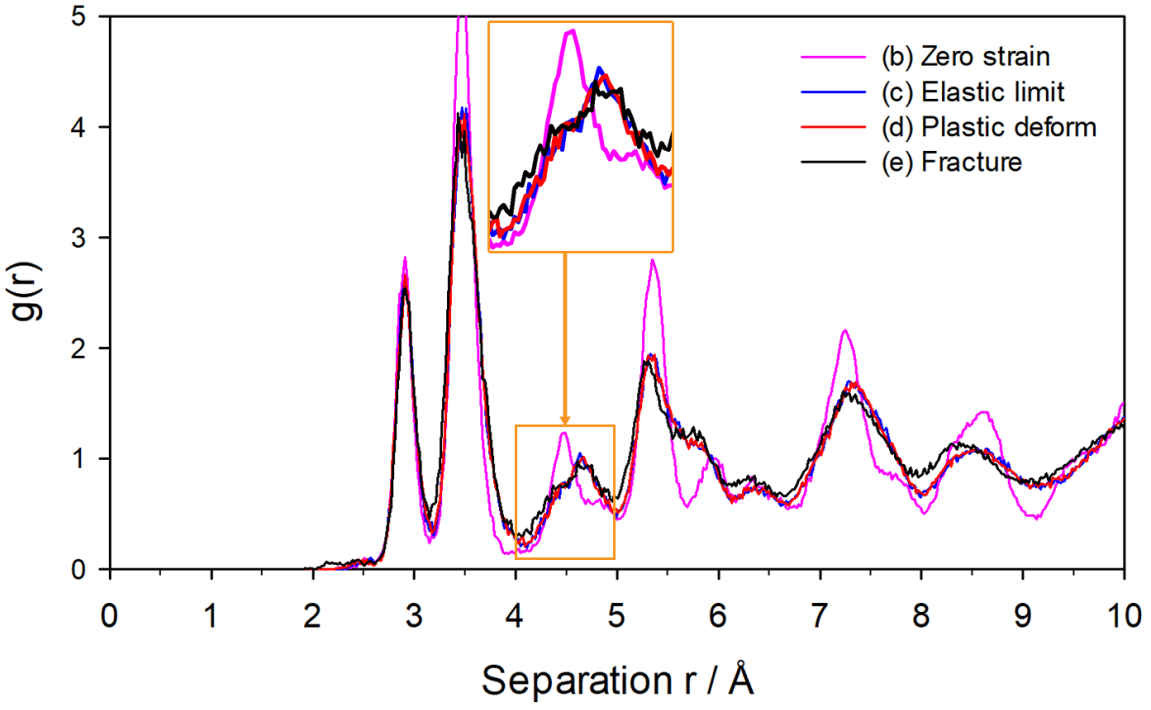

Figure 4-32: Mn-Mn radial distribution functions of the bulk $Li_{0.12}MnO_2$-β at zero strain, plastic deformation and fracture point.

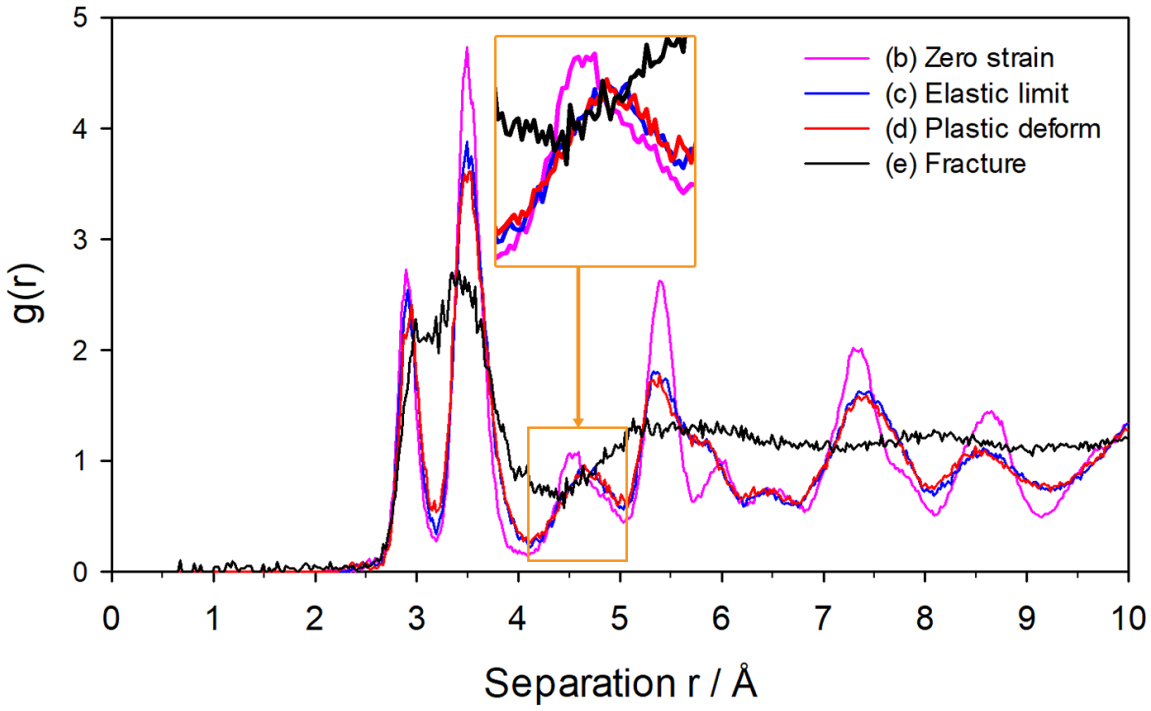

Figure 4-33: Mn-Mn radial distribution functions of the bulk $Li_{0.24}MnO_2$-β at zero strain, plastic deformation and fracture point.

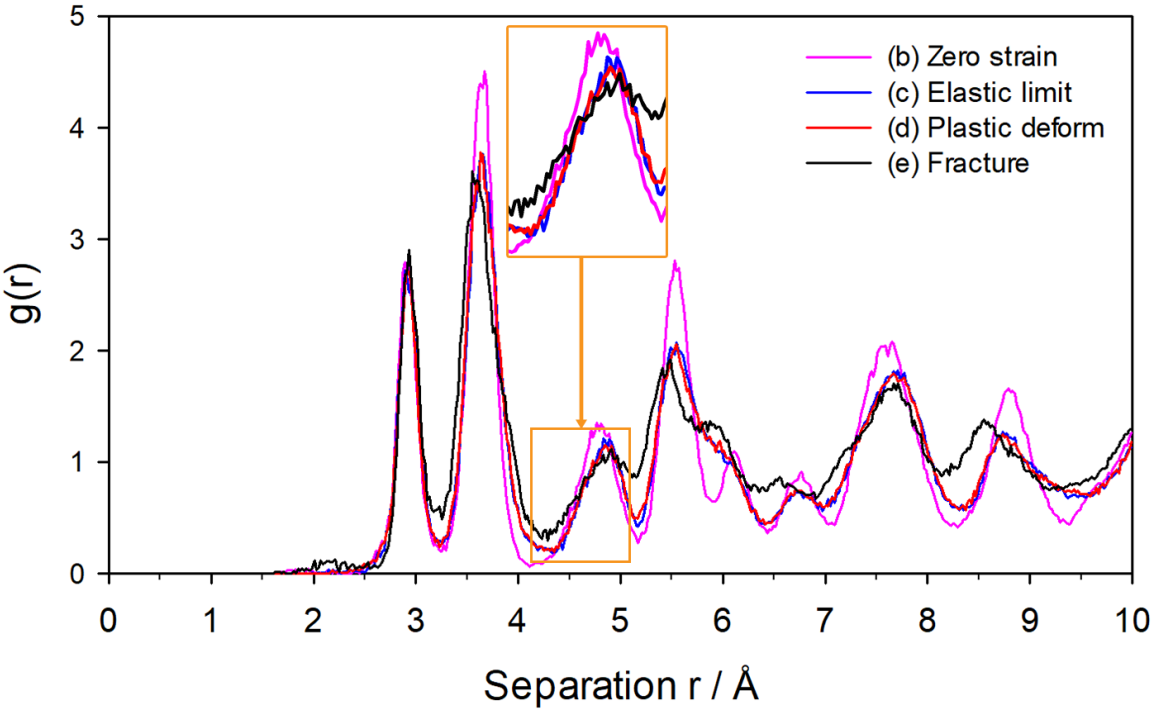

Figure 4-34: Mn-Mn radial distribution functions of the bulk $Li_{0.73}MnO_2$-β at zero strain, plastic deformation and fracture point.

4.6 Uniaxial Tensile Strain on Nanorod Li_xMnO_2-β

4.6.1 Mechanical Properties

Stress vs strain curves for the uniaxial tensile strain on the pristine and lithiated nanorod β-MnO_2 are provided below in Figure 4-35 with the corresponding mechanical properties presented in Table 4-4. Under tensile strain, the nanorod expands elastically up to 4.4, 4.3, 4.6, 4.3 and 3.7 % strain for 0.00, 0.03, 0.12, 0.24 and 0.73 lithium fractions, respectively. The calculated elastic moduli were found to be 79.21, 77.39, 71.75, 67.73 and 64.13 GPa for 0.00, 0.03, 0.12, 0.24 and 0.73 and 0.73 lithium fractions, respectively. These values per Li/Mn are lower than those calculated under compressive stress.

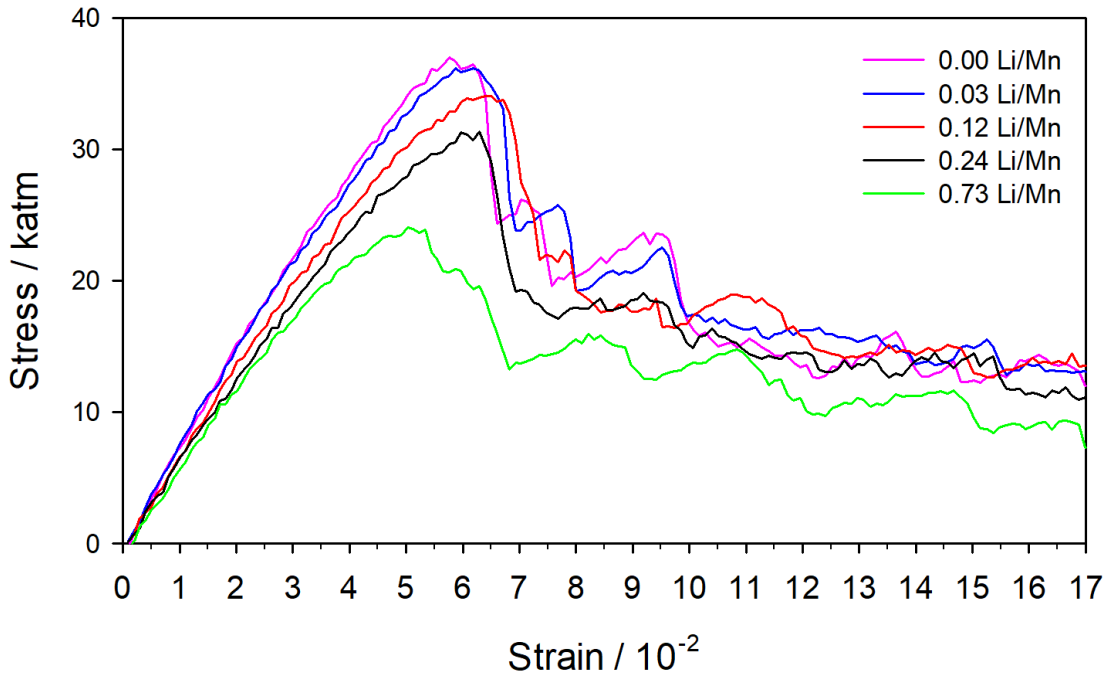

Figure 4-35: Calculated tensile stress versus strain plot for nanorod Li_xMnO_2-β, x = 0.00, 0.03, 0.12, 0.24 and 0.73.

The simulated elastic modulus of 79.21 GPa calculated for our unlithiated nanorod structure is comparable to the value of 77.84 GPa obtained through density functional theory methods. These elastic moduli values indicate that under tensile strain the nanorod becomes more brittle at subsequently higher lithium content.

Structural deformation began at yield stress values of 3.09, 2.96, 2.89, 2.55 and 2.02 GPa for 0.00, 0.03, 0.12, 0.24 and 0.73 lithium fractions, respectively, suggesting that as more lithium ions are intercalated the parent bulk material yielded at subsequently lower stresses.

Table 4-4: Mechanical properties of lithiated nanorod β-MnO_2 under tensile stress.

Li/Mn	Yield Stress		Simulated Elastic modulus (Y)		Exp. (Y)
	katm	GPa	katm	GPa	GPa
0.00	30.48	3.09	677.73	79.21	77.84 [74]
0.03	29.19	2.96	763.73	77.39	
0.12	28.51	2.89	708.10	71.75	
0.24	25.22	2.55	668.45	67.73	
0.73	19.91	2.02	641.30	64.13	

4.6.2 Microstructure of Nanorod Li_xMnO_2-β (x = 0.00, 0.03, 0.12, 0.24 and 0.73)

The microstructural behaviour of the pure and lithiated nanorod β-MnO_2 in response to tensile strain in the elastic region, plastic region and fracture point is presented in diagrams (b), (c), (d) and (e) of Figure 4-36 to Figure 4-40. At zero applied stress/strain, the nanorods are already strained due to lithium-ion intercalation. At 0.00, 0.03, 0.12 and 0.24 Li/Mn, the bulk β-MnO_2 has a rutile-type domain located in the black rectangles comprising 1x1 tunnel structures with the *c*-axis orientated normal to the page. This rutile-type domain has undergone a rutile-to-brookite phase transformation at 0.73 Li/Mn, evident in Figure 4-40 (a), before tensile stress application due to lithium-ion intercalation. Within the early stages of plastic deformation at about 7% strain, the rutile-type domain located within the black rectangles for 0.00, 0.03, 0.12 and 0.24 Li/Mn underwent a transformation to the brookite phase identifiable by zigzag MnO_6 octahedral chains along the direction of the tensile strain.

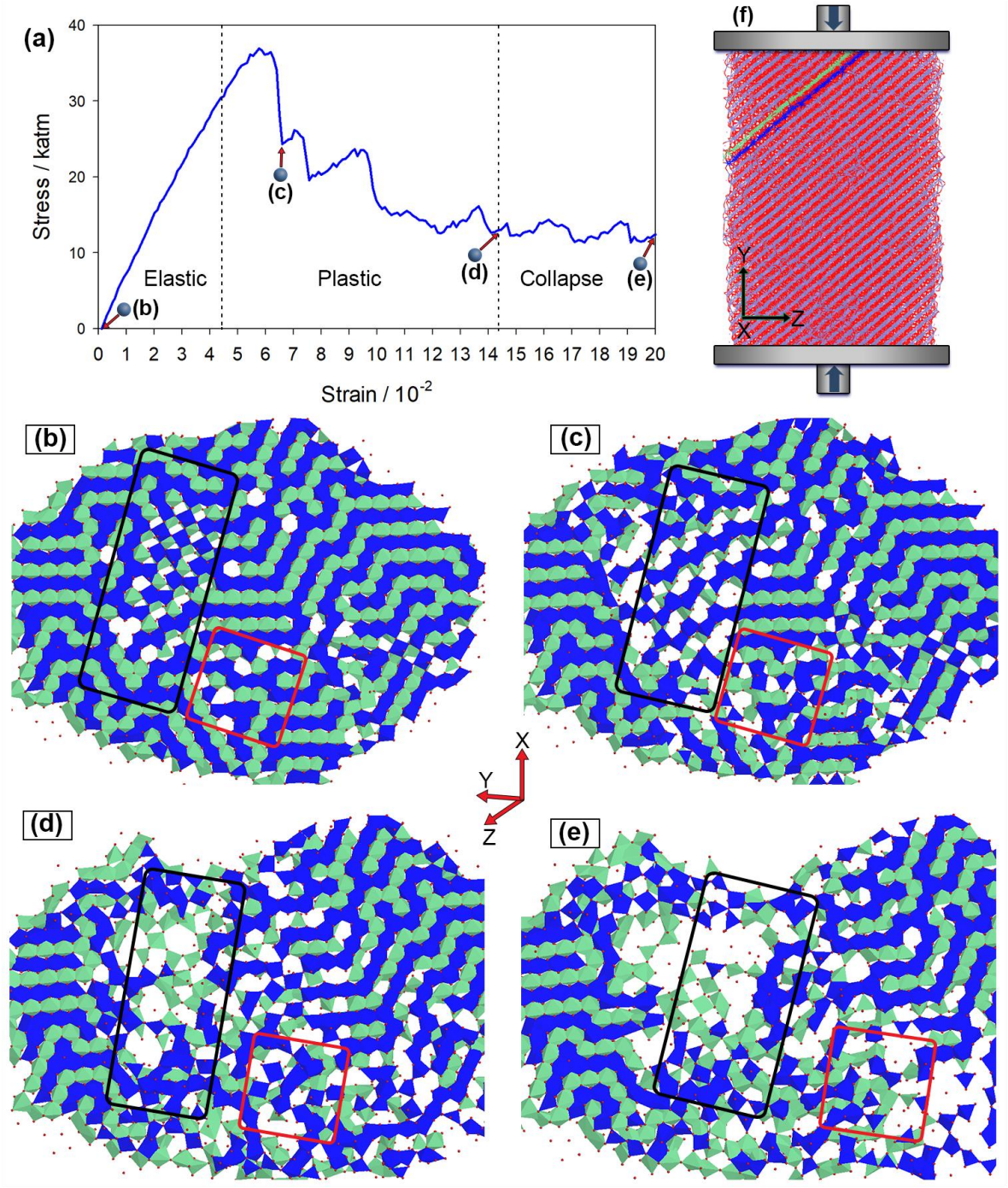

Figure 4-36: Tensile stress-strain plot of nanorod β-MnO_2 and microstructure slices in the (b) elastic, (c, d) plastic and (e) collapse regions. The top MnO_6 octahedral plane is depicted by blue while the bottom plane is depicted by green

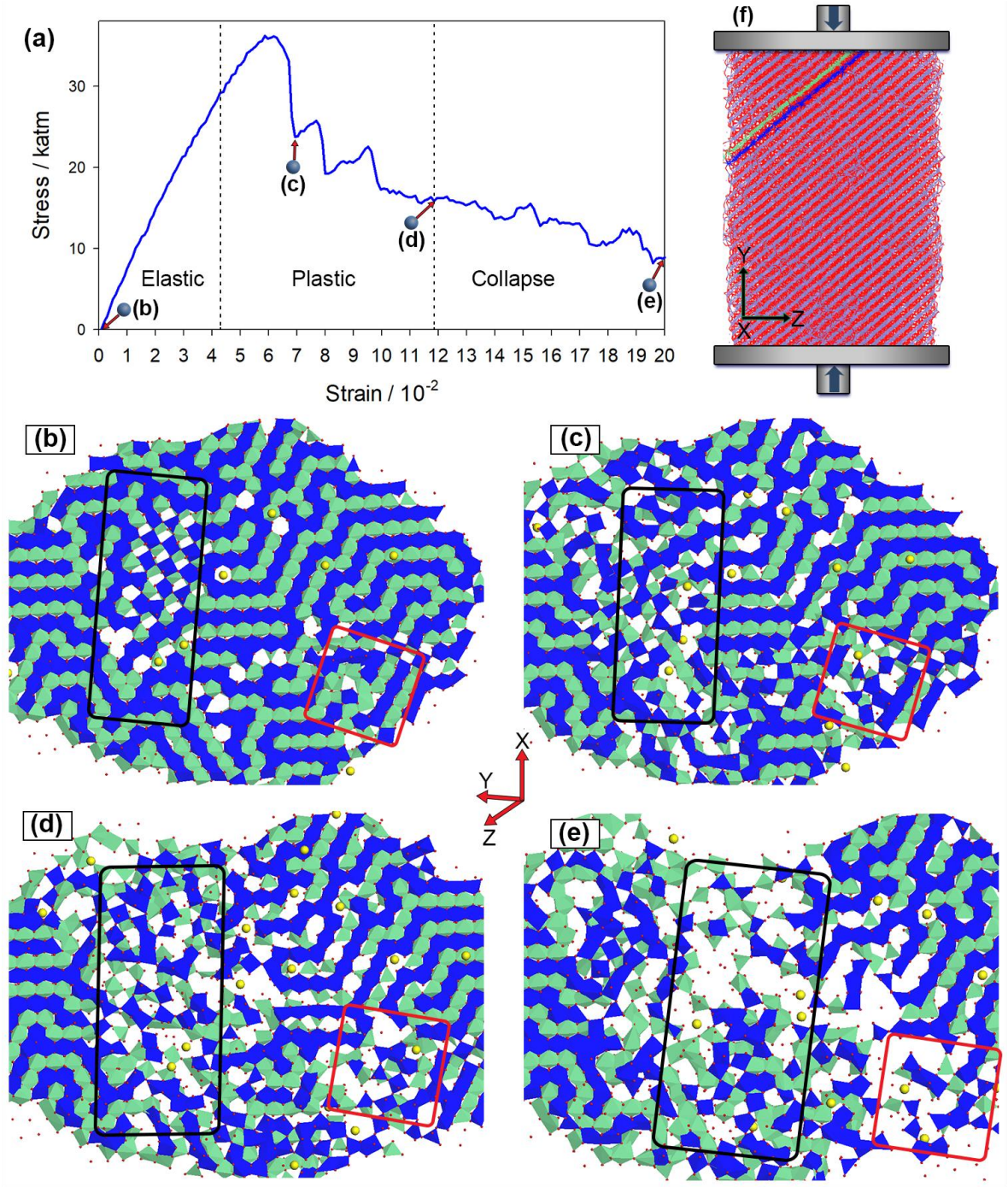

Figure 4-37: Tensile stress-strain plot of nanorod $Li_{0.03}MnO_2$-β and microstructure slices in the (b) elastic, (c, d) plastic and (e) collapse regions. The top MnO_6 octahedral plane is depicted by blue while the bottom plane is depicted by green.

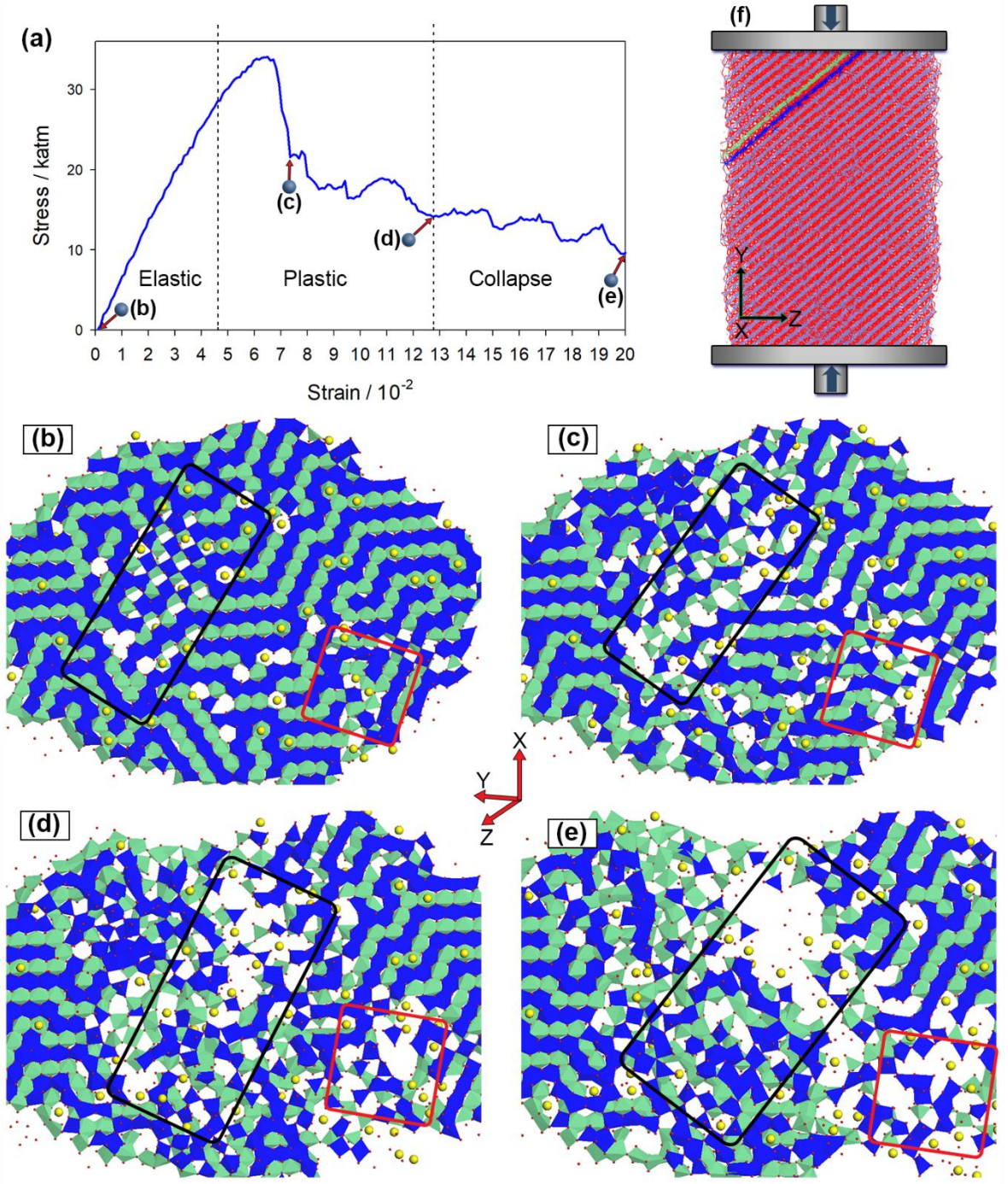

Figure 4-38: Tensile stress-strain plot of nanorod $Li_{0.12}MnO_2$-β and microstructure slices in the (b) elastic, (c, d) plastic and (e) collapse regions. The top MnO_6 octahedral plane is depicted by blue while the bottom plane is depicted by green.

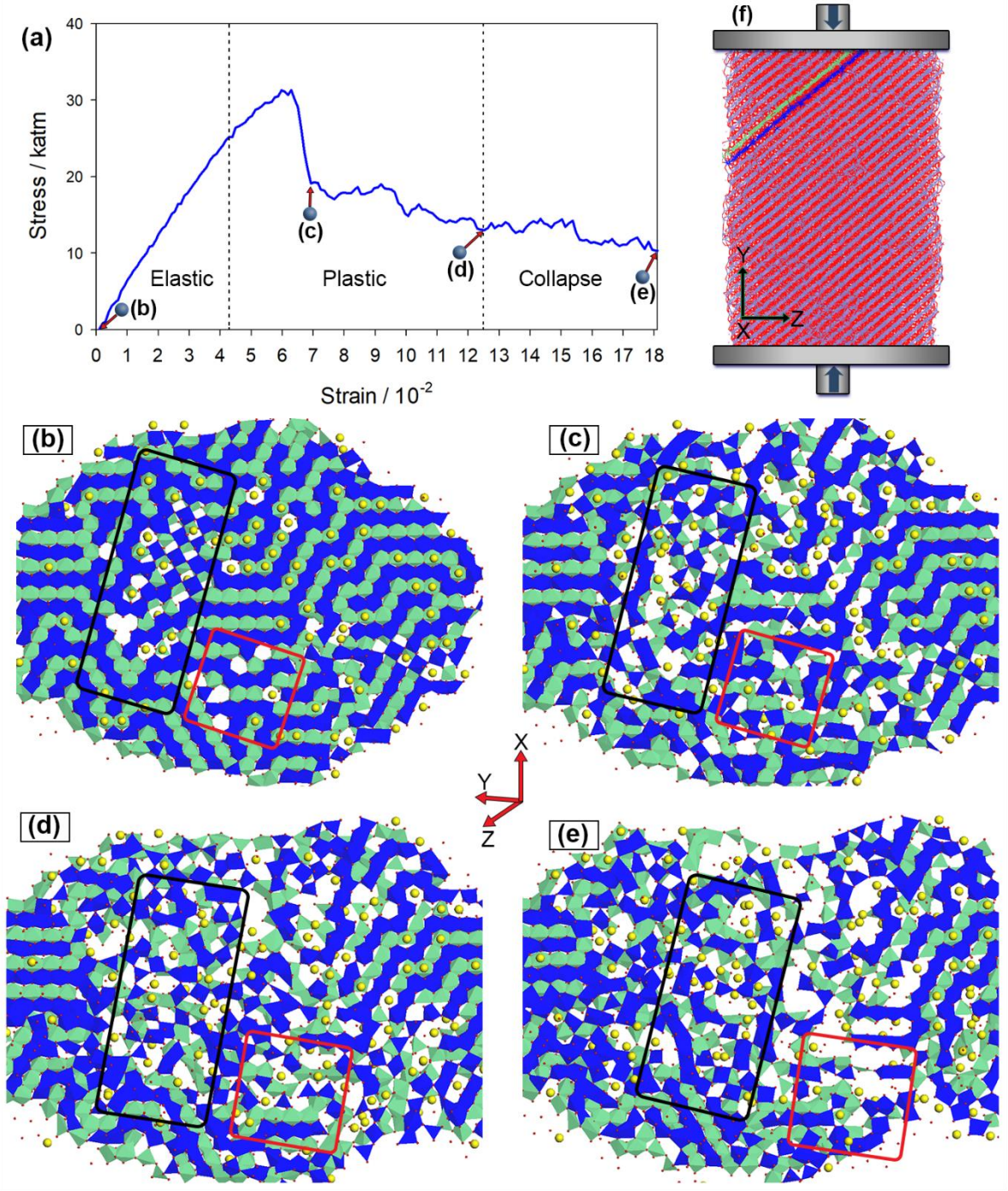

Figure 4-39: Tensile stress-strain plot of nanorod $Li_{0.24}MnO_2$-β and microstructure slices in the (b) elastic, (c, d) plastic and (e) collapse regions. The top MnO_6 octahedral plane is depicted by blue while the bottom plane is depicted by green.

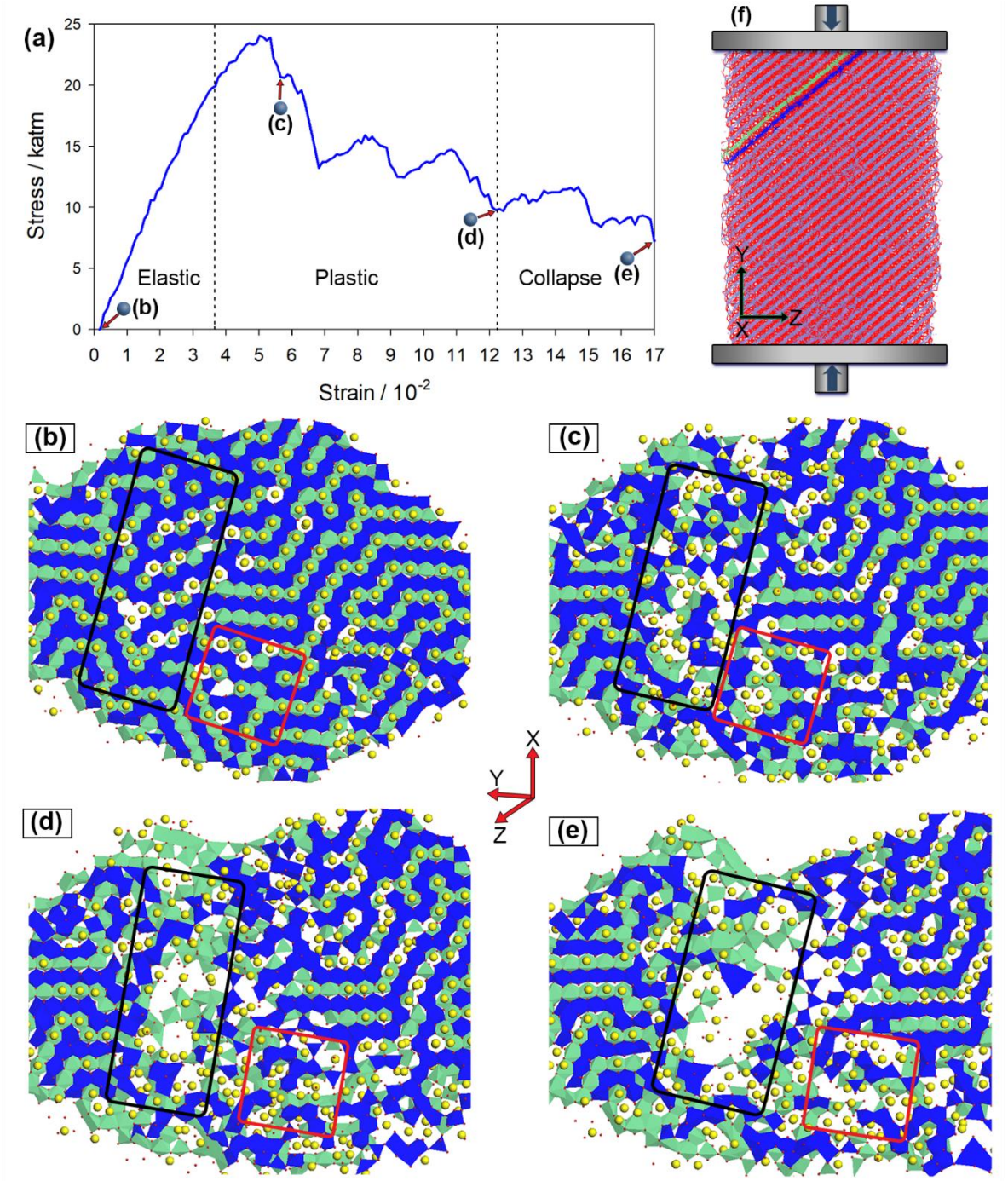

Figure 4-40: Tensile stress-strain plot of nanorod $Li_{0.73}MnO_2$-β and microstructure in the (b) elastic, (c, d) plastic and (e) collapse regions. The top MnO_6 octahedral plane is depicted by blue while the bottom plane is depicted by green.

The crystallinity of this brookite is affected by lithium-ion concentration and reduces with increasing lithium-ion concentration; the brookite phase is clear at 0.00 Li/Mn and degraded at 0.24 Li/Mn. However, the brookite phase at 0.73 Li/Mn is more identifiable than at 0.24 Li/Mn indicating that lithium-ions may have interfered with the rutile-to-brookite transformation under stress application. Phase transformation of nanomaterials under high pressures is well known [72, 77, 78, 79] and has been studied for the production of nanomaterials with new properties. Dong and Song observed a rutile-to-fluorite phase transformation of SnO_2 under compressive stress which reverted back to the rutile phase after decompression [80]. A fluorite-to-rutile transformation of CeO_2 nanorods under tensile strain was observed at strains exceeding 6% in an atomistic simulation study performed by Sayle and Sayle [81]. Additional deformation was initiated from the sub-domain enclosed by a red rectangle where there is a manganese vacancy. As more tensile stress was exerted, the brookite chains broke and as a result the relative microstructural domain amorphised or fractured. At strains greater than 17% the microstructure fractured in the region enclosed by a black rectangle. All nanorods sheared where the octahedral planes above and below the microstructures slid along the *xz*-plane.

4.6.3 Mn-Mn Radial Distribution Functions of Nanorod Li_xMnO_2-β

The radial distribution functions (RDFs) for the nanorod at the zero strain, elastic limit, and plastic region and fracture point are presented in Figure 4-41 to Figure 4-45. The maximums for the second and third peaks shifted to the right as these peaks expanded slightly to the right indicating an increase in the 1x1 tunnel size. The larger peak widths indicate a wide 1x1 tunnel width distribution. Except for $Li_{0.24}MnO_2$-β, the second and third peaks in the RDFs at the fracture point have been restored to their initial positions indicating a reduction in localised stress. However, the resulting reduction in the peak height suggests permanent structural deformation. Similar to the mesoporous β-MnO_2 under compressive stress [36], the RDFs indicate that the nanorod retained the 1x1 tunnel size after fracturing.

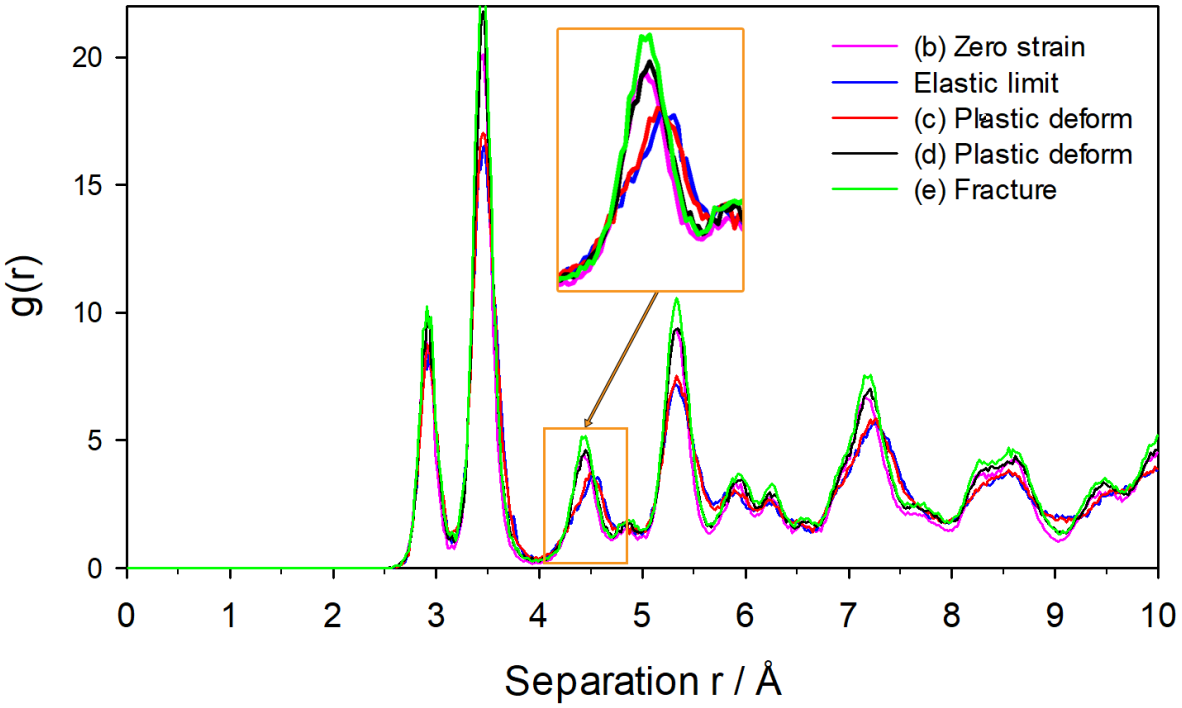

Figure 4-41: Radial distribution functions of the β-MnO_2 nanorod at zero strain, plastic deformation and fracture point.

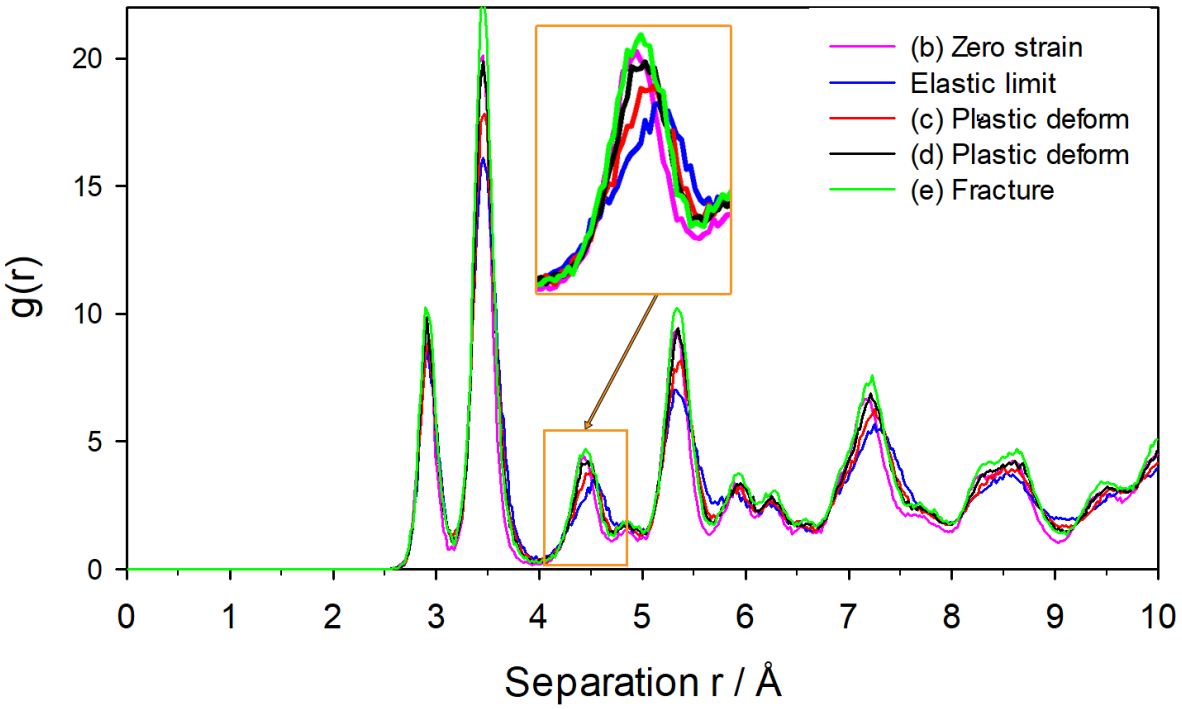

Figure 4-42: Radial distribution functions of the nanorod $Li_{0.03}MnO_2$-β at zero strain, plastic deformation and fracture point.

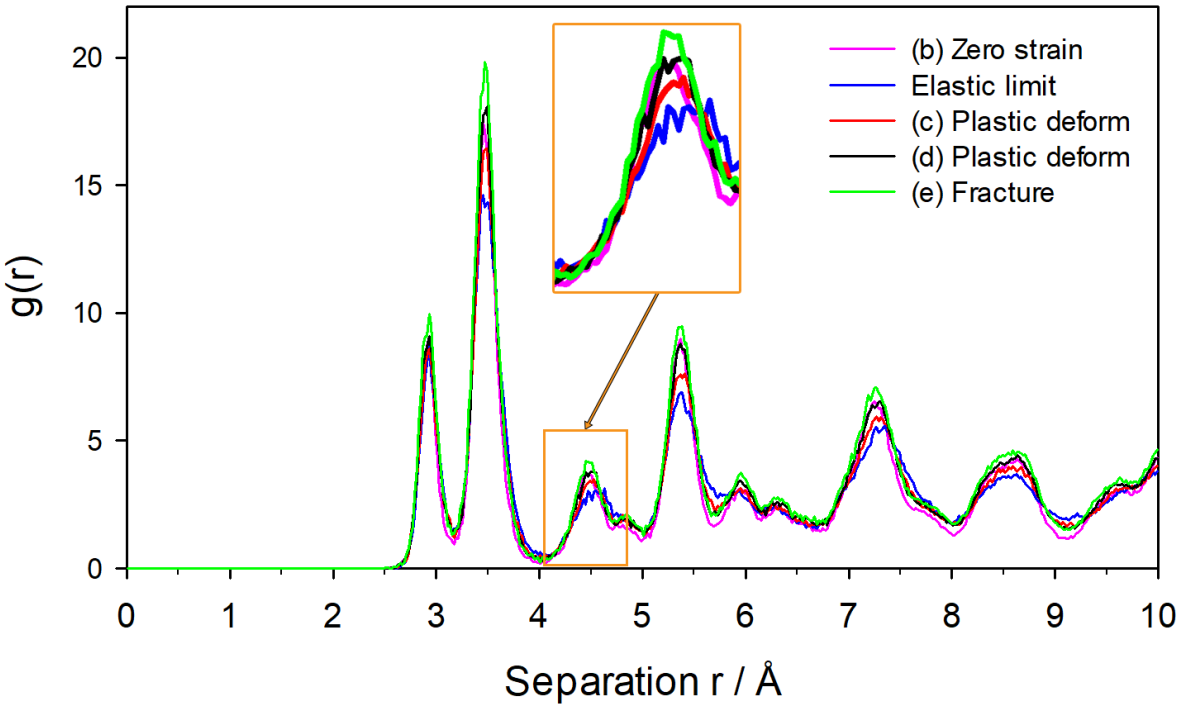

Figure 4-43: Radial distribution functions of the nanorod $Li_{0.12}MnO_2$-β at zero strain, plastic deformation and fracture point.

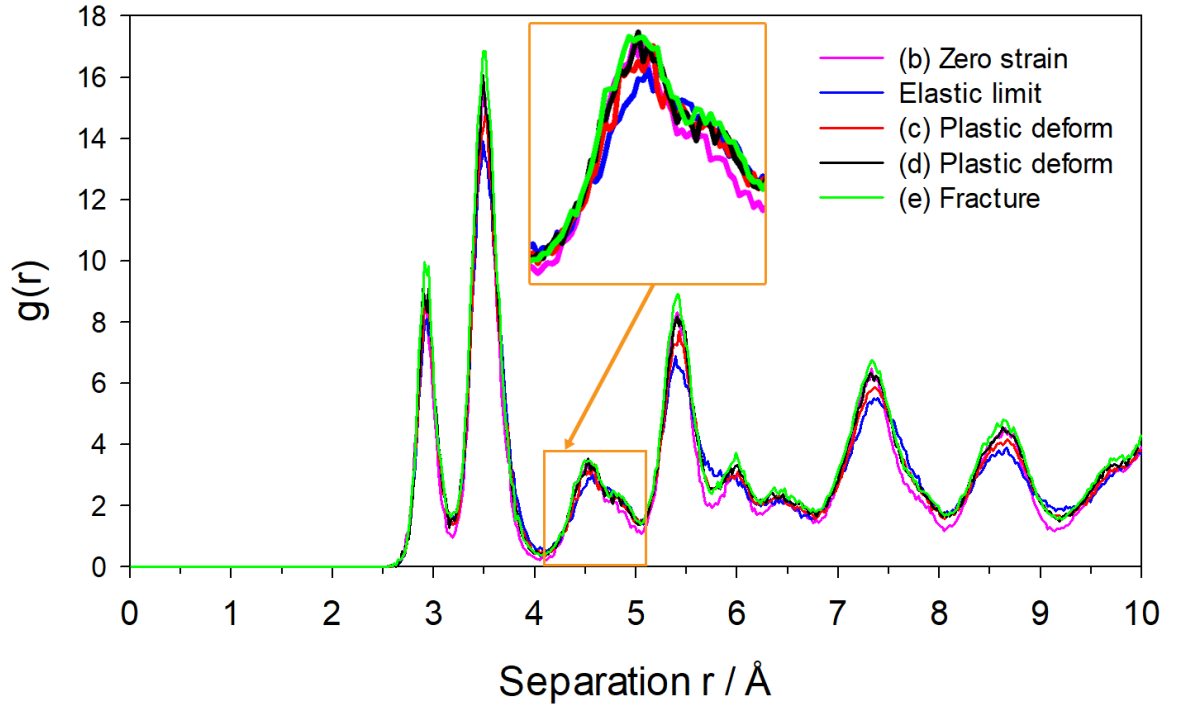

Figure 4-44: Radial distribution functions of the nanorod $Li_{0.24}MnO_2$-β at zero strain, plastic deformation and fracture point.

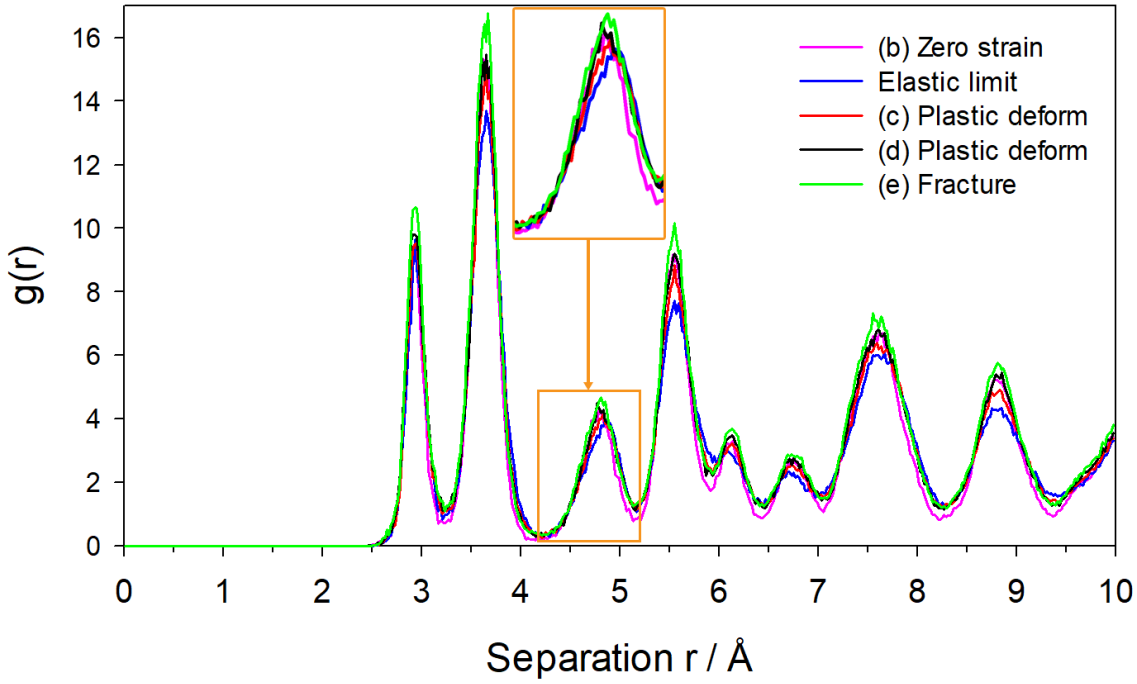

Figure 4-45: Radial distribution functions of the nanorod $Li_{0.73}MnO_2$-β at zero strain, plastic deformation and fracture point.

Chapter 5

Conclusions and Future Work

Realistic models of β-MnO_2 with defect-rich microstructure comprising vacancies, dislocation/stacking faults and grain boundaries were previously generated through simulated amorphisation recrystallisaiton technique based on classical molecular dynamics method [35]. We use the models to study the behaviour of 1x1 tunnels and changes in structural integrity under the localised lithium-ion/sodium-ion intercalation-induced stress and externally applied stress.

5.1 Conclusions

5.1.1 Lithium-ion Insertion

During discharging, a rechargeable lithium-ion battery employing a β-MnO_2 cathode is known to intercalate lithium-ions into the host lattice of the cathode or at the surface [10] where the lithium-ions traverse the tetrahedral and octahedral sites available in the 1x1 tunnels as they diffuse. In light of this, we have developed a program to intercalate lithium-ions into the octahedral sites of the defect-rich β-MnO_2 models allowing us to study in detail some aspects of the intercalation process.

Many studies that have been conducted to address the capacity fading in MnO_2 cathodes during charging and discharging and ascribed it to the phase change to layered spinel, layered MnO_2, etc. Additional studies have employed nanostructuring as a way to mitigate these effects.

Currently, we have performed lithium-ion intercalation into bulk, nanosphere, nanorod, nanosheet and nanoporous β-MnO_2, consisting of approximately 26 000 atoms within classical molecular dynamics simulations to study the microstructural

response and the impact of nanostructuring on the behaviour of β-MnO_2 cathodes. We were able to ignore factors pertaining to intercalating lithium-ions from the surface into the bulk, such as surface area size, exposed surface morphology, surface energy barriers, reduction in the size of 1x1 rutile tunnels and structural degradations at the surface and directly intercalated lithium-ions into the octahedral interstitial sites of the bulk β-MnO_2 up to 85% without any phase transformation to the spinel or layered structure. This is contrary to the known intercalation of no more than 0.2 Li/Mn for bulk β-MnO_2 [19, 40]. This result suggests that the low intercalation in bulk β-MnO_2 may be linked to other factors such as the concentration of lithium-ions at the intercalation point.

In our study lithium-ions were randomly distributed in octahedral sites within the bulk β-MnO_2 resulting in a uniform distribution of lithium-induced stress. Whereas in a real setup, lithium-ions would be highly concentrated at the intercalation point, resulting in a non-uniform distribution of lithium-induced stress within the material, and proceed to propagate to nearby regions as witnessed in the reaction front of SnO_2 nanowires [82]. Contraction and degradation of 1x1 rutile tunnels such as those witnessed in the bulk β-MnO_2 under compressive stress would limit lithium-ion diffusion into the bulk β-MnO_2 thus resulting in a lithium content lower than 0.85 %. The nanosphere, nanorod, nanosheet and nanoporous β-MnO_2 exhibited the same behaviour for all Li/Mn. However, these results also indicate that with a proper design β-MnO_2 has the potential to be intercalated to capacities as high as 0.92 Li/Mn achieved in the work of Jiao and Bruce [3].

The bulk β-MnO_2 experienced the least volume expansion relative to subsequent lithiation when compared to other β-MnO_2 nanostructures. The lack of space or channels commonly found in nanostructures and a smaller surface to bulk ratio may be the limiting factors in the mitigation of lithium-ion induced stress in the bulk material.

5.1.2 Sodium-ion Insertion

As lithium is a limited resource, we have also investigated sodium-ion intercalation into β-MnO_2 bulk and nanostructures. A maximum intercalation of 0.24 Na/Mn without loss of structural integrity was achieved for all nanostructures, as deduced from the microstructures and radial distribution functions. Beyond this sodium concentration, the microstructures collapse and become amorphous. This intercalation limit is similar to that of the electrochemically inactive bulk β-MnO_2 and renders β-MnO_2 unsuitable as a cathode in sodium-ion batteries. This limitation may be ascribed to the large size of the sodium-ions relative to the small size of 1x1 tunnels found in β-MnO_2. This limit may be increased by perhaps adsorbing the sodium-ions on the large surface areas present in the nanostructures as in the adsorption of lithium-ions on the surface of β-MnO_2 nanorods by Kim et al. [10].

5.1.3 Average Intercalation Voltage

Nano sizing has been previously found to enhance the cell voltage in lithium-ion batteries due to perhaps the increased surface-to-volume ratio and reduced path for mobile charges [69]. By approximating entropy, we were able to estimate the average intercalation voltage of the various nanostructures. The trend in average intercalation voltage going from high to low was nanoparticle, nanoporous, nanosheet, nanorod and bulk β-MnO_2. Except for the nanoparticle, the trend in the intercalation voltages is consistent with the surface-to-volume ratios of the respective β-MnO_2 nano architectures and suggests the impact of nanostructuring on cell voltage.

5.1.4 Uniaxial Compressive Stress

Studies on uniaxial compression of the lithiated bulk and nanorod β-MnO_2 show that the 1x1 tunnels in the nanorod shrink but do not collapse while the tunnels in the bulk β-MnO_2 collapse. This result may help explain the electrochemically inactive

nature of the bulk β-MnO_2. The smaller 1x1 tunnels size in the nanorod may lead to reduced lithium-ion diffusion and consequently low rate capability. The nanorod alleviated compressive stress through the evolution and shearing along a grain boundary while the parent bulk β-MnO_2 collapsed at various microstructural facets. We propose that the nanorod β-MnO_2 preserved the 1x1 rutile-type tunnels by expanding into the space located perpendicular to the compressive stress, while the bulk β-MnO_2 responded to compressive stress through severe compression and collapse of the 1x1 rutile-type tunnels. Our studies show that the larger 1x2 or 2x2 tunnels collapse under compressive stress irrespective of the host nanoarchitecture. Thus minimising the amount of 1x2 or 2x2 tunnels during the preparation of the β-MnO_2 nanorods could reduce the degree of structural collapse under compressive stress.

From the pressure versus volume study, the bulk structure experienced more internal pressure than the nanorod at the same strain value. This suggests that the space around the nanorod is crucial in mitigating stress and preventing 1x1 tunnel destruction.

5.1.5 Uniaxial Tensile Stress

In the current study, the origin of deformation and fracture in bulk β-MnO_2 under tensile stress was shown to be related to brookite domains and a grain-boundaries.

Phase transformations have been shown to provide a mechanism for mitigating the effects of compressive or tensile stress imposed on materials. A rutile-to-fluorite phase transformation was previously observed in the work of Dong and Song [80] on SnO_2 under compressive stress. A fluorite-to-rutile transformation of CeO_2 nanorods under tensile strain was also observed at strains exceeding 6% in an atomistic simulation study performed by Sayle and Sayle [81].

Our study shows that the rutile-type domain with 1x1 tunnels oriented perpendicular to the tensile stress in the β-MnO_2 nanorod with 0.00, 0.03, 0.12, and 0.24 Li/Mn underwent a rutile-to-brookite phase transformation at strains exceeding 6%. The nanorod $Li_{0.73}MnO_2$-β also underwent a rutile-to-brookite phase transformation without any external stress application. Thus we suggest that lithium-ion intercalation induced localised tension within the β-MnO_2 nanorod. In both the nanorod and the parent bulk material the brookite phase was succeeded by amorphisation leading to fracture and shearing. Consequently, the minimisation of the brookite in β-MnO_2 cathodes is essential in improving their structural resilience.

5.2 Future Work

Simulation of a reaction front in β-MnO_2 with varying lithium-ion concentrations in a combination of octahedral and tetrahedral sites could shed more insight into the effect of localised lithium-induced stress on the nature of its electrochemical inactivity.

The method used to calculate average intercalation potentials in this study provided rough estimates required to establish trends in the average intercalation potentials across the various nanostructures. More accurate intercalation potentials can be calculated through density functional theory (DFT) methods. As previously shown, the expression for calculating the average intercalation potential is:

$$\bar{V} = -\frac{\Delta G_r}{(x_2 - x_1)F}$$

$$\bar{V} = -\frac{\Delta E_r + P\Delta V_r - T\Delta S_r}{(x_2 - x_1)F} \tag{5.24}$$

The change in the Gibbs free energy is approximated to the change in internal energy of the system, $\Delta G_r \approx \Delta E_r$, where the term $P\Delta V_r$ is of the order of 10^{-5} electron volts whereas ΔE_r is in the order of 3 to 4 electron volts per molecule. The term $T\Delta S_r$ is much smaller than the internal energy and can be omitted with little error [55].

The ONETEP (Order-N Electronic Total Energy Package) DFT package will be used to obtain the necessary internal energies however, the system though larger than in traditional DFT calculations, will be significantly smaller than in the current study.

X-ray diffraction patterns of the bulk and nanorod β-MnO_2 under compressive and tensile stress will be calculated as they have the potential to provide additional insight into the mechanisms that occur during intercalation.

Mechanical properties of the sodium intercalated bulk and nanorod β-MnO_2 will also be performed.

References

[1] “Paris Agreement,” in *2015 United Nations Climate Change Conference*, Paris, 2015.

[2] J.P. Treptow, “Lithium Batteries: A Practical Application of Chemical Principles,” *J. Chem. Edu.,* vol. 80, no. 9, pp. 1015-1020, 2003.

[3] F. Jiao and P.G. Bruce, “Mesoporous Crystalline β-MnO_2-A Reversible Positive Electrode for Rechargeable Lithium Batteries,” *Adv. Mater.,* vol. 19, pp. 657-660, 2007.

[4] T. Liu, Y. Zhang, C. Chen, Z. Lin, S. Zhang and J. Lu, “Sustainability-inspired cell design for a fully recyclable sodium ion battery,” *Nat. Commun.,* vol. 10, no. 1965, 2019.

[5] S.-W. Kim, D.-H. Seo, X. Ma, G. Ceder and K. Kang, “Electrode materials for rechargeable sodium-ion batteries: potential alternatives to current lithium-ion batteries,” *Adv. Energy Mater.,* vol. 2, pp. 70-721, 2012.

[6] D. Linden and T.B. Reddy, Handbook of Batteries, Third ed., McGraw-Hill, 2002.

[7] “how-cells-work,” Johnson Matthey Battery Systems, 2016. [Online]. Available: http://www.jmbatterysystems.com/technology/cells/how-cells-work. [Accessed 27 November 2019].

[8] G.-A. Nazri and G. Pistoia, Lithium Batteries Science and Technology, Springer, 2003.

[9] T. Ohzuku and R.J. Brodd, “An overview of positive-electrode materials for advanced lithium ion batteries,” *J. Power Sources,* pp. 449-456, 2007.

[10] I.Y. Kim, H.-W. Ha, T.W. Kim, Y. Paik, J.H. Choy and S.-J. Hwang, “Origin of improved electrochemical activity of β-MnO_2 Nanorods: Effect of the Mn valence in the precursor on the crystal structure and electrode activity of manganates,” *J. Phys. Rev.,* vol. 113, pp. 21274-21282, 2009.

[11] F. Cheng, J. Zhao, W. Song, C. Li, H. Ma, J. Chen, and P. Shen, “Facile Controlled Synthesis of MnO_2 Nanostructures of Novel Shapes and Their Application in Batteries,” *Inorg. Chem.,* vol. 45, pp. 2038-2044, 2006.

[12] P.G. Bruce, B. Scrosati and J.-M. Tarascon, “Nanomaterials for Rechargeable Lithium Batteries,” *Angew. Chem. Int. Ed.,* vol. 47, pp. 2930-2946, 2008.

[13] Y. Ren, A.R. Amstrong, F. Jiao and P.G. Bruce, “Influence of Size on the Rate of Mesoporous Electrodes for Lithium Batteries,” *J. Am. Chem. Soc.,* vol. 132, pp. 996-1004, 2010.

[14] J.E. Post, “Manganese oxide minerals: Crystal structures and economic and environmental significance,” *Proc. Natl. Acad. Sci,* vol. 96, pp. 3447-3454, 1999.

[15] A.E. Gloria and A.M. Chaka, “First principles calculations of clean, oxidized and reduced β-MnO_2 Surfaces,” *J. Phys. Chem.,* vol. 115, pp. 16992-17008, 2011.

[16] W. Yao and F.J. Millero, “Adsorption of phosphate on manganese dioxide in seawater,” *Environ. Sci. Technol.,* vol. 30, pp. 536-541, 1996.

[17] Q. Yu, C. Wang, X. Li, Z. Li, L. Wang, Q. Zhang, G. Wu, Z. Li, “Engineering an effective MnO_2 catalyst from $LaMnO_3$ for catalytic methane combustion,” *Fuel,* vol. 239, pp. 1240-1245, 2019.

[18] J.P. Tafur, J. Abad, E. Román and A.J.F. Romero, “Charge storage mechanism of MnO_2 cathodes in Zn/MnO_2 batteries using ionic liquid-based gel polymer electrolytes,” *Electrochem. commun.,* vol. 60, pp. 190-194, 2015.

[19] M.M. Thackeray, “Manganese Oxides for Lithium Batteries,” *Prog. Solid State Chem.,* vol. 25, pp. 1-71, 1997.

[20] S.H. Kim and S.M. Oh, “Degradation mechanism of layered MnO_2 cathodes in Zn/$ZnSO_4$/MnO_2 rechargeable cells,” *J. Power Sources,* vol. 72, pp. 150-158, 1998.

[21] Y. Chabre and J. Pannetier, “Structural and Electrochemical Properties of the Proton/Gamma-MnO_2 Systems,” *Prog. Solid State Chem.,* vol. 23, pp. 1-130, 1995.

[22] T.X.T. Sayle, C.R.A. Catlow, R.R. Maphanga, P.E. Ngoepe, and D.C. Sayle, “Generating MnO_2 nanoparticles using Simulated Amorphization and Recrystallization,” *J. Am. Chem. Soc.,* vol. 127, pp. 12828-12837, 2005.

[23] T.X.T. Sayle, P.E. Ngoepe and D.C. Sayle, “Simulating Mechanical Deformation in Nanomaterials with Application for Energy Storage in Nanoporous Architectures,” *ACS Nano,* vol. 3, no. 10, pp. 3308-3314, 2009.

[24] D. Balachandran, D. Morgan, G. Ceder and A. van de Walle, “First-principles study of the structure of stoichiometric and Mn-deficient MnO_2,” *J. Solid State Chem.,* vol. 173, pp. 462-475, 2003.

[25] J. Haines, J.M. Léger and S. Hayou, “Second-order rutile-type to $CaCl_2$-type phase transition in β-MnO_2 at high pressure,” *J. Phys. Chem. Solids,* vol. 56, pp. 965-973, 1995.

[26] D.M. Sherman, “Electronic structures of iron(III) and manganese(IV) (hydr)oxide minerals: Thermodynamics of photochemical reductive dissolution in aquatic environments,” *Geochim. Cosmochim. Acta,* vol. 69, pp. 3249-3255, 2005.

[27] N. Kijima, Y. Sakata, Y. Takahashi, J. Akimoto, T. Kumagai, K. Igarashi and T. Shimizu, “Synthesis and lithium ion insertion/extraction properties of hollandite-type MnO_2 prepared by acid digestion of Mn_2O_3,” *Solid State Ion.,* vol. 180, p. 616–620, 2009.

[28] M.M. Thackeray, M.H. Rossouw, R.J. Gummow, D.C. Liles, K. Pearce, A. De Kock, W.I.F. David and S. Hull, “Ramsdellite-MnO_2 for lithium batteries: the ramsdellite to spinel transformation,” *Electrochim. Acta,* vol. 38, pp. 1259-1267, 1993.

[29] H. Miura, H. Kudou, J.H. Choi and Y. Hariya, “The crystal structure of ramsdellite from Pirika mine,” *J. Fac. Sci., Hokkaido Univ., Ser. 4,* vol. 22, pp. 611 - 617, 1990.

[30] A.H. Heuer, A.Q. He, P.J. Hughes and F.H. Feddrix, in *IBA-2000 Manganese Oxide Symposium*, Chicago, IL, 2000.

[31] W. Bowden, T. Bofinger, F. Zhang, N. Iltchev, R. Sirotina, Y. Paik, H. Chen, C. Grey and S. Hackney, “New manganese dioxide for lithium batteries,” *J. Power Sources,* vol. 165, pp. 609-615, 2007.

[32] Q. Zhou X. Li Y-G. Li B-Z. Tian D-Y. Zhao Z-Y. Jiang, “Synthesis and Electrochemical Properties of Semicrystalline Gyroidal Mesoporous MnO_2,” *Chin. J. Chem,* vol. 24, pp. 835-839, 2006.

[33] T. A. Mellan, K. P. Maenetja, P. E. Ngoepe, S. M. Woodley and R. Grau-Crespo, “Lithium and oxygen adsorption at the β-MnO_2 (110),” *J. Mater. Chem. A,* vol. 47, p. 14799–15168, 2013.

[34] D.C. Sayle and R.L. Johnston, “Evolutionary Techniques in atomistic simulation: thin films and nanoparticles,” *Curr. Opin. Solid St. M.,* vol. 7, pp. 3-12, 2002.

[35] T.X.T. Sayle, R.R. Maphanga and P.E. Ngoepe, “Predicting the Electrochemical Properties of MnO_2 Nanomaterials Used in Li Batteries: Simulating Nanostructure at the Atomistic Level,” *J. Am. Chem. Soc.,* vol. 131, pp. 6161-6173, 2009.

[36] T.X.T. Sayle K. Kgatwane, P.E. Ngoepe and D.C. Sayle, “‘Breathing-crystals’ the origin of electrochemical activity of mesoporous Li–MnO_2,” *J. Mater. Chem. A,* vol. 4, pp. 6456-6464, 2016.

[37] K. Ratshomo , “SOUTH AFRICA’S MANGANESE INDUSTRY DEVELOPMENTS,” Department of Mineral Resources, South Africa, Pretoria, 2013.

[38] J.D. Steenkamp and J. Basson, “The manganese ferroalloys industry in southern Africa,” *J. S. Afr. I. Min. Metall.,* vol. 113, p. 667, 2013.

[39] N. Bhengu, “How can South Africa, a resource rich and labour-abundant economy, employ upstream and downstream mineral beneficiation as a way of developing its economy further? A critical focus on the chromium mineral value chain as a case study (Master's thesis),” University of the Witwatersrand, Johannesburg, 2015.

[40] J.-Y. Luo, J.-J. Zhang and Y.-Y. Xia, “Highly Electrochemical Reaction of Lithium in the Ordered Mesoporous ß-MnO_2,” *Chem. Mater.,* vol. 18, pp. 5618-5623, 2006.

[41] T.X.T. Sayle, C.R.A. Catlow, R.R. Maphanga, P.E. Ngoepe and D.C. Sayle, “Evolving Microstructure in MnO_2 using Amorphisation and Recrystallisation,” *J. Cryst. Growth,* vol. 294, pp. 118-129, 2006.

[42] R.R. Maphanga, S.C. Parker and P.E. Ngoepe, “Atomistic Simulation of the Surface Structure of Electrolytic Manganese Dioxide,” *Surface Science,* vol. 603, pp. 3184-3190, 2009.

[43] G. Ceder, M. Doyle, P. Arora and Y. Fuentes, “Computational modelling and simulation for rechargeable batteries,” *MRS Bulletin,* vol. 27, pp. 619-623, 2002.

[44] R.B. Best, “Atomistic molecular simulations of protein folding,” *Curr. Opin. Struct. Biol.,* vol. 22, pp. 52-61, 2012.

[45] C.R.A Catlow, Computer Modelling in Inorganic Crystallography, Academic Press, 1997.

[46] W. Wiechert, “The role of modeling in computational science education,” *Future Generation Computer Systems,* vol. 19, pp. 1363-1374, 2003.

[47] D.J. Griffiths, Introduction to Quantum Mechanics, Prentice Hall, 1995.

[48] “the-top500-awarding-at-isc-high-performance.html,” ISC High Performance, [Online]. Available: https://www.isc-hpc.com/the-top500-awarding-at-isc-high-performance.html. [Accessed 1 December 2019].

[49] W. Smith and I.T. Torodov, “A Short Description of DL_POLY,” *Mol. Simulat.,* vol. 32, pp. 935-943, 2007.

[50] W. Smith and T.R. Forester, “DL_POLY 2.0: A general-purpose parallel molecular dynamics simulations package,” *J. Mol. Graph.,* vol. 14, pp. 136-141, 1996.

[51] C.R.A. Catlow, “Computational modelling in materials chemistry,” *Pure Appl. Chem.,* vol. 77, pp. 1345-1348, 2005.

[52] R. Houwink and H.K. De Decker, Elasticity, plasticity and structure of matter, 3rd ed., Cambridge University Press, 1971.

[53] E.Y. Vedmedenko, Competing Interactions and Patterns in Nanoworld, Wiley, 2007.

[54] Y.G. Gogotsi and R.A. Andrievski, Materials Science of Carbides, Nitrides and Borides, Springer, 1999.

[55] M.K. Aydinol, A.F. Kohan and G. Ceder, “Ab initio study of lithium intercalation in metal oxides and metal dichalcogenides,” *Phys. Rev. B,* vol. 56, pp. 1354-1365, 1997.

[56] C.-F. Liu, Z.G. Neale and G.-Z. Cao, “Understanding electrochemical potentials of cathode materials in rechargeable batteries,” *Mater. Today,* vol. 19, pp. 109-123, 2016.

[57] H.D. Young, R.A. Freedman and A.L. Ford, University Physics with Modern Physics 12th Edition, San Francisco: Pearson Addison-Wesley, 2008.

[58] A. R. Leach, Molecular Modelling Principles and Applications, 2nd ed., Prentice Hall, 2001.

[59] W.J.H. Borghols, M. Wagemaker, U. Lafont, E.M. Kelder and F.M. Mulder, “Impact of nanosizing in lithiated rutile TiO_2,” *Chem. Mater.,* vol. 20, pp. 2949-2955, 2008.

[60] T.X.T. Sayle, P.E. Ngoepe and D.C. Sayle, “Generating structural distributions of atomistic models of Li_2O nanoparticles using simulated crystallisation,” *J. Mater. Chem.,* vol. 20, pp. 10452-10458, 2010.

[61] M. Thompson, X. Shen and P.B. Allen, “Density functional calculation of electronic structure and phonon spectra of Na_2O,” *Phys. Rev. B,* vol. 79, no. 113108, 2009.

[62] H. Yildirim, J.P. Greely and S.K.R.S. Sankaranarayanan, “Concentration-dependent ordering of lithiated amorphous TiO_2,” *J. Phys. Chem. C,* vol. 117, pp. 3834-3845, 2013.

[63] D.A. Tompsett, S.C. Parker, and M.S. Islam, “Rutile (β-)MnO_2 Surfaces and Vacancy Formation for High Electrochemical and Catalytic Performance,” *J. Am. Chem. Soc.,* vol. 136, pp. 118-1426, 2014.

[64] W. Humphrey, A. Dalke and K. Chulten, “VMD: Visual Molecular Dynamics,” *J. Mol. Graph.,* vol. 14, pp. 33-38, 1996.

[65] J.B.A.A. Elemans, B. van Laar, K.R. van der Veen and B.O. Loopstra, “The crystallographic and magnetic structures of $La_{1-x}Ba_xMn_{1-x}Me_xO_3$ (Me = Mn or Ti),” *J. Solid State Chem.,* vol. 3, pp. 238-242, 1971.

[66] E. Dabush, J. Sariel, I. Dahan and G. Kimmel, “Advances in X-ray Analysis,” vol. 45, pp. 146-151, 2002.

[67] N. Kumar, S. Bhaumik, A. Sen, A.P. Shukla and S.D. Pathak, “One-pot synthesis and first-principles elasticity analysis of polymorphic MnO_2 nanorods for tribological assessment as friction modifiers,” *RSC Adv.,* vol. 7, pp. 34138-34148, 2017.

[68] W.M. Dose, J. Lehr and S.W. Donne, “Characterisation of chemically lithiated heat-treated electrolytic manganese dioxide,” *Mater. Res. Bull.,* vol. 47, pp. 1827-1834, 2012.

[69] P. Balaya, “Size effects and nanostructured materials for energy applications,” *Energy Environ. Sci.,* vol. 1, pp. 645-654, 2008.

[70] K.R. Kganyago, P.E. Ngoepe and C.R.A Catlow, “Voltage Profile, Structural Prediction, and Electronic Calculations for $Mg_xMo_6S_8$,” *Phys. Rev. B,* vol. 67, p. 104103, 2003.

[71] R. Gaillac, P. Pullumbi and F.-X. Coudert, “ELATE: an open-source online application for analysis and visualization of elastic tensors,” *J. Phys.: Condens. Matter,* vol. 28, no. 275201, 2016.

[72] J.Z. Jiang, L. Gerward and J.S. Olsen, “Pressure induced phase transformation in nanocrystal SnO_2,” *Scripta Mater.,* vol. 44, pp. 1983-1986, 2001.

[73] J.Z. Jiang, J.S. Olsen, L. Gerward and S. Mørup, “Enhanced bulk modulus and reduced transition pressure in γ-Fe_2O_3 nanocrystals,” *Europhys. Lett.,* vol. 44, pp. 620-626, 1998.

[74] Y. Jiang, J. C. Deng, Y. H. Ding, J. R. Yin, P. Zhang, “Preparation and Research on the Lateral Elastic Modulus of the MnO_2 Nanowires,” *Adv. Mater. Res.,* vol. 662, pp. 84-87, 2013.

[75] T. Shokuhfar, G.K. Arumugam, P.A. Heiden, R.S. Yassar and C. Friedrich, “Direct Compressive Measurements of Individual Titanium Dioxide Nanotubes,” *ACS Nano,* vol. 3, pp. 3098-3102, 2009.

[76] X.D. Han, Y.F. Zhang, X.N. Zhang, Z. Zhang, Y.J. Hao, X.Y. Guo, J. Yuan and Z.L. Wang, “Low-Temperature in Situ Large Strain Plasticity of Ceramic SiC Nanowires and Its Atomic-Scale Mechanism,” *Nano Lett.,* vol. 7, pp. 452-547, 2007.

[77] S.B. Qadri, E.F. Skelton, J. Yang, B.R. Ratna and J.Z. Hu, “Pressure Induced Structural Transitions in Nanometer Size Particles of PbS,” *Rev. High Pressure Sci. Technol.,* vol. 7, pp. 325-326, 1998.

[78] Z. Wang, S.K. Saxena, V. Pischedda, H.P. Liermann and C.S. Zha, “In situ x-ray diffraction study of the pressure-induced phase transformation in nanocrystalline CeO_2,” *Phys. Rev. B,* vol. 64, no. 012102, 2001.

[79] Y. He, J.F. Liu, W. Chen, Y. Wang, H. Wang, Y.W. Zeng, G.Q. Zhang, L.N. Wang, J. Liu, T.D. Hu, H. Hahn, H. Gleiter, and J. Z. Jiang, “High-pressure behavior of SnO_2 nanocrystals,” *Phys. Rev. B,* vol. 72, no. 212102, 2005.

[80] Z. Dong and Y. Song, “Pressure-induced morphology-dependent phase transformations of nanostructured tin dioxide,” *Chem. Phys. Lett.,* vol. 480, pp. 90-95, 2009.

[81] T.X.T. Sayle and D.C. Sayle, “Elastic Deformation in Ceria Nanorods via a Fluorite-to-Rutile Phase Transition,” *ACS Nano,* vol. 2, pp. 879-886, 2010.

[82] J.Y. Huang, L. Zhong, C.M. Wang, J.P. Sullivan, W. Xu, L.Q. Zhang, S.X. Mao, N.S. Hudak, X.H. Liu, A. Subramanian, H. Fan, L. Qi, A. Kushima and J. Li, “In Situ Observation of the Electrochemical Lithiation of a Single SnO_2 Nanowire Electrode,” *Science,* vol. 330, pp. 1515-1520, 2010.

[83] R. Sharma, M. Agarwal and C. Chakravarty, “Estimating the entropy of liquids from atom–atom radial distribution functions: silica, beryllium fluoride and water,” *Mol. Phys. ,* vol. 106, pp. 1925-1938, 2008.

[84] S.N. Chakraborty and C. Chakravarty, “Entropy, local order, and the freezing transition in the morse liquids,” *Phys. Rev. E,* vol. 76, no. 011201, 2007.

Appendix A

Publications

T. X. T. Sayle, K. Kgatwane, P. E. Ngoepe and D. C. Sayle, 'Breathing-crystals' the origin of electrochemical activity of mesoporous Li–MnO_2, *J. Mater. Chem. A vol. 4, pp. 6156-6464, 2016*

K. M. Kgatwane, P. E. Ngoepe and D. C. Sayle, Simulated Mechanical Properties of the Lithiated β-MnO_2 Nanorod. To be published.

Appendix B

Papers presented at conferences

Local Conferences

K. M. Kgatwane, P. E. Ngoepe and D. C. Sayle, Computational Study of the Mechanical Properties of Lithiated MnO_2 Nanorod, 2017 CHPC National Conference, 3-7 December 2017, Pretoria.

K. M. Kgatwane, P. E. Ngoepe* and D. C. Sayle, Atomistic Simulation Studies of Lithiated MnO_2 Nanostructures, A 60th birthday conference in honour of Prof. P.. E. Ngoepe 8th – 9th January 2013, R40 University of Limpopo Turfloop Campus.

K. M. Kgatwane, P. E. Ngoepe and D. C. Sayle, Atomistic simulation studies on Lithiated Manganese Dioxide Nanostructures, South African Institute of Physics Conference, 12-15 July 2011, Pretoria

K. M. Kgatwane, P. E. Ngoepe and R. R. Maphanga, Atomistic simulation studies of Lithiated MnO_2 nanostructures, South African Institute of Physics Conference, 27 September – 1 October 2010, Pretoria

International Conferences

P. E. Ngoepe, K. M. Kgatwane, M. G. Matshaba and D. C. Sayle, Atomistic simulation studies of lithiated and sodiated TiO_2 nanospheres, 231st Electrochemical Society Meeting, June 2017, New Orleans, USA

P.E. Ngoepe, K. Kgatwane and D.C. Sayle, “Atomistic simulation studies on mechanical properties of lithiated MnO_2 nano-architectures”, 224th Electrochemical Society Meeting, October 2013, San Francisco, USA.

P.E. Ngoepe, K. Kgatwane and D.C. Sayle, “Large scale simulation studies of lithiation in MnO_2”, The 6th International Conference on Advanced Lithium Batteries for Automotive Applications (ABAA6), September 2013, Argonne National Laboratory, Chicago, USA

P. E. Ngoepe, K. M. Kgatwane and D. C. Sayle, Atomistic simulation studies on lithiation of MnO_2 nano-architectures, 224^{th} Electrochemical Society Meeting, October 2013, San Francisco, USA

P. E. Ngoepe, K. M. Kgatwane and D. C. Sayle, Atomistic simulation studies on the volume expansion of MnO_2 nanosphere, 223^{th} Electrochemical Society Meeting, May 2013, Toronto, Canada

K. Kgatwane, P.E. Ngoepe, R.R. Maphanga, T.X.T. Sayle, and D.C. Sayle, “Atomistic simulation study of lithium manganese oxides for Li-ion batteries”, International Battery Association Meeting, April 2011, Cape Town, South Africa

The work has also appeared in the following invited lectures.

B. Shibiri, R.S. Ledwaba, K. Kgatwane, D.C. Salye and P.E. Ngoepe, “Atomistic simulations on structure and mechanical properties of nano-architectured Li-Mn-O Cathode upon Li-intercalation”, 70th Annual International Society Electrochemical Society Meeting, August 2019, Durban, **(Invited Lecture)**

R.S. Ledwaba, K. Kgatwane, D.C. Sayle and P.E. Ngoepe, “Simulation on mechanical properties of electrodes during intercalation”, International Battery Association Conference, March 2018, Jeju, South Korea. **(Invited Lecture)**

R.S. Ledwaba, K. Kgatwane, M.G. Matshaba, D.C. Sayle and P.E. Ngoepe, “Simulated synthesis and characterisation of metal oxide nano-architectures”, African Materials Research Society Conference, December 2017, Gaborone, Botswana **(Invited Lecture)**.

K. Kgatwane, R.S. Ledwaba, M.G. Matshaba, D.C. Sayle and P.E. Ngoepe, “Simulated synthesis and characterisation of composite electrodes”, International Battery Association Conference, March 2017, Nara, Japan. **(Invited Lecture)**.

K. Kgatwane, R.S. Ledwaba, T.X.T. Sayle, D.C. Sayle and P.E. Ngoepe, “Simulated synthesis and characterisation of Li-Mn-O nanostructures”, International Battery Association Conference, March 2016, Nantes, France. **(Invited Lecture).**